Master's thesis

NTNU
Norwegian University of Science and Technology
Faculty of Information Technology and Electrical Engineering
Department of Electric Power Engineering

Dany Josué Tomé Robles

Superconducting Multiphase Wind Power Generator

Improve the nowadays electrical machines for higher power densities and efficiencies

European Wind Energy Master - EWEM
Supervisor: Robert Nilssen
Co-supervisor: Jonas Kristiansen Nøland
Co-supervisor: Jianning Dong (TU Delft)
August 2021

NTNU
Norwegian University of Science and Technology

TU Delft
Delft University of Technology

Dany Josué Tomé Robles

Superconducting Multiphase Wind Power Generator

Improve the nowadays electrical machines for higher power densities and efficiencies

European Wind Energy Master - EWEM

Supervisor: Robert Nilssen
Co-supervisor: Jonas Kristiansen Nøland
Co-supervisor: Jianning Dong (TU Delft)
August 2021

Norwegian University of Science and Technology
Faculty of Information Technology and Electrical Engineering
Department of Electric Power Engineering

NTNU
Norwegian University of
Science and Technology

TU Delft
Delft
University of
Technology

Superconducting Multiphase Wind Power Generator

by

Dany Josué Tomé Robles

in fulfillment of the requirements for the degrees of
MSc in Electrical Engineering at Delft University of Technology
&
MSc-Technology in Wind Energy at Norwegian University of Science and Technology,

under the European Wind Energy Master's programme.

To be defended publicly
on Wednesday August 18, 2021 at TU Delft.

Supervisor:	Dr. ir. J. Dong,	TU Delft
Thesis committee:	Dr. Thiago Batista Soeiro,	TU Delft
	Dr. ir. J. Dong,	TU Delft
	Prof. R. Nilssen,	NTNU
	Prof. J. Nøland,	NTNU

Preface

This report presents the Master's thesis work performed from January until August 2021. The thesis is part of the joint program, European Wind Energy Master (EWEM), from the Faculty of Electrical Engineering, Mathematics & Computer Science at TU Delft and the Faculty of Information Technology and Electrical Engineering at NTNU.

The thesis describes the following: 1) an overall assessment of 3 different configurations for multi-phase AC superconducting machines with Permanent magnets; 2) an optimization to reduce the AC superconductive losses by varying the armature coils' angular position; 3) a new design to improve the power factor and the iron losses reduction.

Most of the work is done at NTNU with the Department of Electric Power Engineering team, with the assessment of the co-supervisor at TU Delft, from the research group of DC Systems, Energy Conversion & Storage at the Department of Electrical Sustainable Energy.

During the evaluation process, it is discovered that multi-phase winding layouts improve the machine's overall performance. Nevertheless, the AC superconducting losses for the armature winding are not further reduced by designing a multi-phase symmetric winding. Thence, a change of the coil's angle position could reduce further the AC losses. This means a 3D design of armature coils is the next step for adequately assessing the superconducting rotating machines.

I want to thank Robert Nilssen for his outstanding support throughout the process by keeping me focused and letting me explore wider boundaries into the deep void of knowledge. Furthermore, I want to thank Jonas Noland for his passion and patience, especially for explaining good modelling in COMSOL. Also, I want to thanks Prof. Jianning Dong to be my co-supervisor at TU Delft and Prof. Thiago Batista Soeiro to be part of the Thesis committee.

Also, I wish to thank my entire family for their unconditional support and love, especially during a pandemic. Last but not least, I would like to thank my friends back in Honduras; their joy and help make the hard work and staying abroad less harsh.

Dany Josué Tomé Robles

Trondheim, August 2021

Abstract

An investigation into AC superconducting coils is performed with a permanent magnet generator for a wind power turbine of 15 MW. Two reference models are sized: on the one hand, a DTU and NREL 15 MW wind turbine model is taken as a reference to set the mechanical speed according to the output power and the mechanical constraints of the blades; and on the other hand, a 10 MW AC superconducting PM design by Dong Liu is taken as a reference to set the geometry and slot-pole combination, and resized the machine to 15 MW. Both reference models are fractional slot concentrated windings.

The aim is to study the effects of multi-phase symmetric windings on the AC HTS coils and the overall performance of a superconducting PM machine. Thus: 1) A comparison is made between 3-phase and 12-phase windings with the same machine geometry. 2) A design of a 24-phase winding is made to endorse the findings and comprehend the multi-phase symmetric windings and their advantages. 3) The AC superconducting losses are assessed for the different winding layouts with the same current and turns per coil, focusing on the behaviour of the magnetic fields into the HTS coils. The analysis found that multi-phase symmetric windings enhance the machine's magnetic behaviour by making it smoother and eliminating the space sub-harmonics. Furthermore, reducing the flux densities' rippling behaviour in the airgap and the iron causes a reduction in hysteresis and dynamic losses. Also, the better winding factor of multi-phase windings improves the output power, making the machine even more compact. Moreover, to achieve an excellent multi-phase symmetric winding layout, the phasors must be unique.

However, it is observed that using symmetric multi-phase windings cannot improve the AC losses and power factor. On the first hand, the hysteretic superconducting losses for HTS tape coils depend on the magnetic flux line's incident angle. On the other hand, the power factor strongly depends on the magnetic energy stored in the magnets, related to the volume and remanent flux density. Furthermore, it is found that having AC superconducting armature coils, the magnetic field repulsion creates a fluctuating behaviour in the airgap, affecting the tangential and radial forces in the machine. Therefore, a parametric sweeping is done to vary the HTS coil's angular position, finding that perpendicular flux lines to the coil's side reduce further the AC losses. Nonetheless, this creates more repulsion of magnetic fields, making a stronger fluctuating magnetic flux density in the airgap, producing higher radial forces that can harm the machine's structure.

A new design is proposed to improve the power factor and prove that having unique phasors into multi-phase symmetric winding layouts enhances the machine's performance. Finally, three main conclusions are made: 1) multi-phase symmetric windings enhance the machine's performance by using unique phasors, helping to reduce further the magnetic rippling behaviour. 2) AC hysteresis superconducting losses and the Meisner effect for HTS tapes firmly depend on the flux lines angle. Thus, a 3D coil must be designed and assess. Finally, 3) Superconducting machines with bulkier permanent magnets can achieve better power factors.

Sammendrag

En undersøkelse av AC-superledende spoler utføres med en permanentmagnetgenerator for en vindkraftturbin på 15 MW. To referansemodeller er dimensjonert: på den ene siden blir en DTU og NREL 15 MW vindturbinmodell tatt som en referanse for å stille den mekaniske hastigheten i henhold til utgangseffekten og de mekaniske begrensningene til bladene; og på den annen side er et 10 MW superledende PM-design av Dong Liu tatt som en referanse for å sette geometri og spaltepolskombinasjon, og endre størrelse på maskinen til 15 MW. Begge referansemodellene er fraksjonerte spaltekonsentrerte viklinger.

Målet er å studere effekten av flerfasede symmetriske viklinger på AC HTS-spolene og den totale ytelsen til en superledende PM-maskin. Og dermed: 1) En sammenligning er laget mellom 3-fasede og 12-fasede viklinger med samme maskingeometri. 2) En utforming av en 24-faset vikling er laget for å godkjenne funnene og forstå de flerfasede symmetriske viklingene og fordelene deres. 3) AC-superledende tap vurderes for de forskjellige viklingsoppsettene med samme strøm og svinger per spole, med fokus på oppførselen til magnetfeltene inn i HTS-spolene. Analysen fant at flerfasede symmetriske viklinger forbedrer maskinens magnetiske oppførsel ved å gjøre den jevnere og eliminere rom-subharmonikken. Videre forårsaker reduksjon av fluktdensitetens krusende oppførsel i luftgapet og jernet en reduksjon i hysterese og dynamiske tap. Dessuten forbedrer den bedre viklingsfaktoren for flerfasede viklinger utgangseffekten, noe som gjør maskinen enda mer kompakt. Videre må fasorene være unike for å oppnå et utmerket flerfaset symmetrisk viklingsoppsett.

Imidlertid observeres det at bruk av symmetriske flerfaseviklinger ikke kan forbedre vekselstrømstap og effektfaktor. På den første siden avhenger de hysteretiske superledende tapene for HTS-båndspoler av magnetfluxlinjens innfallsvinkel. På den annen side avhenger kraftfaktoren sterkt av den magnetiske energien som er lagret i magneter, relatert til volum og gjenværende flytdensitet. Videre er det funnet at å ha vekselstrøm superledende anker spoler, magnetfelt frastøtelse skaper en svingende oppførsel i luftgapet, som påvirker de tangentielle og radiale kreftene i maskinen. Derfor blir en parametrisk feiing gjort for å variere HTS-spolens vinkelposisjon, og finne at vinkelrette flukselinjer til spolesiden reduserer vekselstrømstapene ytterligere. Ikke desto mindre skaper dette mer frastøting av magnetfelt, noe som gir en sterkere svingende magnetisk flytdensitet i luftgapet, noe som gir høyere radiale krefter som kan skade maskinens struktur.

En ny design er foreslått for å forbedre effektfaktoren og bevise at å ha unike faser i flerfasede symmetriske viklingsoppsett forbedrer maskinens ytelse.

Til slutt trekkes tre hovedkonklusjoner: 1) flerfasede symmetriske viklinger forbedrer maskinens ytelse ved å bruke unike faser, noe som bidrar til å redusere magnetisk krusende oppførsel ytterligere. 2) AC-hysterese superledende tap og Meisner-effekten for HTS-bånd er avhengig av fluxlinjevinkelen. Dermed må en 3D-spole utformes og vurderes. Til slutt, 3) Superledende maskiner med større permanente magneter kan oppnå bedre effektfaktorer.

Nomenclature

Abbreviations

AC	Alternating current
Bi-2223	A type of Bismuth Strontium Calcium Copper Oxide alloy
Bi-Sr-C-Cu-O	Bismuth Strontium Calcium Copper Oxide alloy
CICC	Cable-in-Conduit Conductors
DC	Direct current
EuBCO	Europium barium copper oxide alloy
FSCG	Fully Superconducting Generator
FSCW	Fractional Slot Concentrated Winding
HTS	High Temperature Superconductor
HVDC	High-voltage direct current
LCCoE	Levelized Capital Cost of Energy
LCM	Least Common Multiple
LTS	Low temperature superconductor
M	Number of power electronic modules
MC	Matrix converter
MFT	Medium Frequency Transformer
MgB2	Magnesium deboride alloy
Nb3Sn	Niobium-tin alloy
NbTi	Niobium-titanium alloy
NbZr	Niobium-zirconium alloy
PbBi	Lead-bismuth alloy
PMG	Permanent Magnet Generator
PSCG	Partially Superconducting Generator
PTW	Power-to-weigth ratio
REBCO	Rare-earth barium copper oxide alloy
SC	Superconductor/Superconducting/Superconductivity
SCPMG	SC Permanent Magnet Generator
TRL	Technology readiness level
TTW	Torque-to-weight ratio
Yb-Ba-Cu-O	Yttrium Barium Copper Oxide alloy

Parameters

A	Magnetic vector potential
α_m	Magnet's coverage
α_u	Slot pitch angle/Phasor angle/ Slot angle
α_z	Angle of adjacent voltage phasors
A_{sc}	SC area
b	Denominator of q

B_1	Fundamental magnetic flux density
B_{g1}	Airgap's fundamental magnetic flux density
B_ϕ	Angular flux density
B_r	Magnet's remanent flux density/ Radial magnetic flux density
B_{yr}	Rotor's yoke magnetic flux density
C_m	Motional machine's constant
D_{ag}	Airgap's diameter
D_{er}	Rotor's external diameter
D_{ir}	Rotor's internal diameter
D_{is}	Stator's internal diameter
D_{os}	Stator's outer diameter
$\mathcal{E}$	Electromotive force
E_o	No-load RMS induced voltage or Back-EMF / Standard Electric field criterion
ϵ	Coil span
f_e	Electrical frequency
F_r	Radial force
F_t	Tangential force
h_{ag}, δ_{air}, δ	Airgap's length
H_c	Critical magnetic field
h_{sc}	SC height
h_{yr}	Rotor's yoke thickness
h_{ys}	Stator's yoke thickness
I	Current
I_c	Critical current
i_{dq}	dq current
I_u	Slot current
J_c	Critical current density
J_e	Engineering current density
J_{sc}	SC current density
k_C	Carter's coefficient
K_d	Distribution factor
K_i	Lamination stacking factor
K_p	Pitch factor
K_s	Electrical loading
K_{sat}	Iron saturation
K_{sc}	SC material percentage
k_{wdg}	Winding factor
L	Machine's length
λ	Machine's geometry ratio
λ_{dq}	dq flux linkage
L_d, L_q	d-q inductances
l_m	Magnet's height
m	number of phases
MMF	Magnetomotive force

μ_{rec}	Magnet's recoil permeability
N	Number of turns
n	Exponent experimetal factor for E-J power law
N_{coil}	Number of turns per coil
$N_{parallel}$	Number of parallel SC wires
N_{ph}	Number of series-connected turns per phase
N_{sec}	Number of sector divided the machine's geometry
ω	Angular frequency
w_{coil}	SC coil's width
w_m	Magnet's width
w_{sc}	SC width
w_{sl}	Slot width
P	Electrical power
P_{ac_T}	Total AC losses
P_d	Dynamic iron losses
P_e	Eddy current losses
pf	Power factor
P_f	Ferromagnetic hysteresis losses
P_h	Hysteresis iron losses
P_{sc}	Hysteresis superconducting AC losses
ϕ	Electric scalar potential
ϕ_b	Phase belt
Φ_B	Magnetic flux
ϕ_d	Phase displacement for the symmetrical sub-systems
ϕ_p	Phase progression of the symmetrical sub-system
Φ_p	Pole magnetic flux
Φ_{p1}	Pole fundamental magnetic flux
p_r	Pole-pairs
p_r'	Number of pole-pairs in a base winding
Ψ_m	Magnet's flux linkage
q	Number of slots per pole per phase
Q_s	Number of slots
Q_s'	Number of slot in a base winding
s	Phasors skipped in the numbering of the voltage phasor diagram
σ	Conductivity
σ_0	Critical conductivity
σ_n	Normal shear stress
σ_t	Tangential shear stress
t	time/largest common divider
T	Torque
τ_p	Pole pitch
τ_s	Slot pitch
τ_v	Phase zone distribution
T_c	Critical temperature

θ	Angle
Θ_{sv}	Stator current linkage amplitude of vth harmonic
$\mathbf{T_r}$	Radial Maxwell's stress tensor
$\mathbf{T_t}$	Tangential Maxwell's stress tensor
v	Harmonic order
X_a	Armature reactance
y_Q	Coil span in slots
z	numerator of q

Table of Content

List of Figures

List of Tables

1 Introduction

In this chapter, the motivation towards the research topic is discussed. The latest investigations will identify the scientific gap of the multiphase and superconducting machines, followed by the statement of the research question. Finally, the research questions will address the outline of the thesis.

1.1 *Background*

Nowadays, the electric sector is changing towards a sustainable energy supply in which the main goals are efficiency, costs, reduction of fossil fuels, and rationality of the use of resources. The growth of offshore wind power generation has been driven towards bigger and farthest from shore wind parks. Thus the challenge to create more compact and lightweight structures and machines have become a necessity for the industry.

Therefore, designing compact and efficient machines is of utmost importance to renewable energies, especially offshore wind power technologies. One of the technologies that have been investigated through time in electrical machines is the usage of superconductors. Recently three projects have been developed to prove the feasibility of DC superconducting machines, that is, a superconducting field winding to enhance the magnetic loading of the machine. Those are INNWIND, Suprapower, and EcoSwing. The latter has been successfully proved with a technology readiness level (TRL) equal to 7, achieving an airgap shear stress that doubles compared to a Permanent Magnet Generator and a weight reduction up to 24%. Also, has been proved the reliability and robustness of the generator design.

It is important to remark that these European major projects have been carrying out by implementing superconductors into the field windings. However, there has not been any major project of superconductors implemented in the armature windings. The main issue regarding this approach is that superconductivity losses have a strong dependence on the frequency. For instance, in aviation, that requires high-frequency motors, it is a challenge to achieve an AC superconducting motor, nonetheless for an offshore wind power turbine operates at low frequencies, especially for big turbines, the frequency goes even lower due to the mechanical limits of the blades, hub and the whole offshore structure. For this reason, an AC superconducting offshore wind power generator is a relevant design approach to prove the readiness of the nowadays superconducting materials and generator designs.

Another remarkable technology is multiphase electrical machines, which have been barely assessed. Nevertheless, they have been proven to reduce losses, enhance performance, increase torque/power density, and provide more degrees of freedom into the design of the electrical machine. Nonetheless, the primary focus has been on asymmetric windings, which have multiple sets of m-phase windings, letting aside the symmetric windings of high-phase order. The main difference in having symmetric windings is that they are electromagnetically coupled with all the phases. In contrast, asymmetrical ones have multiple sets of windings that are magnetically coupled and electrically isolated.

Moreover, multiphase asymmetric windings have been designed and modelled with superconducting field windings machines, achieving improvements in the performance and reducing AC losses of the superconducting field windings. However, there has not been any investigation into AC superconducting multiphase symmetric armature windings. Thus the investigation will combine the two paths: on the one hand, the superconducting armature windings, and on the other hand, the multiphase symmetric windings.

1.2 *Problem description*

It is known that superconducting coils enhance the power density of an electrical machine, and a multiphase winding provides various advantages and more degrees of freedom to the winding design. The main focus of a multiphase winding has been asymmetrical or split-phase windings, which has multiple sets of symmetrical windings. The most common is to have multiple 3-phase windings. However, to design these windings, all the groups have to be electrically decoupled. Thus, every single set must be controlled independently, meaning power electronics must also be decoupled control systems.

Nonetheless, a high-phase order symmetrical winding could offer wider electric and magnetic loading operability because it is electromagnetically coupled. Therefore, power electronics must control only one electrical system—furthermore, the line-to-line voltage decreases, resulting in less coil insulation thickness.

Therefore, combining the advantages of superconductivity and multiphase windings, high power density machines could be designed. Thus, the main research question is:

> Is it suitable to design a high-phase order symmetrical multiphase superconducting machine for an offshore wind power generator?

1.3 *Problem scope*

The investigation and analysis main focus is the stator with AC superconducting armature windings. Thus, a PM rotor is designed. The following questions will be used to assess the machine's performance with different winding configurations:

- It is suitable to design a PM AC superconducting machine?
- What are the acceptable: 1) AC losses, 2) PM's demagnetization level, 3) Power factor, and 4) Iron losses for a PM AC superconducting machine?

- How does the repulsion of the magnetic field fluxes of the AC superconducting coils affect the radial and tangential forces in an electrical rotating machine?

1.4 Thesis structure

The present work is divided into 11 parts. 1) the introduction, where the scientific gap is discussed and the problem is formulated; 2) the research methodology, where the design process is described, and the conditions for a good comparison are addressed; 3) literature review, where the historical evolution of superconductivity is addressed toward the latest superconducting rotating machine, and multiphase machines are discussed. 4) Wind power technology, a general review of offshore electrical power systems is addressed, a remark into novel wind power generators is discussed, and finally the two reference machine models are addressed; 5) underlaying theory and software, the electromagnetic physical model is described, the design and sizing equations are presented, the superconductivity is discussed, the different losses in superconductors are addressed, the superconducting empirical model known as E-J Power-law is presented, permanent magnet machines are discussed, the winding design layouts are presented and extended to multiphase windings, the current density distribution in a slotted machine is addressed, the iron losses calculations are discussed, the software modeling is described, and finally the power factor calculation is presented for a extended park transformation matrix for multiphase systems; 6) Design, the design philosophy is depicted, the superconductor wire is sized and designed, the fractional slot concentrated winding for 3-phase configuration is sized and designed, then the 12-phase and 24-phase are designed with the same current whilst the number of turns per phase is decreased accordingly; 7) Modelling and analysis, the COMSOL's modeling for the superconducting coil is presented, the set-up for the machines geometries are depicted, the assessment is performed for all the configurations, and a discussion about the results is done and verify with a test model; 8) Optimization, an optimization for the reduction of the AC losses in the superconducting armature coils is performed by changing the angular position of the coils in the slots according to the flux lines tilting angle; 9) a new design is proposed to enhance the AC superconducting PM multiphase machine's performance; 10) conclusions and future work, the conclusions are done in relation to the results, and finally the future work is presented; 11) Bibliography is shown; and 12) the appendix, where the design philosophy is depicted, the data sheet for the iron losses calculations is shown, the Tesla's eggs of Columbus machine are depicted to comprehend multiphase systems, and further graphs are presented related to the new designs.

2 Research methodology

A design of a superconducting machine starts with the selection of the application topology, e.g. Aircraft, wind turbines, trains, etc. Then, following the aim of the thesis, the assessment and reduction of losses for AC superconducting coils with multiphase winding layouts, the use of permanent magnets is the approach developed to focus solely on the armature winding.

For the present work, an offshore wind turbine topology is selected. The aspect ratio and the frequency of the machine are properly computed for 15 MW machine with two reference machine models, respectively. The usage of permanent magnets in the rotor as magnetic loading requires a ferromagnetic core to create a good magnetic flux path, which further implies a reduction in superconductive material. To performed the assessment, three different winding layouts are designed: three-phase (3-phase) winding, a twelve-phase (12-phase) winding, and a twenty-four-phase (24-phase) winding. The latter is proposed to endorse the previous findings and the scientific significance of multiphase windings.

The sizing of the machine consists of keeping the same aspect ratio, electric and magnetic loading. Thus, the 3 models will have the same values, independently of the winding layout design. In addition, a motional constant is introduced to assess the machines independently of the electric and magnetic loading, yielding an easier way to contrast the different output power of the machines, allowing a clearer assessment of the 3 machine's configurations.

To assess the multiphase windings, a FEM electromagnetic analysis is performed in COMSOL. The 3-phase and 12-phase machines share the same geometry, providing a direct comparison between them. On the other hand, the 24-phase machine's assessment is done independently because the geometry is changed to achieve symmetry condition in the winding layout. Nonetheless, some correlations are made with the previous models to enhance the comprehension of the advantages and behaviour of multiphase windings. Specific design considerations are made to have a good overall comparison of the different configurations: 1) the superconductor sizing, designing and modelling are done by considering the entire wire area as superconductive material capable of handling the design current. The AC losses are purely hysteretic superconductive losses calculated from the E-J power law using the resistive losses built-in COMSOL model. 2) the number of turns per coil is fixed to have the same armature coil geometry for each machine configuration, taking advantage of the superconducting properties of allowing a high current value whilst the voltage decreases with the number of turns per phase. And 3) the current is fixed to be the same for the 3 configurations to have a proper comparison. The current is aligned on the q-axis to achieve maximum torque per ampere in the PM machine. This is done by aligning the current to the back-EMF during the no-load condition in COMSOL software.

In the end, an optimization to reduce AC losses is explored. And a new machine design is done to achieve better power factor, reduce iron losses and enhance the torque-to-weight.

3 Literature review

One of the main research towards compact and lightweight generators is the use of superconductors. The discovery of superconductivity was made by the Dutch physicist professor Heike Kamerlingh Onnes in 1911 [9], where the magnetic field lines are expelled from the material, as is shown in figure 1. This first superconductive material was quenched by a field of only 0.07 T. Meissner discovered that the superconductivity is quenched when the magnetic field is raised. The flux lines re-entered into the geometry, but the superconductor material again expelled flux lines when reducing the field. The Meissner effect was fully reversible, indicating that superconductivity is a state of thermodynamic equilibrium and is much more than just zero resistance, which would freeze the flux in place. In 1930 in Leiden, Keesom, and de Haas found that some alloys could remain superconducting up to much higher fields, notably P_bB_i with a critical field at 4.2 K of ~ 1.7 T [10, 11]. Later in 1936, L. V. Shubnikov performed measurements to the magnetization as a function of the applied field on pure lead and lead alloys. The alloys are diamagnetic up to a lower critical H_{c1} field, after which they become partially diamagnetic until a much higher critical H_{c2} field, above which they are resistive, which means a quenching on superconductivity. For increasing alloying additions to the lead, H_{c1} becomes smaller, and H_{c2} becomes larger. This behaviour is known as Type-II superconductivity, with the pure metals showing Meissner behaviour being Type-I superconductivity, purely diamagnetic. Both behaviour curves are fully reversible. [12].

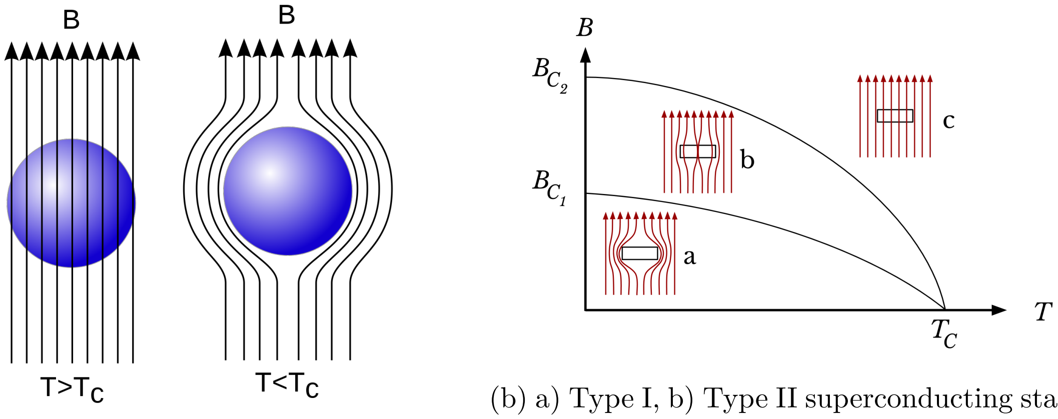

(a) Normal and superconducting states

(b) a) Type I, b) Type II superconducting states and c) normal state

Figure 1: Meissner effect

In the 1950s, a phenomenological theory of superconductivity was described by Ginzburg and Landau, which addresses superconductivity as a macroscopical phenomenon [13]. According to the Ginzburg-Landau Parameter, the type II superconductors, which Abrikosov introduced, form the basis of the superconducting technology that we have today because they can remain superconductive with higher fields compared to type I. This field penetrates the superconductive material in the form of the Abrikosov vortex lattice. Abrikosov predicted that, in the mixed state, the superconductor is threaded by a large number of filaments of normal material, each carrying one quantum of magnetic flux parallel to the applied field. Each filament is surrounded by a vortex of supercurrent and tends to repel neighbouring filaments. The complete system arranges itself in a regular lattice and is held together by the external magnetic field [14, 15]. Later a microscopic explanation to this behaviour was given by Bardeen, Cooper, and Schrieffer (BCS Theory), showing how the electrons could condense into Cooper pairs (two electrons bounded at low temperatures $T < T_c$, T_c: Superconducting Critical Temperature), in which the electrons are attracted to each other via interaction with the lattice phonons [16].

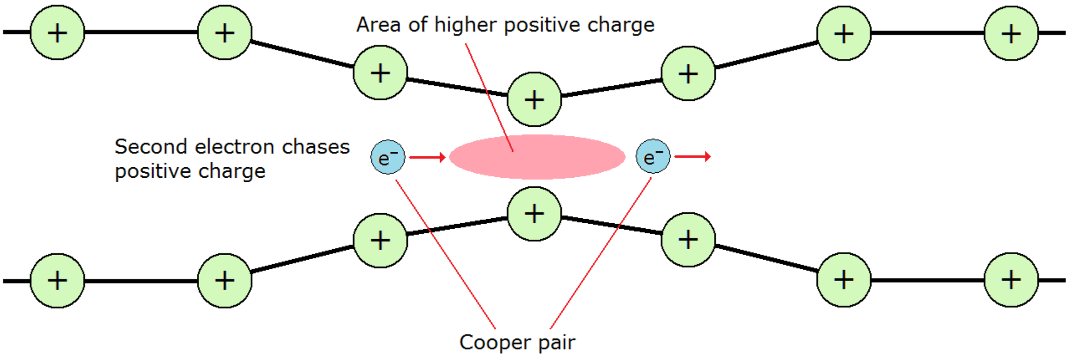

Figure 2: Cooper pair interaction with lattice phonons. Extracted from [1].

Nevertheless, Type II superconductors can operate at much higher applied fields; they cannot support a useful transport current because there is no opposition to the motion of the flux filaments (Vortex). Introducing inhomogeneities ("flux-pinning") to the material improved the transport current. These are known as "hard" or "high-field" superconductors. The strength of the pinning centres determines the critical current density. In the end, the superconductivity is determined by 3 parameters: Temperature T_c, the magnetic field applied H_c, and current density J_c [15].

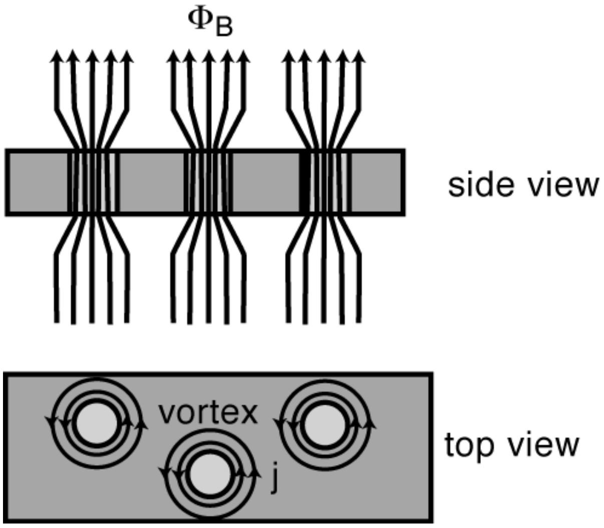

Figure 3: Flux pinning. Extracted from [2].

For engineering, the leap was done in 1961 by Kunzler et al. [17] for the Nb_3Sn, achieving current densities exceeding 1000 A/mm^2 in magnetic fields as large as 8.8 T. Subsequently, the niobium-zirconium (NbZr) and niobium-titanium (NbTi) alloys were shown to display similarly useful properties. Further, to develop superconducting coils and avoid (electrical) degradation and (cryostatic) instability, the superconductor is embedded in a matrix material of high electrical and thermal conductivity (copper is most commonly used), and to slow down the flux unstable movement ("flux jumps"), due to low thermal diffusivity and high magnetic diffusivity, a matrix of high-conductivity typical material is used [15].

Scientists built the AC superconducting machines in the early 1960s. However, AC power losses are linearly dependent on the frequency and the filament diameter. Reduction in AC loss is, therefore, consistent with stability criteria in requiring small filament diameters that must also be effectively decoupled [15]. In 1964 Superconductivity in AC armatures were addressed by [18] concluding that high AC losses and low AC current densities are not economical because of the large refrigeration power needed to cool down.

It is not until the next jump of the High-Temperature Superconductors (HTS) in 1987 by Wu et al. [19] where they synthesized Yb-Ba-Cu-O (YBCO) at $T_c > 77\,\mathrm{K}$, which is at a temperature higher than the liquid nitrogen. This marks a new era in Superconductors, however, synthesizing into wires represented a difficult task. Is up to 1995 (eight years after the discovery), the HTS wire was made with the compound Bi-Sr-C-Cu-O (referred to as BSCCO, $T_c = 110\,\mathrm{K}$), which exceeded the current carrying capability of copper (cooled to the same temperature as BSCCO). Nine years later (2004), the current-carrying capacity of superconducting BSCCO is 15 times greater than its copper counterpart. However, by that time, 3 technological needs are required: cost reduction, AC losses reduction, and operation at higher temperatures to reduce refrigeration power and cryogenic design complexity [20].

Other important achievement in superconductors is the discovery of MgB_2 (Magnesium Diboride) at $T_c = 39\,\mathrm{K}$ by Nagamatsu [21] in 2001. The application range for MgB_2 conductors has two main regions: the "low field" applications using cryogenic free systems able to work in a temperature range around 20 K, and the "high field" region where the conductor could be used like NbTi at 4.2 K but at magnetic fields potentially higher than those currently reachable with this material (around 8 T at 4.2 K) [22]. In comparison, YBCO wire is prone to be damaged due to its coated structure, and currently, its price is relatively high. Compared with YBCO wire and Bi2223 wire, the MgB_2 wire has the merits of low cost, but its critical current is small under the high applied magnetic field [23]. Therefore, in terms of weight and volume, YBCO is a suitable choice. But in terms of price MgB_2 is a better choice [24, 25, 26].

Furthermore, the MgB_2 has been a potential candidate for low AC losses superconductor [27, 28]. The company HyperTech has been developing MgB_2 conductors. In 2017, they achieved a new class of low loss MgB_2 strands with high filament count with a small twist pitch value, with no J_c degradation related to the mechanical handling of the material [29]. Hitachi Ltd has been developing low loss MgB_2 [30]. The most recent development of HyperTech has been in [31] with an average J_e over the 0-3 T sweep of 1320.39 A/mm^2, with a total loss value in the range of 5 W/cm^3 below 150 Hz.

Another improvement into the superconductors wires has been the Cable-in-Conduit Conductors (CICC) designs to withstand mechanical stress, which has been standardized for High Energy Physic projects, such as ITER (International Thermonuclear Experimental Reactor) [32, 33, 34, 35, 36]. It is important to notice that the ITER project, which is the largest nuclear fusion project in the world, will use for the Center Solenoid (transformer primary) a 45 kA Nb_3Sn superconducting conductor designed to operate at 4.5 K up to a maximum magnetic induction of 13 T, providing a required magnetic flux swing of 266.6 Wb to induce up to 15 MA as plasma current (Secondary) [37], therefore the forces that the conductors have to withstand are very high. For the Large Hadron Collider (LHC) case, a work into MgB_2 cabling has been going on to upgrade a superconductor link. These MgB_2 cables are designed to transport the maximum current of 3 kA ($D \approx 7$ mm), 2 × 3 kA co-axial ($D \approx 10$ mm), and 7 kA ($D \approx 9$ mm) at 25 K (1 T) with a temperature margin of 5 K concerning the nominal operating temperature (20 K) [38, 39].

This same path has started in the electrical machines, especially when the cryogenics efficiencies have improved for temperatures between 20 K and 50 K by 5 times. A miniature CICC is proposed in [40, 41]. Other important works as been done for cabling [42], where the current carrying capabilities are studied.

In the case of (RE)BCO materials, RE stands for Rare Earth. A study with high-performance EuBCO stated that due to the high prices of material, it is cheaper to design a machine at 20 K instead of 64 K. This is because, at lower temperatures, the overall superconductivity is enhanced. Thus, stronger flux densities can be generated with less material [43].

To summarize, the superconducting materials represent a clear path to improvement for electrical rotating machines. However, special attention has to be done to low-cost materials, low AC losses capabilities, and High-Medium Temperature comparable to Liquid Hydrogen (LH_2), which will have a bigger market in the coming years [44, 45].

3.1 Superconducting machines

After the advent of HTS, an increase in research and funding has been done towards superconducting generators. Mainly for partially superconducting generators, being focus only on the DC superconducting coil of the Field Windings. With the appearance of HTS wires, the AC losses of superconductors have started to decrease. Therefore an important number of investigations into fully superconducting generators has been accomplished. High-speed and low-speed superconducting machines are presented as follows:

3.1.1 High-speed applications

The high-speed superconducting machines are commonly designed for Aircraft applications.

For fully superconducting machines, it has been found that the highest PTW (Power-To-Weight) values are reached for working point flux densities in the range of 0.55-0.9 T. This behaviour can be attributed to the high sensitivity of the MgB_2 wire to AC loss. Even for the partially superconducting machines with an optimized design, the working point flux density will be around 1 T, which are similar to what a Permanent Magnet Machine could achieve [46].

Furthermore, it has been shown that having iron teeth in a yokeless, fully superconducting machine improves the stator's magnetic performance, and the armature's AC losses are reduced. This is because the AC flux density seen by the superconductive armature is diminished. In terms of PTW, an air-cored fully superconducting machine is the best option with $PTW = 11.7\,\mathrm{kW/kg}$, whereas a slotted yokeless stator machine and a PM machine have $PTW = 6.5\,\mathrm{kW/kg}$, and $PTW = 5.2\,\mathrm{kW/kg}$ respectively [47].

Another area of research is also applying electromagnetic shields to the design to contain the flux densities within machine domains. E.g. is done by using a superconducting shield that prevents the penetration of the flux density to the outside boundaries. However, this design increases the AC losses due to the increased average flux density in the airgap. Nevertheless, the shielded machines could achieve PTW 5 times higher than an iron-cored machine, both having airgap flux densities in a range from 0.45 to 1.3 T [48].

It is important to note that for a high-speed machine, the high-frequency AC fields increase the losses. Thus, the reduction of the number of poles is convenient. The AC losses increase almost linearly with the number of pole pairs, mirroring the frequency-dependent AC loss of the MgB_2 coils. Therefore with a low-pole-count machine, the AC losses are reduced, and so are the cooling requirements. However, the thickness of the yoke increases ($h_y \propto {}^1\!/_p$). Thus the machines with higher pole pairs are the lightest, but also the cooling requirements increase. Hence, to achieve higher performances, the airgap flux density is diminished to around 0.8 T [49, 50, 51].

Therefore, for a high-speed, fully superconducting machine, the average flux density ranges from 0.45 to 1.3 T to maintain low AC losses and achieve higher performances. Thus, using Halbach-NdFeB magnets arrays is an area of further research.

3.1.2 Low-speed applications

In the case of low-speed machines, the research has been done commonly with Offshore Wind Power Turbines.

Opposite to what happens in a high-speed machine, the AC losses due to AC fields in a low-speed machine decrease. Therefore the optimization to achieve higher performances is to increase further the flux densities produced by the rotor. The analysis shows that the achievable minimum total AC loss decreases with increasing airgap flux density. This is because the armature current needs to be decreased to give a safety margin to avoid quenching. On the other hand, when the airgap flux density decreases, armature current can be increased to compensate for the decrease in airgap flux density [52].

Therefore, for a low-speed machine, the sensitivity of superconducting wire to the changing airgap flux is lower, thus achieving higher flux densities improves the machine performance while keeping a safety margin of the current in the superconductor to avoid quenching.

For the case of a PM Superconducting Wind Power Generator, the main problem is the demagnetization of the PMs, which has little relation to the slot of the stator. It is mainly relevant to the design, the PM dimensions, and the current applied to the superconducting (SC) coils, which is the source of the magnetomotive force (MMF). The MMF produced by the SC coil is restricted to avoid PM's demagnetization. With the rising SC coil area per slot, the maximum allowed current, and the current density before demagnetization declined greatly. The airgap flux density is designed to be ($B_g \geq 0.25\,T$). Furthermore, it has been proved that a fully iron-cored machine has better output torque capability and higher efficiency compared to an iron-cored rotor with an air-cored stator [53]. It has also been proved that the fully superconducting machines, comparing to the partially superconducting machine, are lighter and are characterized by a lower cost of the superconductor [26].

In the case of the INNWIND european project, which is a partially (DC) superconducting machine for a wind turbine, scientists concluded that it could not outperform a PM machine [54].

According to the literature, lower AC losses are perceived by the armature superconducting winding for higher airgap flux densities for low-speed machines. Thus, a PM arrangement to achieve those higher magnetic fields is a difficult task. Therefore, due to lower AC losses and PM demagnetization, for a Wind Turbine Generator, the most suitable option to achieve higher performances is to use a fully superconducting machine [55].

Heretofore, scientists have been contributing to the knowledge of superconducting rotating machines in two separate topologies. On the one hand, for aviation, high frequencies contribute to higher AC losses in the superconducting coils; therefore, a reduction in the airgap flux density could lead to smarter design philosophy. And on the other hand, for wind power turbines, the low frequencies allow higher airgap flux densities; hence, fully superconducting machines might be a good design philosophy. However, improvements in the PM rotor's design and a better winding layout could allow a good performance without constructing a fully superconducting machine.

3.2 Demonstrator projects for superconducting machines

The European Union has funded three important projects. All of them partially superconducting generators (PSCG), which means superconductive field windings.

The SUPRAPOWER project, in which MgB_2 is used for the superconducting field windings, and is compared to a Permanent Magnet Generator (PMG) with the same output specifications, has been concluded that the designed PSCG shows a 26% weight reduction concerning a PMG, which permits a tower 11% lighter [56, 57].

The other big project was INNWIND, in which it is proved that having an iron core results in a lower LCCoE (Levelized Capital Cost of Energy) because it requires less superconductive material. Further, using iron teeth do not lead to excessive AC losses, and having a large number of slots per pole per phase can further reduce AC losses. It is found that using segmented armature can reduce the excessive short circuit torque because only one segment is short-circuited. The high short circuit torque is caused by the low inductance, resulting from the absence of iron or larger airgap. The advantages over PMG are not significant. However, to achieve competitive shear stresses and efficiencies, fully iron-cored are preferred, and other LTS and HTS materials are more feasible than MgB_2 due to higher flux densities achieved [54, 58].

Finally, the World's First Full-Scale MW-Class Superconducting Generator on a Direct Drive Wind Turbine, the EcoSwing Project, was successfully proved with a technology readiness level (TRL) equal to 7. The generator was segmented into four independent armature windings to reduce the short-circuit torque and to be able to use low-cost, compact IGBT modules. The air gap shearing stress is doubled in the HTS generator, and the weight reduction over the scaled PMG is 24%. The cryogenic design was fully tested and provided considerable redundancy. The EcoSwing HTS generator sustained three sudden short circuits in the converter system without any damage, which proves the reliability and robustness of the generator design [59, 60, 61].

For high-speed application, the biggest demonstrator of a partially superconducting machine has been the 36.5 MW motor funded by the Office of Naval Research from the USA, with 3 sets of 3-phase drives connected, creating a 9-phase machine. The investigation paper states [62] that the machine has passed all the tests. However, there is no further information regarding this machine.

3.3 Multiphase Generators

Multiphase armature windings have been proposed to increase the torque density, reduce the torque ripple, and enhance faults tolerance. Moreover, in superconducting machines, multiphase windings have been proposed to reduce the space harmonics contents in the armature reaction to reduce the AC losses in the superconducting field windings. Previously, the optimization for poles of various machines has been an important issue. However, none of them has done a winding analysis, which also is relevant due to the rotating MMF and its harmonics.

An initial approach of winding configuration is made for fully superconducting generators (FSCG) by Liu et al. [63]. To achieve higher power densities, the stator is designed toothless due to the high flux densities; however, this has a drawback: the absence of iron reduces the reactance and increases the short-circuit current short-circuit torque higher than 3 p.u. Therefore a fractional slot concentrated winding is suitable due to it has large leakage inductance. However, it has been proved that during a short-circuit event test, a quench of superconductivity is observed due to the short-circuit current is higher than the critical current of the superconductor. Nevertheless, the short-circuit torque is below 2 p.u.

Another approach is to use the multiphase armature windings to reduce the physical airgap. Usually, the physical airgap of a superconducting machine is significant due to AC losses induced by the rotating high flux densities generated by the field winding. It has been proved that the physical airgap can be reduced by applying multiphase armature windings, which results in higher torque production while not compromising the generator performance. The more the phases, the more the decrease in the physical airgap. For example, an asymmetrical 12-phase winding almost achieves a zero alternating field at the HTS field winding. Hence, one notable merit of multiphase windings is smaller ripple magnetic fields on the HTS field winding, which directly reduces AC losses and benefits the cooling system design [64]. Further, it has been proved that using a 6-phase Fractional Slot Concentrated Windings is capable of reducing 90% eddy current losses and 68% AC losses, producing a short-circuit torque below 3 p.u. that is accepted by mechanical structures in the wind turbine [65].

According to [3] the multiphase rotational machines can be divided into 2 categories: symmetrical and asymmetrical or split-phase windings. In which the latter consists of multiple sets of symmetrical sub-systems. For instance, a 15-phase machine shown in figure 4, which is connected to 3 sets of 5-phase symmetrical sub-systems.

$$\begin{aligned}
m &= 5\\
l &= 3\\
\phi_b &= \frac{180^\circ}{m} = 36^\circ\\
\phi_p &= \frac{360^\circ}{m} = 72^\circ\\
\phi_d &= \frac{180^\circ}{m \times l} = 12^\circ
\end{aligned} \tag{1}$$

Where m is the number of phases in the symmetrical sub-system, and l the number of sets of symmetrical sub-systems inside the asymmetrical system. Φ_b is the phase belt, Φ_p is the phase progression of the symmetrical sub-system, and Φ_d is the phase displacement for the symmetrical sub-system sets.

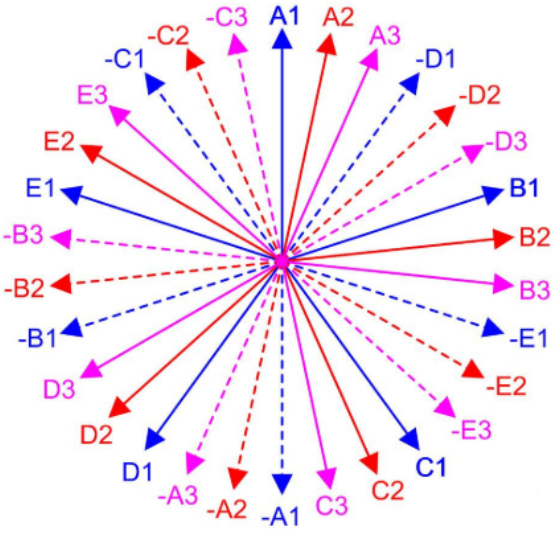

Figure 4: Multiphase asymmetrical windings. Extracted from [3].

Thus, multiphase windings systems can electromagnetically model various generators and reduce the short circuit torque. Moreover, multiphase machines have advantages, since it has a better airgap flux waveform due to a high number of stator phases and has harmonics that contribute to the torque called "Saturation Harmonics". The extra torque is obtained because the flux distribution in the airgap is flattened, avoiding the iron saturation for a wider operational range. A higher number of phases can produce a more sinusoidal magnetic field than the machine having smaller phases, even if it has a similar number of slots. Therefore a multiphase machine improves torque density, decreases cogging torque, reduces ripples produced by the armature reaction interaction with the rotor, reduces rotor losses, and is more fault-tolerant. [66, 67, 68, 69].

According to Masmoudi [70], a winding made up of m phases, with m an odd integer higher than unity, which is shifted by an electrical angle equal to $\frac{2\pi}{m}$, where the phases are concentrated in m slot pairs of N turns each and are fed by sinusoidal currents. These have a RMS-value I_{rms} and an angular frequency ω and are shifted by $\frac{2\pi}{m}$. The resulting fundamental rotating flux density is expressed as follows:

$$B_1(\theta, t) = \frac{\mu_0}{\delta_{air}} \frac{2}{\pi} N_{ph} \sqrt{2} I_{rms} \frac{m}{2} \cos\left(\theta - \omega t\right) \tag{2}$$

Therefore, it can be said that by increasing the number of phases, the magnetic rotating field increases. However, this is true if the magnetic circuit is not saturated. For conventional machines, the benefit of increasing the number of phases is the subdivision of the power in m circuits. In case of a failure of one circuit, the power reduction is equal to 1/m of the total power.

The discussion has focused on different winding layouts, machine configurations, and topologies for superconductive and multiphase machines. However, only DC superconductive machines have been assessed to a technology readiness level 7.

AC superconductive machines have not been appropriately assessed, especially the AC losses solely produced by the superconducting armature winding. Furthermore, PM superconducting machines are still an open question regarding the feasibility of a good machine. Moreover, in terms of multiphase armature windings, these configurations have been assessed only as asymmetrical windings, with multiple sets of electrically isolated windings.

An investigation into AC superconducting symmetrical multiphase machines to achieve compactness and feasibility is relevant. Furthermore, the usage of PM machines contributes to two utmost questions: feasibility of Superconducting PM machines and the assessment solely to the AC armature superconducting coils. As previously discussed, restricting the MMF could help to reduce the demagnetization of PMs. However, it is also true that wind turbines can achieve optimal performances with higher airgap flux densities without having too much AC losses due to low-frequency operation. Thus, a proper assessment of a superconducting PM machine has to be done, considering that it has to double the shear stress of a conventional machine.

4 Wind Power Technology

In this section, the wind offshore systems are addressed to have a holistic insight into the system. The elimination of an HVAC substation is discussed by introducing multiphase generators and multi-modular wind turbines. The superconducting wind offshore power generator is discussed. And finally, the reference models are presented.

The growth of offshore wind power generation has been driven towards bigger and farthest from shore wind turbines, thus to transport the energy from the wind park to a shore electrical substation demands the use of DC cables for distances longer than 50 km [4]. An offshore platform to hold the HVDC substation needs to be built to achieve an HVDC link from the wind park. This platform connects all the HVAC links from the different wind turbines arrays [71], as is shown in figure 5. In addition, exploring large wind turbines farther from shore has proven to increase capacity factors to 40%-50% [72].

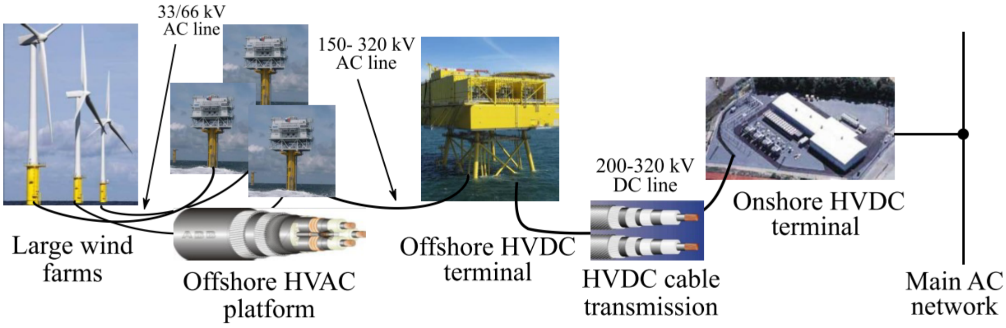

Figure 5: Common topology for HVDC offshore connection. Extracted from [4]

The growth in offshore wind power technologies leads to a wide field of research in many areas. From the mechanical point of view to the power electronics behind the control and robustness of the wind park integration into the electrical grids complying with the standards and regulations. In the specific field of generators, many different approaches have been investigated. For instance, investigations into eliminating the offshore HVAC platforms are caring out by two different approaches: multiphase transformerless generators and multi-modular wind turbines. This gives a necessarily multidisciplinary approach, meaning one must take the generator design itself into account and the power electronics and the interconnection between the wind turbine arrays. That being said, these investigations need a holistic and multidisciplinary approach. Nevertheless, being these approaches intrinsically wider have left behind some important issues to address to achieve higher technology readiness.

4.1 Multiphase transfomerless machine

In [73] a multiphase transformerless generator is presented. It uses multiple rectifier converters connected in series to increase the voltage at the DC-Link terminal, thus boosting the DC terminals voltages, allowing the possibility to eliminate offshore HVAC platforms. The topology for a multiphase transformerless generator is to connect every m-phase set to a single rectifier module and then connect in series the output DC voltage of all modules to elevate the DC voltage of all modules as is shown in figure 6.

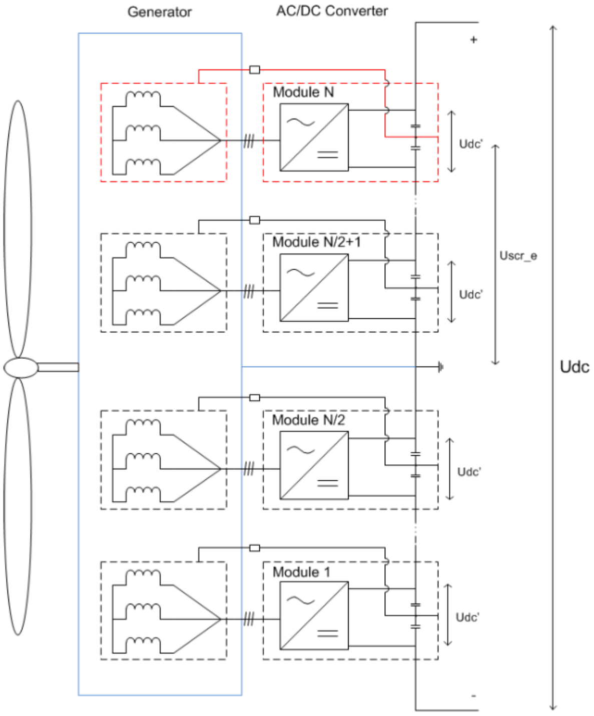

Figure 6: Multiphase transformerless topology. Extracted from [5]

According to Olsen [5] when the voltage at the DC-link is increased since the converters are galvanically connected to the generators, there are more possibilities to have an electrical breakdown. Thus, eliminating any possibility of short-circuits the electrical insulation and overall design of the generator and electronic components must accurately set up. To reduce the impact of the insulation thickness, an air-cored generator is proposed [74, 14]. Other literature suggests the use of MMC [75] and series-connected DC module for each phase of the generator [76]. In [77, 14] an N insulated stars, or a split drive train feeding is lightly addressed. These technologies need further investigation into the compactness and feasibility of ironless generators for wind offshore power plants. It is known that having an ironless generator will need more space into the hub of the wind turbine [78], thus this will lead to a higher complexity into the hub and blade design of the wind turbine. Furthermore, to achieve compactness, this configuration will need superconducting coils to reduce the machine size.

4.2 Multi-modular wind turbines

The other approach consists of a DC series-connected wind turbine array to increase the DC voltage and therefore eliminate the need for offshore substations, both HVAC and HVDC [6, 79] as is shown in figure 7. However, the foundation of this approach resides in the fact that eliminating offshore platforms does not takes into account the number of new components into every single wind power turbine hub that potentially could lead towards bigger wind turbine platforms to support the weight of the overall components, thus putting more complexity into the design of floating offshore platforms.

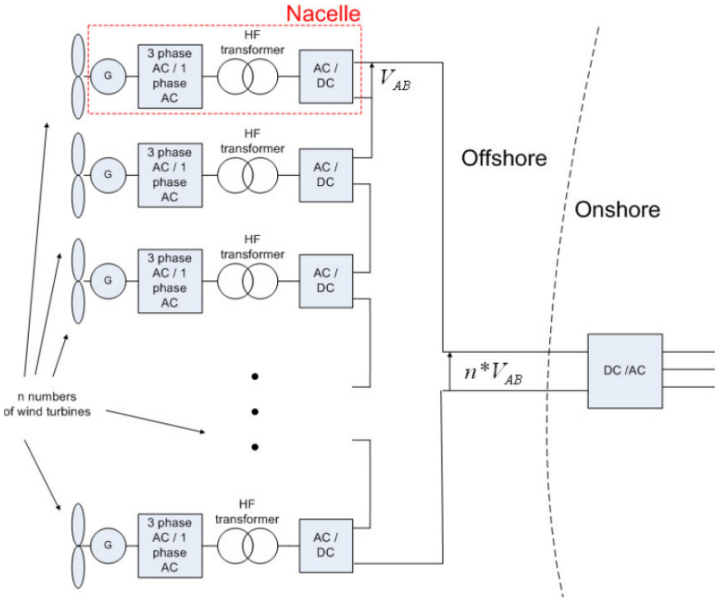

Figure 7: Multi-modular Offshore Wind Turbines. Extracted from [6].

Based on figure 7, another possible configuration is the use of a gearbox to divide the power into three generators. Then connect in series the DC terminals of each generator inside the wind turbine, and subsequently connect in series the DC voltage of different wind turbines to increase even more the DC voltage [80]. However, this leads towards more complexity and weight to the overall wind turbine.

To adequately address a DC series-connection and galvanic isolation, a multiphase topology shown in figure 8 is proposed as a possible candidate. The configuration consists of a multiphase generator connected to matrix converters and high-frequency transformers connected to rectifiers, where the DC terminal voltage can be increased further, as is shown in figure 8. The overall configuration depends on the transformers power capability and the number of phases.

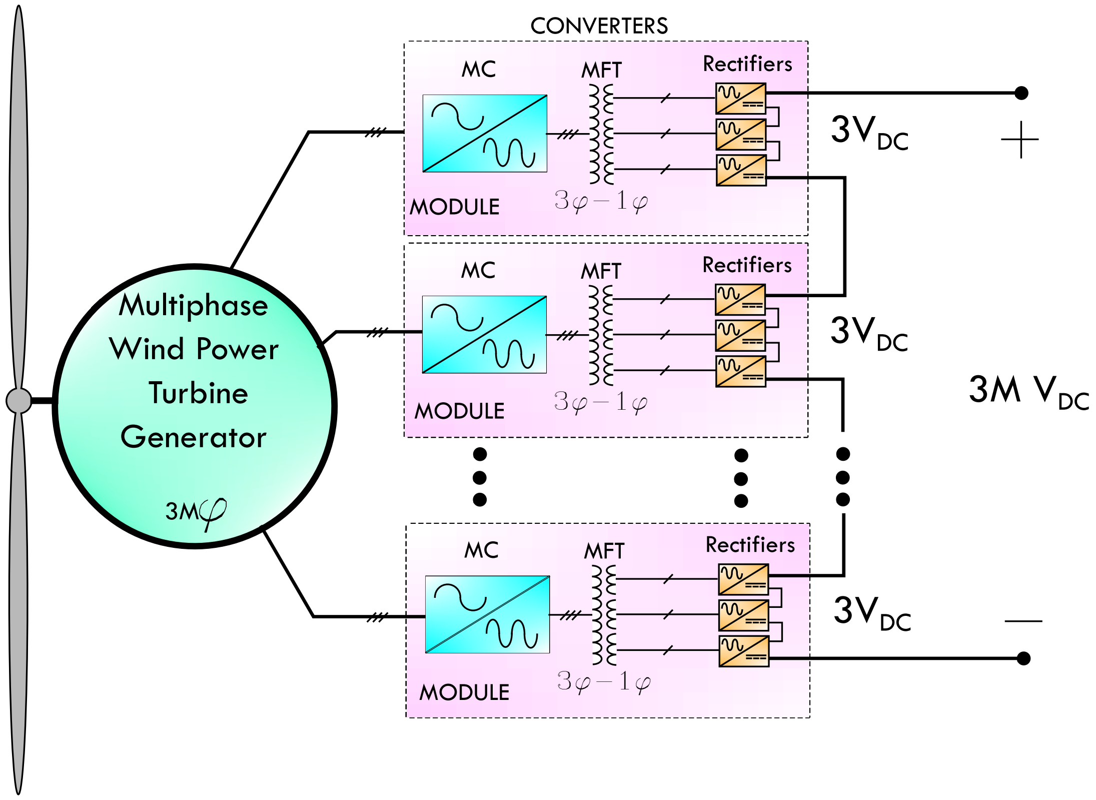

Figure 8: Multiphase machine and power electronics topology proposal

4.3 Superconducting generator

As previously discussed, superconducting generators can double the shear stress compared to a conventional generator, which means a reduction in the latter's size. However, one of the issues of superconducting field winding is the rotating cooling system, even though that could be easily changed to an outer rotor with a rotating armature winding whilst increasing the complexity of the generator.

The other approach, which is the one selected for current work, is an AC superconducting generator with permanent magnets. This approach reduces the complexity of a rotating cryogenic cooling system or a rotating armature winding. The main challenge to this approach is the AC losses of the superconductors, but the new fabrication process of the materials could reduce further the AC losses. For instance, for a laser-scribing fabrication technique, the HTS wire can further reduce the losses proportionally to the number of filaments scribed, as is shown by Suzuki et al. [81]. Moreover, due to the low-frequency operation of offshore wind turbines, the AC losses are less sensitive due to changing of airgap flux density.

Therefore, a reference model has to be set up to address the fundamental knowledge of the topic in a peer-review manner to achieve higher technology readiness.

4.4 Offshore wind power generator reference models

To start designing an offshore wind turbine, it is important to consider the mechanical constraints. For instance, a superconducting 20 MW generator with the size of a 10 MW conventional generator does not have the same RPMs due to the mechanical constraints of the design of the blades. Therefore, choosing a specific power of design also means selecting the right RPMs. In the end, the offshore wind turbine power selection will impact the blades, the size of the hub, the monopile or the platform.

A 15MW reference model is selected to perform the correspondent analysis to develop the next generation of offshore wind turbines. The International Energy Agency (IEA) has developed a wind reference model in collaboration with the National Renewable Energy Laboratory (NREL) and the Technical University of Denmark (DTU) [82], in which the generator is an outer rotor direct-drive permanent magnet with a fractional slot concentrated winding layout of $^2/_5$ slots per pole per phase. It uses copper for the armature winding. The slot-pole combination is of a high order, meaning 240 slots and 200 poles. However, superconductive coils are not very flexible when inserting them into a high order slot-pole combination. Therefore, only the power, the slots per pole per phase, and the rated speed are inputs for the present work.

Consequently, the coil's bending, AC losses, and winding layout must be considered when designing a superconductive machine. For example, dong Liu et al. [83] worked in permanent magnet superconducting generators design, in which the power factor and the demagnetization of the PM are assessed during normal and short circuit operation. However, to account for the minimum bending diameter of SC wires, an armature winding with fractional slot concentrated winding is a much simpler and safer candidate. In addition, due to the high field harmonics and eddy currents produced in the PMs, these can be segmented to cut off the path of eddy currents.

Dong Liu et al. states that a good design must reduce the power factor of the machine to around 0.6 to see the benefit of having SC windings, achieving $120\,\mathrm{kN/m^2}$ of shear stress, and around double the shear stress of a conventional PM machine. However, due to the low power factor, it will need a power electronic converter of which capacity is 50% larger than the converter for a $pf = 0.9$. Thus the cost of the converter will partly cancel the benefit of the small size and low weight of the generator. Moreover, having a high armature field reaction causes demagnetization at such low power factors. Finally, it shows that having a design with modular cryostats can reach high shear stress for low power factors.

In [84] Dong Liu et al. performed a study into power factor and shear stress with two designs: $q = 0.4$ and $q = 1$, obtaining similar results as the previous one. Hence, scientists must further investigate special designs for the SCPMG configurations to obtain a high shear stress capability and an acceptable power factor.

The NREL and Liu's machine parameters are taken as references for the present work.

5 Underlaying theory and software

In this section the scientific foundations are discussed. The Maxwell equations are reviewed and how these applies to present work. The designing equations in which relays the background of the rotating machines are mentioned. The superconductor dimensioning and AC losses calculations are addressed. The winding design layouts are discussed in order to consider the multiphase configurations. The iron losses calculations are reviewed. And finally, the software to make the analysis is addressed. The majority of the following equations are based in [85, 7].

5.1 Electromagnetic background

James Clerk Maxwell wrote his electromagnetic theory with 20 equations [86], in which Maxwell unified the electric and magnetic phenomena in a single theory of electromagnetism. At that era, William Rowan Hamilton developed a three-dimensional space algebra in which the complex numbers were involved as a non-commutative algebra, also known as quaternions. As Maxwell states in his treatise regarding the coordinate system developed by Descartes and Quaternions:

> But for many purposes in physical reasoning, as distinguished from calculation, it is desirable to avoid explicitly introducing the Cartesian coordinates, and to fix the mind at once on a point of space instead of its three coordinates, and on the magnitude and direction of a force instead of its three components. This mode of contemplating geometrical and physical quantities is more primitive and more natural than the other, although the ideas connected with it did not receive their full development till Hamilton made the next great step in dealing with space, by the invention of his Calculus of Quaternions [86, p. 8-9]

Thus, this approach was brand new but also very complex and not widely accepted. Therefore, later on, Heaviside re-wrote Maxwell's equation into the 4 modern vectorial notation that is widely spread and known [87], as is presented in the following:

$$\begin{aligned}
\nabla \cdot \mathbf{E} &= \frac{\rho}{\epsilon_0} \\
\nabla \cdot \mathbf{B} &= 0 \\
\nabla \times \mathbf{E} &= -\frac{\partial \mathbf{B}}{\partial t} \\
\nabla \times \mathbf{B} &= \mu_0 \left(\mathbf{J} + \epsilon_0 \frac{\partial \mathbf{E}}{\partial t} \right)
\end{aligned} \tag{3}$$

After the success of Maxwell's electromagnetism theory, many scientists created various technological artefacts. The most known are Nikola Tesla and Thomas Edison because of the AC-DC current wars. However, at the same time, Tesla presented his alternating current generator, Galileo Ferraris, already had designed a similar machine. Nonetheless, the impact of this development in electromagnetism to generate electricity came when these types of machines were introduced to society to electrify the world's main cities.

To achieve power transmission, the German electrical engineer Oskar von Miller promoted the demonstration of an experimental three-phase transmission system at the technical exhibition of Frankfort in 1891. The transmission line was 175 km long, delivering a 200kW three-phase power at 12.5kV. The electrical engineers who designed the system were Charles Eugene Lancelot Brown of Oerlikon and Michael von Dolivo-Dobrowolsky of AEG; it was a three-phase modification of Tesla's two-phase system. Then in 1893, the major commercial three-phase transmission system worldwide of 16 km was made in Sweden by Jonas Wenström [88].

In the case of electrical machines, Ampere's law is used to compute the analytical models. For ferromagnetic materials, the H-field is small due to the high permeability. Applying the line integration of the magnetic field strength around the current is a good approach to solve magnetic circuits and equivalent simplified versions.

$$\oint_C \mathbf{H} \cdot d\mathbf{l} = NI \tag{4}$$

In magnetic circuits, this is commonly known as magnetomotive force (MMF). The SI unit of MMF is Ampere-turn (AT). In general, a rotating MMF of constant amplitude will be produced by an m-phase winding excited by balanced m-phase currents of frequency f when the respective phase axes are located $2\pi/m$ electrical radians apart in space. The amplitude of this MMF wave will be $m/2$ times the maximum contribution of any one phase.

Production of a rotating MMF wave and the corresponding rotating magnetic flux density is key to multiphase rotating electrical machinery. It is the interaction of this magnetic flux density wave with that of the rotor which produces torque. Constant torque is produced when the rotor-produced magnetic flux rotates in synchronism with that of the stator. The generalization of a rotating MMF for an m-phase machine can be expressed as follows:

$$\begin{aligned} i_m &= \hat{i}\cos\left[\omega t + \phi - (l-1)\frac{2\pi}{m}\right] \\ \mathbf{F}_m &= \sum_{l=1}^{m} N \cdot i_m \cdot e^{j(l-1)\frac{2\pi}{m}} = \frac{m}{2} \cdot N \cdot \hat{i} \cdot e^{j(\omega t+\phi)} \end{aligned} \tag{5}$$

N is the number of turns, m the number of phases, $\hat{\imath}$ the current amplitude, ω the angular electrical speed, ϕ an arbitrary phase angle, and t as the time. It can be seen that with the increase in the number of phases, keeping the same number of turns and current amplitude, the amplitude of the total magnetomotive force increases at the same rate. However, when it comes to design an electrical machine, the variables are not kept constant; this is to account for undesired behaviour such as iron saturation.

To calculate the induced voltage the Maxwell-Faraday's law is used as follows:

$$\hat{\mathcal{E}} = -N \left| \frac{d\Phi_B}{dt} \right| = -N\omega_e \hat{\Phi}_B \tag{6}$$

Which states that a time changing magnetic flux passing through a coil with N number of turns will generate an opposing electromotive force equal to the magnetic flux times the angular frequency and the number of turns.

5.2 Sizing & designing equations

The present work is aimed to design a 15 MW AC superconducting PM offshore wind power generator based upon a 10 MW generator from [83, 84]. Therefore, a proper sizing of the machine is performed according to [89]. The following sets of equations are used:

$$\begin{aligned}
P &= \frac{\pi^2}{\sqrt{2}} k_{wdg} D_{ag}^2 L \frac{f_e}{p_r} B_{g1} K_s \\
\lambda &= \frac{L}{D_{ag}} \\
\tau_s &= \frac{\pi D_{is}}{Q_s} \\
\tau_p &= \frac{\pi D_{er}}{2p_r}
\end{aligned} \tag{7}$$

Where τ_s is the slot pitch, τ_p is the pole pitch, λ is the machine geometry ratio, B_{g1} is the fundamental of the magnetic flux density and K_s is the RMS value of the linear current density. The latter can be calculated by the slot current per slot pitch:

$$K_s = \frac{I_u}{\tau_s} = \frac{N_s I}{\tau_s} \tag{8}$$

N_s is the number of turns per slot, and I is the rated RMS current. Then, to calculate the geometry of the machine the following calculations are performed:

$$\begin{aligned} D_{is} &= D_{ag} + h_{ag} \\ D_{er} &= D_{is} - 2h_{ag} - 2l_m \\ w_m &= \left(D_{er} + 2l_m\right)\frac{\pi}{2p_r}\alpha_m \\ h_{yr} &= \frac{\phi_p/2}{B_{yr}Lk_i} \\ D_{ir} &= D_{er} - 2h_{yr} \\ h_{ys} &= \frac{B_g}{B_{ys}k_i}\alpha_m\frac{\tau_p}{2} \end{aligned} \tag{9}$$

D_{is} is the internal stator's diameter, D_{er} is the external rotor's diameter, w_m is the magnet's width, h_{yr} is the rotor's yoke height, D_{ir} is the internal rotor's diameter, and h_{ys} is the stator's yoke height.

The values for the stator's teeth width, stator's slot width, and stator's slot height are not calculated due to a superconducting cable requires much less slot useful area, therefore the size of these three parameters is too small in order to have a cooling system. Thus, an empirical approximation is done to compute the width based on having equal width for slot and teeth, and approximated 102 mm for the slot height in order to insert any type of cooling system.

To calculate the no-load RMS induced voltage (or Back-EMF) in one phase of the stator winding by the DC magnetic excitation flux Φ_p of the rotor, the following equations are used:

$$E_0 = \sqrt{2}\pi f_e k_{wdg}\Phi_p N_{ph} \tag{10}$$

Where f_e is the electrical frequency, k_{wdg} is the winding factor, Φ_{p1} is the fundamental of the magnetic excitation flux, and N_{ph} is the number of series-connected turns per phase. For the case of a double-layer winding this parameter are obtained as follows:

$$\begin{aligned}
k_{wdg} &= k_d k_p \\
k_d &= \frac{\sin\left(\frac{\pi}{2m}\right)}{z\sin\left(\frac{\pi}{2mz}\right)} \\
k_p &= \cos\left(\frac{\epsilon}{2}\right) \\
N_{ph} &= \frac{N_c Q_s}{m} \\
\Phi_{p1} &= L\int_0^{\tau_p} B_{g1}\sin\left(\frac{\pi}{\tau_p}x\right)dx = \frac{2}{\pi}\tau_p B_{g1} L \\
\Phi_p &= B_g w_m L
\end{aligned} \tag{11}$$

Where $\epsilon = \pi - \alpha_u$ is the coil span angle, $\alpha_u = 2\pi\frac{p_r}{Q_s}$ is the slot pitch angle, Q_s the number of slots, p_r the number of pole pairs, m is the number of phases, z is the numerator of the slots per pole per phase $q = \frac{Q_s}{2p_r m}$ for a fractional slot concentrated winding, also is the Q_s/m number of coils in $2p_r$ pole unit. w_m is the magnet width, and L is the machine length. The reactance can be calculated as follows:

$$X_a = 4\mu_0 m f\frac{(N_{ph}k_{wdg})^2}{\pi p_r}\frac{t_p L}{k_C h_{ag} k_{sat} + l_m/\mu_{rrec}} \tag{12}$$

5.3 Superconducting wires

The main characteristic of a superconductor is its high conductivity and that the magnetic field fluxes are expelled from the material. These characteristics originate the property of zero DC resistance under specific conditions: temperature of the material, current, magnetic field inside the material, and pressure. The latter property is particularly essential for room temperature superconductivity [90], while the others are important for low and high-temperature superconductivity $(4 - 77\,K)$.

To avoid quenching of superconductivity, the first three parameters presented above must be within the critical range. This depends on the material and the production of it. For electrical machines, the superconductor AC losses have to be reduced to obtain a good performance of the generator or motor. Thus, the M_gB_2 is a good candidate due to low AC losses, and low price [31]. However, this wire is produced with a cylindrical shape, which means that the magnetic field fluxes are isotropic around the whole material, yet this is true for one wire. In the case of an electrical machine, the coils are constructed with several wires in which the penetration of magnetic field fluxes depends on the arrangements of the wire in the coil's racetrack. Thus the hysteretic, coupling and eddy losses will depend on these arrangements.

5.3.1 AC losses in a superconductor

For changing currents in a purely superconducting material, the losses are being caused by the hysteresis loss. Nonetheless, a superconductor wire is made by different non-superconducting layers to account for stability, strength, and insulation. Once these layers are incorporated into the wire, there are three types of losses taking place in the wire, e.g., eddy current losses due to conducting layers such as copper; coupling losses along with the metal layer between superconducting material filaments; and ferromagnetic losses that are the hysteresis losses of the metal itself.

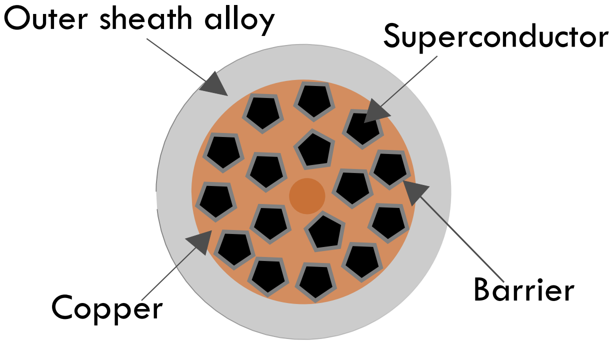

Figure 9: Superconducting wire

Therefore, the total AC losses in a superconductor wire depends on the hysteresis losses of the superconducting material, the eddy current losses of the normal conducting materials, the coupling losses between transport current materials, and the ferromagnetic hysteresis losses. This is written as follows:

$$P_{AC_T} = P_{sc} + P_e + P_c + P_f \tag{13}$$

5.3.2 Superconducting modeling

The most commonly known superconductive model describes the current-voltage characteristics of type-II superconductors as a power law, $V\alpha(I/Ic)^n$, with $n \gg 1$, which from the computational point of view renders the well-known form of the material law for the electric field, also called the E-J power law:

$$\mathbf{E}\left(\mathbf{J}\right) = E_o \left(\frac{|\mathbf{J}|}{J_c}\right)^n \tag{14}$$

This is a local but macroscopical approach that allows solution of the Maxwell equations inside the superconducting domains within diverse mathematical formulations. Where,

J_c is the critical current density of the superconductive material defined within the standard electric field criterion $E_0 = 1\mu V/cm$, which is commonly measured under direct current–voltage measurements with I-V curves typically showing power factors n $>$ 20 [91].

In figure 10 the E-J power law is described. The higher the n-value, the better the superconductor, which means that for a critical current, there is no voltage; thus, the resistivity is equal to zero.

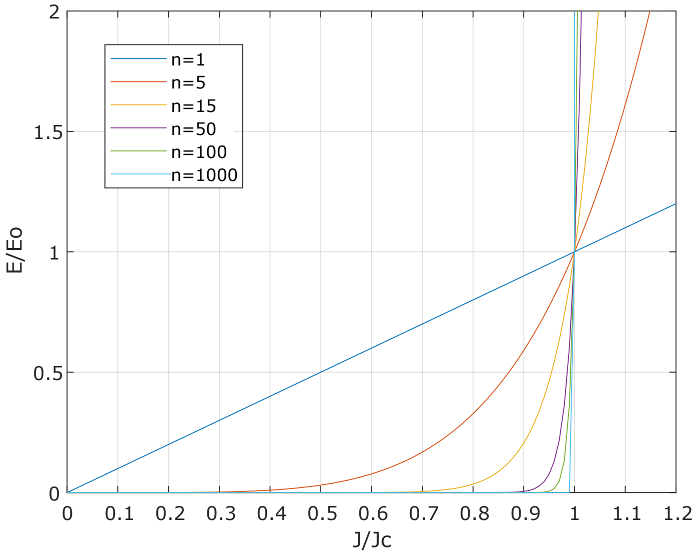

Figure 10: E-J power law

Furthermore, to design and model the superconductor, the engineering current density is used. This is the current density of the whole wire. Normally, the current density of the superconducting material, due to its small area, is tens of thousands A/mm^2. However, the superconductive area in the whole wire represents 10 to 20% of the total area of the wire. Therefore, the engineering current density is computed as follows:

$$J_e = K_{sc} \cdot J_{sc} \tag{15}$$

Where K_{sc} is the percentage of the superconductive material in the total wire's area. Nonetheless, for the case of this work, the data available are the transport current of the coil, the area of the wire and the number of parallel wires to achieve the needed transport current. Thus, the engineering current density can be computed as follows:

$$J_e = \frac{I}{N_{parallel} \cdot A_{sc}} \tag{16}$$

5.4 Permanent Magnet Machines

Permanent magnet (PM) machines are becoming a more common choice to wind power turbines due to eliminating the need for a gearbox, thus reducing size, cost, and maintenance, especially for offshore wind farms. PM machines can be categorized according to the magnetic flux path in the airgap, e.g., radial, axial, and transverse flux machines. For the scope of the present work, a radial magnetic flux path is considered. Radial PM machines can be further classified into interior rotors and outer rotors. For this thesis, the interior rotor is selected because an outer stator allows more space for cooling the superconducting windings.

A permanent magnet (PM) is modeled by the Ampere's law, which are treated as sources of the magnetic field. The permeability of the magnets is very close to unity, which is same as air. PMs are also called hard magnetic materials, meaning ferromagnetic materials with a wide hysteresis loop.

The basis for the evaluation of a PM is the left-hand quadrant of the hysteresis loop, called demagnetization curve. When a opposite external magnetic field intensity is applied to a permanent magnet the flux density drops down to the a certain magnitude, then if the external field is removed the flux density returns to the initial point according to a minor hysteresis loop. Thus, applying a external magnetic field intensity has reduced the remanence, or remanent magnetism. The minor hysteresis loop may usually be replaced with little error by a straight line called the recoil line, which as a slope called the recoil permeability μ_{rec}.

The intrinsic properties of a PM are:

- Remanent magnetic flux density, B_r, or remanence, is the magnetic flux density corresponding to zero external magnetic field intensity. High remanence means the magnet can support higher magnetic flux density in the air gap fo the magnetic circuit.
- Coercive field strength H_c, or coercivity, is the value of demagnetizing field intensity necessary to bring the magnetic flux density of the PM to zero. High coercivity means that a thinner magnet can be used to withstand the demagnetization field.
- Intrinsic demagnetization curve is the portion of the $B_i = f(H)$ hysteresis loop located in the upper left-hand quadrant. In which, for $H = 0$ the intrinsic magnetic flux density is $B = B_r$.
- Recoil magnetic permeability μ_{rec}, is the ratio of the magnetic flux density to magnetic field intensity at any point on the demagnetization curve,

$$\mu_{rec} = \mu_o \mu_{rrec} = \frac{\Delta B}{\Delta H} \tag{17}$$

- Maximum magnetic energy per unit produced by a PM in the external space is equal to the maximum magnetic energy density per volume,

$$w_{max} = \frac{(BH)_{max}}{2} \tag{18}$$

For PMs with linear demagnetization curve, i.e., NdFeB magnets, the coercive field strength at room temperature can simply be calculated on the basis of B_r and μ_{rrec} as:

$$H_c = \frac{B_r}{\mu_0 \mu_{rrec}} \tag{19}$$

The magnetic flux density produced in the air gap h_{ag} by a PM with linear demagnetization curve and its height l_m placed in a magnetic circuit with infinitely large magnetic permeability and airgap h_{ag} is, approximately,

$$B_g \approx \frac{B_r}{1 + \mu_{rrec} h_{ag}/l_m} \tag{20}$$

The first harmonic of the air-gap magnetic flux density is:

$$B_{g1} = \frac{2}{\pi} \int_{-0.5\alpha_m \pi}^{0.5\alpha_m \pi} B_g \cos\alpha \, d\alpha = \frac{4}{\pi} B_g \sin\frac{\alpha_m \pi}{2} \tag{21}$$

Where α_m is the pole-to-arc ratio of the magnet width. In case to take into account for the leakage permeance of the Airgap the Carter's coefficient is calculated as follow:

$$\begin{aligned} k_C &= \frac{\tau_s}{t_s - \gamma_1 h_{ag}} \\ \gamma_1 &= \frac{4}{\pi}\left[\frac{w_{sl}}{2h_{ag}} \arctan\left(\frac{w_{sl}}{2h_{ag}}\right) - \ln\sqrt{1 + \left(\frac{w_{sl}}{2h_{ag}}\right)^2}\right] \\ B_g &= \frac{B_r}{1 + \mu_{rrec} h_{ag} k_C / l_m} \end{aligned} \tag{22}$$

Where k_C is the Carter's coefficient factor, τ_s the slot pitch, h_{ag} the airgap length, and w_{sl} the slot width.

To produce torque in an electrical machine, the flux linkage and the stator currents must have an angle between them. This is shown in the following torque equation:

$$
\begin{aligned}
T &= \frac{m}{2} \cdot p_r \cdot |\lambda_{\mathbf{dq}} \times \mathbf{i_{dq}}| \\
T &= \frac{m}{2} \cdot p_r \cdot |\lambda_{\mathbf{dq}}| \cdot |\mathbf{i_{dq}}| \cdot \sin\theta
\end{aligned} \tag{23}
$$

For a PM machine, the torque can be divided into two types depending on the rotor topology. A PM machine without reluctance torque, and on the other hand, a PM machine with reluctance torque. The torque for these topologies are shown as follows:

$$T = \frac{m}{2} \cdot p_r \cdot \Psi_m \cdot i_q \tag{24}$$

$$T = \frac{m}{2} \cdot p_r \cdot (L_d - L_q) \cdot i_q \cdot i_d \tag{25}$$

Where Ψ_m is the flux linkage of the magnet in the d-axis direction. The flux's path for permanent magnets is shown in figure 11. Where figure 11a depicts the surface-mounted PM rotor, which is the most common topology where the PMs produce the torque. It is important to notice that the flux lines of the permanent magnets are aligned in the d-axis. Thus, for any other PM configuration in the rotor, the flux lines determined the d-axis position. In figure 11b, a synchronous reluctance machine is depicted where the q-axis follows the flux guides. Synchronous reluctance machine are the simplest synchronous machines. The smaller the quadrature-axis inductance and the higher the direct-axis inductance, the higher the power, therefore an optimum inductance ratio is reached when there are flux guides and flux barriers approximately in the ratio of 50:50.

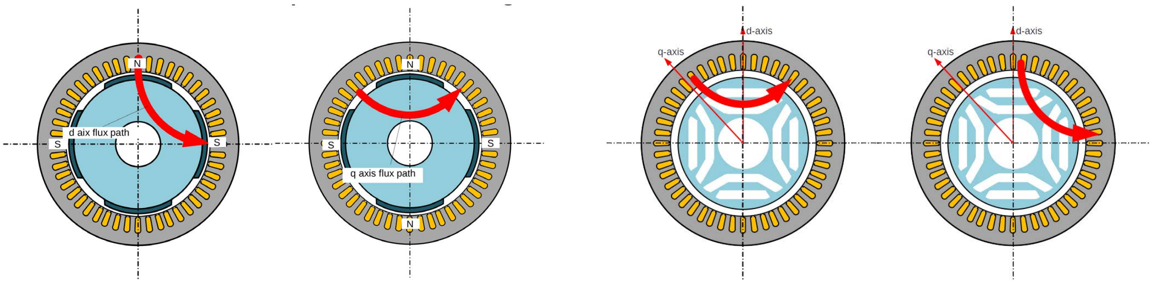

(a) Surface mounted PM machine (b) Synchronous reluctance machine

Figure 11: Topologies of PM rotors for two types of torque production

Further on, the combination of both torque types is possible by punching the magnets in the interior of the rotor. These types of configuration are an important and active area of research. For the scope of the present work, a surface mounted PM machine is designed. Hence, to achieve the maximum torque per ampere, the output current must be on the q-axis.

5.5 Winding design layouts

As previously discussed, the operating principle of electrical machines is based on the interaction between the flux linkage and the currents flowing in the windings of the machine. The windings can be grouped according to their function. For PM machines, the armature windings are the only ones present on the electrical machine.

Well-designed armature windings create a rotating field at a synchronous speed. The flux created in the airgap is called the armature reaction. Under these conditions, the electrical machine can fulfil the energy conversion. Therefore, the power is transmitted between an electrical system and a mechanical system.

The AC armature phase windings produce a rotating field of m-phase windings. The simplest AC winding that produces a rotating field is a two-phase symmetrical winding. And the most used multiphase winding is a 3-phase winding. For higher phase-order windings, the most common winding layout is an asymmetrical or "split-phase" winding. N sets of 3-phase windings are phase-shifted from each other in the stator to produce a rotating field with redundancy. To understand the difference between an asymmetrical and symmetrical winding layout, a 12-phase winding layout is constructed.

For a asymmetrical system the following variables are defined: the total number of phases is $l \times m = 12$, and the number of 3-phase windings set is $l = 4$, where $m = 3$. Then the phase belt, phase progression and the phase displacements are compute as follows:

$$\begin{aligned} \phi_b &= \frac{180^\circ}{m} = 60^\circ \\ \phi_p &= \frac{360^\circ}{m} = 120^\circ \\ \phi_d &= \frac{180^\circ}{m \times l} = 15^\circ \end{aligned} \tag{26}$$

And for a symmetrical system the following variables are defined: the total number of phases is still $l \times m = 12$, but the number of set is $l = 1$, thus, there is one winding system with $m = 12$. Therefore, the phase belt, phase progression and the phase displacements are compute as follows:

$$\begin{aligned} \Phi_b &= \frac{180^\circ}{m} = 15^\circ \\ \Phi_p &= \frac{360^\circ}{m} = 30^\circ \\ \Phi_d &= 0^\circ \end{aligned} \tag{27}$$

Important to notice, the phase displacement is zero because there is just only one winding system. And for this case, it has a coil span of 11, which is a reduced or short pitch winding. In figure 12 the 2 windings are compared.

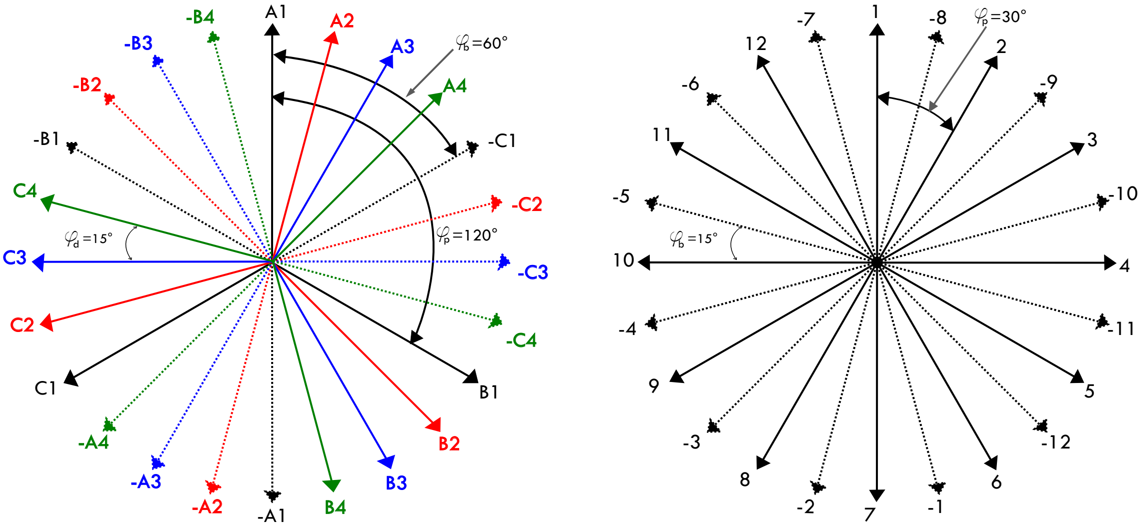

(a) Asymmetrical winding (b) Symmetrical winding

Figure 12: Comparison between asymmetrical and symmetrical 12-phase winding

The phase windings are distributed along the periphery of the air-gap, in which each pole covers 180° electrical degrees, and it is expressed by the pole pitch τ_p.

The phase windings can be divided into phase zones, which is written as:

$$\tau_V = \frac{\tau_p}{m} \tag{28}$$

The number of zones will be $2p_r m$. The phase zones are symmetrically distributed along the airgap periphery to have equal electrical degrees distances. For instance, the smartest way to distribute the phases among the armature winding in a 3-phase machine is to have phase zones of 60° electrical degrees. Therefore a positive and negative zone is present equally. In figure 13 the simplest three phase machine is present, where the phase zones are distributed with a 60° electrical degree angle.

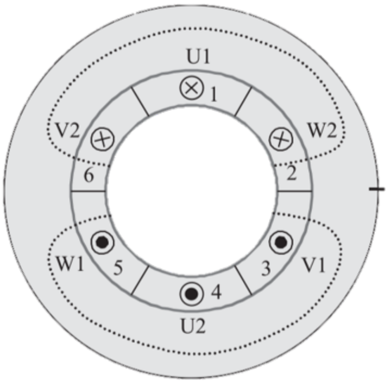

Figure 13: Simplest three phase machine. Extracted from [7].

The coil span is calculated as

$$y_Q = \frac{Q_s}{2p_r} \tag{29}$$

Each phase zone has associated a phasor, thus, the angle between each phasor is as follows

$$\alpha_u = \frac{360° \cdot p_r}{Q_s} \tag{30}$$

The m-phase stator current linkage amplitude of the harmonic υ can be written as

$$\hat{\Theta}_{s\upsilon} = \frac{m}{2}\frac{4}{\pi}\frac{N_{ph}k_{wdg}}{2p_r\upsilon}\sqrt{2}I \tag{31}$$

This is true only if the slot currents for each slot are equal.

5.5.1 Integer winding layouts

According to the number of slots per pole per phase q, the winding layouts can be divided into integer and fractional. The most used type is integer winding layouts. The simplest 3-phase machine presented in figure 13 is a integer winding layout with $q = 1$. For more complex windings layouts, additional characteristics are taken into account to design the windings. These can be listed as follows:

- Number of layers: Commonly, single layer and double layer.

- Concentrated, where the phase's turns are inserted in one slot. And distributed winding, where the turns are distributed over more than one slot.
- Full and fractional pitch winding. Where the latter consists of a reduced or expanded voltage phasor angle. It is used to reduce harmonic content in the machine.
- Alternate coil pitching, which is applied with double-layer windings, or more.

Furthermore, the requirements to achieve a balanced system are:

- For double-layer winding, $^{Q_s}/_{m} \in \mathbb{N}$, and the number of wound coils is equal to Q_s.
- For single-layer winding, $^{Q_s}/_{2m} \in \mathbb{N}$, and the number of wound coils is equal to $Q_s/2$.

For multiphase winding layouts, where $m > 3$, the comparison over different configurations for superconducting armature windings is more complex due to the slot-pole combination and the width of the slots, which has a side effect on the superconducting armature windings due to the maximum bending of the coils.

For instance, an example case is comparing 3, 6 and 12 phases winding layouts with $q = 1$, which is the simplest winding layout. A reduced pitch design has to be done to generate symmetrical phasors for the 6-phase and 12-phase windings, as is shown in figure 14. However, for high-phase order winding layouts, to keep the number of slots per pole per phase fixed, the pole-pairs must be changed accordingly. E.g. if the number of slots is $Q_s = 48$, the pole-pairs is a follows: $p_r = 8$ for 3-phase winding, $p_r = 4$ for 6-phase winding, and $p_r = 2$ for 12-phase winding. Meaning that the electrical frequency for each configuration will change. Thus, one cannot achieve a proper comparison.

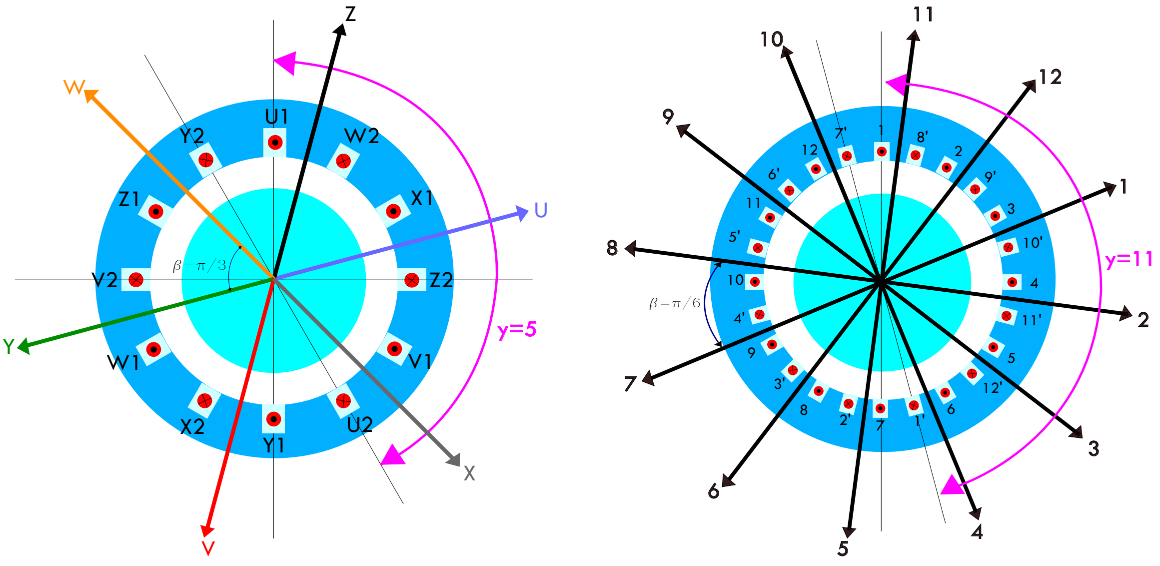

(a) 6-phase (b) 12-phase

Figure 14: Multiphase integer winding layouts

On the other hand, if the slots per pole per phase is not fixed for the multiphase winding configuration. One cannot compare the high-order multiphase winding layout because the winding layout is no longer an integer for a higher phase number. Instead, it is a fractional winding layout. However, going even further, one can increase the slots number to have integer multiphase winding layouts. Still, the smaller width of the teeth might jeopardize the bending of the superconducting coils.

Therefore, to have a proper comparison between different multiphase winding layout configurations, fractional slots per pole per phase is proved to be advantageous over integer windings.

5.5.2 Fractional winding layouts

As the integer winding layouts, the fractional ones can be designed with a different number of layers, concentrated or distributed, full or fractional pitch, and alternate coil pitching. Nonetheless, the simplest fractional winding layout design is a double-layer concentrated full pitch winding.

For the case of m-phase fractional slot windings, to design a winding layout it is useful to comply with certain conditions. First, q has to be reduced so that the numerator and the denominator are the smallest possible integers as follows:

$$q = \frac{Q_s}{2p_r m} = \frac{z}{b} \tag{32}$$

If the denominator b is an odd number, the winding is the first-grade winding, and when b is an even number, the winding is of the second grade. For a fractional slot winding, the base-winding is longer and contains Q'_s slots, which mean that it is necessary to proceed a distance p'_r pole pairs before a coil side of the same phase again meets exactly the peak value of the flux density. So, as every Q'_s phase over p'_r times is circled, t layers are created in the voltage phasor diagram. Therefore, in each electrical machine, there are t electrically equal slot sequences.

To compute the number of layers of a voltage phasor diagram t, the largest common divider of Q_s and p_r is calculated. Then, the number of phasor of a single turn in a voltage phasor diagram Q'_s, the number of revolutions around a single layer when numbering a voltage phasor diagram can be calculated, and the phasor skipped in the numbering of the voltage phasor diagram s can be calculated as follows:

$$\begin{aligned} t &= gcd(Qs, pr) \\ Q'_s &= \frac{Q_s}{t} \\ p'_r &= \frac{p_r}{t} \\ s &= \frac{p_r}{t} - 1 \end{aligned} \tag{33}$$

Therefore, the angle α_z of adjacent radii voltage phasor diagram is as follows

$$\alpha_z = \frac{2\pi}{Q_s} t \tag{34}$$

Then the slot angle α_u is correspondingly a multiple of the phasor angle α_z

$$\alpha_u = \frac{p_r}{t} \alpha_z = p'_r \alpha_z \tag{35}$$

Now the symmetry conditions can be fulfilled in order to have a symmetrical winding. For the case of symmetrical fractional slot windings the following conditions must be achieved.

5.5.3 The first condition of symmetry

For a single-layer windings, it is required that in the equation

$$\frac{Q_s}{2m} = p_r q = p_r \frac{z}{b}, \quad \frac{p_r}{b} \in \mathbb{N} \tag{36}$$

Correspondingly, for double-layer windings, the first condition of symmetry requires that in the equation

$$\frac{Q_s}{2m} = 2p_r q = 2p_r \frac{z}{b}, \quad \frac{2p_r}{b} \in \mathbb{N} \tag{37}$$

Double-layer windings gives wider range of alternative. E.g., for $p_r = 1$, the single-layer can be only integral slot winding $b = 1$, whereas the double-layer $b = 2$.

5.5.4 The second condition of symmetry

This condition is related to the divider t of Q_s and p_r. Which, in the end, can be written simply in the form: b and m cannot have a common divider.

$$\frac{b}{m} \notin \mathbf{N} \tag{38}$$

5.5.5 Base windings

The base winding is the smallest part that can be repeated. Integer slot winding has always 2 poles in the base winding, and usually have many repetitions. Fractional slot winding cover several poles in the base winding. The base winding can be classify in first grade and second grade for fractional slot base windings. In table 3 the parameters to determine the base winding are described.

	Base winding of first grade	Base winding of second grade	
Parameter q	$q = z/b$		
Denominator b	$b \in \mathbb{N}_{odd}$	$b \in \mathbb{N}_{even}$	
Parameter Q'_s/m	${}^{Q'_s}/_{m} \in \mathbb{N}_{even}$	${}^{Q'_s}/_{m} \in \mathbb{N}_{odd}$	
Parameter Q_s/m	${}^{Q_s}/_{tm} \in \mathbb{N}_{even}$	${}^{Q_s}/_{tm} \in \mathbb{N}_{odd}$	
Divider t, the largest common divider of Q and p_r	$t = gcd(Q_s, p_r)$		
Slot angle α_u expressed with voltage phasor angle α_z	$\alpha_u = b\alpha_z = b\frac{2\pi}{Q_s}t$	$\alpha_u = \frac{b}{2}\alpha_z = b\frac{\pi}{Q_s}t$	
Type of winding	Single-layer windings Double-layer windings	Single-layer windings	Double-layer windings
Number of slots Q'_s of a base windings	$Q'_s = \frac{Q_s}{t}$	$Q'_s = 2\frac{Q_s}{t}$	$Q'_s = \frac{Q_s}{t}$
Number of pole pairs p'_r of a base windings	$p'_r = \frac{p_r}{t} = b$	$p'_r = 2\frac{p_r}{t} = b$	$p'_r = \frac{p_r}{t} = \frac{b}{2}$
Number of layers t' in a voltage phasor diagram for a base winding	$t' = 1$	$t' = 2$	$t' = 1$

Table 3: Fractional slot base windings' parameters

5.5.6 The third condition of symmetry

An additional condition of symmetry for multiphase windings is necessary. For the purpose of this work a three-phase double-layer fractional slot concentrated winding is selected, with $q = \frac{2}{5}$, $Q_s = 48$ and $p_r = 20$. Thus, the symmetry conditions are achieved as follows:

$$\begin{aligned} \frac{2p_r}{b} &= \frac{2 \cdot 20}{5} = 8 \in \mathbb{N} \\ \frac{b}{m} &= \frac{5}{3} \notin \mathbb{N} \end{aligned} \tag{39}$$

Same for the case in which $m = 12$, with $q = 1/10$ for $Q_s = 48$ and $p_r = 20$.

$$\begin{aligned} \frac{2p_r}{b} &= \frac{2 \cdot 20}{10} = 4 \in \mathbb{N} \\ \frac{b}{m} &= \frac{10}{12} = \frac{5}{6} \notin \mathbb{N} \end{aligned} \tag{40}$$

And for the case in which $m = 24$, $q = 1/20$ for $Q_s = 48$ and $p_r = 20$, the following is obtained:

$$\begin{aligned} \frac{2p_r}{b} &= \frac{2 \cdot 20}{20} = 2 \in \mathbb{N} \\ \frac{b}{m} &= \frac{20}{24} = \frac{5}{6} \notin \mathbb{N} \end{aligned} \tag{41}$$

The three winding layouts complied with the symmetry conditions. Nonetheless, the base windings for the three winding layouts configurations are independent of the phases. Therefore, $Q'_s = 12$ and $p'_r = 5$ are the same for the 3 configurations, indicating that a double-layer fractional slot concentrated winding cannot be achieved for more than 12 phases. This means that for the case of $m = 24$, the slots per phase in the base winding is less than 1. Therefore, the third condition for symmetry in a double-layer fractional slot concentrated windings can be described as follows:

$$\frac{Q'_s}{m} \in \mathbb{N} \tag{42}$$

Which states that to achieve a multiphase winding, the slots per phase in a base winding shall be an integer number. E.g., if an m-phase machine is not multiple of 3 leads to a different number of slots that must be multiple m. For instance, if a 9-phase machine wants to be constructed with a $Q_s = 48$ and $p_r = 20$, it is impossible because the number of slots per phase is fractional. Thus, a stator in which Q_s is not multiple of m cannot be constructed. Hence, a slot-pole combination of $Q_s = 45$ and $p_r = 20$ will have 1 slot per phase, which gives a well designed multiphase machine.

Therefore, to achieve a 24-phase winding layout a 24 slots and 11 pole-pairs is selected.

In figure 15 the three base windings layouts are depicted. Where the slot angle for $m = 3$ and $m = 12$ is $\alpha_u = \frac{5\pi}{6}$, whilst for $m = 24$ the angle is $\alpha_u = \frac{11\pi}{12}$.

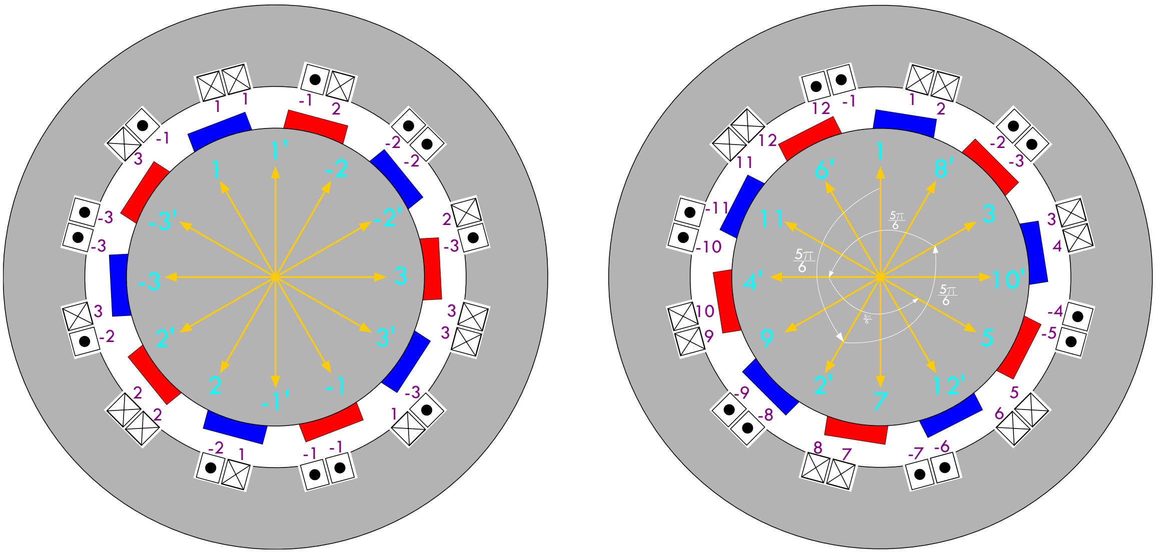

(a) 3-phase winding (b) 12-phase winding

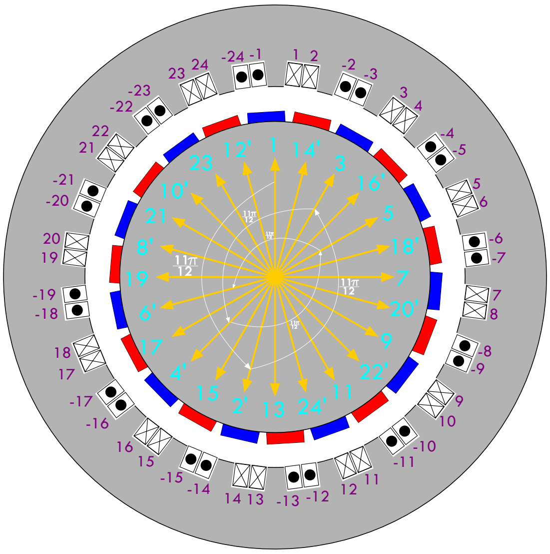

(c) 24-phase winding

Figure 15: Basis winding layout comparison

Once the base winding is known, the slot current is computed by adding the current of the two coils in the same slot. For instance, in figure 16 the slot currents in per unit are depicted. For the case of $m = 3$ there are two different values for slot current, one is depicted in the figure 16a and the other is the double of the current; this is because of how the 3-phase winding is designed. There are always two adjacent phases in the same slot for the case of $m = 12$ and $m = 24$.

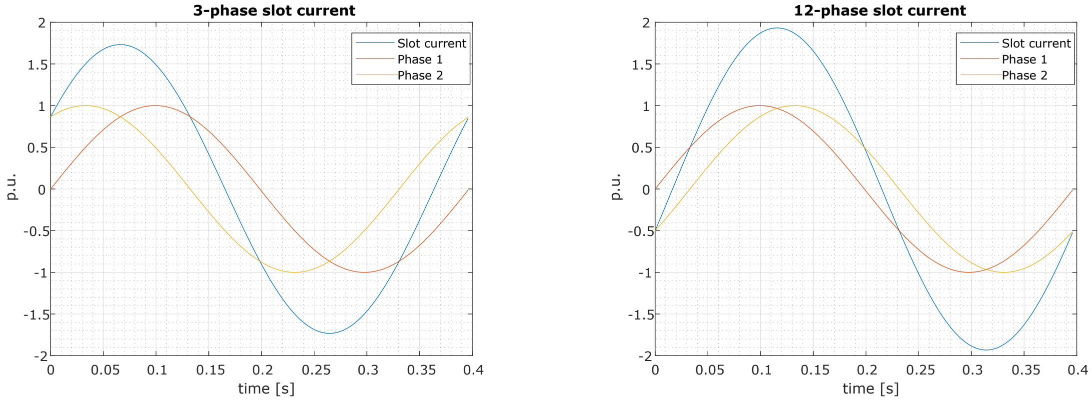

(a) 3-phase slot current (b) 12-phase slot current

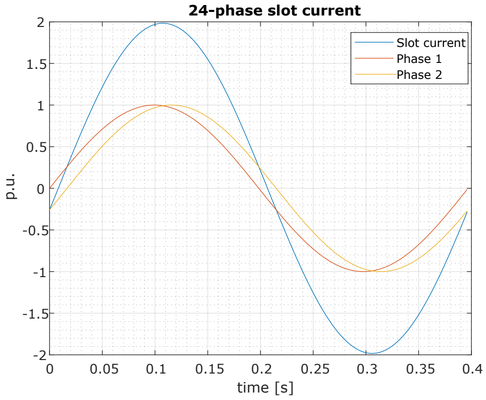

(c) 24-phase slot current

Figure 16: Slot current behaviour comparison

From this, one can expect to have a slightly higher slot current for a high-phase order winding layout. Further on, the shear stress can be computed by the slot current and the airgap flux density as follows:

$$\sigma_t = K_s B_g = \frac{I_u}{t_s} B_g \tag{43}$$

5.5.7 MMF Harmonics

A fast analysis of MMF harmonics is performed based on the winding calculation program from NTNU, and Madescu et al [92]. To compute the MMF harmonics for multiphase windings the per unit MMF for each slot is determined at a specific time t. Commonly, for three-phase machine the time is choose at the peak of one of the current phases, implying that the other phases are half of the peak current, therefore a code can be made by adding or substracting the phase current at each slot according to the winding layout. However, this principle cannot be applied for a multiphase winding, so the computation for each slot current or MMF per slot at certain time is required. Due to the simplicity of the winding layouts for $m = 12$ and $m = 24$ the MMF per slot can be expressed as follows for $t = T/4$:

$$MMF(k) = (-1)^k \cdot \left[\sin\left(\frac{\pi}{2} - \frac{2\pi}{m} \cdot (k-1)\right) + \sin\left(\frac{\pi}{2} - \frac{2\pi}{m} \cdot k\right)\right] \tag{44}$$

Where k represents the numbering of the slot. Then, a Fourier series analysis is performed to obtain the space harmonics.

$$F_\mu = \sum_{k=1}^{Q_s} \frac{MMF(k)}{\mu\pi} \cdot \exp\left(i \cdot \mu \cdot \theta_k\right) \tag{45}$$

θ_k is the angle position in space at $t = T/4$, and μ is the mechanical space harmonic, when is equal to the pole-pair $\mu = p_r$ it is known as the working harmonic of the machine. Moreover, the angle shall be computed for each slot as follows:

$$\theta_k = (k-1) \cdot \frac{2\pi}{Q_s} \tag{46}$$

And finally each space harmonic is calculated by the absolute value for every μ. In figure 17 the MMF harmonics for the 3 winding layouts is presented.

$$MMF_\mu = |F_\mu| \tag{47}$$

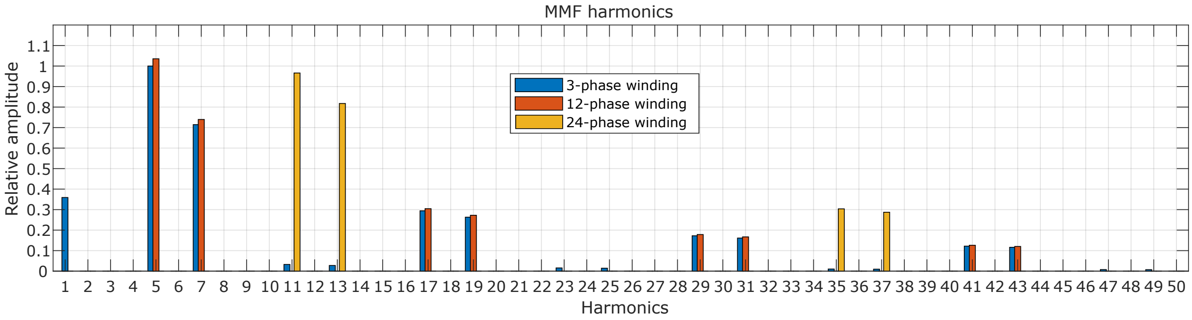

Figure 17: MMF spectra harmonics

It is shown that for the 3-phase, 12-phase, and 24-phase winding layouts, the working harmonic is equal to the base pole-pairs. Further, the 12-phase winding layout does not have a space subharmonic, and the working harmonic is higher, so a better performance is expected. There are no space subharmonics for the 24-phase winding layout; however, the working harmonic amplitude is less than the 3-phase winding layout; thus, much less torque ripple and less torque are expected.

5.6 Cogging and ripple torque

Permanent magnet machines have been used in a variety of applications. One of the drawbacks of these machines is the pulsating torque produced by the sum of cogging torque and ripple torque. The cogging torque results from the interaction of permanent magnet MMF harmonics (rotor magnetic flux) and the airgap permeance harmonics due to slotting (stator magnetic reluctance), which are the fringing fields. Cogging torque is independent of the stator excitation. The ripple torque is produced by the interaction of stator current MMF and rotor electromagnetic properties: (1) mutual or alignment torque, results from the interaction of stator MMF and rotor magnetic flux distribution; and (2) reluctance torque, results from the interaction of stator MMF and the angular variation of the rotor magnetic reluctance. [93], [94].

For the present work, ripple torque is assessed as the reduction in the overall pulsating torque of designing different winding layouts. However, even though the cogging torque is not thoroughly analyzed, it affects the overall pulsating torque behaviour. Thus, to achieve a good comparison over different topologies that do not share the same slot-pole combination, a cogging torque performance parameter is considered to assess them.

Neglecting the armature reaction and magnetic saturation, the cogging is a periodic oscillation that depends on the slot-pole combination of the machine geometry. The fundamental frequency of the cogging torque can be calculated as a function of the number of slots Q_s, the number of pole pairs p_r, and frequency f [85] as follows:

$$f_c = Q_s \cdot n_s = Q_s \frac{f}{p_r} \qquad if \qquad N_{cog} = \frac{2p_r}{GCD(Q_s, 2p_r)} = 1 \tag{48}$$

$$f_c = 2 \cdot n_{cog} \cdot f \quad n_{cog} = \frac{LCM(Q_s, 2p_r)}{2p_r} \quad if \quad N_{cog} \geq 1 \tag{49}$$

The higher the n_{cog}, the lesser the cogging torque, which means that achieving a higher least common multiple (LCM) for a slot-pole combination reduces the cogging torque. For the present work, the LCM for the 3-phase and 12-phase machines is $LCM(48, 40) = 240$. Meanwhile, the 24-phase machine is $LCM(48, 44) = 528$. Hence, it is expected to have a reduction in cogging torque due to the slot-pole combination. This is why one cannot compare a 24-phase machine directly with the other topologies.

There are several ways to minimize the cogging torque effect, where each variety has its own drawbacks and advantages. Some of them include [95]:

- Skewing slot and/or magnets
- Shaping the magnets (Surface parallel, surface axial, bread-loaf, etc.)
- Auxiliary (dummy) slots or teeth
- Optimizing the relative magnet width (polar arc/pole pitch)
- Fractional number of slots per pole (Q/2p) (High prime slots) (Harmonic cancellation)
- Stepped skewing of magnet blocks – Broadbent Shift
- Smoothing slotting - Slot opening (harmonic cancellation)
- The amplitude and frequency is influenced by the slot/pole combination. (Harmonic cancellation)
- Iron path, airgap length and axial length optimization.

For the present work, the magnets are surface axial with a smoother corners design with an arc length of 10% the height of the magnets, the relative magnet width is set to be 80%, and the number of slots per pole is fractional.

5.7 Current density distribution in a slotted machine

In a slotted machine, the conductor is distributed in a certain way to cover the whole useful area of the slot. The current density applied in the conductor will behave exponentially from the bottom of the slot to the part that is closer to the airgap. This behaviour is a result of the eddy currents generated in the soft magnetic material of the iron. This is known as the external-field skin effect.

In an alternating current-carrying conductor, the eddy currents are induced in the iron, and the lower magnetic permeability of the airgap compared to the iron creates a leakage flux. Then, the iron's eddy currents in the proximity of the conductor create a skin depth effect that repels the current density distribution towards the lower eddy current proximity, and that is towards the leakage flux in the airgap proximity.

This behaviour also varies if there is a single or double-layer winding. Hence, single-layer and double-layer windings are modelled in COMSOL to show this behaviour. In figure 18 the two windings layouts model are depicted.

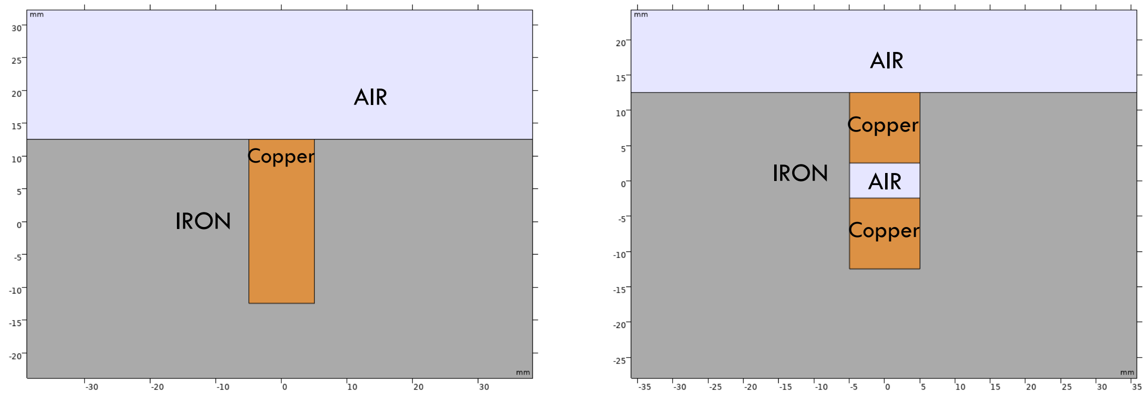

(a) Single-layer (b) Double-layer

Figure 18: Slot model

In the single-layer winding layout slot model the current density distribution increases exponentially without any discontinuity, as it is depicted in figure 19 for a 50 Hz current of 1 A.

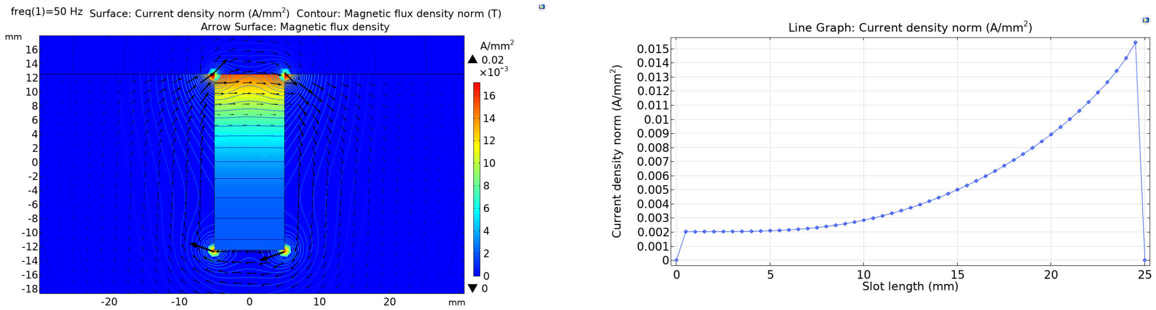

(a) Magnetic behaviour (b) Current density distribution

Figure 19: Slot effect in a single layer winding

The current density distribution presents a discontinuity for a double-layer winding layout slot model because it has an air space between the two conductors. Even though there is a change in the permeability, at that location, the eddy currents are big enough to repel the current density distribution towards the airgap, where the major leakage flux is located, and no eddy currents are flowing.

In figure 20 the current density distribution shows that the conductor part closer to the airgap has the higher current density distribution. However, it can be noticed that in the middle section, due to the air space between the conductors, there is an increase in the current density distribution due to the flux leakage.

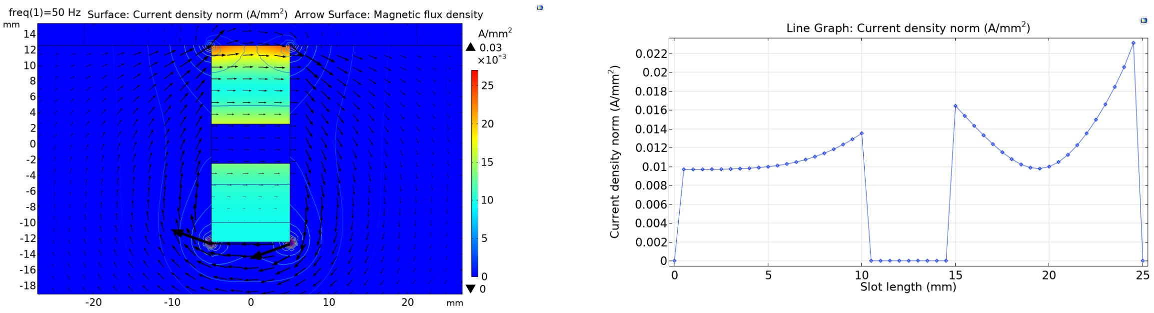

(a) Magnetic behaviour

(b) Current density distribution

Figure 20: Slot effect in a double layer winding

Furthermore, it is essential to remark that the flux density lines flow from one tooth to another. However, in a slotted superconducting machine, the tooth is not close to the conductors due to the cryogenic insulation. Therefore, leakage fluxes surround the superconductors, creating different flux density patterns, making the intuition into the skin depth effect harder due to eddy currents.

5.8 Iron losses calculation

There are various methods to calculate the iron losses of a rotating machine. The most common is the loss separation in which the static losses are the hysteresis energy losses when the frequency approaches to zero, and the dynamic losses which are related to the eddy currents circulating in the lamination of the iron yoke. This can be represented by the following equation:

$$p = K_h \cdot \hat{B}^2 \cdot f + K_e \cdot \hat{B}^2 \cdot f^2 \tag{50}$$

Where K_h and K_e can be often fitted to material data based on a least-square-method. This model was first proposed by Jordan in 1924 [96]. Then in 1998 an expansion to this equation was proposed by Bertotti, introducing a third term to the loss separation theory: the anomalous (excess) loss component [97, 98, 99], which can be express as follows:

$$\begin{aligned} p &= p_h + p_e + p_a \\ p &= K_h \cdot \hat{B}^{\alpha} \cdot f + K_e \cdot \hat{B}^2 \cdot f^2 + K_a \cdot \hat{B}^{1.5} \cdot f^{1.5} \end{aligned} \tag{51}$$

Where K_e, K_h, K_a and α are constants that depends on the material. And p, p_h, p_e and p_a are the total iron loss density, the hysteresis density loss, the eddy current density loss, and the anomalous density loss components, which units are [W/kg].

In order to determine the coefficients the CAL2 method is used. For this approach the α coefficient of the hysteresis loss density is set to 2, where the eddy current coefficient is replaced by a dynamic coefficient and the anomalous losses are not present due to the accuracy of the power coefficient of 1.5, whilst the hysteresis coefficient is kept as the Bertotti's model. The CAL2 method is expressed as follows:

$$p_{CAL2} = K_h(f,B) \cdot \hat{B}^2 \cdot f + K_d(f,B) \cdot \hat{B}^2 \cdot f^2 \tag{52}$$

According to [100] the third order polynomial to fit K_h and K_d for a low frequency range machine (e.g. $< 400Hz$) can be assumed to vary only in terms of the magnetic flux density $\hat{B}$, thus the third order polynomial curve fit for the propose of this work are described as follows:

$$\begin{aligned} K_h(\hat{B}) &= k_{h0} + k_{h1}\hat{B} + k_{h2}\hat{B}^2 + k_{h3}\hat{B}^3 \\ K_d(\hat{B}) &= k_{d0} + k_{d1}\hat{B} + k_{d2}\hat{B}^2 + k_{d3}\hat{B}^3 \end{aligned} \tag{53}$$

Where k_{hj} and k_{dj} for $j = 0,1,2,3$ are constant to be determined by the curve fit. This is done by inserting these expressions into equation 52 and using the specific loss data for the iron core material in a curve fitting tool.

In order to compute the losses of the machine, the calculation has to be done in time domain due to the Finite Element Analysis is built on time-stepping behaviour. In [101] the time domain calculation loss density components are formulated as follows:

$$\begin{aligned} p_h &= \frac{1}{\pi T}\int_0^T K_h(f_1,\hat{B}) \cdot B(t) \cdot \left[\frac{dB(t)}{dt}\right] \cdot dt \\ p_d &= \frac{1}{2\pi^2 T}\int_0^T K_d(f_1,\hat{B}) \cdot \left[\frac{dB(t)}{dt}\right]^2 \cdot dt \end{aligned} \tag{54}$$

Therefore, to compute the losses in the machine the next equation is used:

$$\begin{aligned} P_h &= \rho L N_{sector} \iint_S p_h \, dS \\ P_d &= \rho L N_{sector} \iint_S p_d \, dS \end{aligned} \tag{55}$$

Where ρ is the density of the material, L the length of the machine, N_{sector} is the number of segments or sector in which the entire machine is divided to be simulated in COMSOL, and S is the total integration area of the iron core of the machine.

5.9 Software

To analyzed with the Finite Element Method, the software to be used is COMSOL. For the case of physics interface of magnetic's rotating machinery the electromagnetic formulation is done with the vector and scalar potential [102] as follows:

$$\mu\sigma\frac{\partial \mathbf{A}}{\partial t} - \nabla \times (\nabla \times \mathbf{A}) = -\nabla\phi \tag{56}$$

Once the vector potential is obtained from the partial equation, the following parameters are determined by COMSOL:

$$\begin{aligned} \mathbf{B} = \nabla \times \mathbf{A} \longrightarrow \mathbf{H} &= \frac{\mathbf{B}}{\mu} \\ \nabla \times \mathbf{H} &= \mathbf{J} \\ \mathbf{E} &= -\frac{\partial \mathbf{A}}{\partial t} - \nabla\phi \end{aligned} \tag{57}$$

5.9.1 Superconducting formulation

To properly model the superconductor the E-J power law in COMSOL rotating magnetic machinery, the E-J power law has to be rewritten in terms of conductivity as follows:

$$\begin{aligned} |\mathbf{E}| &= |E_0| \cdot \frac{|\mathbf{J}|}{J_c} \cdot \left(\frac{|\mathbf{J}|}{J_c}\right)^{n-1} \\ \frac{|\mathbf{J}|}{|\mathbf{E}|} &= \sigma\left(\mathbf{J}\right) = \frac{J_c}{E_0} \cdot \frac{1}{\left(\frac{|\mathbf{J}|}{J_c}\right)^{n-1}} = \sigma_0 \cdot \left(\frac{J_c}{|\mathbf{J}|}\right)^{1-n} \\ \frac{\sigma\left(\mathbf{E}\right)}{\sigma_0} &= \left(\frac{\sigma\left(\mathbf{E}\right) \cdot |\mathbf{E}|}{\sigma_0 \cdot E_0}\right)^{1-n} = \left(\frac{\sigma_0}{\sigma\left(|\mathbf{E}|\right)}\right)^{n-1} \cdot \left(\frac{\mathbf{E}}{E_0}\right)^{1-n} \\ \sigma\left(\mathbf{E}\right)^n &= \sigma_0^n \left(\frac{|\mathbf{E}|}{E_0}\right)^{1-n} \\ \sigma\left(\mathbf{E}\right) &= \sigma_0 \left(\frac{|\mathbf{E}|}{E_0}\right)^{1/n-1} \end{aligned} \tag{58}$$

Nonetheless, to account for the non-bounded origin [103] the following consideration is made:

$$\sigma\left(\mathbf{E}\right)=\sigma_0\left|\frac{|\mathbf{E}|-E_0}{E_0}\right|^{1/n-1} \tag{59}$$

Therefore, the electric field is calculated by the equation 14 and then inserted in the equation 59. With this approach is possible to simulate a superconducting coil. However, it is important to notice due to the new bounded origin; the firsts time steps will be higher than expected; nonetheless, after a few steps, it damps out.

For the case of the AC losses, the superconductor material is assumed to be the entire geometry of the coil. The current density is computed as the engineering current density to account for the percentage of superconducting material in the whole wire, as is shown in the next section of the machine's design. Thus, the losses are determined only by hysteretic behaviour by the following:

$$Q_{loss}=\frac{1}{T}\int_{t_0}^{t_0+T}\left[\iint_S \mathbf{J}\cdot\mathbf{E}\,dS\right]dt, \tag{60}$$

To account for the transient phenomena fue to the bounded origin condition $t_0=T$.

It is important to notice, according to Sumption et al. [31], the hysteresis losses are higher than coupling losses for low-frequency behaviour. The ferromagnetic hysteresis losses and eddy current losses of the other materials inside the superconductor wire are ignored.

5.9.2 Arkkio's method

COMSOL calculates the forces by integrating the Maxwell stress tensor over the entire outer boundary of the domain selection. Since the method is based on surface integration, the computed force is sensitive to mesh size. Therefore, it is important to have a sufficiently accurate mesh to compute the force or torque correctly.

Arkkio's Method to calculate the torque is selected, as this has proven to be faster and produce good results at lower mesh quality. According to [104], the torque variation as a function of the radius may be as high as 50% from the average value when a typical finite element mesh is used. Therefore, Arkkio has proposed a method based on the principle of virtual work for two dimensions, where the true torque is independent of the radius, such that the torque can be integrated over a cross-sectional area of the air-gap, as is shown in figure 21. From this, the following equation is derived:

$$T=\frac{L}{\mu_0(r_o-r_i)}\int_S rB_rB_\phi\;dS \tag{61}$$

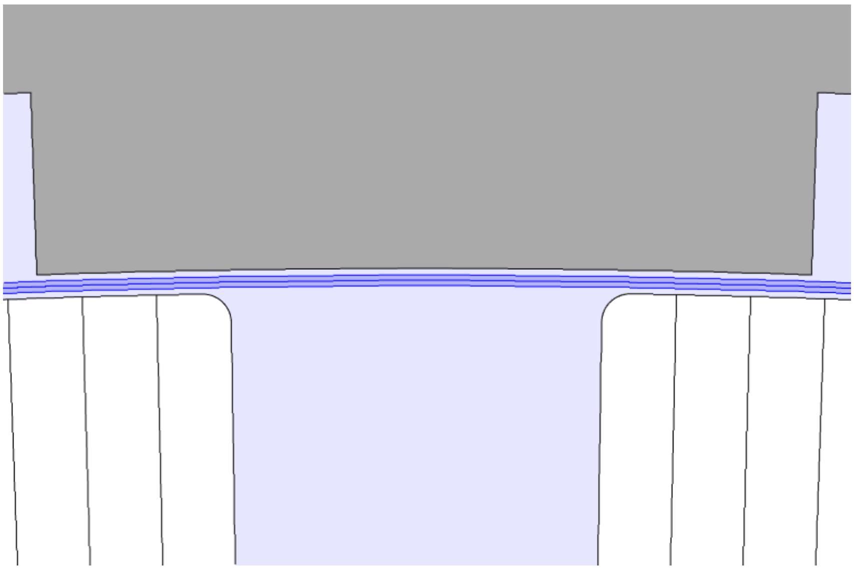

Figure 21: Arkkio's band in the airgap

Where L r_o, r_i and S are the length of the machine, outer radius and inner radius of the Arkkio's band, and the cross-sectional area of the air-gap, respectively, the calculation of the force acting on a body is then found by integrating Maxwell's stress tensor in cylindrical coordinates over the Arkkio's band. The tensor components in flux density quantities are formulated as follows:

$$\begin{aligned} \mathbf{T_t} &= \frac{1}{\mu_0}\left(B_r B_\phi\right) \\ \mathbf{T_r} &= \frac{1}{\mu_0}\left(B_r^2 - B_\phi^2\right) \end{aligned} \tag{62}$$

Therefore the Force over the Arkkio's band is calculated as follows:

$$\begin{aligned} F_t &= \frac{L}{\mu_0(r_o - r_i)} \int_S B_r B_\phi \, dS \\ F_r &= \frac{L}{\mu_0(r_o - r_i)} \int_S \left(B_r^2 - B_\phi^2\right) \, dS \end{aligned} \tag{63}$$

An important observation is a relationship between the magnetic angle θ and the force angle α. The latter is twice the former $\alpha = 2 \cdot \theta$, which means that theoretically, with a $\theta = 45°$, the largest tangential force is achieved. Hence, the largest torque by the machine is obtained.

As a result of segmenting the machine in COMSOL to reduce the computation time, the shear stress has to be calculated according to the number of poles of the segmented region of Arkkio's integration band.

The Arkkio's method torque is defined as a variable, and the integration band is defined as an integration path with the respective domains selected, all inside definitions in COMSOL.

To calculate the shear stresses over the airgap, the following equations are used:

$$\begin{aligned}\sigma_t &= \frac{F_t \cdot N_{sec}}{\pi \cdot D_{ag} \cdot L} \\ \sigma_n &= \frac{F_n \cdot N_{sec}}{\pi \cdot D_{ag} \cdot L}\end{aligned} \tag{64}$$

5.10 Power factor

In power system analysis, the power factor is a well-known feature to assess the goodness of an electrical system. The power factor is directly related to the field windings or permanent magnets capability to supply enough magnetic energy for rotating electrical machines. The machines share their magnetic energy into the armature windings and the field windings or permanent magnets. For the latter, the magnetic energy is fixed according to the remanent magnetic flux density of the magnets.

An electrical machine with a power factor different from the unit will need an inductive or capacitive compensation. An offshore wind turbine direct-drive PM generator is connected to a grid through power electronics. Therefore, to reduce the stress in the components, the power factor is preferred to be at close as possible to unity.

Different methods can do the calculation of the power factor. However, the modelling of a PM generator is done with maximum torque per ampere technique. Thus, the current is set on the q-axis, and the angle is known, providing enough data to performed a dq0-transformation in COMSOL. With dq voltages, the power factor and the reactance per unit can be calculated.

The dq0-transformation is well-known for 3-phase electrical systems. Nonetheless, for high-phase order, there is not a standard definition for a dq0-transformation. Mathematically speaking, a transformation is a projection from a reference frame to another. E.g., the dq0-transformation inputs are the 3 phases voltages or currents, and the outputs are the d, q and zero axes of the inputs. Furthermore, a dq-transformation can be explained similar to a rotation group. A triangle is circumscribed in a circle, and a map is applied to have only two axes, direct and quadrature. In figure 22 the mapping is shown, where the A, B and C axes are transformed into the d and q axes. The rotation arrow depicts that the 3-phase system is moving, whereas the dq axes are static.

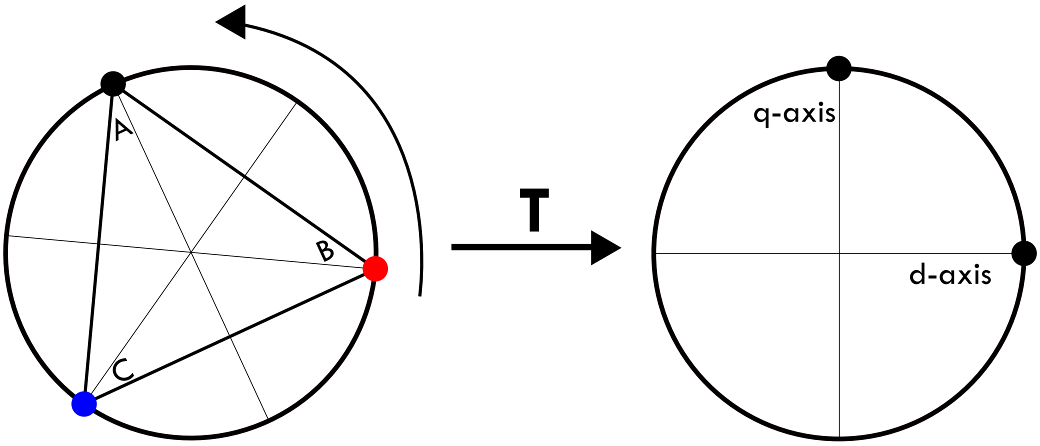

Figure 22: dq-transformation for a 3-phase electrical symmetrical system

In the present work, an extension for the dq0-transformation is done to 12 and 24 phases. However, due to the thesis's scope, it is not developing and investigating a new transformation. Additional degrees of freedom for high-phase order windings are not investigated. The only values required are the d and q axes to compute the power factor and reactance per unit. Thus, similar to a 3-phase electrical symmetrical system, a 12-phase can be explained as a rotating group, as is shown in the figure 23.

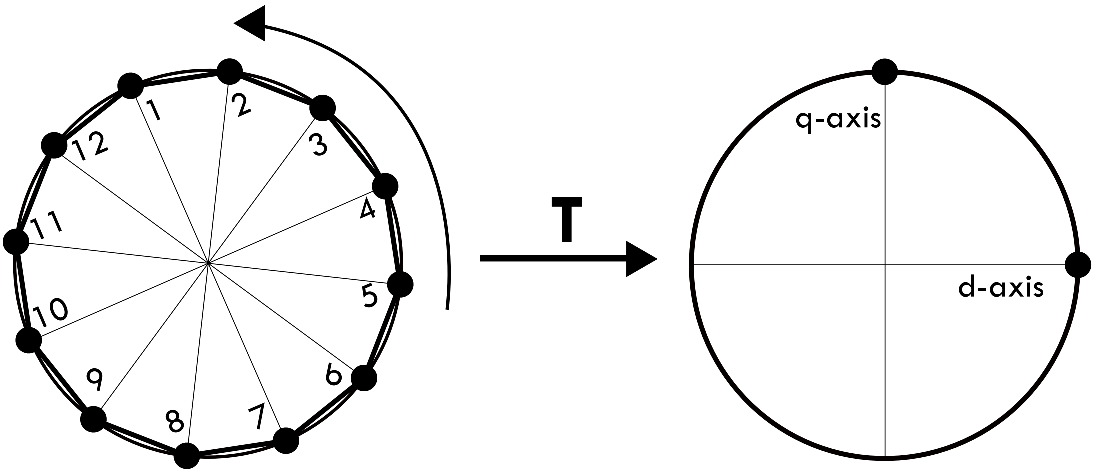

Figure 23: dq-transformation for a 12-phase electrical symmetrical system

Therefore, an n-phase electrical symmetrical system can be explained as a rotation group in which a geometric figure is circumscribed inside a circle. Every phase represents an axis connected to every vertex of the geometric figure. Thereafter the phase axes are transformed into the direct and quadrature axes by a linear transformation matrix.

It is important to notice that the 0-axis is not represented in the geometrical mapping because it is dimensionless and non-rotating. In symmetrical components, the 0-axis is called the zero-sequence voltage or current, which serves as a feature to assess the symmetry or unbalance of the electrical system and as common-mode voltage in electronics.

The dq0-transformation matrix for a 12-phase symmetrical electrical system is written as follows:

$$\begin{bmatrix} v_q \\ v_d \\ v_0 \end{bmatrix} = \frac{2}{12} \begin{bmatrix} \cos(\theta) & \cos(\theta - 2\pi/12) & \cos(\theta - 4\pi/12) & \cos(\theta - 6\pi/12) & \cdots \\ \sin(\theta) & \sin(\theta - 2\pi/12) & \sin(\theta - 4\pi/12) & \sin(\theta - 6\pi/12) & \cdots \\ \frac{1}{2} & \frac{1}{2} & \frac{1}{2} & \frac{1}{2} & \cdots \\ \cdots & \cos(\theta - 8\pi/12) & \cos(\theta - 10\pi/12) & \cos(\theta - 12\pi/12) & \cos(\theta - 14\pi/12) & \cdots \\ \cdots & \sin(\theta - 8\pi/12) & \sin(\theta - 10\pi/12) & \sin(\theta - 12\pi/12) & \sin(\theta - 14\pi/12) & \cdots \\ \cdots & \frac{1}{2} & \frac{1}{2} & \frac{1}{2} & \frac{1}{2} & \cdots \\ \cdots & \cos(\theta - 16\pi/12) & \cos(\theta - 18\pi/12) & \cos(\theta - 20\pi/12) & \cos(\theta - 22\pi/12) \\ \cdots & \sin(\theta - 16\pi/12) & \sin(\theta - 18\pi/12) & \sin(\theta - 20\pi/12) & \sin(\theta - 22\pi/12) \\ \cdots & \frac{1}{2} & \frac{1}{2} & \frac{1}{2} & \frac{1}{2} \end{bmatrix} \tag{65}$$

Hence, a dq-transformation is simply a projection of n-phase axes to the direct and quadrature axes.

Finally, the dq0-transformation for a 24-phase symmetrical electrical system is as follows:

$$\begin{bmatrix} v_q \\ v_d \\ v_0 \end{bmatrix} = \frac{2}{24} \begin{bmatrix} \cos(\theta) & \cos(\theta - 2\pi/24) & \cos(\theta - 4\pi/24) & \cos(\theta - 6\pi/24) & \cdots \\ \sin(\theta) & \sin(\theta - 2\pi/24) & \sin(\theta - 4\pi/24) & \sin(\theta - 6\pi/24) & \cdots \\ \frac{1}{2} & \frac{1}{2} & \frac{1}{2} & \frac{1}{2} & \cdots \\ \cdots & \cos(\theta - 8\pi/24) & \cos(\theta - 10\pi/24) & \cos(\theta - 12\pi/24) & \cos(\theta - 14\pi/24) & \cdots \\ \cdots & \sin(\theta - 8\pi/24) & \sin(\theta - 10\pi/24) & \sin(\theta - 12\pi/24) & \sin(\theta - 14\pi/24) & \cdots \\ \cdots & \frac{1}{2} & \frac{1}{2} & \frac{1}{2} & \frac{1}{2} & \cdots \\ \cdots & \cos(\theta - 16\pi/24) & \cos(\theta - 18\pi/24) & \cos(\theta - 20\pi/24) & \cos(\theta - 22\pi/24) \\ \cdots & \sin(\theta - 16\pi/24) & \sin(\theta - 18\pi/24) & \sin(\theta - 20\pi/24) & \sin(\theta - 22\pi/24) \\ \cdots & \frac{1}{2} & \frac{1}{2} & \frac{1}{2} & \frac{1}{2} \\ \cdots & \cos(\theta - 24\pi/24) & \cos(\theta - 26\pi/24) & \cos(\theta - 28\pi/24) & \cos(\theta - 30\pi/24) \\ \cdots & \sin(\theta - 24\pi/24) & \sin(\theta - 26\pi/24) & \sin(\theta - 28\pi/24) & \sin(\theta - 30\pi/24) \\ \cdots & \frac{1}{2} & \frac{1}{2} & \frac{1}{2} & \frac{1}{2} \\ \cdots & \cos(\theta - 32\pi/24) & \cos(\theta - 34\pi/24) & \cos(\theta - 36\pi/24) & \cos(\theta - 38\pi/24) \\ \cdots & \sin(\theta - 32\pi/24) & \sin(\theta - 34\pi/24) & \sin(\theta - 36\pi/24) & \sin(\theta - 38\pi/24) \\ \cdots & \frac{1}{2} & \frac{1}{2} & \frac{1}{2} & \frac{1}{2} \\ \cdots & \cos(\theta - 40\pi/24) & \cos(\theta - 42\pi/24) & \cos(\theta - 44\pi/24) & \cos(\theta - 46\pi/24) \\ \cdots & \sin(\theta - 40\pi/24) & \sin(\theta - 42\pi/24) & \sin(\theta - 44\pi/24) & \sin(\theta - 46\pi/24) \\ \cdots & \frac{1}{2} & \frac{1}{2} & \frac{1}{2} & \frac{1}{2} \end{bmatrix} \tag{66}$$

Needless to say, other investigations into multiphase symmetrical systems as been accomplished for control of electrical drives or wind turbine generators. The most common multiphase systems investigated are 5-phase and 7-phase systems [105, 106, 107, 108, 109, 110, 111], in which they claim that it is feasible to develop an extended dq-transformation how it was presented above. Additionally, they claim that it is possible to add more degrees of freedom to the control algorithms with high-phase order electrical symmetrical systems by optimum harmonic voltage injection. E.g., a 5-phase electrical symmetrical system dq0-transformation will have 2 more axes, a d_3 and q_3 axes, representing the third-order harmonic in a direct and quadrature reference frame. And, it is extended for a 7-phase machine, where a d_5 and q_5 axes are added to represent fifth-order harmonics. However, as the rotation group representation examples explained before, the dq-transformation is a projection of the n-phase system to a dq-axes system. Thus, independently of the number of phases, the dq-axes can also be extended to control different harmonic orders.

6 Design

The philosophy for the design of a superconducting machine is not well defined. Thus a conventional philosophy is used. The procedure is shown in figure 79 at the appendix, in which a few distinctions are made, compared to conventional design philosophy, these are:

1. The superconductor is selected to be a tape geometry and resized for convenience and to reduce the complexity of designing an AC superconducting coil.
2. The space for the thermal insulation is considered. Thus, a 50mm space between the superconductors and the iron is designed. Having a fixed space means that the useful area for the conductor usually calculated is not done any more for a superconductor due to its high current density.
3. When having a double-layer design, the slot current for different winding layouts according to the number of phases will vary; therefore, that variation is included in the design model.
4. The machine constant is changed to a motional constant, in which the volume of the airgap is rotating at the electrical frequency times a constant $\pi^2 \cdot K_{wdg}/p_r$. This approach facilitates the analysis between different winding layouts by isolating this motional constant. For comparison purposes, the winding factor is the only value that changes, except for the 24-phase machine where the pole-pairs change. Moreover, the electric and magnetic loadings are analysed separately. And the power can be computed as follows:
$$S = C_m \cdot K_s \cdot B_g \tag{67}$$
Where the constant C_m is
$$C_m = \frac{\pi^2 \cdot k_{wdg}}{p_r} \cdot f_e \cdot D_{ag}^2 \cdot L \tag{68}$$

Furthermore, since the design takes as a reference machine a 3-phase winding layout, the high-order ($m > 3$) phase winding layout are multiples of 3 to comply with the number of slots of the stator. The 12-phase machine is chosen because it is the highest possible multiphase system for the same geometry as the 3-phase machine. Finally, the 24-phase machine is chosen to double the phases of a 12-phase machine and endorse multiphase machines' findings.

6.1 Superconductor sizing and design

A reference superconductor geometry is resized [112, 43, 113]. With this model, one can calculate the AC losses by assuming a laser-scribing fabrication technique of 10 filaments per HTS wire, which means a reduction of 10 times the AC losses. The reference values of the width and the height of the superconductor are 0.1 mm and 5 mm, respectively. The reference rated peak current applied in the wire is $I_r = 1460\,A$, and the parallel superconductors to form the AC superconducting coil are $N_{parallel} = 9$. To determine the engineering current density of the wire and the critical current, the previous data is used as follows:

$$J_e = \frac{I_r}{A_{sc} \cdot N_{parallel}} = \frac{1460}{9 \cdot 5 \cdot 0.1} = 324.4\,\mathrm{A/mm^2} \tag{69}$$

To calculate the critical current, the following is done:

$$I_c = \frac{I_r}{N_{parallel}} = \frac{1460}{9} = 162.2\,\mathrm{A} \tag{70}$$

Normally, to design a superconductor, the critical current is diminished to an operational current from 50% to 75% to give a safe margin. So, it is assumed that Miura and Komiya et al. already computed this safe margin in the reference superconductor.

Furthermore, the geometry is increased to be more manageable and achieve a higher critical current: the width is doubled, and the height is 4 times larger, which means that are 8 superconductors in parallel forming the entire wire, as is shown in figure 24. With this new geometry, the following values are obtained:

$$\begin{aligned} I_c &= 8 \times 162.2 = 1297.7\,\mathrm{A} \\ J_e &= 324.4\,\mathrm{A/mm^2} \\ A_{sc} &= 4\,\mathrm{mm^2} \end{aligned} \tag{71}$$

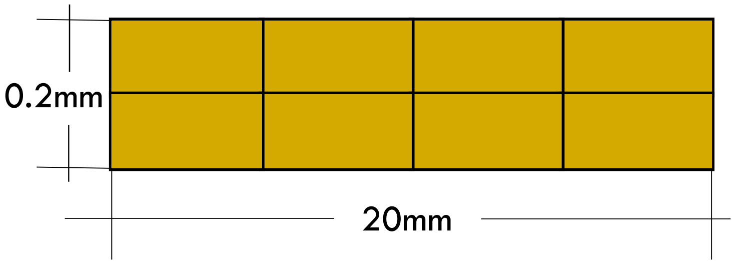

Figure 24: Superconductor wire geometry. Not in scale

With the critical current capability of the superconductor is possible to compute the number of parallel strands in order to achieve the desired transport current of the rotating machine.

6.2 Fractional Slot Concentrated Winding

In order to make a good design of the machine, the following specifications from the 15 MW reference machine are taken into account: fractional slot concentrated winding with $q = 2/5$, $P = 15\,\text{MW}$, and $n = 7.56\,\text{rad/s}$. And from Dong Liu et al [83, 84], the machine geometry, specifically the airgap's diameter and the machine's length in order to obtain at least the double of the shear force in comparison to a conventional machine. The values are: $D_{ag} = 5.4\,\text{m}$ and $L = 1.215\,\text{m}$.

6.2.1 3-phase machine

The inputs for the design and sizing are: reference power; reference airgap diameter and reference machine's length to achieve the double of the shear stress compared to a conventional machine; the mechanical angular speed according to the power of the wind turbines and the mechanical constraints of the blade design; number of pole-pairs; number of slots; number of phases; reference voltage; magnetic flux density remanent of the magnets; stator and rotor yoke's magnetic flux density; percentage of magnet coverage per pole; and magnet height. The values are presented in table 4.

Parameter	Description	Value
P_{old}/P_{new}	Power	10 MW/15 MW
D_{ag}	Airgap diameter (old)	5.4 m
L	Machine's length (old)	1.215 m
n_{old}/n_{new}	Mechanical angular speed	9.6 rad/s/7.56 rad/s
m	Number of phases	$3, 12, 24$
Q_s	Number of slots	48
p_r	Number of pole-pairs	20/22
V	EMF, where $V(m) = 3V/m$	$3300/\sqrt{3}$
B_{yr}	Rotor's yoke flux density	1.3 T
B_{ys}	Stator's yoke flux density	1.1 T
B_r	Magnet's flux density remanent	1.47 T
l_m	Magnet's height	80 mm
α_m	Magnet's coverage percentage	0.8

Table 4: Input parameters for the design and sizing of the machine

The ratio of the geometry of the machine is computed in order to find the new airgap diameter and length of the machine by fixing the ratio. The ratio is calculated as follows:

$$\lambda = \frac{L}{D_{ag}} = \frac{1.215}{5.4} = 0.2250 \tag{72}$$

Then the equation 7 is used to obtain the new values of the airgap length and machine length, and the slot pitch and pole pitch. The airgap can be calculated by the following:

$$h_{ag} = \frac{D_{ag}}{1000} = \frac{6.6938}{1000} = 6.6938\,\mathrm{mm} \tag{73}$$

In the reference machine from Dong Liu et al., the airgap length is not a thousandth of the airgap diameter but instead a thousandth of the outer stator diameter. However, to calculate the outer stator diameter, the airgap length is needed. Therefore an approximation is made by having a ratio between the airgap diameter and the outer stator diameter of the reference machine. Then the airgap is calculated to be h_{ag} =7.4 mm.

The geometry of the machine can be computed by equations 9 and 11. From the equation 67 the linear current density can be computed. And the number of turns per phase and per coil are calculated as follows:

$$\begin{aligned} N_{ph} &= \frac{V(m)}{\sqrt{2}\pi f_e k_{wdg}\phi_{p1}} \approx 240 \\ N_{coil} &= \frac{N_{ph}}{2p_r q} = 15 \end{aligned} \tag{74}$$

It was found in the simulation that the demagnetization is around 20%, therefore the back EMF voltage is computed by taking into account the demagnetization as follows:

$$\hat{E}_0 = 2 \cdot q \cdot N_{coil} \cdot \omega_e \cdot k_{wdg} \cdot B_g 1 \cdot L \cdot Dag \cdot 0.80 \approx 2200\,\mathrm{V} \tag{75}$$

Hence, the current can be calculated directly from the normal power equation as follows:

$$\hat{I}_r = \frac{P}{\frac{m}{2} \cdot \hat{E}_0} \approx 4500\,\mathrm{A} \tag{76}$$

With the rated peak current, the parallel wires of the superconductor are calculated to be $N_{parallel} = 4$.

6.2.2 12-phase and 24-phase machine

For a multiphase ($m > 3$) winding, an additional degree of freedom to the design is introduced. This means that to compare with a 3-phase machine, either the voltage or the current must be fixed. Nevertheless, for a superconducting machine, the higher current capability is one of its strengths. Hence, to achieve a proper comparison within multiphase windings for a superconducting machine the voltage is reduced to keep the number of turns per coils and the current fixed. Thus, the number of turns per phase is decreased accordingly. Nonetheless, due to the winding factor is enhanced by having a multiphase winding, the calculation of the turns per phase is computed from the turns per coil to assure a good comparison of the same stator geometries. Then for a 12-phase machine, the number of turns per phase is calculated as follows:

$$N_{ph_{12\phi}} = 2 \cdot p_r \cdot q \cdot N_{coil} = 2 \cdot 20 \cdot \frac{1}{10} \cdot 15 = 60 \tag{77}$$

And for the 24-phase machine the number of turns is as follows:

$$N_{ph_{24\phi}} = 2 \cdot p_r \cdot q \cdot N_{coil} = 2 \cdot 22 \cdot \frac{1}{20} \cdot 15 = 30 \tag{78}$$

In table 5 the design parameters are presented. The superconducting multiphase PM rotating machine can be built in COMSOL with these parameters. The diferences between the topologies are:

- The winding factor is different due to the winding distribution and the pitch factor. Where for the multiphase winding, the distribution factor is better because there is one slot per phase. And for the case of a 24-phase winding layout, the pitch factor is better due to the slot-pole combination.
- The Back EMF voltages are different to fix the current and the number of turns per coil to maintain the same geometry. This means that the number of turns per phase is decreasing accordingly.
- For the 24-phase winding layout, it has a different number of pole pairs, the frequency, the pole pitch, and the flux per pole changes, which means that the yoke's height of the rotor and stator changes accordingly.
- The motional constant depicts the superiority of multiphase windings. Thus, it is expected that a winding layout with more phases can deliver more output power, hence, achieve a higher torque-to-weight ratio of an electrical rotating machine.

Topologies		3-phase machine	12-phase machine	24-phase machine
Parameters	**Description**	**Value**		
D_{ag}	Airgap diameter	6.6938 m		
D_{ir}	Interior rotor diameter	6.1158 m		6.1531 m
D_{er}	External rotor diameter	6.5264 m		
D_{is}	Interior stator diameter	6.7013 m		
D_{os}	Exterior stator diameter	7.3589 m		7.3158 m
L	Machine's length	1.5061 m		
Q_s	Number of slots	48		
p_r	Number of pole-pairs	20		22
V_{rms}	Terminal voltage	3300 V	825 V	412.5 V
B_r	Magnet's flux density remanent	1.47 T		
l_m	Magnet height	80 mm		
τ_s	Slot pitch	0.4386 m		
τ_p	Pole pitch	0.5126 m		0.4660 m
f_e	Electrical frequency	2.5200 Hz		2.7720 Hz
ω_m	Mechanical angular frequency	7.5600 rad/s		
k_{wdg}	Winding factor	0.933	0.9659	0.9914
C_m	Motional constant	78.3001 m^3/s	81.0622 m^3/s	83.2038 m^3/s
N_{coil}	Turns per coil	15		
N_{ph}	Turn per phase	240	60	30
I_r	Rated current	4500 A		

Table 5: Design and sizing parameter

7 Modelling and Analysis

In this section, the modelling of the superconducting formulation in COMSOL is discussed. The analysis of the different winding layouts is performed by comparing: the iron losses, AC superconducting hysteresis losses, the shear stress behaviours in time, the magnetic and force angles according to Maxwell's stress tensor analysis, the harmonics analysis, and power factor analysis. Finally, an optimization in the angle of the coils is proposed to reduce the AC superconducting hysteresis losses.

7.1 Superconducting formulation

One of the present thesis scopes is to assess the AC superconducting hysteresis losses in an AC superconducting multiphase PM machine for 3 different winding layouts with $m = 3, 12, 24$. Hence, the superconducting wire design is not an objective. Thus, to reduce the complexity of the simulation of AC superconducting coils, a tape geometry is chosen. Nonetheless, this type of superconductors introduces a magnetic angle dependency due to the anisotropic behaviour. This can be expressed in the E-J power-law model by assuming an effect into the critical current density $J_c = J_c(\mathbf{B})$ and the n-factor $n = n(\mathbf{B})$. However, for the present thesis and the lack of data, this is not modelled.

The limitations and constraints of the present superconductor model are:

- No dependency of the external and self-field magnetic flux density to the critical current density and the n-factor.
- The whole wire geometry is assumed to be superconductive by applying the engineering current density, therefore the only losses present are the hysteretic losses.
- No temperature dependence, thus no thermal coupled model.
- Due to lack of data of the reference superconductor, the n-factor is assumed to be fixed with a value of 25. The exponent factor is handpicked to be in between MgB_2 and REBCO typical values [114, 29].

The superconductor is modelled as an entire superconductive surface with an engineering current density. The coil geometry with its 15 turns is depicted in figure 25, where the number of parallel strands is incorporated in the total area of one turn. This means, one turn has a height of $h_{sc} = 20\,\text{mm}$ and a width of $w_{sc} = 0.2 \times 4 = 0.8\,\text{mm}$, in which for the whole coil the width is 15 times the width of one turn, $w_{coil} = 12\,\text{mm}$.

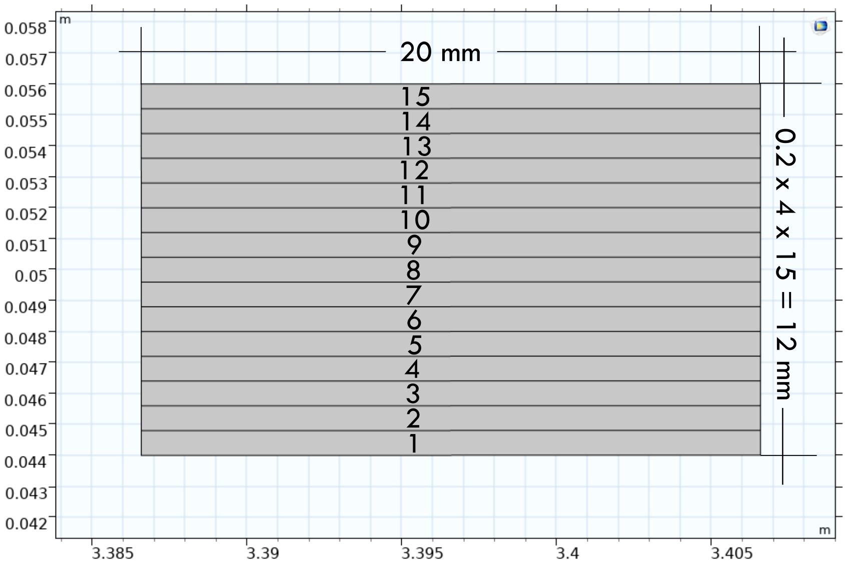

Figure 25: Superconductor coil

For the COMSOL physics interface known as magnetic rotating machinery, the coils can be modelled as a multi-turns coil or as a single turn coil. For the first one, the current density in the whole coil is assumed to be constant. Thus an ultra-high conductivity must be defined to account for the superconductivity of the coils. However, this approach does not account for the magnetic behaviour of a superconducting material, which is repelling the magnetic flux lines to enter the material. On the other hand, in a single turn coil modelling, COMSOL can model the current density according to the E-J power law, which means that the current density is no longer constant, is rather non-linear, and the flux lines are repelled from the superconductive material. In figure 26 two test models are depicted. In figure 26a it can be seen that the flux lines and magnetic flux density inside the superconductor material are higher compared to what is shown in figure 26b.

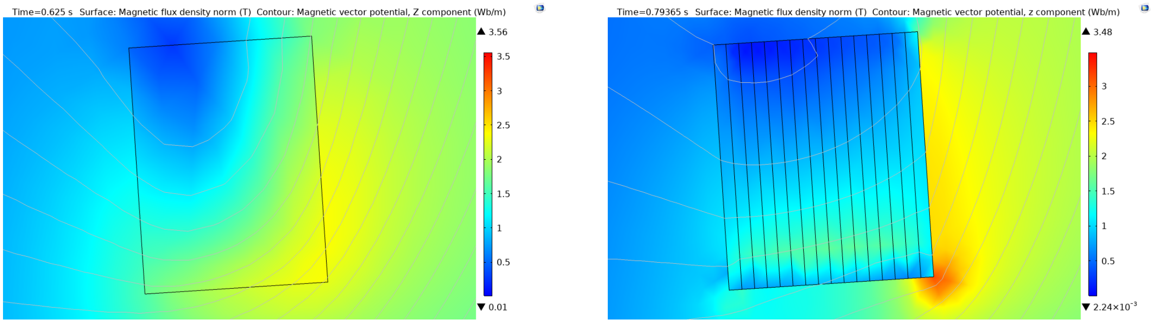

(a) Ultra-high conductivity (b) Superconductivity

Figure 26: Comparison between constant and non-linear conductivity superconductor model

7.2 COMSOL set-up for 3-phase and 12-phase machine

To model and analyze the behaviour of a superconducting multiphase machine, a geometry is modelled as follows:

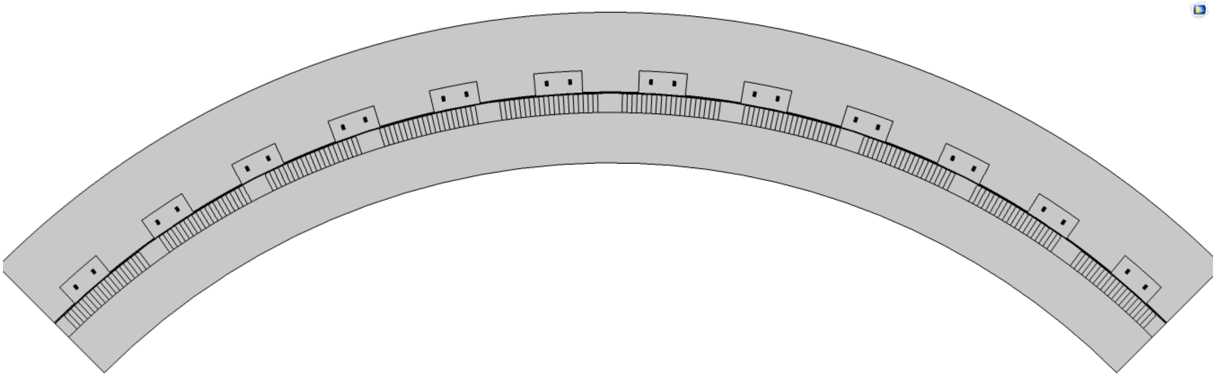

Figure 27: 3-phase and 12-phase machine geometry

The basis winding for both winding configurations is 12 slots, the COMSOL model is a quarter of the whole geometry. To account for the losses in the permanent magnets for a 2D modelling, the PMs are segmented into 20 parts to reduce the eddy currents. The coils are modelled radially, taking as a reference model the work done by Xue et al. [115].

For all models, the mesh is built with 240 mesh elements per pole in the airgap to reduce the noises in the calculations. The time steps are calculated by dividing a complete cycle of 2 poles, representing 480 mesh elements. Hence the time step is $T/480$. The mesh is constructed as follows:

- The identity boundary pairs are distributed with 240 mesh elements per pole and assigned with edge elements. First, the static boundary is created, then the edges are copied to the moving boundary.
- The edge elements are copied to the airgap Arkkio's band to defined an equal band in the static and moving parts of the mesh.
- The side mesh elements of the teeth are symmetrically distributed with a maximum size of 2.5 mm. And the tip of the teeth with a maximum size of 2 mm accounts for the mesh created in the airgap band.
- The rest of the air is meshed with triangular elements. Is calibrated for plasma materials and with "extremely fine" elements.
- The coils are meshed with Quad elements with a maximum size of 0.5 mm. Calibrated as plasma.

- Finally, the iron is meshed with triangular elements calibrated as plasma with a maximum size of 15 mm.

The mesh of the machine is presented in figure 28. The same values for the mesh are used for all the models presented in this work.

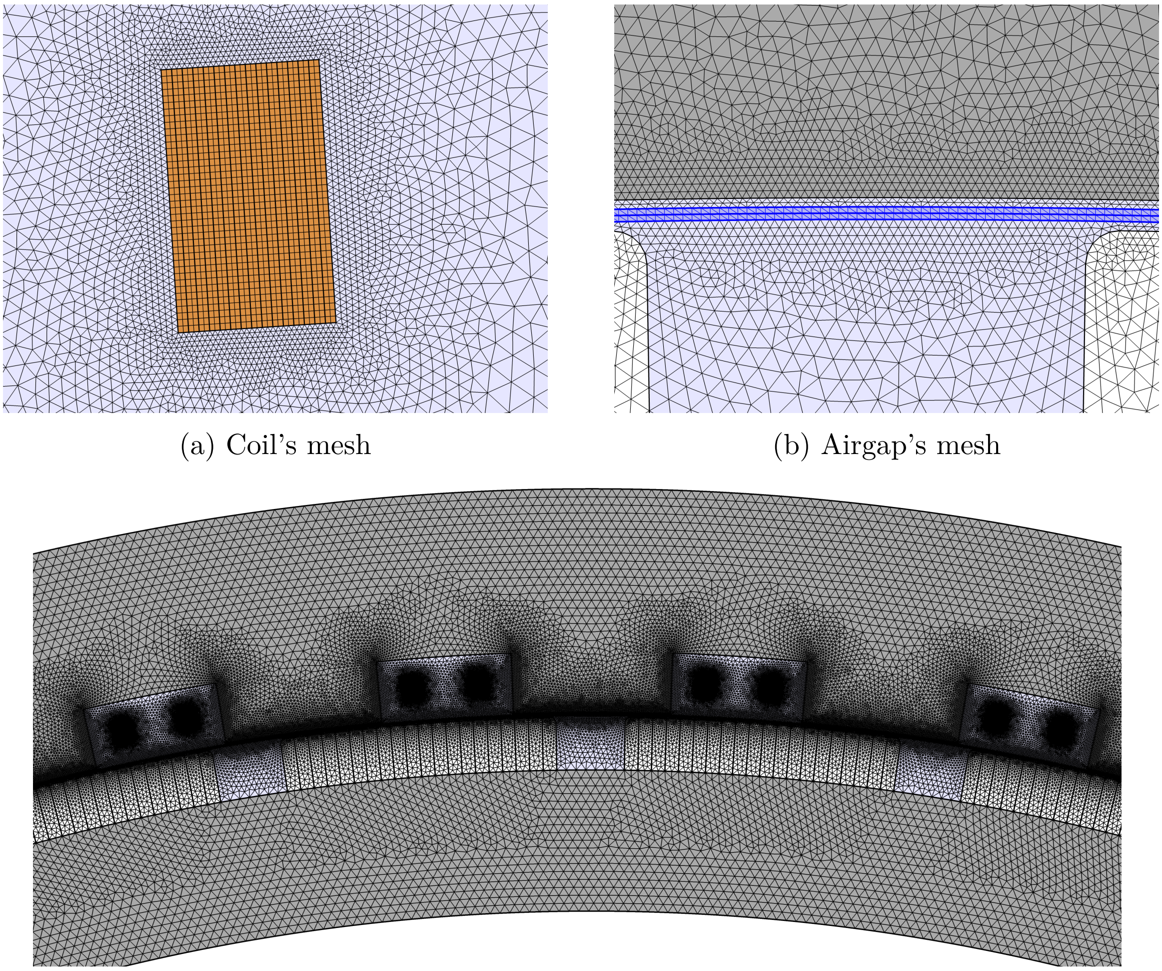

(a) Coil's mesh

(b) Airgap's mesh

(c) Geometry

Figure 28: Meshing

7.3 Analysis of the 3-phase and 12-phase machines

The 3 machines are sized to have 15 MW of power. However, it is straightforward to compared two similar geometries, and make a proper analysis. The analysis consist in compared different electrical and magnetic properties of the results. The methodology is to start with the most commonly known property to the most complex to calculate.

The output current for all the models is 4500 A. However, the waveforms are phase-shifted accordingly to the number of phases. In figure 29 the currents for the 3-phase and the

12-phase machine are depicted. The current is on the q-axis to achieve maximum torque per ampere; thus, it is assumed that the power electronics can deliver the amount of reactive power, and the control algorithm for a 12-phase machine is already developed.

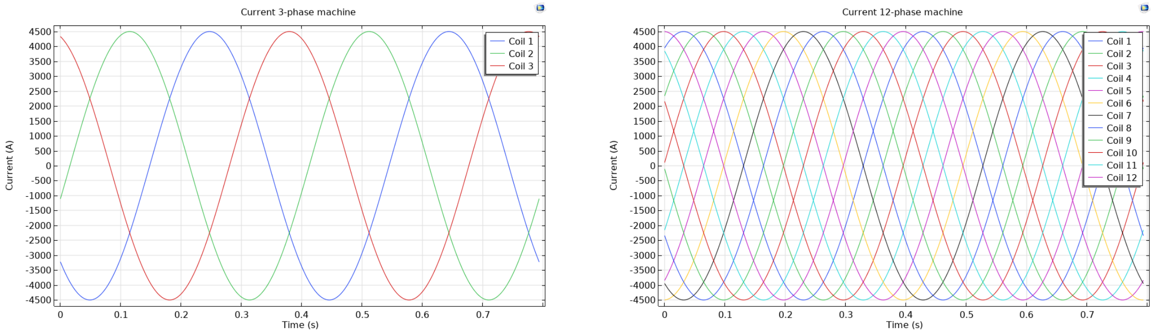

(a) 3-phase machine (b) 12-phase machine

Figure 29: Current comparison

The voltage generated by the winding layouts is shown in figure 30. It is important to notice that the 3-phase winding layout creates a distorted voltage. It contains a zero-axis voltage, which means that it has a third harmonic that is not producing useful torque to the machine. Nonetheless, for a 12-phase winding layout, there is no zero-axis voltage due to a third harmonic. Nonetheless, both voltages may have other harmonics, these are going to be assess in the section for the harmonic analysis.

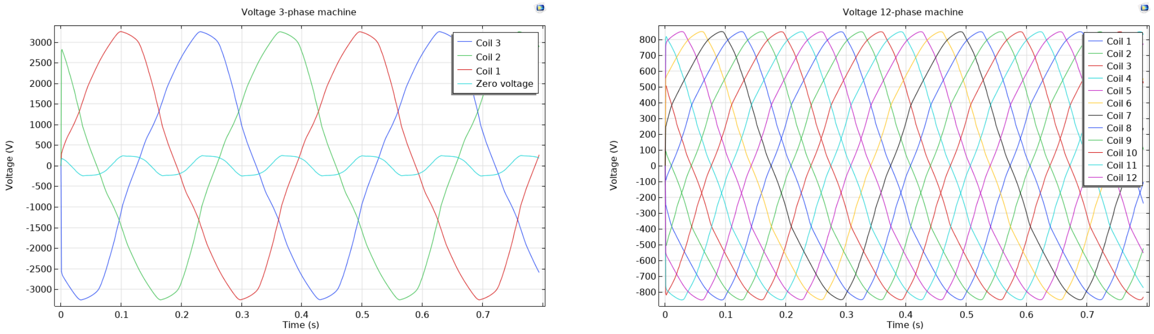

(a) 3-phase machine (b) 12-phase machine

Figure 30: Voltage comparison

In figure 31 the power for 3-phase and 12-phase machines are compared. At first glance, the 3-phase machine suggests a better overall performance. However, with a deeper view of the graphs, the following is found: (1) the power production, for the same geometry and output current, is higher for the 12-phase machine due to a better winding factor and higher main space harmonic; (2) the amplitude of the rippling behaviour is less for the 12-phase machine. This is because the time and space harmonics produce better performance for the 12-phase machine; and (3) in the 12-phase machine, a fluctuating behaviour is observable in the computation with the Arkkio's method, that for 3-phase machine case is less noticeable due to the graph's scale, which can be related to a fluctuation of the magnetic flux densities in the airgap due to the magnetic flux lines repelled from the superconducting coils.

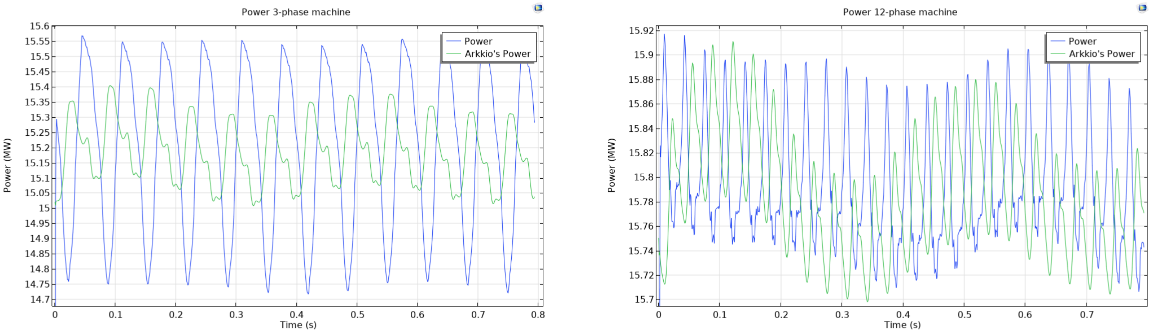

(a) 3-phase machine

(b) 12-phase machine

Figure 31: Power comparison

To observe better the behaviour of the power for the 2 machine models the data is plotted in the same graphs to have a better comparison. In figure 32 the power of both machines is depicted, it can be seen that the fluctuating behaviour is the same for both machine, the power ripple is less for the 12-phase machine, and the higher power output of the 12-phase machine.

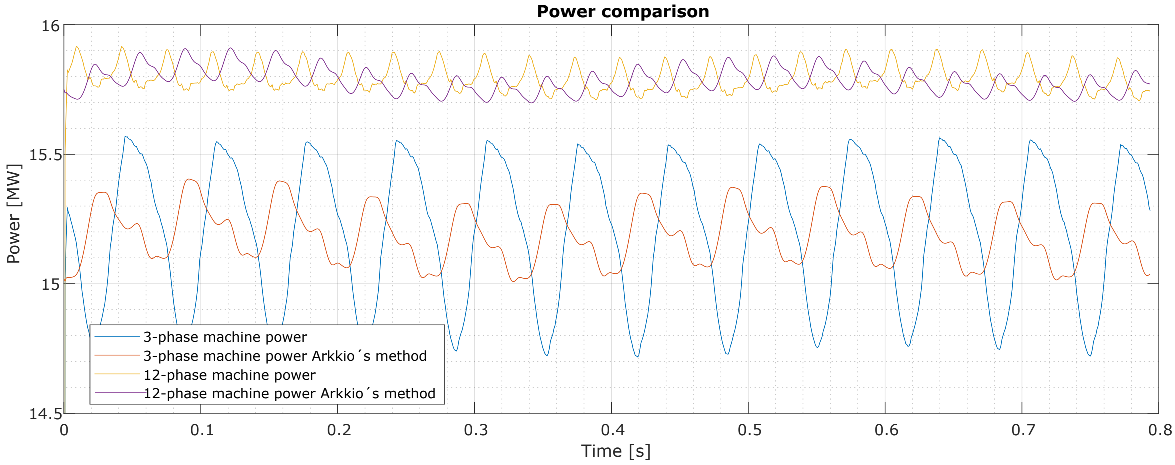

Figure 32: Power behaviour

According to Pyrhönen, the conventional shear stress for an air-cooled machine is around 59.5 kPa, so at least to double that, the shear stress of a superconducting machine should be around 120 kPa. For the present work, the calculated shear stresses surpass this criterion. Therefore, in table 6 the shear stress values are presented, in which they tripled the shear stress compared to a classical machine.

Table 6: Shear stress

Topology	Shear stress
3-phase machine	182.3201 kPa
12-phase machine	189.4736 kPa

7.3.1 Airgap analysis

A more specific analysis is performed in the airgap to assess the fluctuating behaviour of the magnetic flux density in the airgap. A line graph is plotted for the airgap magnetic flux density. The line is selected between the moving part and the static part of the COMSOL model, and because only a quarter of the machine is modelled, the x-axis is from 0 to 90°. Nonetheless, due to the winding layout consist of fractional slot concentrated windings, the flux density graph of the airgap is not well-defined as an integer winding. However, it is possible to make some remarks out of the two graphs.

Even though the 3-phase and 12-phase winding layouts are completely different in terms of harmonics, winding factor and electromagnetic properties, in the end, the waveforms depict mostly the slot-pole combination, which is the same for both winding layouts, yet looking at the graphs can spot some small difference. For instance, in figure 33, every peak represent a slot, but the peak values for the same slot at each winding layout is not the same. These values are related to the harmonics acting on the airgap. Thus, the harmonic analysis section will further explain these differences.

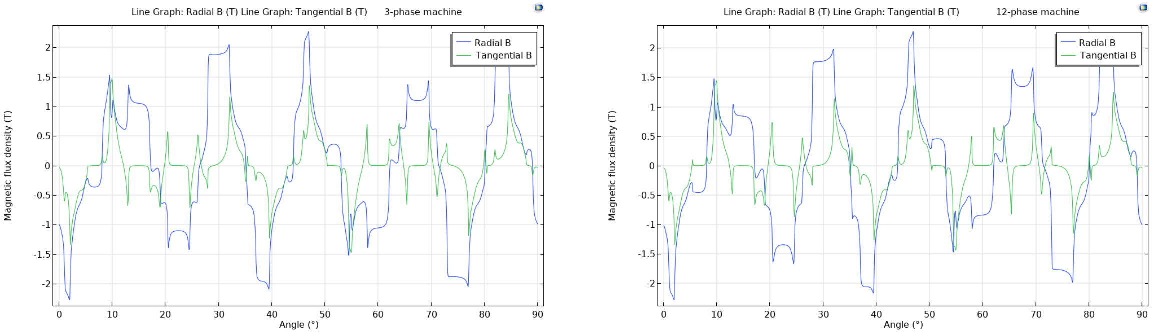

(a) 3-phase machine

(b) 12-phase machine

Figure 33: Magnetic flux density line graph comparison

To show the magnetic behaviour, the graphs are plotted in time. Therefore, the average magnetic flux density and the magnetic angle in Arkkio's band are calculated. Now is possible to assess the fluctuating behaviour. On the one hand, the magnetic flux density fluctuates at synchronous speed, likewise the magnetic angle. On the other hand, the ripple of the magnetic behaviour is smoother for the 12-phase machine, and the overall magnetic flux density average in the airgap is higher.

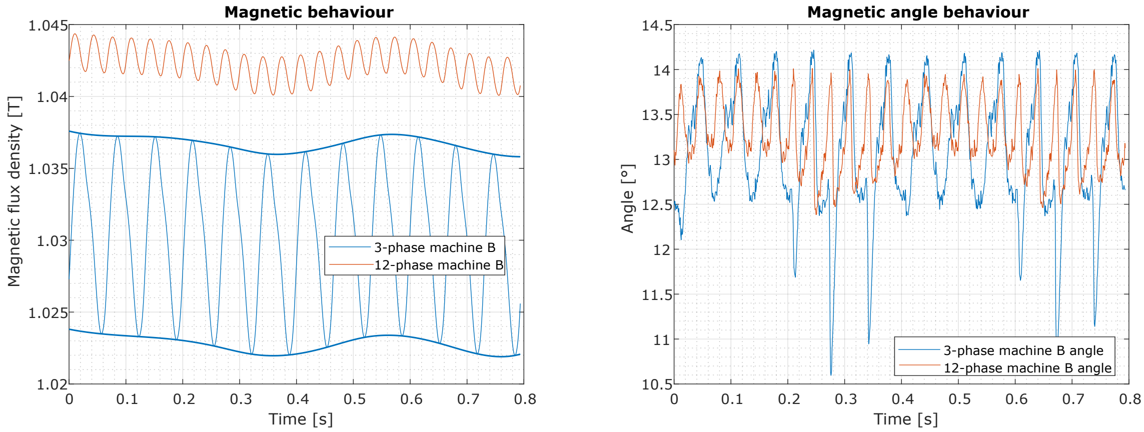

(a) Average airgap magnetic flux density

(b) Airgap magnetic angle

Figure 34: Magnetic flux density airgap behaviour comparison

Needless to say, a rotating machine contains a rotating magnetic field at a synchronous speed. Hence, this fluctuating magnetic behaviour in the airgap is due to the rotating magnetic flux density and the superconducting coils that repel the flux lines. For instance, in figure 35 an example of the average magnetic flux density behaviour in the airgap is shown for a non-superconducting formulation or an ultra-high conductivity, where the magnetic flux lines are not repelled from the coils. In this example, it can see that the fluctuating behaviour is not present. Thus, from this example, it can conclude that this fluctuating behaviour in the airgap of the machine is produced by the superconducting coils repelling the magnetic flux lines.

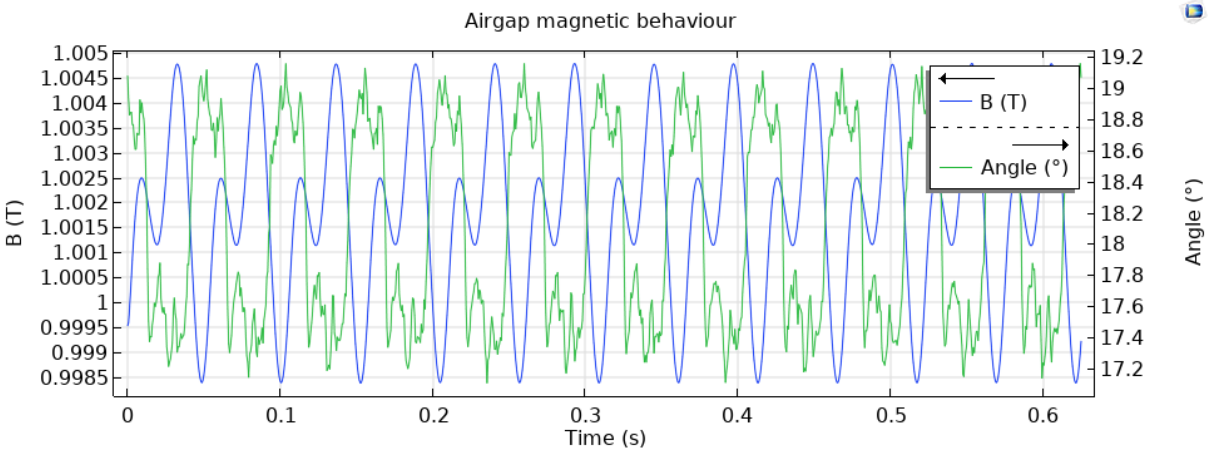

Figure 35: Example of the average magnetic flux density airgap behaviour for a non-superconducting formulation

7.3.2 Ripple and fluctuating behaviour analysis

The ripple is mostly generated due to the geometry of the machine, which is the slot-pole combination. For the present work, the 3-phase and the 12-phase machines have the same slot combination. Thus, one should obtain similar results. However, the ripple is not just only cause by the slot-pole combination. The winding layout also affects the magnetic flux interaction in the airgap.

A 3-phase machine contains space sub-harmonics and a third time-harmonic, as shown in the voltage graphs for the zero-axis voltage. This is due to the winding layout. For a fractional slot concentrated winding of a 3-phase system, one of the smarter design philosophies is to achieve a slot per pole per phase with a denominator equal to 2 to eliminate space sub-harmonics. Nonetheless, for a fractional slot concentrated 3-phase winding machine, that is only possible for $q = 1/2$, in which the winding factor is not optimal neither the slot-pole combination to reduce the torque ripple. Hence, one of the most common designs is $q = 2/5$. However, it presents an unbalance slot current behaviour, as is shown in figure 36a. This slot current behaviour creates the space sub-harmonics and the zero-axis voltage. Whereas the 12-phase winding layout does not present any unbalance in the slot currents, all are the same, as is shown in figure 36b.

From figure 15 in the theory section, it is straightforward to observe that in the case for the 3-phase winding, there some slots that the current is going in (or out), as well as one coil current going in and the other coil going out in the same slot. On the other hand, for the 12-phase and 24-phase winding layouts, the current of the coils in the slots are either going out or in, but not a combination. Therefore, the slot current for the later winding layouts is symmetrical, do not present unbalance.

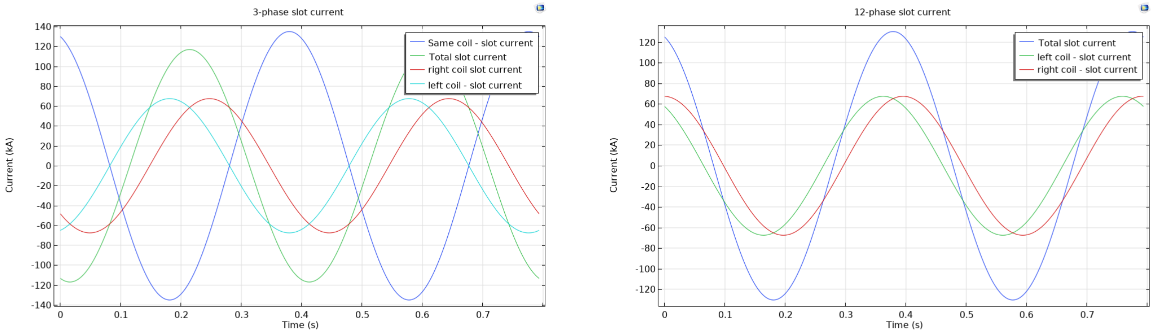

(a) 3-phase machine (b) 12-phase machine

Figure 36: Slot current behaviour comparison

The fluctuating magnetic flux density in the airgap affects the power and torque ripple and affects the mechanical forces acting on the machine. The torque and the power, as previously discussed, can be calculated from Maxwell's stress tensor components. Further, with this tensor, it can calculate the radial forces acting on the machine. Thus, the radial forces acting on the airgap of the machine are computed to depict its behaviour upon the machine in figure 37. As expected, in figure 37a the fluctuating behaviour appears in the radial forces acting in the airgap of the machine, while the ripple is reduced for the 12-phase machine. On the other hand, in figure 37b the angle between the tangential and radial forces is as expected according to Maxwell's stress tensor analysis, in which the forces angle is around the double of the magnetic angle. Moreover, it shows that with a higher armature reaction, the angle between the tangential and radial forces is increased even further.

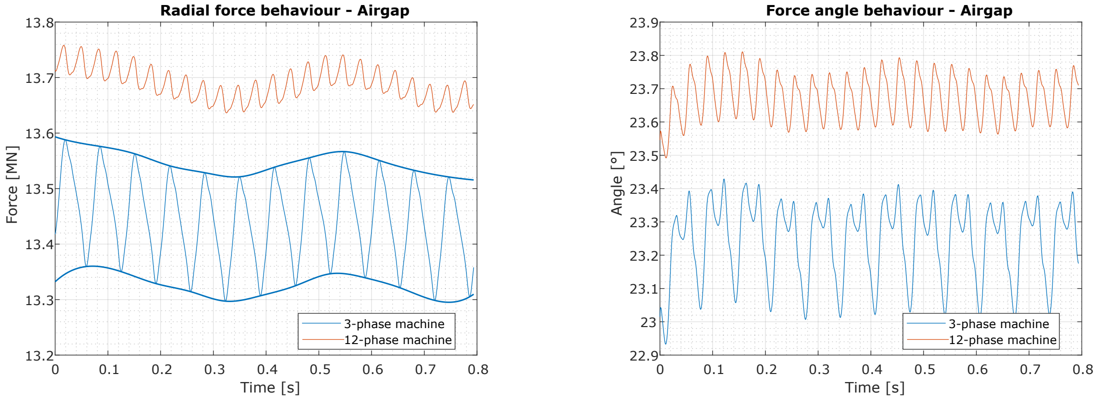

(a) Radial force airgap

(b) Force angle airgap

Figure 37: Forces behaviour comparison

Theoretically, the optimal angle between the radial and tangential magnetic components should be 45 °, giving a 90 ° angle between the radial and tangential force, implying that the radial force decreases to zero.

Moreover, this fluctuating behaviour appears to affect also in the magnetization of the permanent magnets. Nonetheless, the PMs are modelled as multiple sections to reduce the losses created by the eddy losses. The PM magnetic flux density behaviour is still affected by the fluctuation of airgap magnetic flux density as is shown in figure 38.

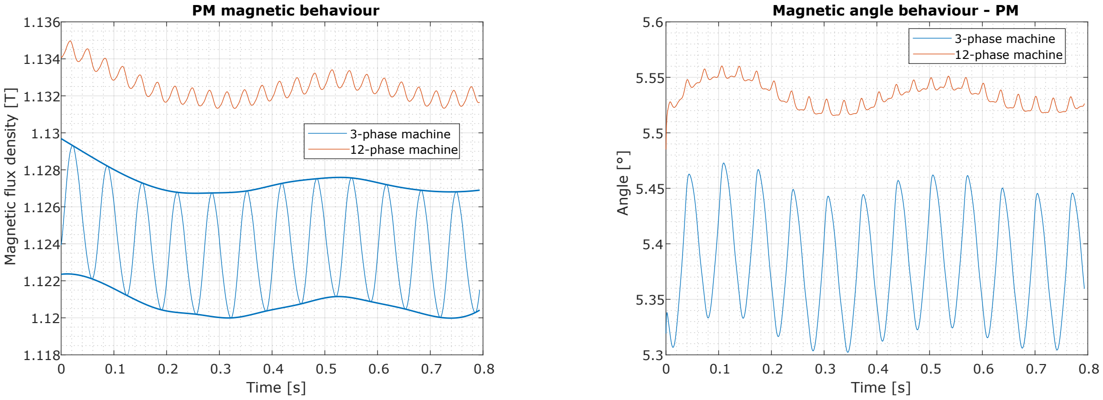

(a) Magnetic flux density PMs

(b) Magnetic angle PMs

Figure 38: Magnetic flux density PM behaviour comparison

Furthermore, it is important to notice that the average magnetization of the PMs for a 12-phase machine is higher than a 3-phase machine. Regardless of how strong the armature reaction of a multiphase machine is, the magnetization is not further reduced than the 3-phase machine. Nonetheless, the ripple variation in which the PMs are encountered is less for the 12-phase machine, meaning a better magnetic flux density distribution along the airgap by reducing the ripple of flux density and the demagnetization of the PMs. This result can further be interpreted as a reduction in the PMs losses. However, nowadays fabrication process achieves very high PM efficiencies with low losses due to the lamination. Additionally, for fully superconducting machines, this behaviour could be beneficial.

7.3.3 Harmonic analysis

Harmonic analysis is performed to comprehend and analyse the differences between the 2 graphs of the magnetic flux densities in the airgap line for both machines. Further on, a time-harmonic analysis is carried out for the phase voltage of each machine. For the case of the space harmonics, in figure 39b shows that a 12-phase machine does not have a space sub-harmonic, whilst it has a higher value of the working harmonic. This accounts for the better performance of the 12-phase machine compared to the 3-phase machine.

On the other hand, for the time harmonics, the 12-phase machine depicts a reduction in the third-order harmonics, as is shown in figure 39a.

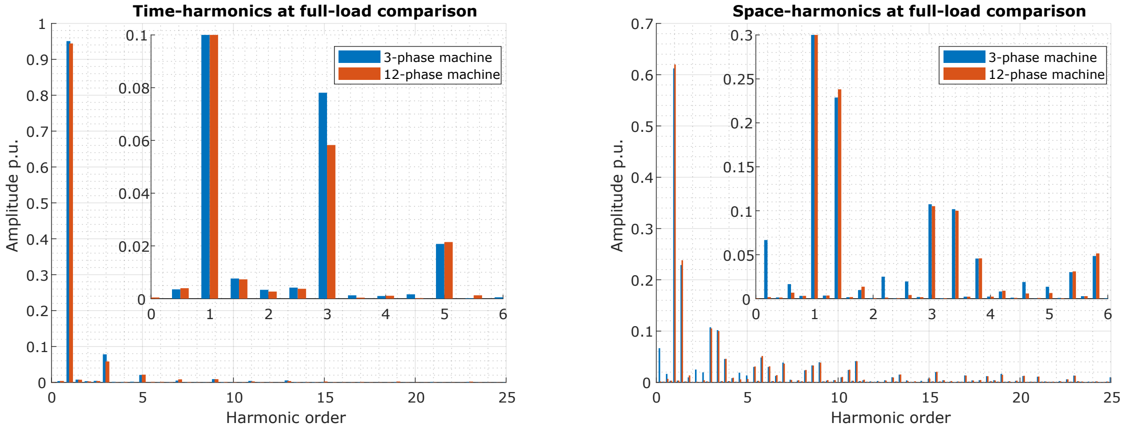

(a) Time harmonics

(b) Space harmonics

Figure 39: Harmonics analysis comparison

The harmonic analysis shows that a 12-phase machine has a better performance by eliminating the space sub-harmonics, increasing the working space harmonic, and reducing the third-order harmonics. These advantages are presented throughout the graphs: higher power output, no zero-axis voltage, less torque ripple, and smoother behaviour of the magnetic flux density in the airgap.

7.3.4 Iron losses analysis

To assess the advantages of the magnetic behaviour of a multiphase machine, the iron losses are calculated based on the CAL2 method, where the hysteresis and dynamic losses coefficients vary to the peak value of the magnetic flux density in the iron for each time step. In figure 40 the iron losses between the 3-phase and the 12-phase machine are compared. The values are based upon the 3-phase machine losses to see the differences. In figure 40a the iron losses are presented relative to the total input power of each machine topology. For the case of the 3-machine, the total iron losses represent 24.284 % of the total machine power. While, for the 12-phase machine, the total losses are 20.799 %. Then in figure 40b the losses are compared between the 2 topologies, having a reduction of around 14 % of iron losses for the 12-phase machine compared to the 3-phase machine.

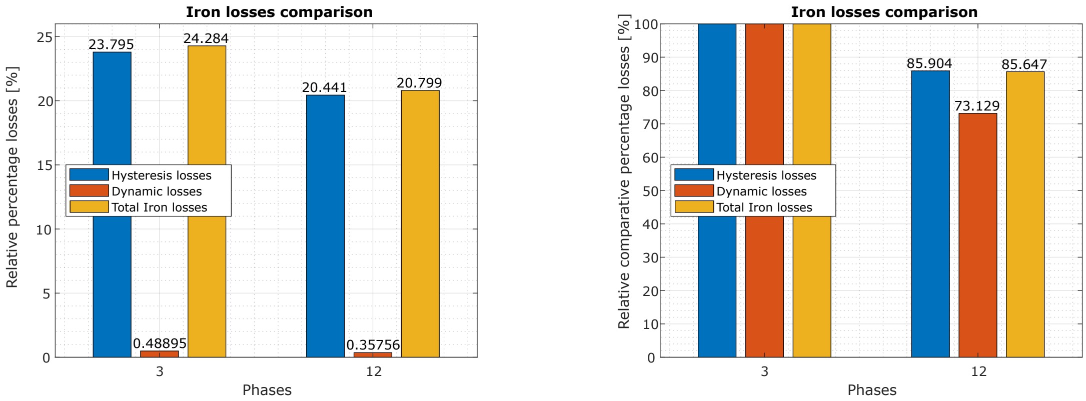

(a) Relative losses to the total input power

(b) Relative comparative losses

Figure 40: Iron losses

It is straightforward that the iron losses for the same geometry are higher for a 3-phase machine, even when the output power is less. Therefore, one can say that a 12-phase machine has a better distribution of the magnetic flux inside the iron, even for higher output power with the same geometry or iron path for magnetic flux. The hysteresis and dynamic losses are further reduced for a symmetric multiphase machine.

7.3.5 Superconducting AC losses

The AC losses in the superconducting coils for the present model are calculated with the resistive heating built-in model in COMSOL. The electric field and the current density are used to compute the losses. For the present work, the AC losses are calculated in the second cycle to account for the transient behaviour during the first cycle. Only the hysteresis losses into the superconductive material are calculated because the other wire's layers are not modelled. In table 7 the AC losses for the 2 topologies are presented.

Topology	AC losses
3-phase	83 055.8158 W
12-phase	83 644.4696 W

Table 7: Superconducting AC losses

There is no further outcome of the AC losses in terms of reduction or increment due to changing a multiphase winding layout. The current density of both topologies is the same because the coils' operating current is 4500 A, and the number of turns per coil is 15. Thus, the slight increment in the AC losses for the 12-phase machine can be related to the higher output power of the machine. Also, the higher winding factor can further increase the electric field. However, there is no improvement in the AC losses.

Moreover, the penetration of the magnetic flux density inside the coils is depicted in figure 41. It shows a smoother maximum flux density behaviour for a 12-phase machine and a similar behaviour for the average magnetic flux density among all the coils. Nonetheless, it does not contribute to the total AC losses reduction. However, for a better superconductive formulation, this could have a stronger influence on superconductivity.

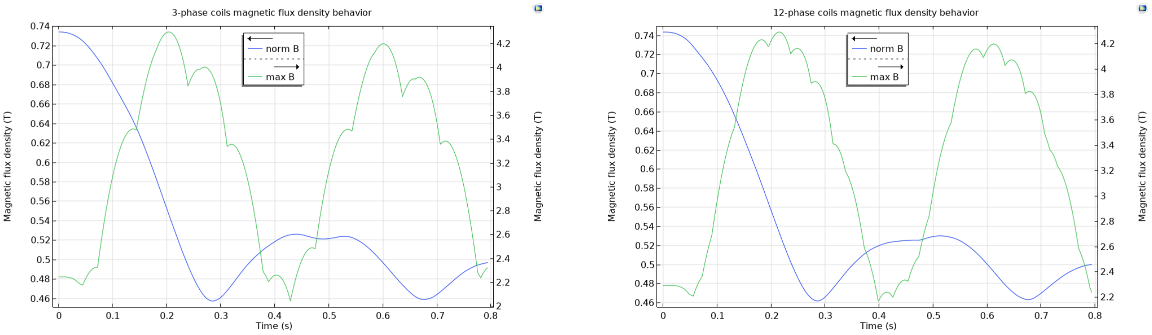

(a) 3-phase machine

(b) 12-phase machine

Figure 41: Magnetic flux density in the coils behaviour comparison

The winding layout design in terms of phases does not represent a solution to reduce the AC losses in superconducting armature coils. Hence, one can make a deeper analysis of the behaviour of the flux lines inside the slots. As discussed in the theory section, the slot effect into the coils represents an important significance in understanding the flux lines behaviour. Normally, in a well-design slotted machine, the flux lines will travel from tooth to tooth horizontally. However, as the superconductivity requires a cryostat to cool down the coils, a wider slot area must be designed. Thus, the flux lines do not travel from tooth to tooth; how is it shown in figure 42. Instead, the flux lines travel from the closest air paths to the coils, and when they get closer to the airgap, the flux lines are tilted accordingly to the machine's level of magnetic and electric loading. The higher concentration of flux lines in the right tooth is because the rotor motion direction, in this case, is moving counterclockwise.

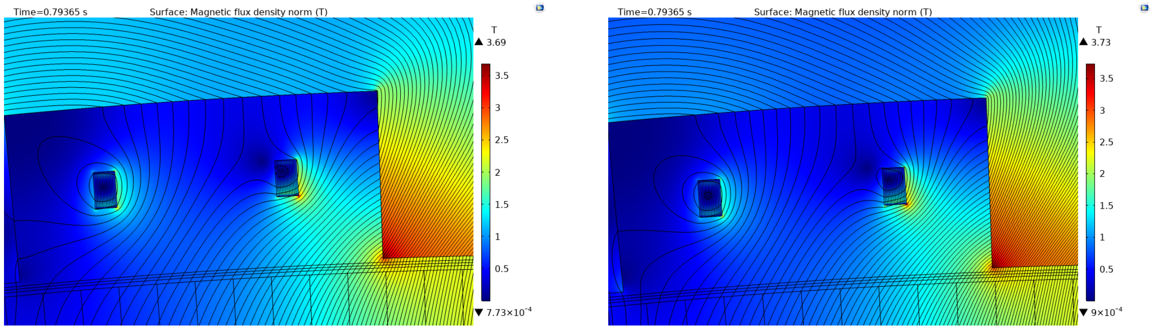

(a) 3-phase machine (b) 12-phase machine

Figure 42: Magnetic flux lines in the slots comparison

Taking as reference behaviour the horizontal flux lines in a well-designed machine, and taking into account the tilted angle of the flux lines near the airgap due to magnetic loading, it is not suggested to have a radial (vertical) design location of tape coils because it is not a smart solution to reduce AC losses. The non-linearity of the conductivity creates a strong distribution of the current density. Some parts of the superconductive material area have lower conductivity, meaning that they will have higher losses in the superconductive material.

The current density distribution results from the AC currents flowing and the flux lines crossing the coils, pushing the current density to the boundaries of the wire. Better known as skin effect. Further analysis must tilt the coils to produce a better distribution of the current density to account for the anisotropy of the wire geometry and the flux lines angle.

7.3.6 Power factor analysis

For a good overall performance of a wind power generator, the power factor is an important parameter to assess because of the stress in the power electronics components to deliver the reactive power needed to operate the machine. Thus, a comparison of power factors between the two machines is made.

Power factor calculation

The current of the machine was set to be in phase with the back EMF at no-load condition. Therefore, the angle between the voltage at load condition and the q-axis is known. A park transformation of the voltage at load condition is done, then the calculation of the power factor is as follows:

$$p_f = \frac{V_q}{\sqrt{V_d^2 + V_q^2}} \tag{79}$$

The average value obtained with this calculation are:

Topology	Power factor
3-phase	0.72734
12-phase	0.73175

Table 8: Power factor comparison

There is not a significant difference between the two results. However, compared to the reference superconducting model, the power factor is enhanced. This is due to the stronger permanent magnets used of $B_r = 1.47\,\mathrm{T}$.

A 12-phase winding layout cannot enhance the power factor. The power factor for both topologies is the same because they share the same number of turns per slots, the current and the reluctance. From a magnetic energy perspective, both machines will have the same distribution of magnetic energy. The magnetic energy created by the rotor's permanent magnets will be the same because they share the same geometry. Furthermore, if the number of turns per coil is changed to reduce the reluctance, the current has to be increased. Hence, the overall magnetic energy in the armature winding will be the same for both topologies.

Furthermore, the reactance in per unit can be calculated with the power factor as follows:

$$X_{p.u.} = \sqrt{1 - p_f^2} \tag{80}$$

In figure 43 the behaviour of the power factor and the reactance in p.u. over time is depicted. The graphs are mirrored plots of each other. However, again the ripple for the 12-phase machine is reduced compared to the 3-phase machine.

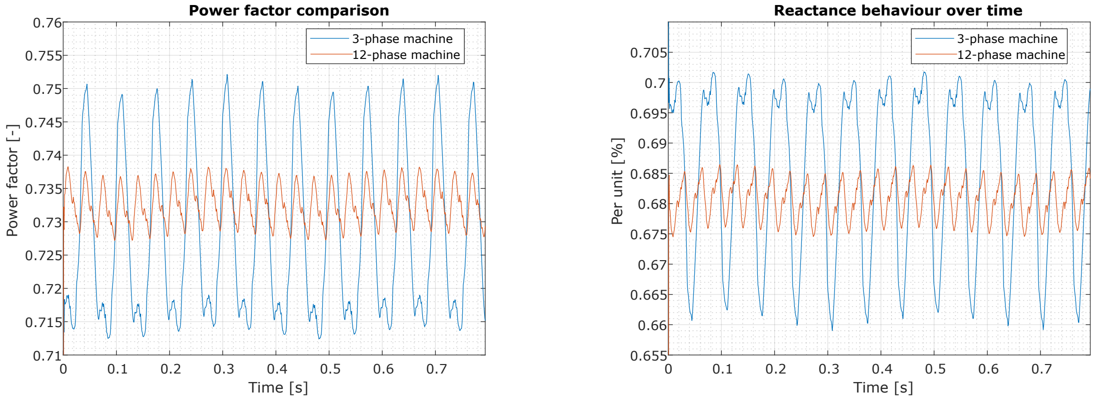

(a) Power factor

(b) Reactance in p.u.

Figure 43: Power factor and reactance behaviour comparison

7.3.7 Overall comparison

An overview of the performance of the 2 machines comparison is depicted in figure 44, where is clearly to see that the 12-phase machine has some advantages in terms of the iron losses. Which is related to the better distribution among the whole machine of the magnetic flux density, and no space sub-harmonics. And the output power that is enhanced due to the better winding factor.

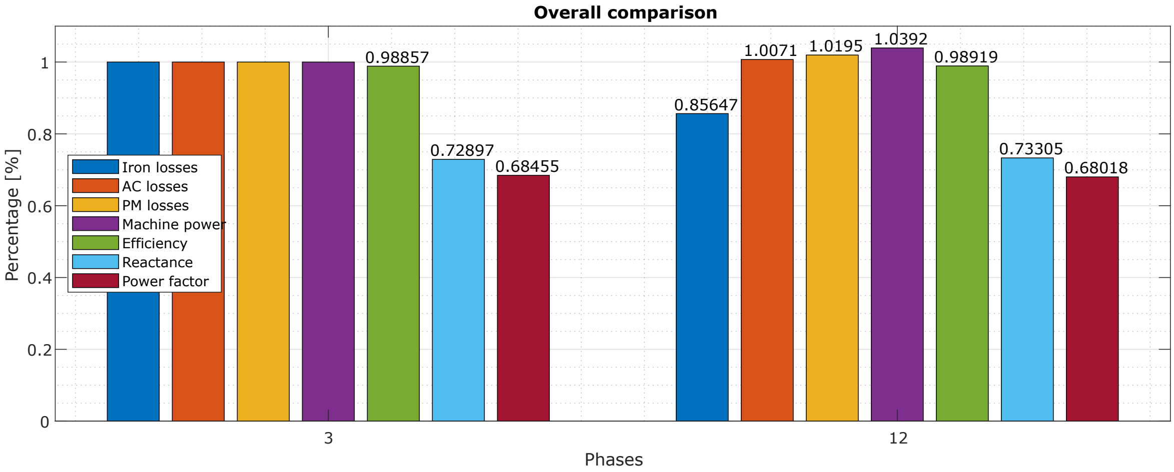

Figure 44: Overall comparison for 15 MW generator

Up to this point, the comparison between a 3-phase and 12-phase symmetric winding layouts with the same geometries, same number of turns per coil, and same current show that a multiphase symmetric winding layout enhances the magnetic flux density behaviour to be smoother, which improves the torque and power ripple, and the iron losses by hysteresis and dynamic losses are reduced. However, the hysteretic superconducting AC losses, the power factor, the reactance per unit, and the efficiency are almost similar for both configurations. The power output is increased for the 12-phase machine due to better winding factor, no space sub-harmonics, and higher value of the working space harmonic. However, one must prove further improvements for multiphase symmetric winding layouts to make it a standard choice.

7.4 Analysis of the 24-phase machine

To have a deeper understanding and achieve further improvement into multiphase symmetric winding layouts, the 24-phase machine is analysed. To generate the 24-phase voltages, the geometry is changed from 20 to 22 pole-pairs to comply with the symmetry conditions. This changes the frequency and the flux per pole, as well as the thickness of the yoke.

Moreover, to model the machine, the number of segments or sections is changed from 4 to 2. This is due to the number of slots of the basis winding is $Q_s' = 24$. In figure 45 the geometry of a 24-phase machine is depicted.

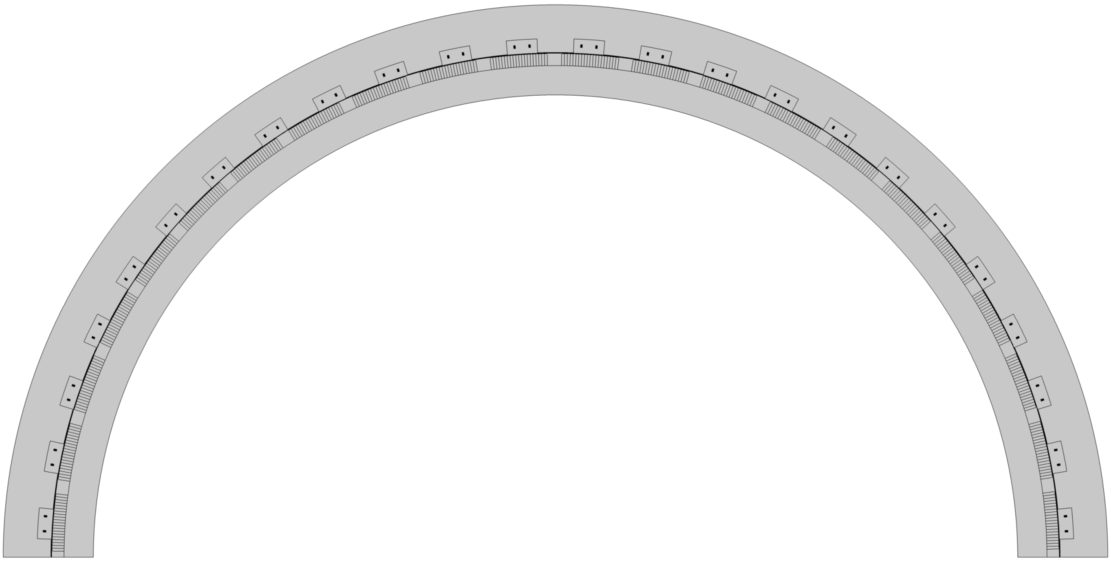

Figure 45: 24-phase machine geometry

In figure 46 the currents and voltages are shown to verify that is a symmetrical winding layout.

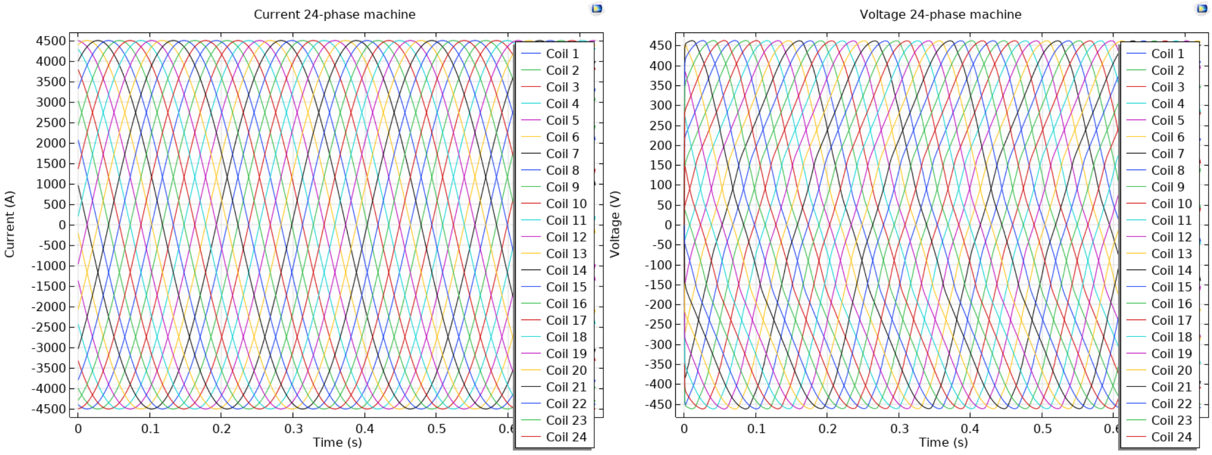

(a) Currents (b) Voltages

Figure 46: 24-phase machine

The output power comparison for all the machines is depicted in figure 47. The 24-phase machine has advantages over the others in performance by achieving a higher output power and a torque ripple reduction. The output power is improved mainly because the electrical frequency increases due to the larger number of pole pairs. The torque ripple is reduced due to the slot-pole combination and better winding layout. The cogging torque is further diminished because the slot-pole combination gives a higher Least Common Multiple (LCM). Meaning that with symmetric multiphase winding layouts is possible to achieve very high LCMs whilst complying with the symmetry conditions and eliminating space sub-harmonics.

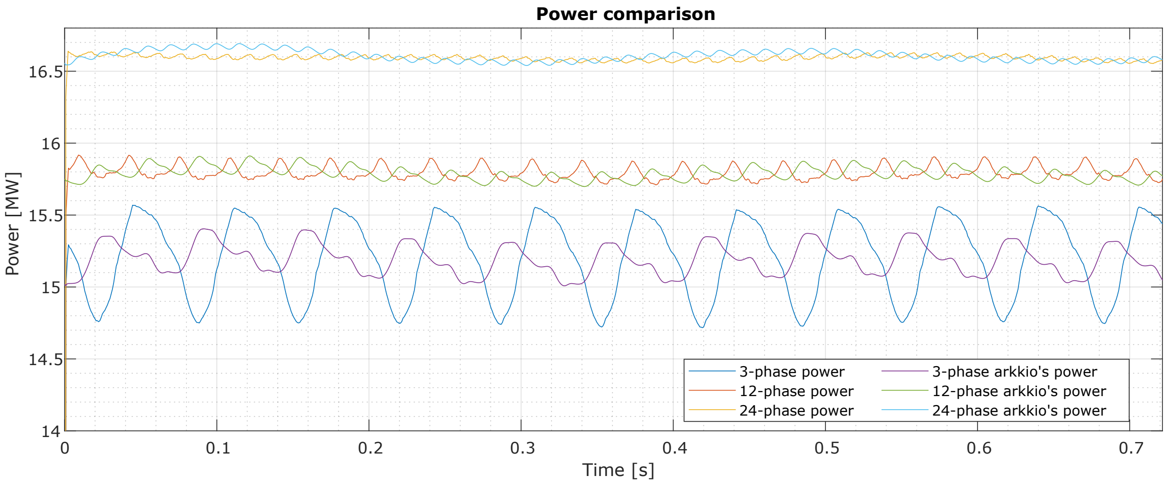

Figure 47: Power comparison with a 24-phase machine

Further, the shear stress is also improved for the 24-phase machine, as is shown in figure 48. This is related to the machine's loading, which directly impacts the magnetic and force angle. Producing higher shear stress for the same magnetic loading, one can expect more demagnetization due to the stronger MMF.

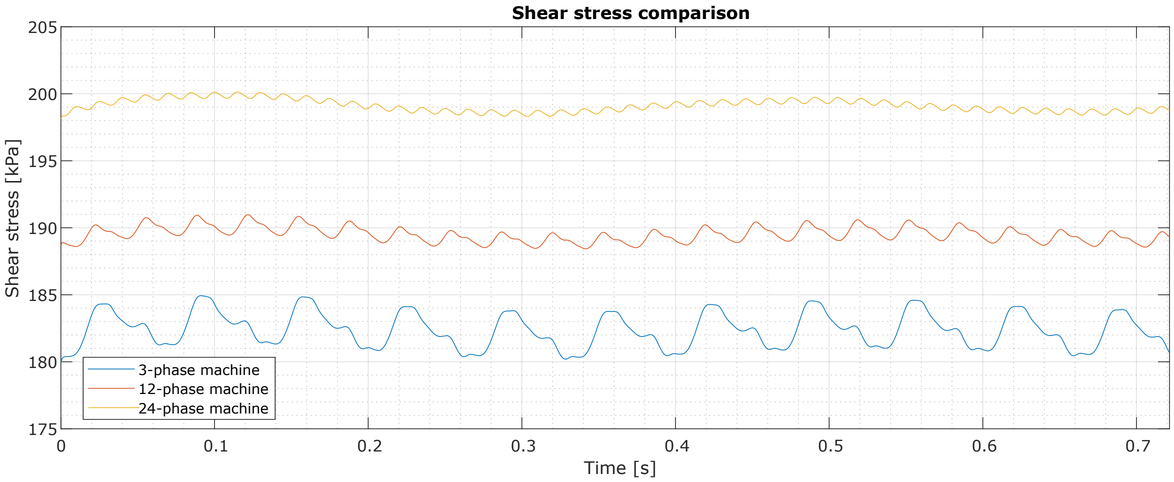

Figure 48: Shear stress comparison over time

The airgap flux density is slightly decreased compared to the 12-phase machine. This is because the 24-phase machine has a higher armature reaction due to the higher frequency, and the flux per poles is decreased due to the magnet's width. In figure 49 the airgap magnetic flux density is presented, where depicts the norm and the angle. This shows that even if the magnetic loading is lower, the higher armature reaction due to the higher electrical frequency can further increase the magnetic angle.

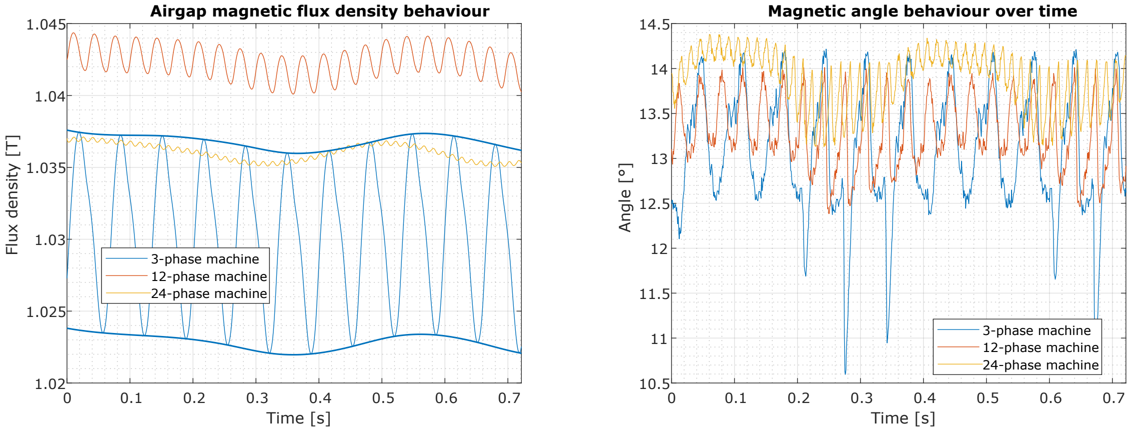

(a) Average airgap magnetic flux density (b) Airgap magnetic angle

Figure 49: Magnetic flux density airgap behaviour comparison

An important remark for the 24-phase machine is that the magnetic angle is further tilted due to the higher armature reaction, which means that the force angle is also increased. According to Maxwell's stress tensor, it can decrease the radial forces compared to the 12-phase machine. This behaviour is shown in figure 50.

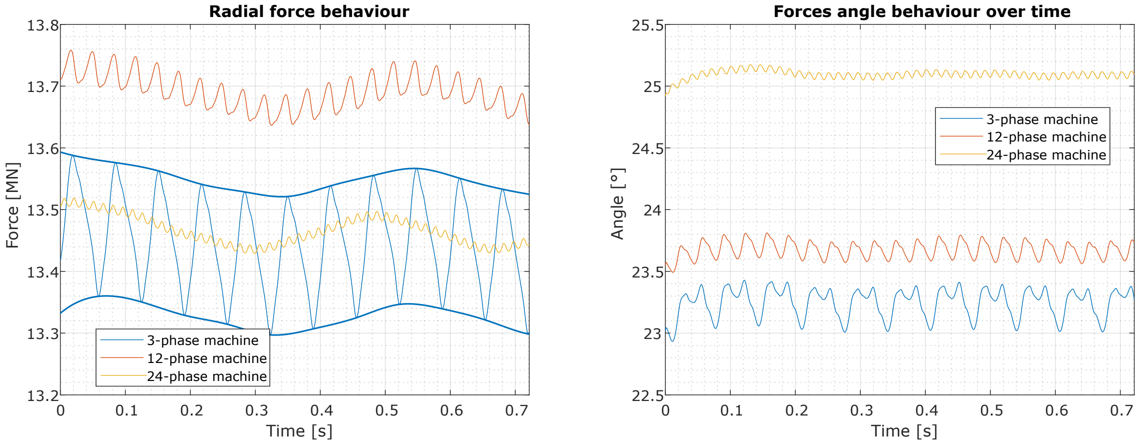

(a) Radial force airgap (b) Force angle airgap

Figure 50: Forces behaviour comparison

For the case of the magnetization of the permanent magnets, the stronger armature reaction does not help to improve the demagnetization in comparison to the 12-phase machine, and the magnetic angle inside the permanent magnets is further increased, as is shown in figure 51. The tilting of the magnetic angle inside the magnets will contribute to a lower power factor because of the lower radial magnetic flux density.

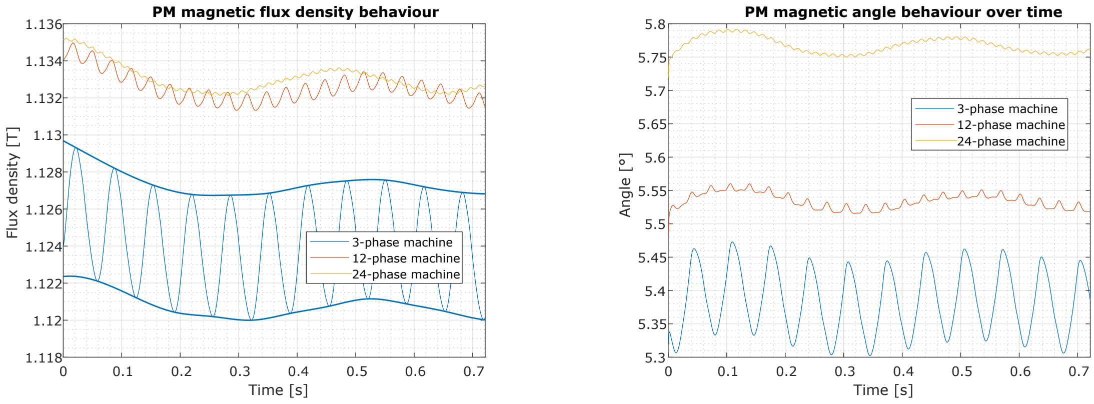

(a) Magnetic flux density PMs (b) Magnetic angle PMs

Figure 51: Magnetic flux density PM behaviour comparison

The harmonic analysis shown in figure 52 depicts what was expected in comparison to the other models in terms of space harmonics. However, the fundamental time-harmonics for the multiphase machine are slightly diminished at full-load operation.

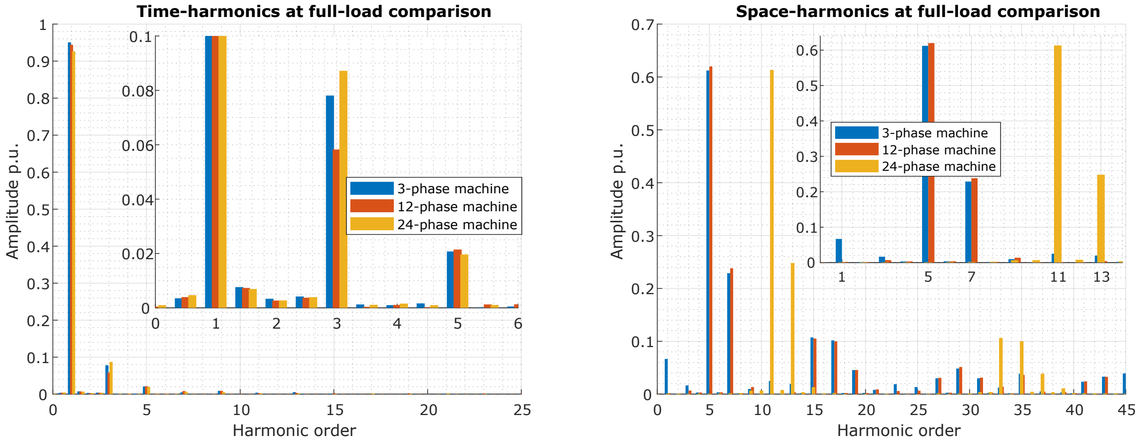

(a) Time harmonics (b) Space harmonics

Figure 52: Harmonics analysis comparison

The power factor is reduced due to the higher armature reaction of the machine that demagnetizes more the PM's, while the reactance is increased accordingly, as is shown in figure 53.

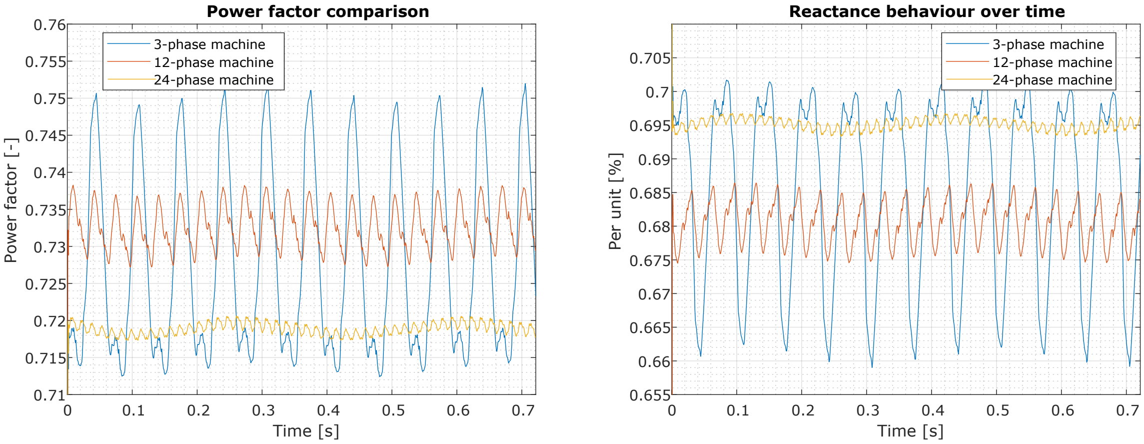

(a) Power factor

(b) Reactance in p.u.

Figure 53: Power factor and reactance behaviour comparison

Hitherto, implementing symmetrical multiphase windings, in which the airgap's smoother magnetic flux density behaviour reduces the torque ripple, is insufficient to achieve a good machine performance because the average value of the power factor is not improved in comparison to conventional winding layout design. Nonetheless, the rippling behaviour of the power factor is enhanced. Moreover, this is important because it means that the direct and quadrature voltages are smoother, making the machine's controllability easier. Furthermore, a different approach must be taken to enhance the power factor and achieve a good machine design.

7.4.1 Superconducting AC losses

For the 24-phase machine, the AC losses are calculated as the previous models, obtaining 72 042.4797 W of losses in the armature coils. Compared to the 2 previous models, the 24-phase machine has reduced the AC losses in the coils by around 13.26 %.

Nonetheless, this behaviour is not a result of the smoother behaviour of the magnetic field. Instead, it represents that the tilting angle of the magnetic flux lines is higher, producing a change in the hysteretic superconducting AC losses.

It is important to remark that the AC losses can be reduced per every filament scribed by applying laser-scribing fabrication technique. For instance, if the wire is scribed with 10 filaments, the AC losses are reduced to a tenth of the non-scribed version. In table 9 the AC losses are presented for all the models with the assumption of the laser scribing technique to reduce further the AC losses.

Model/Fabrication	Non-scribed	Scribed - 10 filaments
3-phase machine	83 055.8158 W	8305.58 W
12-phase machine	83 644.4696 W	8364.45 W
24-phase machine	72 042.4797 W	7204.25 W

Table 9: AC superconducting losses comparison with laser-scribing technique

7.5 Discussion

Having more phases eliminates the sub-harmonics and enhance the performance of the machine. Even though a multiphase machine could have a lower fundamental time-harmonic, the output power is higher because the working space-harmonic can be higher and most essentially does not have space sub-harmonics. Thus, the torque ripple is further diminished due to smoother magnetic flux density behaviour and a higher LCM value slot-pole combination while achieving symmetry conditions and eliminating space sub-harmonics.

The winding layout does not influence the superconducting AC losses. However, it is seen that due to the bigger slot area for the cryostat, the magnetic flux lines do not travel from tooth to tooth, which means that the slot effect for a good design is not achieved. Instead, the flux lines travel with a tilted angle related to the magnetic loading of the machine. Hence, a different angular position of the coils could reduce the AC losses.

For the case of the power factor, the multiphase winding layout does not enhance the performance to achieve a well-designed machine. Although the demagnetization for a multiphase machine is reduced, the power factor is not further improved. Therefore, it is suggested to investigate other designs for permanent magnets rotors with higher flux densities and better capability to withstand demagnetization.

Furthermore, the superconducting machine's compactness creates a high armature winding reaction. This creates a strong fluctuation in the magnetic field in the airgap due to the repelled flux lines from the superconducting coil. A resized to a larger airgap length, based on the machine's power, can reduce the airgap flux density fluctuation. However, this effect is not eliminated, and the output power is diminished. Therefore, more work into this has to be done.

In the 24-phase machine, the AC losses in the superconducting armature coils are reduced. But this effect is because of the further tilting of the magnetic angle due to the higher armature reaction of a 24-phase winding. Hence, the flux lines enter more perpendicular to the coil's side, reducing the AC losses. Furthermore, the machine's performance is enhanced as expected by increasing the number of phases in the armature winding.

7.5.1 Tesla's egg of Columbus

To understand the behaviour of a multiphase machine, a test verification machine is designed and modelled to comprehend and explain further the implications of having multiphase electrical systems. The machine is a Tesla's egg of Columbus, in which 5 different winding configurations are tested. The model is based on Gezer et al. design [116], with an extension to more phases. To design the multiphase windings, they have to be short-pitch to properly achieved the symmetry conditions and obtain the rotating magnetic field without pulsations. The parameters used are the following:

Parameters	**Description**	**3-phase**	**6-phase**	**12-phase**	**24-phase**	**48-phase**
N	Number of turns per coil	256	128	64	32	16
I_r	Rated current [A]			10		
D_{os}	Outer stator diameter [mm]			310		
D_{is}	Inner stator diameter [mm]			170		
D_{or}	Outer "rotor" diameter [mm]			150		
D_{ir}	Inner "rotor" diameter [mm]			120		
f	Frequency [Hz]			60		

Table 10: Tesla's egg of Columbus input parameters

For the 3-phase machine system, the stator is divided into 6 phase bands of 60°, as is shown in figure 54. The colours show the phase: green is phase 1, yellow is phase 2, and purple is phase 3. The brighter colours represent that the current is going inside the plane. Only The 3-phase Tesla's egg of Columbus is depicted because the notable differences are only the coils set-up, e.g. the 6-phase machine is divided into 12 phase bands of 30°, and so forth for the other configurations. The rest of the geometries are shown in the appendix in figure 80.

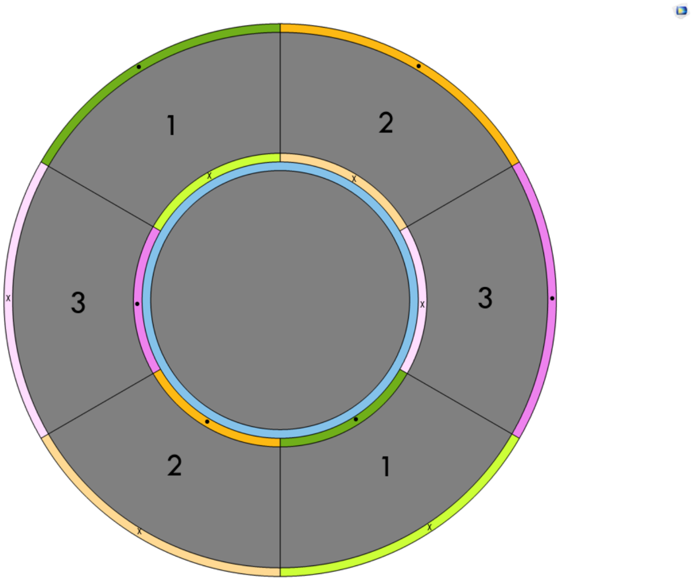

Figure 54: Geometry of a 3-phase Tesla's egg of Columbus

The magnetic flux density in the airgap is analyzed by obtaining the graphs for the average and the maximum magnetic fields. As is shown in figures 55, 56, 57, as the number of phases increases, the fluctuating of the magnetic flux density is diminished. On the one hand, the average magnetic flux density is increased while having a smoother behaviour. On the other hand, the maximum magnetic flux density variation is decreased until a practically constant behaviour for the 48-phase Tesla's machine. More plots for the magnetic flux density in the iron are shown in the appendix in figure 83, in which the magnetic flux density behaviour is further improved and smooth by increasing the number of phases.

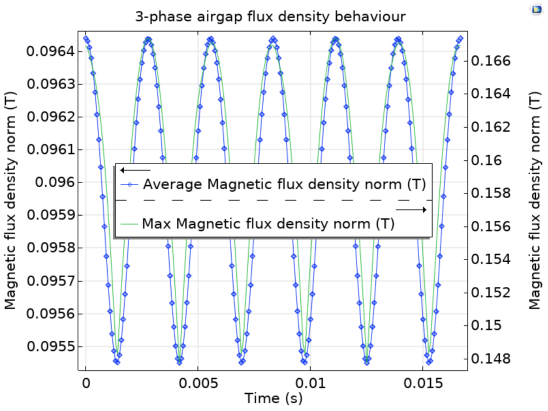

(a) 3-phase (b) 6-phase

Figure 55: Tesla's egg of Columbus comparison 1

Nonetheless, there is no improvement in the magnetic behaviour between the 3-phase and 6-phase machine. This is because symmetrical 6-phase windings have the same number of unique voltage phasors as a 3-phase winding, which cannot improve the magnetic behaviour.

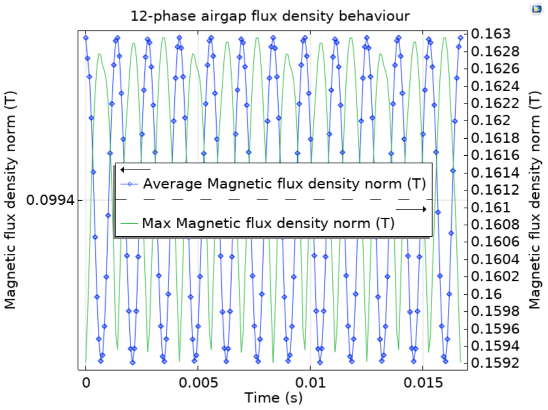

(a) 12-phase (b) 24-phase

Figure 56: Tesla's egg of Columbus comparison 2

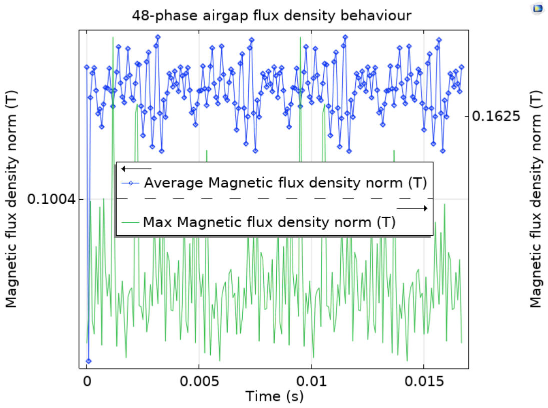

Figure 57: 48-phase Tesla's egg of Columbus

For instance, figure 58 shows that the power per phase for a 6-phase machine will contribute to the ripple of the power at the same level as the 3-phase machine which means that it has redundant phasors with the same angle.

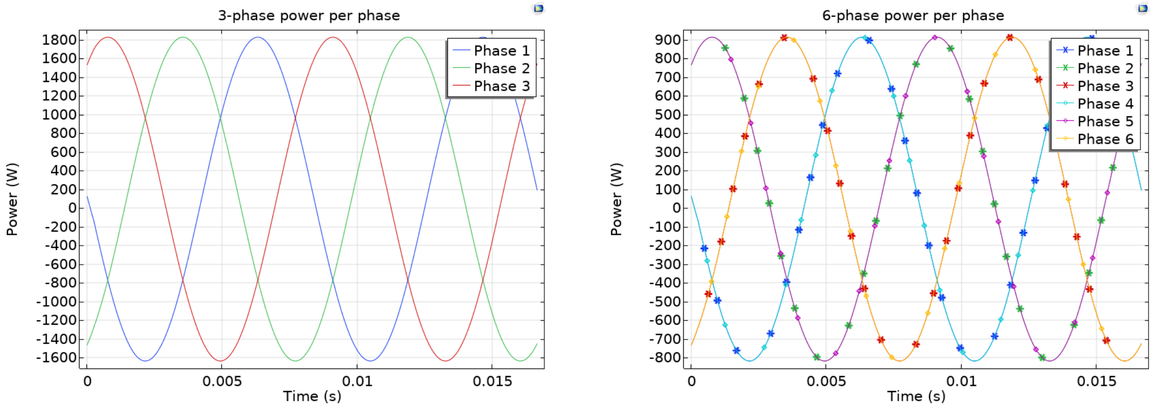

(a) 3-phase

(b) 6-phase

Figure 58: power per phase comparison

Further on, in figure 59 the phase-shift between power per phase for higher phase order machines creates more unique phasors. However, due to 12, 24 and 48 are multiples of 2, all of them will have redundant phasors that will not contribute to the ripple reduction and enhance the magnetic behaviour in the machine. Thus, the smarter way to design a symmetric multiphase winding layout is to achieve unique phasors, which means to have an odd number of phases for the electrical system.

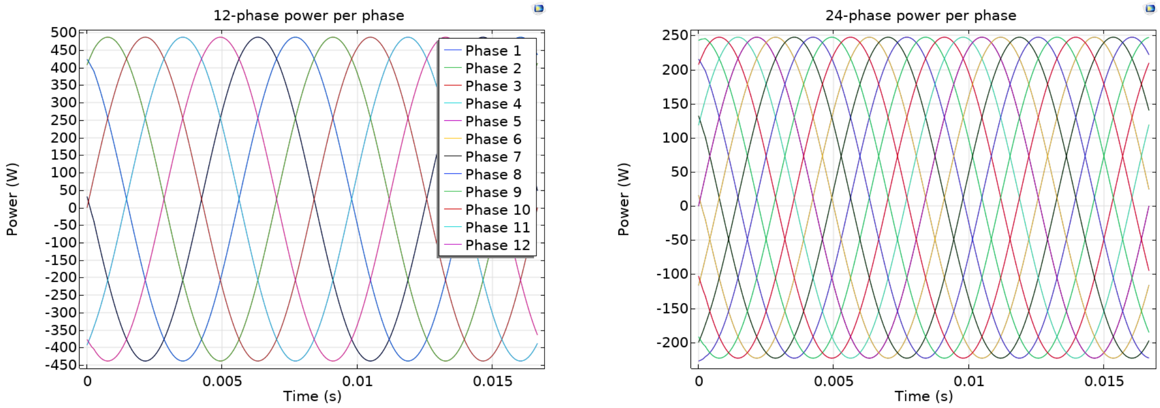

(a) 12-phase (b) 24-phase

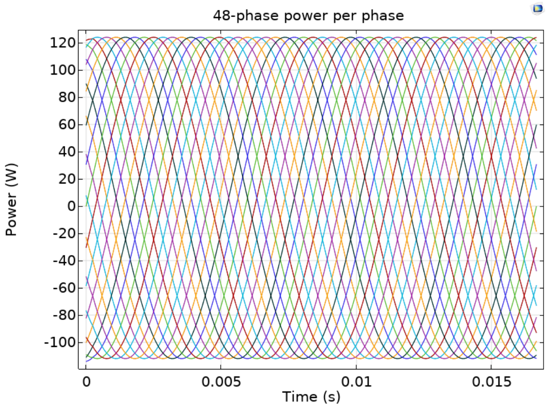

(c) 48-phase

Figure 59: power per phase comparison 12, 24 and 48 phases

The number of turns per phase is decreased accordingly to the number of phases of the machine. However, the power output obtained for high-phase order machines are enhanced to a certain degree. This is due to the winding factor is enhanced for more phases thanks to a better winding distribution. Nonetheless, this improvement of the power and voltages can be made for a 3-phase system by a better winding distribution. The power and voltages graphs are shown in the appendix.

As previously discussed, the more phases in the electrical system, the smoother the behaviour of the overall magnetic flux densities in the machine. Further, the rippling behaviour of the torque is directly connected to the power ripple. Thus, the mechanical behaviour created by magnetic fields interaction between the armature reaction, rotor and reluctances influence the electrical behaviour. Hence, a smoother magnetic fields behaviour creates a smoother electrical power behaviour.

Therefore, to have a good symmetrical multiphase design, the number of phases must ensure that unique phasors windings are designed to reduce the rippling behaviour and enhance the machine's overall performance.

8 Optimization

8.1 AC losses reduction

To reduce further the AC losses in the superconductive material due to hysteresis, the flux lines in the slots and the airgap have to be taken into account to known the optimal tilt angle of the AC superconducting armature coils. For instance, if the coils are located in a tangential (horizontal) direction the AC losses can be reduced up to 19%, as is shown in figure 60.

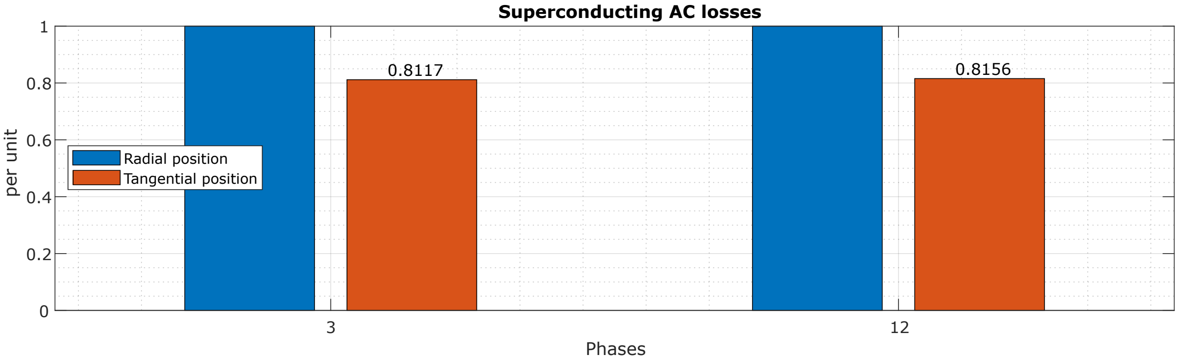

Figure 60: AC losses comparison for the position angle

In figure 61 the flux lines in the slots are depicted for the tangentially positioned coils. Even the coils are tilted, the flux lines do not travel parallel to the height of the coils.

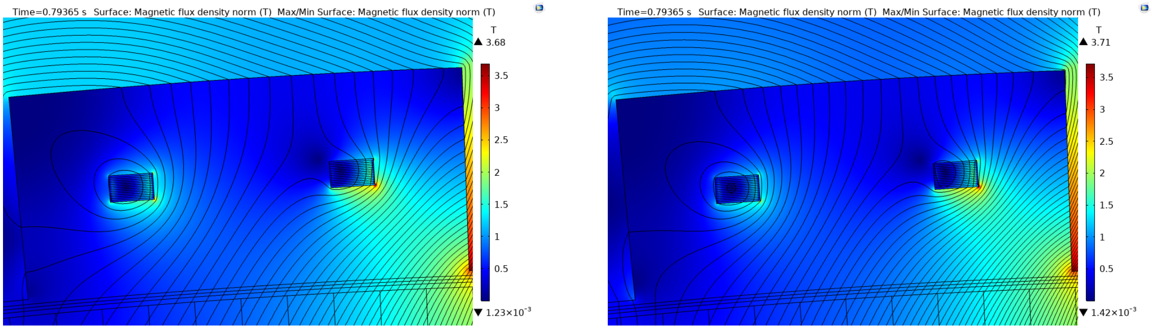

(a) 3-phase machine (b) 12-phase machine

Figure 61: Magnetic flux lines in the slots comparison

Therefore, an optimization for the optimal angle is performed with the 12-phase machine. In table 11 the AC losses are presented with the dependency of the coil's angle. First, the angle is measure from the tangential position (0°) towards the clockwise direction. Then, a manual parametric sweep over the coil's angular position is performed from 0° to 45°, in 5° steps.

Coil angle	**AC losses**
$0\,°$	68.2201 kW
$-5\,°$	63.3444 kW
$-10\,°$	59.3590 kW
$-15\,°$	55.2684 kW
$-20\,°$	51.7830 kW
$-25\,°$	49.6070 kW
$-30\,°$	47.6165 kW
$-35\,°$	46.4383 kW
$-40\,°$	46.8285 kW
$-45\,°$	47.4000 kW

Table 11: AC losses - coil's angle dependency

From table 11, the AC losses in a superconducting coil depend on the angular position of the coil concerning the tilting angle of the magnetic flux lines influencing the airgap due to the compactness and loading of the machine. It is found that with a $-35\,°$, the AC losses are further reduced to 46.4383 kW. In figure 62, the slot magnetic behaviour is depicted. The flux lines reach perpendicularly to the coils at a $-35\,°$. This means that to reduce further the AC losses in a tape superconductor coil, the flux lines have to hit the side of the coil's geometry perpendicularly.

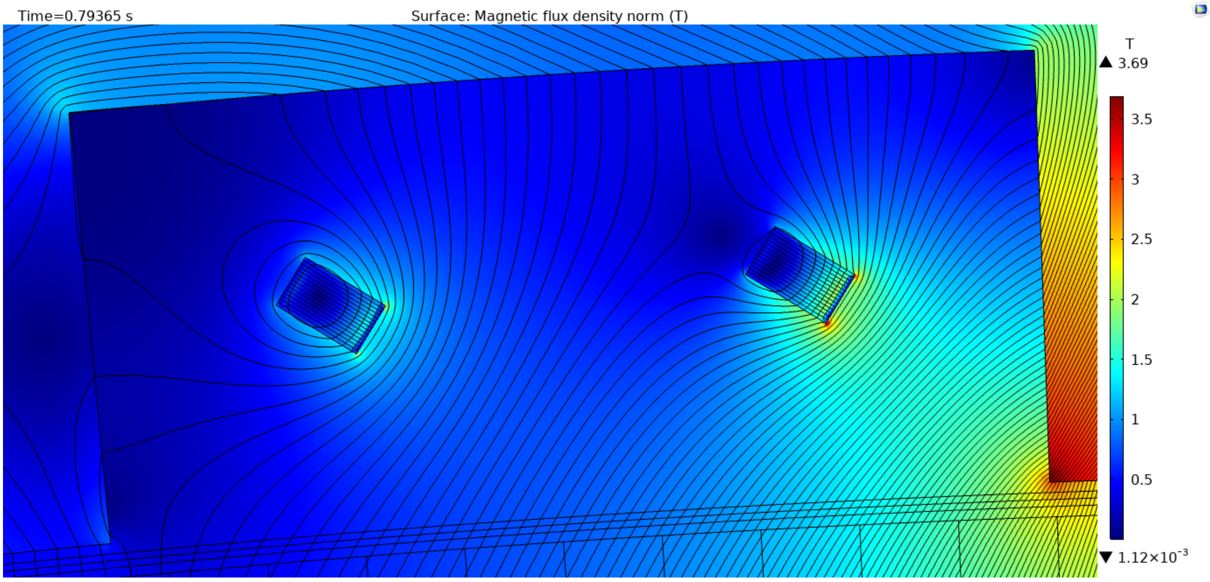

Figure 62: Flux lines with a coil's angular position of $-35\,°$

Nonetheless, the flux lines tilting angle not only depends on the compactness and loading of the machine. Also, it depends on the geometry of the slot, the iron path created for the flux lines. Thus, the left coil will have a different number and angle of incident flux lines than the right one, as is shown in figure 62. Table 12 shows a manual parametric sweeping of the left coil's angular position whilst the right coil's angle is fixed. It demonstrates that the AC losses can be further reduced if the coil's geometry varies depending on the slot side in which it is constructed.

Left coil angle	Right coil angle	AC losses
$-30\,°$	$-35\,°$	46.1453 kW
$-25\,°$	$-35\,°$	45.9993 kW
$-20\,°$	$-35\,°$	45.8149 kW
$-15\,°$	$-35\,°$	45.9966 kW

Table 12: Left coil angle variation

Figure 63 depicts the slight change in the left coil's angular position. The flux lines are more perpendicular to the side of the two coils, achieving even lower AC losses.

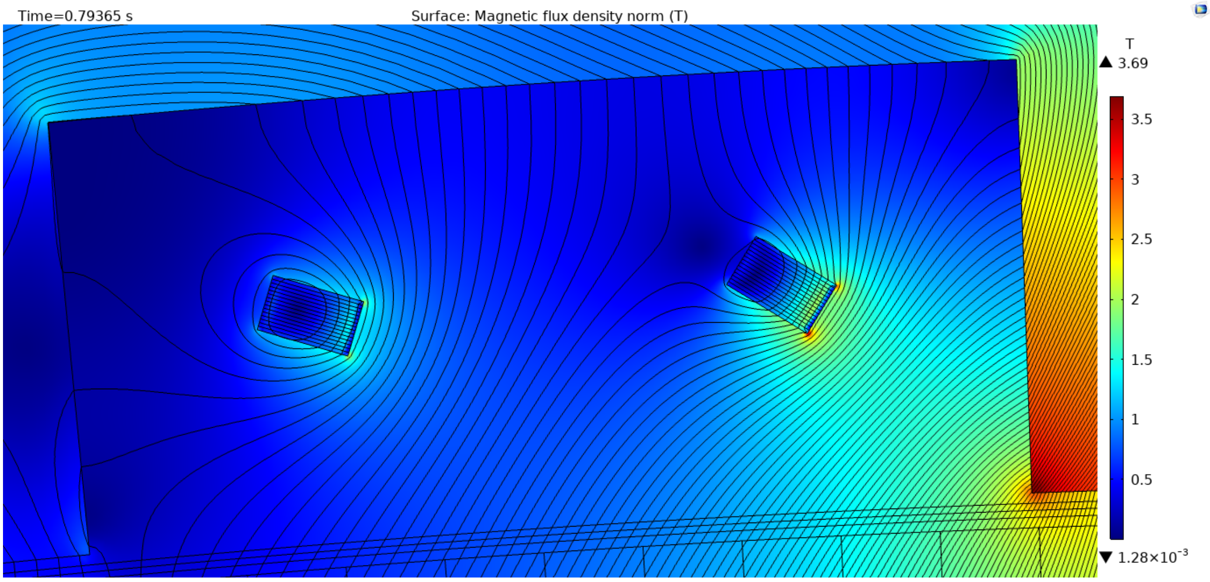

Figure 63: Sweeping only for the left coil

Further, the magnetic flux density fluctuating behaviour in the airgap is increased due to the perpendicular flux lines impact the coil's side, as is shown in figure 64, where Arkkio's method calculation of the power depicts the precise magnetic behaviour. Hence, reducing the AC losses by finding the optimum angular position of the coil regarding the tilting angle of the magnetic flux lines counteracts the fluctuating behaviour of the magnetic flux densities in the airgap by increasing it because the coil at that optimum angle repels even more, the magnetic fields.

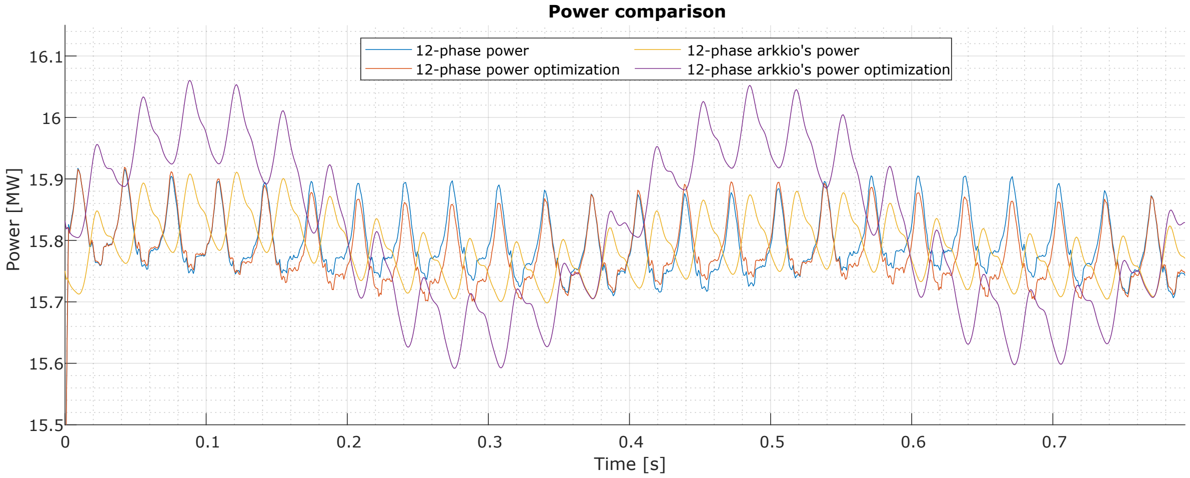

Figure 64: Fluctuating behaviour due to angular position of the coils

The superconducting hysteretic AC losses for a tape coil have a strong dependence on the angular position of the coil. Thus, to improve the design of AC superconducting armature windings, future works must perform the coil's design in 3D to comprehend the losses behaviour over the whole machine length. Moreover, due to the angular dependency and tilting of the flux lines according to the machine's loading, the AC coils must be addressed and designed with non-planar structures to account for the different percentage of loading of the machine and the variation of the magnetic flux lines along the airgap.

8.2 Discussion

The superconducting armature coils are susceptible to the topology of the slots due to the behaviour of the magnetic flux lines. Furthermore, different magnetic loading creates different flux lines behaviours with a tilted angle that influences the AC losses in the superconductor. Therefore, further research into the optimization of superconducting armature coils has to be independent of the magnetic angle of the flux lines or the loading of the machine.

Special attention to the angle position of the tape superconductor due to the flux lines tilting angle has to be considered to reduce the AC losses while not increasing the magnetic flux density fluctuating behaviour at the airgap. Future work must perform a 3D design of an armature superconducting coil to improve the AC losses and the fluctuating behaviour.

9 Design proposal

In this section the knowledge adquired from the previous analysis and discussion is put into practice by proposing a design in which the power factor is enhanced and the rippling behaviour is further smooth without having the need of too many phases.

First, a new PM rotor is proposed is which the demagnetization is decreased by increasing the magnet's volume. Second, a 13-phase symmetrical winding layout is proposed to achieve a higher performance than a 12-phase and 24-phase machine. And lastly, the two proposal are consolidated into a 13-phase AC superconducting bulky-PM machine, in which the iron losses and output power are compared to the 12-phase machine.

9.1 New rotor design approach

The demagnetization of the permanent magnets can be reduced by increasing their volume. Hence, a rotor's design approach is proposed to prove that it can enhance its magnetization and power factor for an AC superconducting machine.

The magnet's length is increased more than the double, in which 120 mm is inserted into the rotor yoke, and 80 mm comes out of the rotor, given a total of 200 mm of magnet's length. Moreover, the rotor's yoke height is increased by 80 mm to have a good iron path for the magnetic fluxes and avoid saturation. And the airgap's diameter is increased by 160 mm. The new rotors design approach is shown in figure 65.

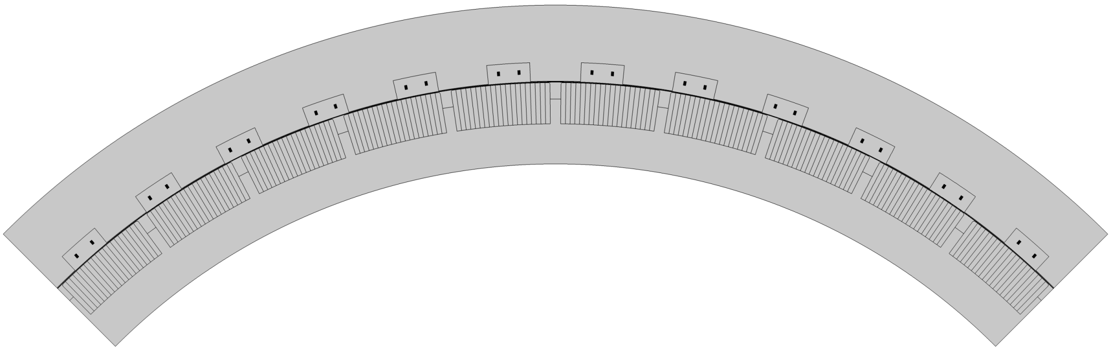

Figure 65: New rotor design approach for a 12-phase machine

The results of the simulation are shown in table 13. The power factor is enhanced up to $p_f = 0.85$, reducing the reactive compensation from the power electronics and reducing the demagnetisation. Since the magnetic loading is strengthened, the electrical loading decreases accordingly to achieve the same output power. Hence, the shear stress is 191 kPa, which triples the conventional machine's shear stress while reinforcing the overall performance.

Variable	**Description**	**Value**
p_f	Power factor	0.8543
X	Reactance	0.5179 pu
$P_{12\phi}$	Output power	16.5509 MW
I_r	Rated current	4050 A
V_t	Terminal voltage	872.0083 V
l_m	Magnet's length	200 mm
h_{yr}	Rotor's yoke height	314.97 mm
D_{ag}	Airgap's diameter	6.8538 m
σ_t	Shear stress	191.4447 kPa
B_{airgap}	Airgap's magnetic flux density	1.1772 T
Demagnetization	Magnet's demagnetization	10.0106 %

Table 13: New rotor's design geometry and outputs

A possible candidate for enhancing the power factor is presented in this thesis by increasing the volume of the magnets. Likewise, if the flux density of the magnets increases, the higher magnetic energy can further boost the power factor. Hence, a new rotor's design approach can improve the power factor. However, other approaches as Hallbach's PM arrangements can contribute to increasing the power factor.

9.2 13-phase machine

To achieve a better multiphase symmetrical winding layout, a 13-phase machine is proposed. Compared to a 24-phase, it has 1 more unique phasor, which further improves the rippling behaviour. In order to achieve a 13-phase voltages the slot pole combination for the base winding is: $Q_s = 13$ and $p_r = 6$. The total number of slots is $Q_s = 52$, and the total number of pole-pairs is $p_r = 24$. This gives an LCM equal to 624, higher than the 24-phase machine, meaning less cogging torque is expected. A quarter of the machine is simulated in COMSOL, as is shown in figure 66.

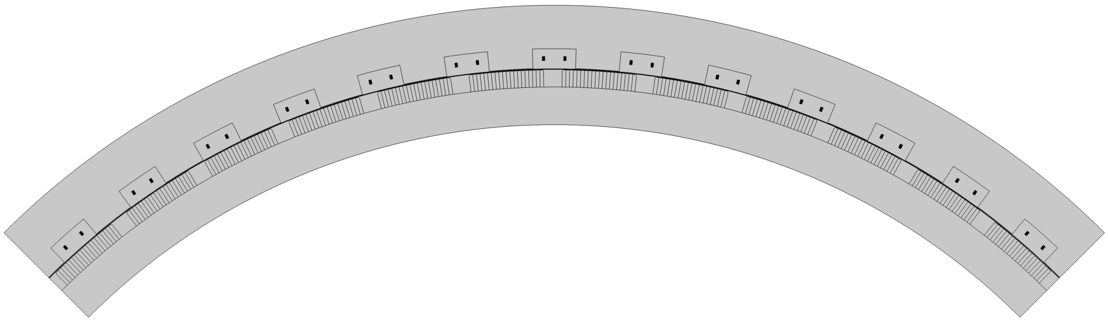

Figure 66: 13-phase machine geometry

Before the simulation, the MMF spectra for the 13-phase base winding layout is calculated, in which the 6th-order space harmonic is the working harmonic, and there are no space sub-harmonics, as is shown in figure 67.

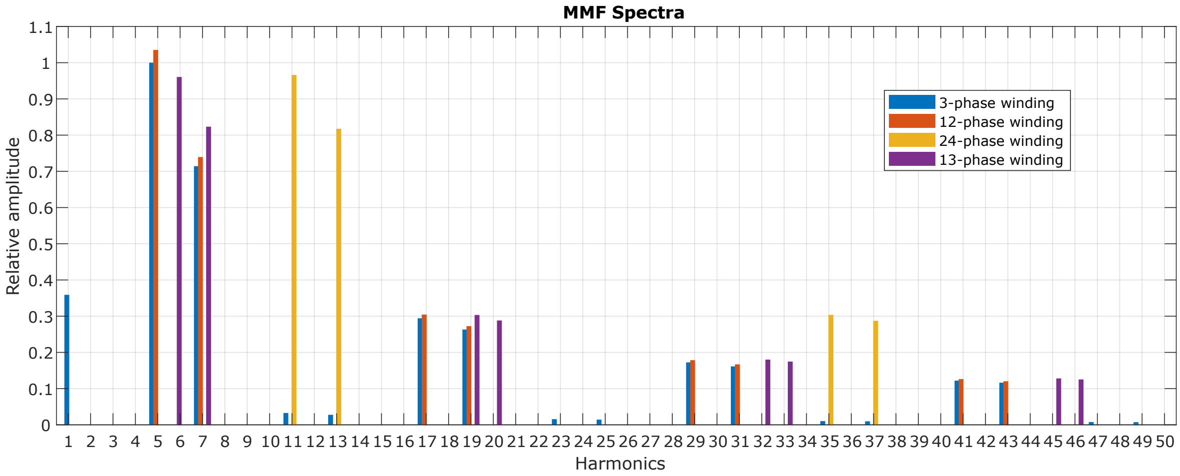

Figure 67: MMF spectra calculation

The power of the machine is depicted in figure 68. The rippling behaviour is even further reduced compared to the 24-phase due to the extra unique phasor. Moreover, the output power is increased because of the higher electrical frequency due to the 12 pole-pairs.

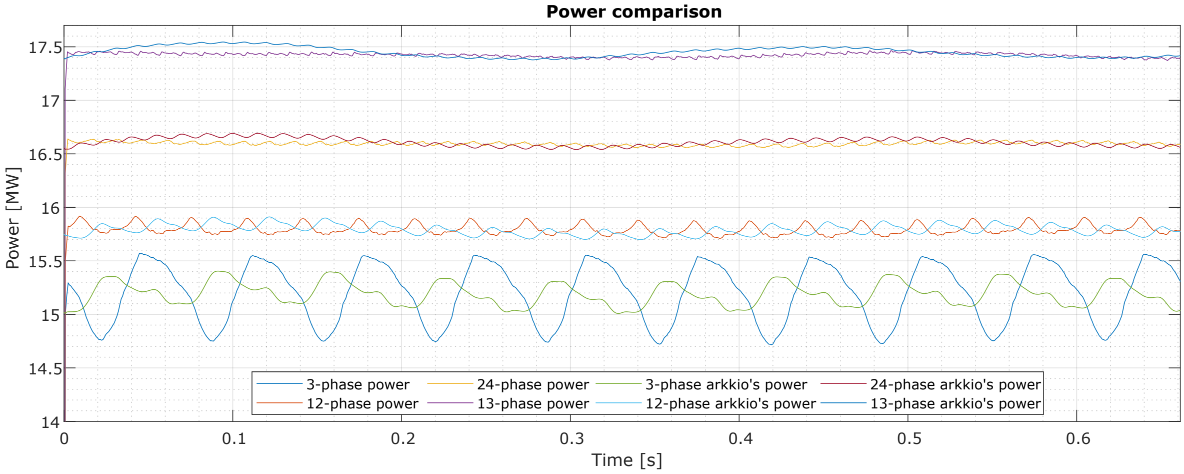

Figure 68: 13-phase machine output power

The rest of the figures are presented in the appendix because the behaviour follows the same trend as the output power. However, for the power factor and reactance case, figure 69 shows an unexpected rippling behaviour.

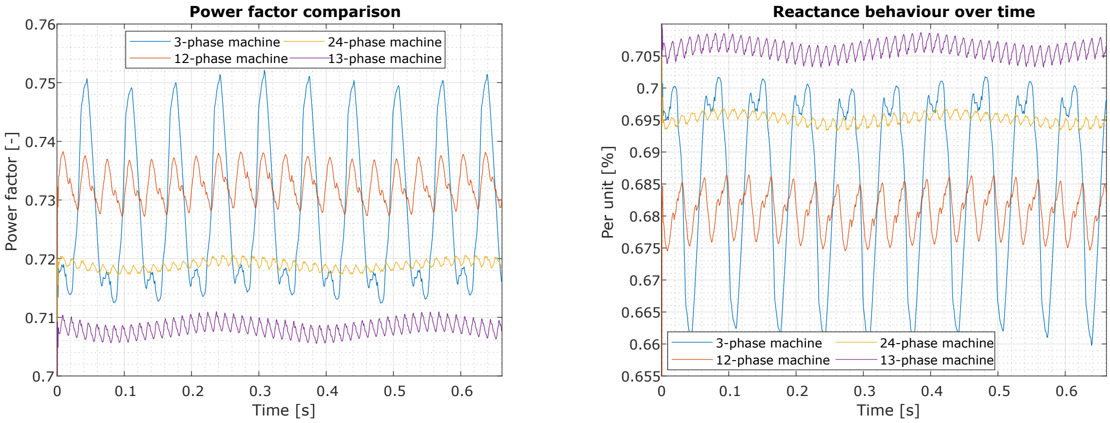

(a) Power factor

(b) Reactance per unit

Figure 69: 13-phase machine power factor and reactance comparison

The unexpected rippling behaviour is because this winding layout has a zero-sequence voltage, shown in figure 70a. And due to the power factor and reactance are calculated using the v_d and v_q voltages, in which this 3rd-order harmonic is present in the v_d voltage as is shown in figure 70b. Hence, the final computation is affected by this variation. Nonetheless, by a star connection this ripple can be eliminated.

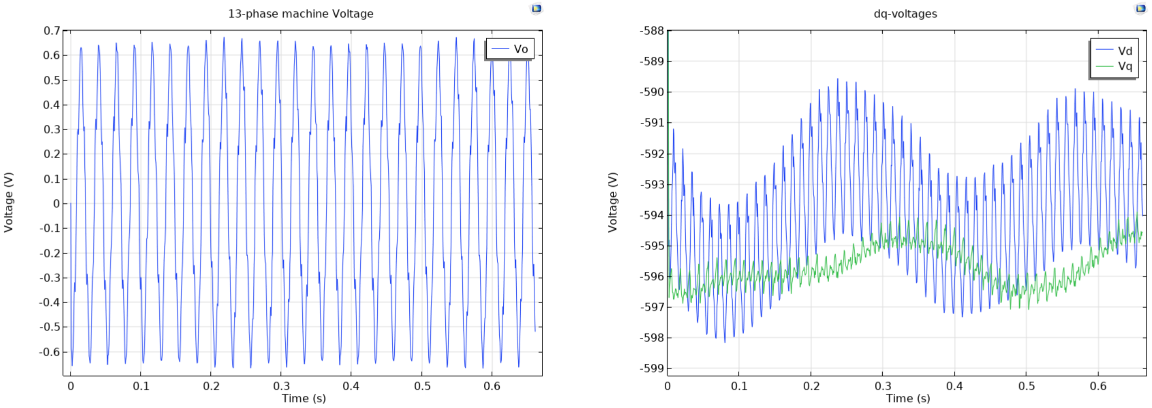

(a) Zero-sequence voltage

(b) dq voltages

Figure 70: Extra rippling behaviour: zero-sequence voltage

In table 14 the outcomes of the 13-phase machine are presented. Important to notice that the superconducting AC losses are further decreased, but this is due to the tilting of the magnetic flux density angle in the airgap, thus the flux lines are more perpendicular to the superconducting coil's side.

Variable	Description	Value
p_f	Power factor	0.7078
X	Reactance	0.7062 pu
$P_{13\phi}$	Output power	17.4137 MW
I_r	Rated current	4500 A
V_t	Terminal voltage	915.9966 V
l_m	Magnet's length	80 mm
h_{yr}	Rotor's yoke height	177.04 mm
D_{ag}	Airgap's diameter	6.6938 m
σ_t	Shear stress	209.0459 kPa
B_{airgap}	Airgap's magnetic flux density	1.0258 T
Demagnetization	Magnet's demagnetization	23.6759 %
V_0	Zero sequence voltage	0.6727 V
P_{SC}	Superconducting AC losses	59 726.2453 W

Table 14: 13-phase machine design geometry and outputs

It has been proved that a 13-phase machine with 1 extra unique phasor can improve the smoother behaviour of the magnetic flux densities in the airgap, which affects the overall operation regime of the electrical rotating machine.

9.3 Final design proposal

The above proposals are united into one machine. An AC superconducting 13-phase machine with bulky magnets is designed and simulated to prove the improvement in terms of power factor, compactness and reduction of iron losses. A quarter of the geometry of the final design is shown in figure 71, and the whole machine is depicted in figure 72.

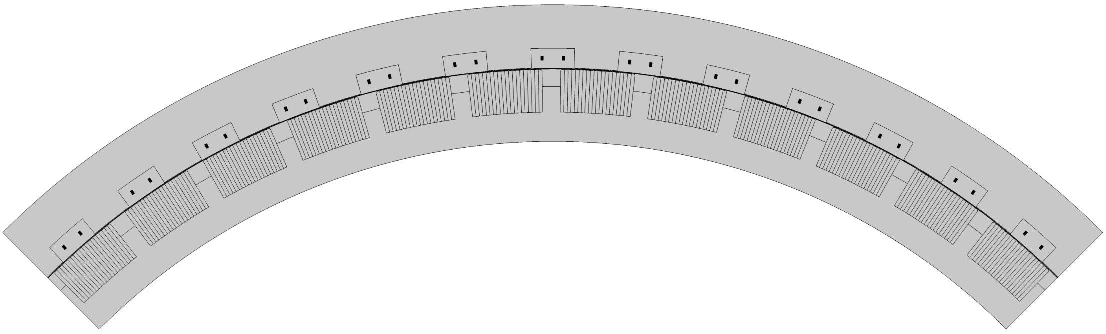

Figure 71: 13-phase bulky PM AC superconducting wind power generator

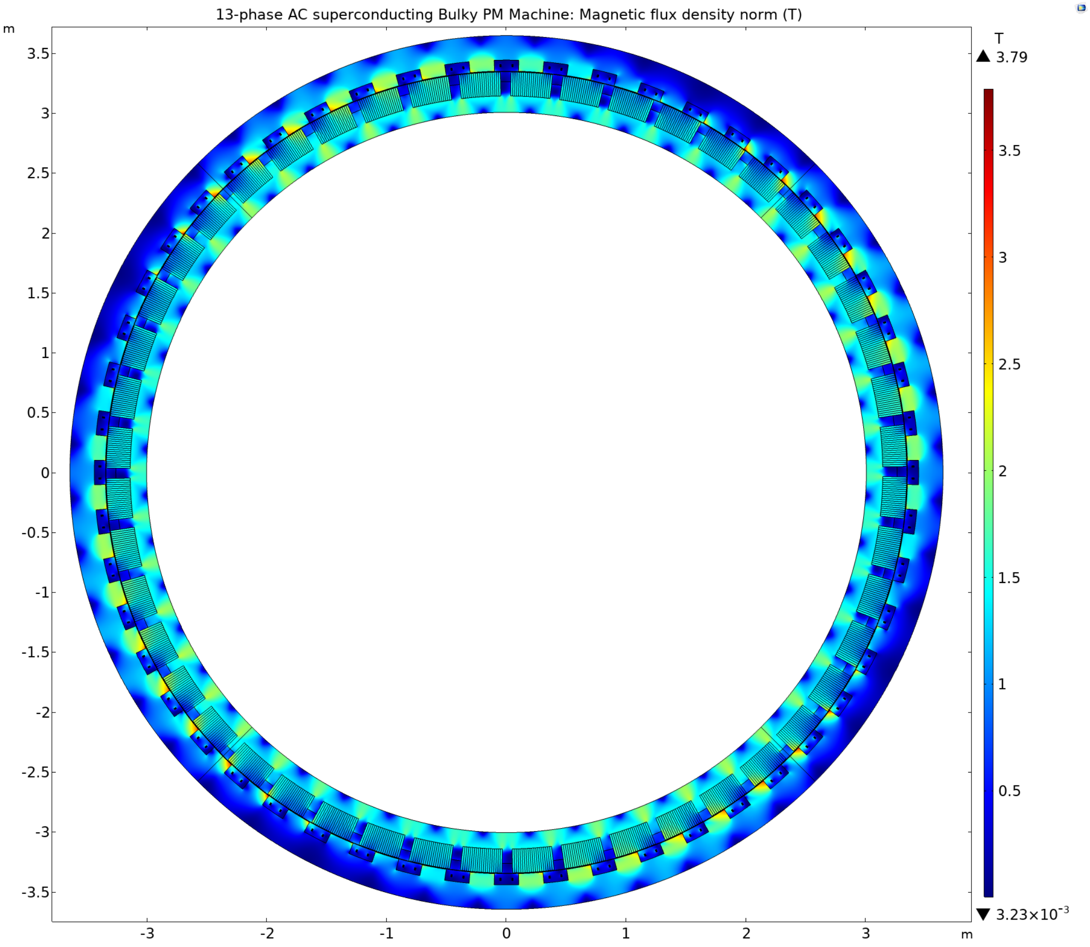

Figure 72: Simulation new design proposal

A power factor of 0.80 is achieved, with a per unit reactance of 0.6. Which means that the power electronics are less stress by reactive power compensation. In table 15 the overall outcomes are presented.

Variable	**Description**	**Value**
p_f	Power factor	0.8063
X	Reactance	0.5903 pu
$P_{13\phi}$	Output power	16.9774 MW
I_r	Rated current	4050 A
V_t	Terminal voltage	863.0098 V
l_m	Magnet's length	200 mm
h_{yr}	Rotor's yoke height	257.04 mm
D_{ag}	Airgap's diameter	6.6938 m
σ_t	Shear stress	205.6836 kPa
B_{airgap}	Airgap's magnetic flux density	1.0897 T
Demagnetization	Magnet's demagnetization	10.3564 %
V_0	Zero sequence voltage	0.7399 V
P_{SC}	Superconducting AC losses	60 697.9940 W

Table 15: Final design geometry and outputs

The iron losses are computed for the final design. It is proved that the iron losses are further reduced than a 12-phase machine because the rippling behaviour of the magnetic flux density is smoother due to the additional unique phasor. The comparison is made by relating the percentage of each machine type losses. Then the 3-phase machine is taken as a reference, making a relative weighting between the net percentage of iron losses in which the 3-phase is reference as 100%. Furthermore, the figure 73 shows that relatively the eddy current losses for the 13-phase machine are higher, but this is due to the higher electrical frequency in which it operates.

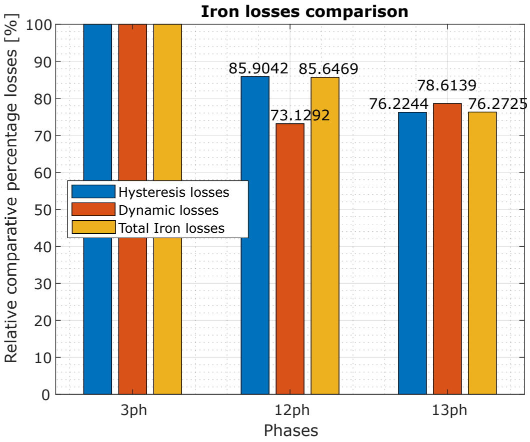

Figure 73: Iron losses comparison - Final proposal

The iron losses values are presented in table 16. The new design proposal can reduce the total iron losses further, even if the total output power is higher.

Model	Hysteresis losses	Dynamic losses	Total iron losses	Relative iron losses
3-phase machine	36 407.4966 W	748.1087 W	37 155.6054 W	24.28 %
12-phase machine	32 502.6804 W	568.5514 W	33 071.2318 W	20.80 %
13-phase machine	30 793.0813 W	652.5778 W	31 445.6591 W	18.52 %

Table 16: Iron losses comparison

The efficiency is calculated as follows:

$$\eta = \frac{P_{out}}{P_{out} + {}^{P_{loss}}\!/_{COP} + P_{iron}} \times 100\% \tag{81}$$

Here, P_{out}, P_{loss}, COP and P_{iron} are output power, AC losses in armature windings, coefficient of performance of cryocooler, and iron loss respectively. Where the COP is set to 0.06 at 65 K according to [43]. The AC superconducting hysteresis losses are calculated assuming ten scribed filaments, resulting in a tenth of the FEA values.

Topology	Efficiency (η)
3ph machine	98.8571 %
12ph machine	98.9192 %
24ph machine	99.0651 %
13ph machine	99.2220 %
Final proposal	99.8145 %

Table 17: Calculated efficiency [8]

It is shown that the new proposal offers the highest efficiency. However, the calculation does not take into account the magnet losses.

Finally, the torque density is calculated for all the topologies presented in this report. In table 18 the torque-to-weight is depicted. In comparison to the work done by Sung et al. [117], in which an HTS field winding for a wind power generator has a TTW=137.3832 Nm/kg for the active weight, whereas, for the present paper, the TTW for the 3-phase machine is 137.8322 Nm/kg, which validates the design. Overall, the 13-phase machine has the highest TTW. However, the power factor is 0.7. Therefore, the power electronics needed can make bulkier the wind turbine in a holistic approach. Nonetheless, the final proposal offers a relatively good power factor of 0.8 and a higher TTW than the conventional 3-phase machine.

Parameter	3ph	12ph	24ph	13ph	Final Proposal
W_{iron}	124.1029 ton	124.1029 ton	113.8873 ton	103.8549 ton	99.2655 ton
$W_{SC}{}^{1}$	284.1975 kg	284.1975 kg	284.1975 kg	307.8806 kg	307.8806 kg
$W_{mag}{}^{2}$	14.7915 ton	14.7915 ton	14.7902 ton	14.7901 ton	36.3237 ton
$W_{total}{}^{3}$	139.1790 ton	139.1790 ton	114.1863 ton	118.9529 ton	135.8971 ton
$TTW_{active}{}^{4}$	137.8322 Nm/kg	143.2685 Nm/kg	183.4497 Nm/kg	184.9122 Nm/kg	157.8013 Nm/kg
$TTW_{Total}{}^{5}$	75.8077 Nm/kg	78.7977 Nm/kg	100.8973 Nm/kg	101.7017 Nm/kg	86.7907 Nm/kg

[1] The weight density of the REBCO superconducting tape is 8.19 g/cm^3 according to [112].

[2] The neodymium magnet density is set to 7.4 g/cm^3.

[3] Active weight of the machine.

[4] The Torque-To-Weigth is calculated with FEA values.

[5] TTW calculated by assuming a non-active mass of 55 % of the total machine's weight.

Table 18: Torque-to-weight (TTW) topologies comparison [8]

9.3.1 Power electronics

The power factor's improvement reduces the costs of power electronics due to fewer requirements for reactive power compensation. Furthermore, one advantage of symmetrical multiphase windings is that the power electronics control algorithms do not have to decouple the multiple sets of windings. Thus, the controllability of the electrical drive is easier. Figure 74 shows a proposal connection for the converter connection of a 13-phase machine, in which the following dq-reference frames are incorporated: 3rd, 5th, 7th, 9th, and 11th order harmonics. This is because to construct a square matrix with the odd-order harmonics; the highest harmonic must be $m-2$. However, one must control only the current in the q0-axis to achieve a maximum torque per ampere. The other parameters are set to zero unless field weakening and harmonic injection techniques are implemented.

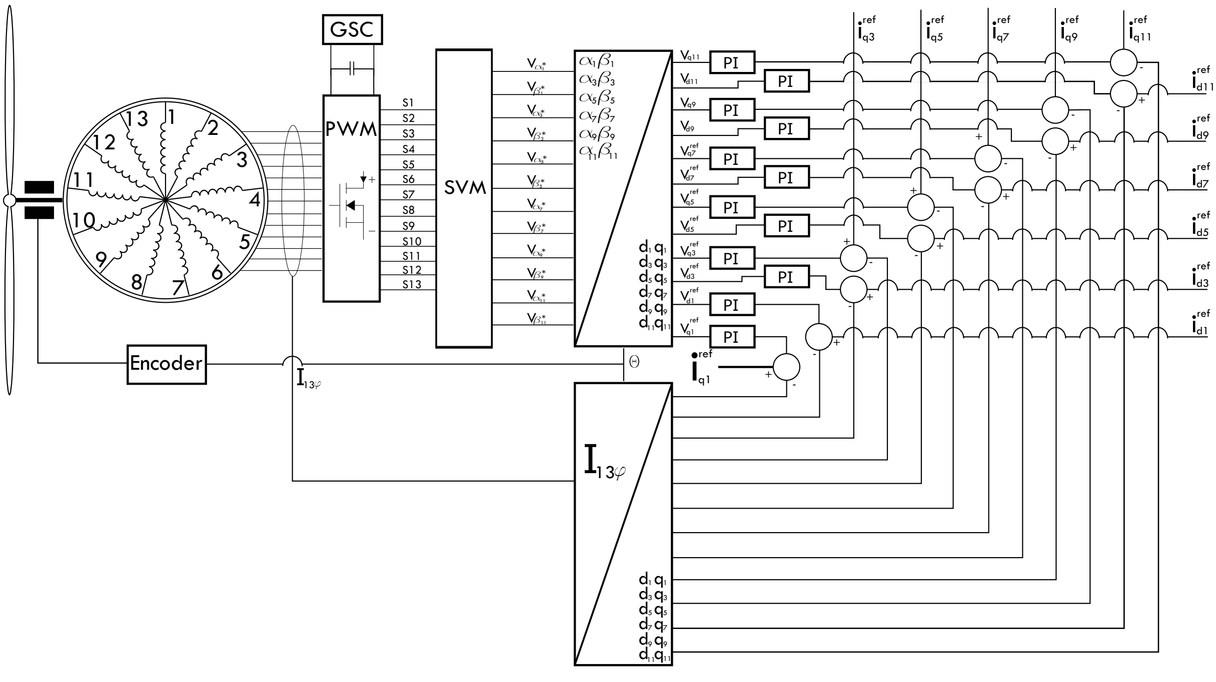

Figure 74: 13-phase machine side converter connection

10 Conclusions and future work

This section presents the conclusions per the research question, the results obtained, and the new knowledge acquired during the discussions. Finally, the future work is discussed.

10.1 Conclusion

The design of superconducting generators depends on the application, the topology, and the superconducting coils' design, which contemplates the material, the superconductivity, the layers, the critical values, and the fabrication process. For AC superconducting coils, the main issue is the hysteretic losses, which are sensitive to the incident angle of the magnetic flux lines. Changing the coil's angular position can further reduce the hysteretic losses if the tilting angle of the flux lines is known, which means that to reduce losses, one must already know the radial and tangential values for the magnetic flux densities in the airgap. However, the coil's angular position only accounts for a particular load level, e.g. at full load or 50% load. Furthermore, if the flux lines hit perpendicular to the coil's side, not only the hysteretic losses are reduced, but also the repulsion of the magnetic flux densities is increased. Hence, the fluctuating behaviour in the airgap is increased, creating bigger radial forces fluctuations that can harm the rotating machine. Therefore, a 2D design and analysis of AC superconducting coils cannot decide whether it is a good design or not. Nonetheless, it is possible to understand the behaviour and the foundation of the hysteretic losses and fluctuating magnetic behaviour according to the flux line tilting angle due to the loading of the machine.

Moreover, the machine's performance is evaluated by calculating the power factor, iron losses, PM's demagnetization, output power, harmonic content, and Shear stress. It is found that using symmetric multiphase systems with unique phasors improves the rippling behaviour of the magnetic flux densities along with the whole machine, which means that the iron losses are further reduced. The PM's demagnetization can be enhanced. However, not enough to achieve a good performance. The superior magnetic flux density distribution is due to the better winding distribution achieved with symmetric multiphase windings. First, the space sub-harmonics are eliminated, meaning designers can do better layouts for fractional slot concentrated windings. A higher Least Common Multiple of slots and poles can be achieved because symmetric multiphase fractional slot windings give more degrees of freedom to the design, meaning lower cogging torque. Second, the better winding factor improves the output power and shear stress of the machine. Lastly, the smoother magnetic behaviour creates fewer iron hysteresis losses and dynamic losses. However, symmetric multiphase windings cannot further improve the power factor. This is because the distribution of magnetic energy is similar to all the winding layout if the rotor's magnetic loading is not changed. Thus, to achieve a better power factor, the rotor's design is changed to bulkier PMs. Resulting in higher magnetic energy storage that can withstand the demagnetization produced by the high armature reaction of the superconducting coils. Therefore, with increased PM's volumes and unique phasors for symmetric multiphase windings can achieve better designs.

A 13-phase symmetric multiphase AC superconducting bulky PM wind power generator is presented as a potential candidate to achieve compactness and better performances compared to conventional machines. It has been proved that with this design, the shear stress can be tripled in comparison to a classical machine while having a power factor of 0.8 and a per-unit reactance of 0.6. Furthermore, the torque-to-weight is 86.7907 Nm/kg with an efficiency of 99.8145 %.

10.2 Future work

The AC superconducting coils must be designed in 3D to account for different angular positions with the same lengths. A 3D superconducting coil design means exploring twisted coils, roebel cables, among others. To design non-planar 3D AC superconducting coils that do not depend on the flux lines angles of the machine, it can operate at different loading regimes. Further, the simulation has to be enhanced with an optimal formulation in which more layers of the superconducting wire are taken into account. Furthermore, future works must explore electromagnetic shielding to reduce the airgap flux density behaviour due to the repelled fields, also known as Meisner effect.

A new rotor design is presented to withstand the higher armature reaction's demagnetization and improve the power factor. However, having bulkier PMs increase the materials, which impacts the costs of the machine. Moreover, having bigger PMs, the losses are increased. Therefore, an assessment of the loss of bulkier PMs is of utmost importance. Thus, future works must investigate further development into new PM rotor designs to decrease demagnetization and improve the power factor. Moreover, a proper design must consider the Maxwell Stress Tensor because increasing the magnetic loading means decreasing the electric loading to keep the same power at the same machine's dimensions. Thus, the angle between radial and tangential forces is reduced, which increases the radial forces that can harm the machine's integrity.

Further investigation into an LCOE optimization of a AC superconducting symmetric multiphase winding layouts with bulkier PMs must be done.

Finally, future works must investigate a new control scheme for multiphase machines with symmetrical windings with unique phasors. Moreover, a generalization of a dq0-transformation in which the reference frames of the direct and quadrature axes are understood to have a well-defined matrix to achieve superior controllability. The advantage of symmetrical windings over asymmetrical ones is that only one system is controlled. Future work must investigate an LCOE optimization of AC superconducting symmetric multiphase winding layouts with bulkier PMs considering the power electronics.

Bibliography

[1] "Cooper pair image source." [Online]. Available: https://dc.edu.au/wp-content/uploads/cooper-pair-phonon.png

[2] "Flux pinning image source." [Online]. Available: https://scienceblogs.com/startswithabang/2011/10/22/weekend-diversion-lift-me-up-q

[3] A. Tessarolo, "Modelling and analysis of multiphase electric machines for high-power applications," Ph.D. dissertation, University of Trieste, 2011. [Online]. Available: http://paduaresearch.cab.unipd.it/4076/

[4] R. Ryndzionek and Ł. Sienkiewicz, "Evolution of the HVDC link connecting offshore wind farms to onshore power systems," *Energies*, vol. 13, no. 8, 2020.

[5] P. K. Olsen, S. Gjerde, R. M. Nilssen, J. Hoelto, and S. Hvidsten, "A Transformerless generator-converter concept making feasible a 100 kV light weight offshore wind turbine: Part i - The generator," *2012 IEEE Energy Conversion Congress and Exposition, ECCE 2012*, pp. 247–252, 2012.

[6] A. B. Mogstad, M. Molinas, P. K. Olsen, and R. Nilsen, "A power conversion system for offshore wind parks," *IECON Proceedings (Industrial Electronics Conference)*, pp. 2106–2112, 2008.

[7] J. Pyrhönen, T. Jokinen, and V. Hrabovcov, *Design of Rotating Electrical Machines*. Chichester, UK: John Wiley & Sons, Ltd, dec 2008. [Online]. Available: http://doi.wiley.com/10.1002/9780470740095

[8] D. Tome, R. Nilssen, and J. K. Nøland, "Comparison of ac-superconducting multi-phase symmetric-winding topologies for wind power generators with passive pm rotors," Aug 2021. [Online]. Available: https://www.techrxiv.org/articles/preprint/Comparison_of_AC-Superconducting_Multi-Phase_Symmetric-Winding_Topologies_for_Wind_Power_Generators_with_Passive_PM_Rotors/15123966/1

[9] D. van Delft and P. Kes, "The discovery of superconductivity," *Physics Today*, vol. 63, no. 9, pp. 38–43, sep 2010. [Online]. Available: http://snf.ieeecsc.org/sites/ieeecsc.org/files/RN16e.pdfhttp://physicstoday.scitation.org/doi/10.1063/1.3490499

[10] M. N. Wilson, "100 Years of superconductivity and 50 years of superconducting magnets," *IEEE Transactions on Applied Superconductivity*, vol. 22, no. 3, 2012.

[11] W. H. Keesom and W. J. de Haas, "The influence of magnetic field on supraconductors," vol. 208, no. b, 1930.

[12] A. Shepelev, "The Discovery of Type II Superconductors (Shubnikov Phase)," *Superconductor*, vol. 2, 2010.

[13] L.-P. Lévy, *Ginzburg-Landau Theory.* Berlin, Heidelberg: Springer Berlin Heidelberg, 2000, pp. 285–307. [Online]. Available: https://doi.org/10.1007/978-3-662-04271-7{_}13

[14] A. A. Abrikosov, "Type ii superconductors and the vortex lattice," *Uspekhi Fizicheskikh Nauk*, vol. 174, no. 11, pp. 1234–1239, 2004.

[15] M. Hadlow, J. Baylis, and B. Lindley, "Superconductivity and its applications to power engineering," *Proceedings of the Institution of Electrical Engineers*, vol. 119, no. 8R, p. 1003, 1972.

[16] J. Bardeen, L. N. Cooper, and J. R. Schrieffer, "Theory of superconductivity," *Phys. Rev.*, vol. 108, pp. 1175–1204, Dec 1957. [Online]. Available: https://link.aps.org/doi/10.1103/PhysRev.108.1175

[17] J. E. Kunzler, E. Buehler, F. S. L. Hsu, and J. H. Wernick, "Superconductivity in nb_3sn at high current density in a magnetic field of 88 kgauss," *Phys. Rev. Lett.*, vol. 6, pp. 89–91, Feb 1961. [Online]. Available: https://link.aps.org/doi/10.1103/PhysRevLett.6.89

[18] Z. J. J. Stekly and H. H. Woodson, "Rotating Machinery Utilizing Superconductors," *IEEE Transactions on Aerospace*, vol. 2, no. 2, pp. 826–842, 1964. [Online]. Available: http://ieeexplore.ieee.org/document/4319673/

[19] M. K. Wu, J. R. Ashburn, C. J. Torng, P. H. Hor, R. L. Meng, L. Gao, Z. J. Huang, Y. Q. Wang, and C. W. Chu, "Superconductivity at 93 k in a new mixed-phase yb-ba-cu-o compound system at ambient pressure," *Phys. Rev. Lett.; (United States)*, vol. 58:9, 3 1987.

[20] D. Gubser, "Superconductivity: An Emerging Power-Dense Energy-Efficient Technology," *IEEE Transactions on Appiled Superconductivity*, vol. 14, no. 4, pp. 2037–2046, dec 2004. [Online]. Available: http://ieeexplore.ieee.org/document/1362681/

[21] J. Nagamatsu, N. Nakagawa, T. Muranaka, Y. Zenitani, and J. Akimitsu, "Superconductivity at 39 K in magnesium diboride," *Nature*, vol. 410, no. 6824, pp. 63–64, mar 2001. [Online]. Available: http://www.nature.com/articles/35065039

[22] R. Penco and G. Grasso, "Recent development of MgB2-based large scale applications," *IEEE Transactions on Applied Superconductivity*, vol. 17, no. 2, pp. 2291–2294, 2007.

[23] X. Zhu and M. Cheng, "Design and analysis of 10 MW Class HTS exciting double stator direct-drive wind generator with stationary seal," *IEEE Access*, vol. 7, pp. 51 129–51 139, 2019.

[24] G.-D. Nam, H.-J. Sung, B.-S. Go, M. Park, and I.-K. Yu, "Design and Comparative Analysis of MgB2 and YBCO Wire-Based-Superconducting Wind Power Generators," *IEEE Transactions on Applied Superconductivity*, vol. 28, no. 3, pp. 1–5, apr 2018. [Online]. Available: http://ieeexplore.ieee.org/document/8269284/

[25] V. Q. Dao, C. S. Kim, C. Lee, J. Choi, M. Park, and I. K. Yu, "Design and comparison analysis of 3 T superconducting magnets using MgB2 and 2G HTS wires for DC induction heaters," *IEEE Transactions on Applied Superconductivity*, vol. 29, no. 5, pp. 11–15, 2019.

[26] S. Grieco, Y. D. Nyanteh, and P. J. Masson, "Monte Carlo Design Space Exploration of Superconducting Wind Generator Using MgB2 and YBCO Conductors," *IEEE Transactions on Applied Superconductivity*, vol. 26, no. 3, pp. 3–7, 2016.

[27] M. Tomsic, M. Rindfleisch, J. Yue, K. McFadden, J. Phillips, M. D. Sumption, M. Bhatia, S. Bohnenstiehl, and E. W. Collings, "Overview of MgB 2 Superconductor Applications," *International Journal of Applied Ceramic Technology*, vol. 4, no. 3, pp. 250–259, jul 2007. [Online]. Available: http://doi.wiley.com/10.1111/j.1744-7402.2007.02138.x

[28] P. Kovac, I. Husek, J. Kovac, T. Melisek, M. Kulich, and L. Kopera, "Filamentary MgB2 Wires with Low Magnetization AC Losses," *IEEE Transactions on Applied Superconductivity*, vol. 26, no. 6, pp. 2–6, 2016.

[29] F. Wan, M. D. Sumption, M. A. Rindfleisch, M. J. Tomsic, and E. W. Collings, "Architecture and Transport Properties of Multifilamentary MgB2 Strands for MRI and Low AC Loss Applications," *IEEE Transactions on Applied Superconductivity*, vol. 27, no. 4, pp. 1–5, 2017.

[30] J. Xi, X. Pei, J. Sheng, H. Tanaka, Y. Ichiki, M. Zhang, and W. Yuan, "Experimental Test and Analysis of AC Losses in Multifilamentary MgB2 Wire," *IEEE Transactions on Applied Superconductivity*, vol. 29, no. 5, pp. 2–6, 2019.

[31] M. D. Sumption, F. Wan, M. Rindfleisch, and M. Tomsic, "Ac loss of superconducting materials-refined loss estimates of mgb2 wires for superconducting motors and generators," *AIAA Propulsion and Energy Forum and Exposition, 2019*, no. August, 2019.

[32] K. Yoshida, Y. Takahashi, N. Mitchell, D. Bessette, H. Kubo, M. Sugimoto, Y. Nunoya, and K. Okuno, "Proposals for the final design of the ITER central solenoid," *IEEE Transactions on Applied Superconductivity*, vol. 14, no. 2, pp. 1405–1409, 2004.

[33] J. Schultz, T. Antaya, J. Feng, C.-y. Gung, N. Martovetsky, J. Minervini, P. Michael, A. Radovinsky, and P. Titus, "The ITER Central Solenoid," in *21st IEEE/NPS Symposium on Fusion Engineering SOFE 05*, vol. 00, no. C. IEEE, sep 2005, pp. 1–4. [Online]. Available: http://ieeexplore.ieee.org/document/4018908/

[34] P. Libeyre, C. Beemsterboer, D. Bessette, Y. Gribov, C. Jong, C. Lyraud, N. Dolgetta, N. Mitchell, and T. Vollmann, "An optimized central solenoid for ITER," *IEEE Transactions on Applied Superconductivity*, vol. 20, no. 3, pp. 398–401, 2010.

[35] D. Everitt, W. Reiersen, N. Martovetsky, R. Hussung, S. Litherland, K. Freudenberg, L. Myatt, D. Hatfield, M. Cole, D. K. Irick, R. Reed, C. Lyraud, P. Libeyre,

D. Bessette, C. Jong, N. Mitchell, F. Rodriguez-Mateos, and N. Dolgetta, "ITER Central Solenoid design," *2013 IEEE 25th Symposium on Fusion Engineering, SOFE 2013*, 2013.

[36] A. B. Oliva, P. Aprili, B. Bellesia, E. B. Rebollo, T. Boutboul, P. C. De Sousa, M. P. C. Lino, M. Cornelis, P. Gavouyere-Lasserre, R. Harrison, A. Hernandez, M. Jimenez, A. Loizaga, M. Martinez, P. Readman, G. Romano, D. Rossi, C. Sborchia, P. Valente, E. Viladiu, R. Batista, V. Casarin, C. Kostopoulos, A. L. Bue, E. Pompa, E. Pozuelo-Segura, B. S. Lim, S. Koczorowski, C. Luongo, N. Mitchell, and L. Poncet, "Toward Completion and Delivery of the First EU ITER Magnets," *IEEE Transactions on Applied Superconductivity*, vol. 30, no. 4, 2020.

[37] T. Schild, G. Rossano, N. Martovetsky, D. Everitt, K. Freudenberg, T. Reagan, D. Vandergriff, J. Smith, D. Mullins, R. Potts, A. Stephens, P. Libeyre, P. Decool, C. Brun, C. Nguyen Thanh Dao, A. Bruton, C. Cormany, E. Gaxiola, C. Jong, N. Mitchell, A. Mariani, and J. Pallisa, "Preparation of the ITER Central Solenoid Assembly," *IEEE Transactions on Applied Superconductivity*, vol. 30, no. 4, 2020.

[38] A. Ballarino, "Development of superconducting links for the Large Hadron Collider machine," *Superconductor Science and Technology*, vol. 27, no. 4, 2014.

[39] K. Konstantopoulou, J. Hurte, J. Fleiter, and A. Ballarino, "Electro-Magnetic Performance of MgB2 Cables for the High Current Transmission Lines at CERN," *IEEE Transactions on Applied Superconductivity*, vol. 29, no. 5, pp. 5–9, 2019.

[40] J. P. Voccio, P. C. Michael, L. Bromberg, and S. Hahn, "Solid-cryogen-stabilized, cable-in-conduit (CIC) superconducting cables," *IOP Conference Series: Materials Science and Engineering*, vol. 101, no. 1, 2015.

[41] P. C. Michael, J. Kvitkovic, S. V. Pamidi, P. J. Masson, and L. Bromberg, "Development of MgB2-Cabled Conductors for Fully Superconducting Rotating Electric Machines," *IEEE Transactions on Applied Superconductivity*, vol. 27, no. 4, pp. 7–11, 2017.

[42] A. A. Nosov, L. V. Potanina, K. S. Marinin, S. S. Fetisov, and V. S. Vysotsky, "Influence of Cabling on Current Carrying Capabilities of MgB2 Superconductors," *IEEE Transactions on Applied Superconductivity*, vol. 28, no. 4, pp. 16–20, 2018.

[43] S. Miura, M. Iwakuma, and T. Izumi, "Lightweight Design of Tens-MW Fully-Superconducting Wind Turbine Generators with High-Performance REBa2Cu3Oy Wires," *IEEE Transactions on Applied Superconductivity*, vol. 30, no. 4, pp. 3–8, 2020.

[44] "Global hydrogen market to see 18.6%/y growth through 2022," *Focus on Catalysts*, vol. 2018, no. 12, p. 2, 2018.

[45] "Global hydrogen market insights, 2020-2024 by production process, end-user, generation system and region," *Focus on Catalysts*, vol. 2020, no. 5,

p. 2, may 2020. [Online]. Available: https://linkinghub.elsevier.com/retrieve/pii/S1351418020301598

[46] M. Corduan, M. Boll, R. Bause, M. P. Oomen, M. Filipenko, and M. Noe, "Topology Comparison of Superconducting AC Machines for Hybrid Electric Aircraft," *IEEE Transactions on Applied Superconductivity*, vol. 30, no. 2, 2020.

[47] C. D. Manolopoulos, M. F. Iacchetti, A. C. Smith, P. M. Tuohy, X. Pei, P. Miller, and M. Husband, "Comparison between Coreless and Yokeless Stator Designs in Fully-Superconducting Propulsion Motors," *IEEE Transactions on Applied Superconductivity*, vol. 30, no. 6, 2020.

[48] R. Sugouchi, H. Honda, Y. Hase, M. Shuto, M. Konno, T. Izumi, M. Komiya, S. Miura, M. Iwakuma, K. Yoshida, T. Sasayama, T. Yoshida, K. Yamamoto, and Y. Sasamori, "Conceptual Design and Electromagnetic Analysis of 2 MW Fully Superconducting Synchronous Motors with Superconducting Magnetic Shields for Turbo-Electric Propulsion System," *IEEE Transactions on Applied Superconductivity*, vol. 30, no. 4, 2020.

[49] M. Boll, M. Corduan, S. Biser, M. Filipenko, Q. H. Pham, S. Schlachter, P. Rostek, and M. Noe, "A holistic system approach for short range passenger aircraft with cryogenic propulsion system," *Superconductor Science and Technology*, vol. 33, no. 4, 2020.

[50] Y. Terao, A. Seta, H. Ohsaki, H. Oyori, and N. Morioka, "Lightweight Design of Fully Superconducting Motors for Electrical Aircraft Propulsion Systems," *IEEE Transactions on Applied Superconductivity*, vol. 29, no. 5, pp. 5–9, 2019.

[51] S. S. Kalsi, K. A. Hamilton, and R. A. Badcock, "Superconducting rotating machines for aerospace applications," *2018 Joint Propulsion Conference*, 2018.

[52] T. Balachandran, D. Lee, and K. S. Haran, "Optimal design of a fully superconducting machine for 10- mw offshore wind turbines," *2019 IEEE International Electric Machines and Drives Conference, IEMDC 2019*, pp. 1903–1909, 2019.

[53] X. Huang, C. Zhou, K. Zhang, L. Wu, J. Zhang, and W. Cao, "Comparison of electromagnetic performance of scpm wind power generators with different topologies," *IEEE Transactions on Applied Superconductivity*, vol. 29, no. 2, pp. 13–17, 2019.

[54] D. L. Asger Bech Abrahamsen and H. Polinder, "Final assessment of superconducting (SC) and Pseudo Direct Drive (PDD) generator performance indicators (PI ' s). Document information," INNWIND Project, Tech. Rep. Deliverable D 3.44, 2017. [Online]. Available: https://www.innwind.eu/-/media/Sites/innwind/Publications/Deliverables/DeliverableD344{_}FinalAssessmentSCandPDD{_}Final{_}27October2017{_}Uploaded.ashx?la=da{&}hash=1E1B17BAFF6FCE3176C6356834F96495F7E1F809

[55] M. Feddersen, K. S. Haran, and F. Berg, "AC Loss Analysis of MgB2-Based Fully Superconducting Machines," *IOP Conference Series: Materials Science and Engineering*, vol. 279, no. 1, 2017.

[56] I. Marino, A. Pujana, G. Sarmiento, S. Sanz, J. M. Merino, M. Tropeano, J. Sun, and T. Canosa, "Lightweight MgB 2 superconducting 10MW wind generator," *IOP Science : Superconductor Science and Technology*, vol. 29, no. no. 2, pp. 1–11, 2016.

[57] E. Union, "SUPRAPOWER: Superconducting, reliable, lightweight, and more powerful offshore wind turbine," This project has received funding from the European Union's Seventh Programme for research, technological development and demonstration under grant agreement number: 308793, Tech. Rep., 2017. [Online]. Available: https://cordis.europa.eu/docs/results/308/308793/final1-suprapower-final-report-tecnalia-20170922-rev-1.pdf

[58] D. Liu, "Increasing the Feasibility of Superconducting Generators for 10 MW Direct-Drive Wind Turbines," Ph.D. dissertation, TU Delft, 2017.

[59] A. Bergen, R. Andersen, M. Bauer, H. Boy, M. ter Brake, P. Brutsaert, C. Bührer, M. Dhallé, J. Hansen, H. ten Kate, J. Kellers, J. Krause, E. Krooshoop, C. Kruse, H. Kylling, M. Pilas, H. Pütz, A. Rebsdorf, M. Reckhard, E. Seitz, H. Springer, X. Song, N. Tzabar, S. Wessel, J. Wiezoreck, T. Winkler, and K. Yagotyntsev, "Design and in-field testing of the world's first ReBCO rotor for a 3.6 MW wind generator," *Superconductor Science and Technology*, vol. 32, no. 12, p. 125006, dec 2019. [Online]. Available: https://iopscience.iop.org/article/10.1088/1361-6668/ab48d6

[60] X. Song, A. Bergen, T. Winkler, S. Wessel, M. T. Brake, J. Kellers, H. Putz, M. Bauer, H. Kyling, H. Boy, E. Seitz, C. Buhrer, P. Brutsaert, J. Krause, A. Ammar, J. Wiezoreck, J. Hansen, A. V. Rebsdorf, and M. Dhalle, "Designing and Basic Experimental Validation of the World's First MW-Class Direct-Drive Superconducting Wind Turbine Generator," *IEEE Transactions on Energy Conversion*, vol. 34, no. 4, pp. 2218–2225, 2019.

[61] X. Song, C. Buhrer, A. Molgaard, R. S. Andersen, P. Brutsaert, M. Bauer, J. Hansen, A. V. Rebsdorf, J. Kellers, T. Winkler, A. Bergen, M. Dhalle, S. Wessel, M. T. Brake, J. Wiezoreck, H. Kyling, H. Boy, and E. Seitz, *Commissioning of the World's First Full-Scale MW-Class Superconducting Generator on a Direct Drive Wind Turbine.* IEEE, 2020, vol. 35, no. 3.

[62] B. Gamble, G. Snitchler, and T. Macdonald, "Full power test of a 36.5 MW HTS propulsion motor," *IEEE Transactions on Applied Superconductivity*, vol. 21, no. 3 PART 2, pp. 1083–1088, 2011.

[63] D. Liu, U. Hasanov, C. Ye, X. Gou, and X. Wang, "Design Considerations and Short-Circuit Characteristics of Fully Superconducting Wind Turbine Generators," *Asia-Pacific Power and Energy Engineering Conference, APPEEC*, vol. 2020-September, no. 2018, pp. 6–11, 2020.

[64] D. Liu, X. Song, F. Deng, and J. Dong, "Investigation Into Multi-Phase Armature Windings for High-Temperature Superconducting Wind Turbine Generators," *IEEE Transactions on Applied Superconductivity*, vol. 30, no. 4, pp. 1–5, jun 2020. [Online]. Available: https://ieeexplore.ieee.org/document/8962154/

[65] D. Liu, X. Song, and J. Dong, "Performance of Multi-Layer and Stator-Shifting Fractional-Slot Concentrated Windings for Superconducting Wind Turbine Generators under Normal and Short-Circuit Operation Conditions," *IEEE Transactions on Applied Superconductivity*, vol. 30, no. 4, 2020.

[66] C. H. Lee, "Saturation Harmonics of Polyphase Induction Machines," *Transactions of the American Institute of Electrical Engineers. Part III: Power Apparatus and Systems*, vol. 80, no. 3, pp. 597–603, 1961.

[67] A. S. Thomas, Z. Q. Zhu, R. L. Owen, G. W. Jewell, and D. Howe, "Multiphase Flux-Switching Permanent-Magnet Brushless Machine for Aerospace Application," *IEEE Transactions on Industry Applications*, vol. 45, no. 6, pp. 1971–1981, 2009.

[68] V. Kindl, Z. Ferkova, and R. Cermak, "Spatial harmonics in multi-phase induction machine," in *2020 ELEKTRO*, May 2020, pp. 1–4.

[69] V. Kindl, R. Cermak, Z. Ferkova, and B. Skala, "Review of time and space harmonics in multi-phase induction machine," *Energies*, vol. 13, no. 2, 2020.

[70] A. Masmoudi, *Design and Electromagnetic Feature Analysis of AC Rotating Machines*, ser. SpringerBriefs in Electrical and Computer Engineering. Singapore: Springer Singapore, 2019. [Online]. Available: http://www.springer.com/series/10059http://link.springer.com/10.1007/978-981-13-0920-5

[71] M. D. Prada-Gil, J. L. Domínguez-García, F. Díaz-González, and A. Sumper, *Offshore Wind Power Plants (OWPPS)*. John Wiley & Sons, Ltd, 2016, ch. 6, pp. 109–140. [Online]. Available: https://onlinelibrary.wiley.com/doi/abs/10.1002/9781119115243.ch6

[72] IEA. Offshore wind outlook 2019. [Online]. Available: https://www.iea.org/reports/offshore-wind-outlook-2019

[73] M. Parker, C. Ng, L. Ran, P. Tavner, and E. Spooner, "Power control of direct drive wind turbine with simplified conversion stage transformerless grid interface," in *Proceedings of the 41st International Universities Power Engineering Conference*, vol. 1, 2006, pp. 65–68.

[74] S. S. Gjerde, P. K. Olsen, and T. M. Undeland, "A transformerless generator-converter concept making feasible a 100 kV low weight offshore wind turbine Part II - The converter," in *2012 IEEE Energy Conversion Congress and Exposition (ECCE)*. IEEE, sep 2012, pp. 253–260. [Online]. Available: http://ieeexplore.ieee.org/document/6342815/

[75] T. M. Iversen, S. S. Gjerde, and T. Undeland, "Multilevel converters for a 10 MW, 100 kV transformer-less offshore wind generator system," *EPE Joint Wind Energy and T and D Chapters Seminar*, 2012.

[76] A. A. Elserougi, M. I. Daoud, A. S. Abdel-Khalik, A. M. Massoud, and S. Ahmed, "Series-connected multi-half-bridge modules converter for integrating multi-megawatt wind multi-phase permanent magnet synchronous generator with dc grid," *IET Electric Power Applications*, vol. 11, no. 6, pp. 981–990, 2017.

[77] R. Barrera-Cardenas and M. Molinas, "Comparison of wind energy conversion systems based on high frequency AC-Link: Three-phase Vs. Single-phase," *15th International Power Electronics and Motion Control Conference and Exposition, EPE-PEMC 2012 ECCE Europe*, pp. 1–8, 2012.

[78] Z. Zhaoqiang, "IRONLESS PERMANENT MAGNET GENERATORS FOR DIRECT-DRIVEN OFFSHORE," Doktoravhandlinger, NTU Norges teknisk-naturvitenskapelige universitet, 2015.

[79] A. Garcés and M. Molinas, "A study of efficiency in a reduced matrix converter for offshore wind farms," *IEEE Transactions on Industrial Electronics*, vol. 59, no. 1, pp. 184–193, 2012.

[80] ——, "High frequency wind energy conversion from the ocean," *2010 International Power Electronics Conference - ECCE Asia -, IPEC 2010*, pp. 2056–2061, 2010.

[81] K. Suzuki, J. Matsuda, M. Yoshizumi, T. Izumi, Y. Shiohara, M. Iwakuma, A. Ibi, S. Miyata, and Y. Yamada, "Development of a laser scribing process of coated conductors for the reduction of AC losses Related content," 2007.

[82] E. Gaertner, J. Rinker, L. Sethuraman, F. Zahle, B. Anderson, G. Barter, N. Abbas, F. Meng, P. Bortolotti, and W. Skrzypinski, "Definition of the IEA 15-Megawatt Offshore Reference Wind Turbine," National Renewable Energy Laboratory NREL, Tech. Rep., 2020.

[83] D. Liu, X. Song, and X. Wang, "Design challenges of direct-drive permanent magnet superconducting wind turbine generators," in *Proceedings - 2020 International Conference on Electrical Machines, ICEM 2020.* Institute of Electrical and Electronics Engineers Inc., aug 2020, pp. 640–646.

[84] D. Liu, X. Song, X. Wang, M. Elhindi, U. Hasanov, X. Gou, and C. Ye, "Short-circuit characteristics of superconducting permanent magnet generators for 10 MW wind turbines," *IEEE Transactions on Applied Superconductivity*, vol. 31, no. 5, pp. 4–8, 2021.

[85] J. F. Gieras, *Permanent Magnet Motor Technology Design and Applications*, 2010.

[86] J. C. Maxwell, *A Treatise on Electromagnetism.* Oxford: Clarendon Press, 1873. [Online]. Available: https://www.aproged.pt/biblioteca/MaxwellI.pdf

[87] O. Heaviside, *Electrical Papers.* New York and London: Macmillan & Co, 1894. [Online]. Available: https://openlibrary.org/books/OL7173470M/Electrical_papers

[88] A. Allerhand, "A Contrarian History of Early Electric Power Distribution [Scanning Our Past]," *Proceedings of the IEEE*, vol. 105, no. 4, pp. 768–778, mar 2017.

[89] S. Vaschetto, A. Tenconi, and G. Bramerdorfer, "Sizing procedure of surface mounted PM machines for fast analytical evaluations," *2017 IEEE International Electric Machines and Drives Conference, IEMDC 2017*, vol. 63, 2017.

[90] E. Snider, N. Dasenbrock-Gammon, R. McBride, M. Debessai, H. Vindana, K. Vencatasamy, K. V. Lawler, A. Salamat, and R. P. Dias, "Room-temperature superconductivity in a carbonaceous sulfur hydride," *Nature*, vol. 586, no. 7829, pp. 373–377, oct 2020. [Online]. Available: https://doi.org/10.1038/s41586-020-2801-z

[91] B. C. Robert, M. U. Fareed, and H. S. Ruiz, "How to choose the superconducting material law for the modelling of 2G-HTS coils," *Materials*, vol. 12, no. 7, pp. 1–19, 2019.

[92] G. Madescu, E. Berwanger, M. Biriescu, and M. Mot, "FAST ANALYSIS OF MMF HARMONICS CONTENT IN THREE-PHASE ELECTRICAL MACHINES," Tech. Rep. 2, 2018. [Online]. Available: http://acad-tim.tm.edu.ro/FastMMF/

[93] T. M. Jahns and W. L. Soong, "Pulsating torque minimization techniques for permanent magnet AC motor drives-a review," *IEEE Transactions on Industrial Electronics*, vol. 43, no. 2, pp. 321–330, Apr. 1996, conference Name: IEEE Transactions on Industrial Electronics.

[94] Z. Q. Zhu and D. Howe, "Influence of design parameters on cogging torque in permanent magnet machines," *IEEE Transactions on Energy Conversion*, vol. 15, no. 4, pp. 407–412, 2000.

[95] J. Tasker, T. Collyer, and A. Wearing, "Cogging torques [electric machines]," in *1997 Eighth International Conference on Electrical Machines and Drives (Conf. Publ. No. 444)*, Sep. 1997, pp. 205–209, iSSN: 0537-9989.

[96] A. Krings, "Iron Losses in Electrical Machines - Influence of Material Properties, Manufacturing Processes, and Inverter Operation," Ph.D. dissertation, KTH Royal Institute of Technology, 2014. [Online]. Available: http://www.diva-portal.org/smash/get/diva2:717326/FULLTEXT01.pdf

[97] S. F. Haukvik, "Comparison of iron loss calculation models including rotational loss," Ph.D. dissertation, Norwegian University of Science and Technology, 2020.

[98] G. Bertotti, "General properties of power losses in soft ferromagnetic materials," *IEEE Transactions on Magnetics*, vol. 24, no. 1, pp. 621–630, 1988.

[99] G. Bertotti, A. Boglietti, M. Chiampi, D. Chiarabaglio, F. Fiorillo, and M. Lazzari, "An improved estimation of iron losses in rotating electrical machines," *IEEE Transactions on Magnetics*, vol. 27, no. 6, pp. 5007–5009, 1991.

[100] T. H. Akinaga, T. Staudt, W. Hoffmann, C. E. Soares, A. A. De Espindola, and J. P. Bastos, "A comparative investigation of iron loss models for electrical machine design using FEA and experimental validation," in *Proceedings - 2018 23rd International Conference on Electrical Machines, ICEM 2018.* Institute of Electrical and Electronics Engineers Inc., oct 2018, pp. 461–466.

[101] D. M. Ionel, M. Popescu, M. I. McGilp, T. J. E. Miller, S. J. Dellinger, and R. J. Heideman, "Computation of Core Losses in Electrical Machines Using Improved Models for Laminated Steel," *IEEE Transactions on Industry Applications*, vol. 43, no. 6, pp. 1554–1564, 2007. [Online]. Available: https://ieeexplore.ieee.org/stamp/stamp.jsp?tp=&arnumber=4384995http://ieeexplore.ieee.org/document/4384995/

[102] R. Brambilla, F. Grilli, and L. Martini, "Development of an edge-element model for AC loss computation of high-temperature superconductors," *Superconductor Science and Technology*, vol. 20, no. 1, pp. 16–24, jan 2007. [Online]. Available: https://iopscience.iop.org/article/10.1088/0953-2048/20/1/004

[103] R. Brambilla, F. Grilli, L. Martini, M. Bocchi, and G. Angeli, "A finite element method framework for modeling rotating machines with superconducting windings," *arXiv*, vol. 28, no. 5, 2017.

[104] Antero Arkkio, "Analysis of induction motors based on the numerical solution of the magnetic field and circuit equations," Ph.D. dissertation, Helsinki University of Technology, Espoo, 1987. [Online]. Available: http://lib.tkk.fi/Diss/198X/isbn951226076X/isbn951226076X.pdf

[105] G. Yang, J. Yang, S. Li, Y. Wang, H. Hussain, L. Yan, and R. Deng, "Overmodulation Strategy for Seven-phase Induction Motors With Optimum Harmonic Voltage Injection Based on Sequential Optimization Scheme," *IEEE Transactions on Power Electronics*, vol. 8993, no. c, pp. 1–1, 2021. [Online]. Available: https://ieeexplore.ieee.org/document/9442326/

[106] S. Spas, S. Kowarschik, J. Laumer, M. Wiesinger, and W. Hackmann, "Five-Phase IPMSM: Torque Density Improvement by Third Harmonic Injection," in *2020 International Symposium on Power Electronics, Electrical Drives, Automation and Motion (SPEEDAM).* IEEE, jun 2020, pp. 779–786. [Online]. Available: https://ieeexplore.ieee.org/document/9161863/

[107] V. Tomasov, A. Usoltsev, D. Vertegel, P. Szczepankowski, R. Strzelecki, and N. Poliakov, "Optimized Space-Vector Modulation Schemes for Five-Phase Precision Low-Speed Drives with Minimizing the Stator Current Ripple," *Proceedings - 2020 IEEE 14th International Conference on Compatibility, Power Electronics and Power Engineering, CPE-POWERENG 2020*, no. 1, pp. 279–284, 2020.

[108] M. Hossam H. H., A.-R. Youssef, and M. Essam E. M., "Improved Perturb and Observe MPPT Algorithm of Multi-Phase PMSG Based Wind Energy Conversion System," in *2019 21st International Middle East Power Systems Conference (MEPCON).* IEEE, dec 2019, pp. 97–102. [Online]. Available: https://ieeexplore.ieee.org/document/9008004/

[109] Y. Chen and B. Liu, "Design and analysis of a five-phase fault-tolerant permanent magnet synchronous motor for aerospace starter-generator system," *IEEE Access*, vol. 7, pp. 135 040–135 049, 2019.

[110] C. Chen, H. Zhou, G. Wang, and G. Liu, "Unified Decoupling Vector Control of Five-Phase Permanent-Magnet Motor with Double-Phase Faults," *IEEE Access*, vol. 8, pp. 152 646–152 658, 2020.

[111] H. H. Mousa, A. R. Youssef, and E. E. Mohamed, "Model Predictive Speed Control of Five-Phase PMSG Based Variable Speed Wind Generation System," *2018 20th International Middle East Power Systems Conference, MEPCON 2018 - Proceedings*, pp. 304–309, 2019.

[112] M. Komiya, T. Aikawa, H. Sasa, S. Miura, M. Iwakuma, T. Yoshida, T. Sasayama, A. Tomioka, M. Konno, and T. Izumi, "Design Study of 10 MW REBCO Fully Superconducting Synchronous Generator for Electric Aircraft," *IEEE Transactions on Applied Superconductivity*, vol. 29, no. 5, pp. 1–6, aug 2019. [Online]. Available: https://ieeexplore.ieee.org/document/8675517/

[113] M. Komiya, R. Sugouchi, H. Sasa, S. Miura, M. Iwakuma, T. Yoshida, T. Sasayama, K. Yamamoto, A. Tomioka, M. Konno, and T. Izumi, "Conceptual Design and Numerical Analysis of 10 MW Fully Superconducting Synchronous Generators Installed with a Novel Casing Structure," *IEEE Transactions on Applied Superconductivity*, vol. 30, no. 4, 2020.

[114] K. Tsuchiya, A. Kikuchi, A. Terashima, K. Norimoto, M. Uchida, M. Tawada, M. Masuzawa, N. Ohuchi, X. Wang, T. Takao, and S. Fujita, "Critical current measurement of commercial REBCO conductors at 4.2 K," *Cryogenics*, vol. 85, pp. 1–7, jul 2017.

[115] S. Xue, A. S. Thomas, Z. Q. Zhu, L. Huang, A. Duke, R. E. Clark, and Z. Azar, "Influence of Coil Location and Current Angle in Permanent Magnet Wind Power Generators with High Temperature Superconducting Armature Windings," *IEEE Transactions on Applied Superconductivity*, vol. 31, no. 1, 2021.

[116] A. Gezer, M. O. Gülbahçe, and D. A. Kocabaş, "Generalised model of multiphase tesla's egg of columbus and practical analysis of 3-phase design," *Istanbul University - Journal of Electrical and Electronics Engineering*, vol. 18, no. 2, pp. 151–158, 2018.

[117] H.-J. Sung, M. Park, B.-S. Go, and I.-K. Yu, "A study on the required performance of a 2G HTS wire for HTS wind power generators," *Superconductor Science and Technology*, vol. 29, no. 5, p. 054001, may 2016. [Online]. Available: https://iopscience.iop.org/article/10.1088/0953-2048/29/5/054001

11 Appendix

11.1 Materials

M235-A35 iron material is used in the yoke of stator and rotor to calculate the iron losses. The datasheet is presented in figure 75.

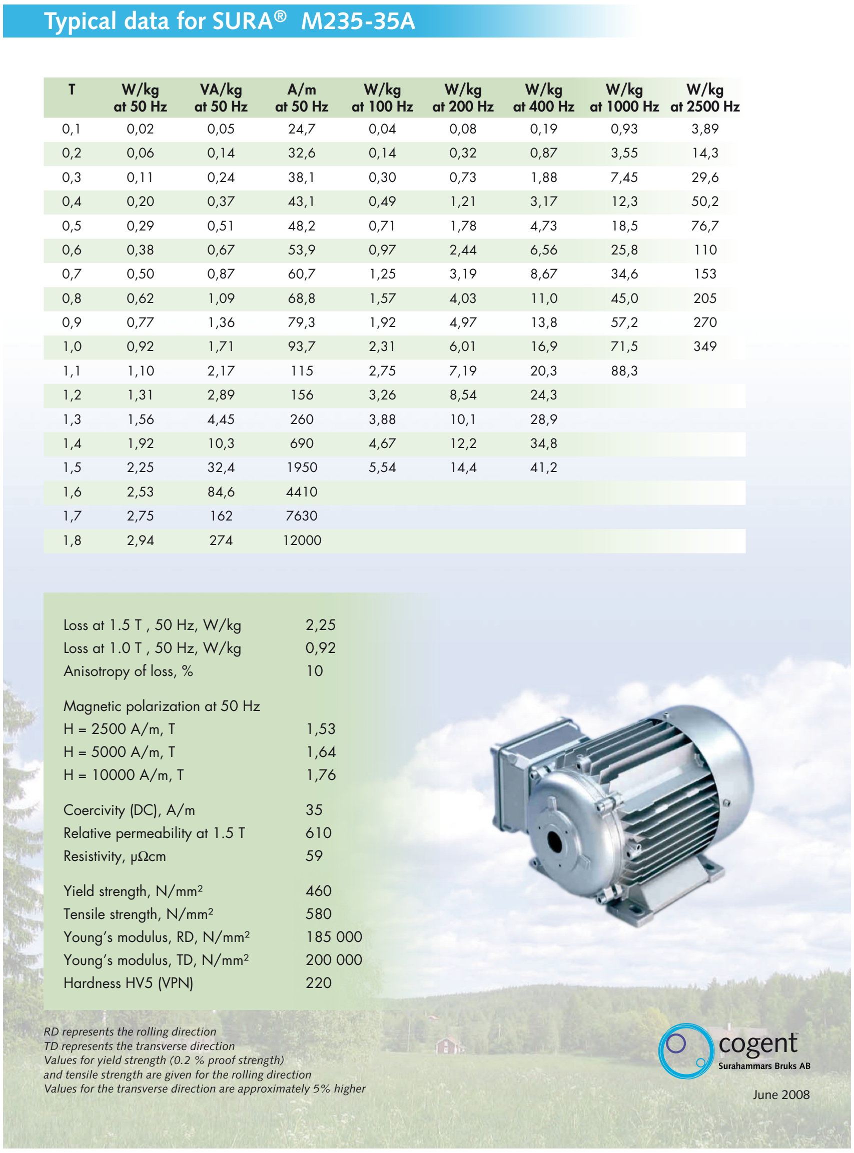

Typical data for SURA® M235-35A

T	W/kg at 50 Hz	VA/kg at 50 Hz	A/m at 50 Hz	W/kg at 100 Hz	W/kg at 200 Hz	W/kg at 400 Hz	W/kg at 1000 Hz	W/kg at 2500 Hz
0,1	0,02	0,05	24,7	0,04	0,08	0,19	0,93	3,89
0,2	0,06	0,14	32,6	0,14	0,32	0,87	3,55	14,3
0,3	0,11	0,24	38,1	0,30	0,73	1,88	7,45	29,6
0,4	0,20	0,37	43,1	0,49	1,21	3,17	12,3	50,2
0,5	0,29	0,51	48,2	0,71	1,78	4,73	18,5	76,7
0,6	0,38	0,67	53,9	0,97	2,44	6,56	25,8	110
0,7	0,50	0,87	60,7	1,25	3,19	8,67	34,6	153
0,8	0,62	1,09	68,8	1,57	4,03	11,0	45,0	205
0,9	0,77	1,36	79,3	1,92	4,97	13,8	57,2	270
1,0	0,92	1,71	93,7	2,31	6,01	16,9	71,5	349
1,1	1,10	2,17	115	2,75	7,19	20,3	88,3	
1,2	1,31	2,89	156	3,26	8,54	24,3		
1,3	1,56	4,45	260	3,88	10,1	28,9		
1,4	1,92	10,3	690	4,67	12,2	34,8		
1,5	2,25	32,4	1950	5,54	14,4	41,2		
1,6	2,53	84,6	4410					
1,7	2,75	162	7630					
1,8	2,94	274	12000					

Loss at 1.5 T , 50 Hz, W/kg	2,25
Loss at 1.0 T , 50 Hz, W/kg	0,92
Anisotropy of loss, %	10
Magnetic polarization at 50 Hz	
H = 2500 A/m, T	1,53
H = 5000 A/m, T	1,64
H = 10000 A/m, T	1,76
Coercivity (DC), A/m	35
Relative permeability at 1.5 T	610
Resistivity, μΩcm	59
Yield strength, N/mm^2	460
Tensile strength, N/mm^2	580
Young's modulus, RD, N/mm^2	185 000
Young's modulus, TD, N/mm^2	200 000
Hardness HV5 (VPN)	220

RD represents the rolling direction
TD represents the transverse direction
Values for yield strength (0.2 % proof strength)
and tensile strength are given for the rolling direction
Values for the transverse direction are approximately 5% higher

cogent
Surahammars Bruks AB

June 2008

Figure 75: M235-35A Datasheet

The B-H curve used in COMSOL is presented in figure 76.

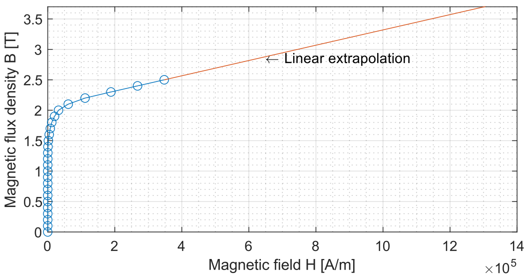

Figure 76: B-H curve for M235-A35 iron material

In figure 77 the fitting curves for the hysteresis and dynamic losses are depicted.

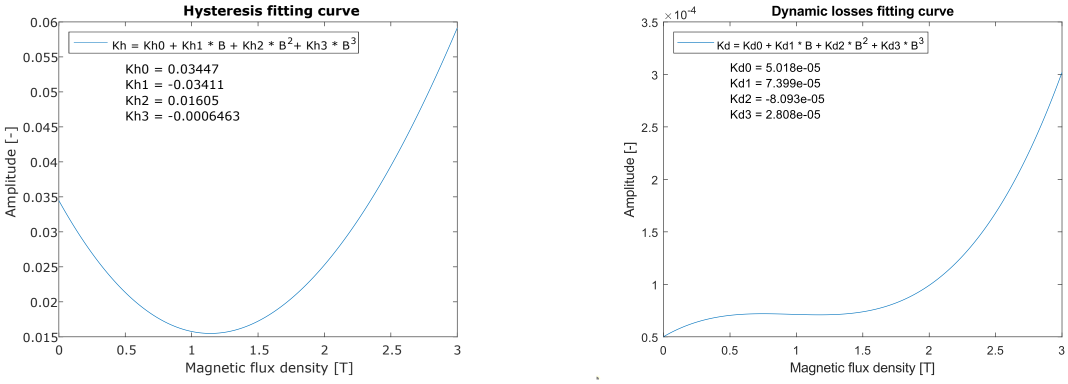

(a) Hysteresis (b) Dynamical

Figure 77: Fitting curves

To generate these curves, the fitting MATLAB App is used as is shown in figure 78.

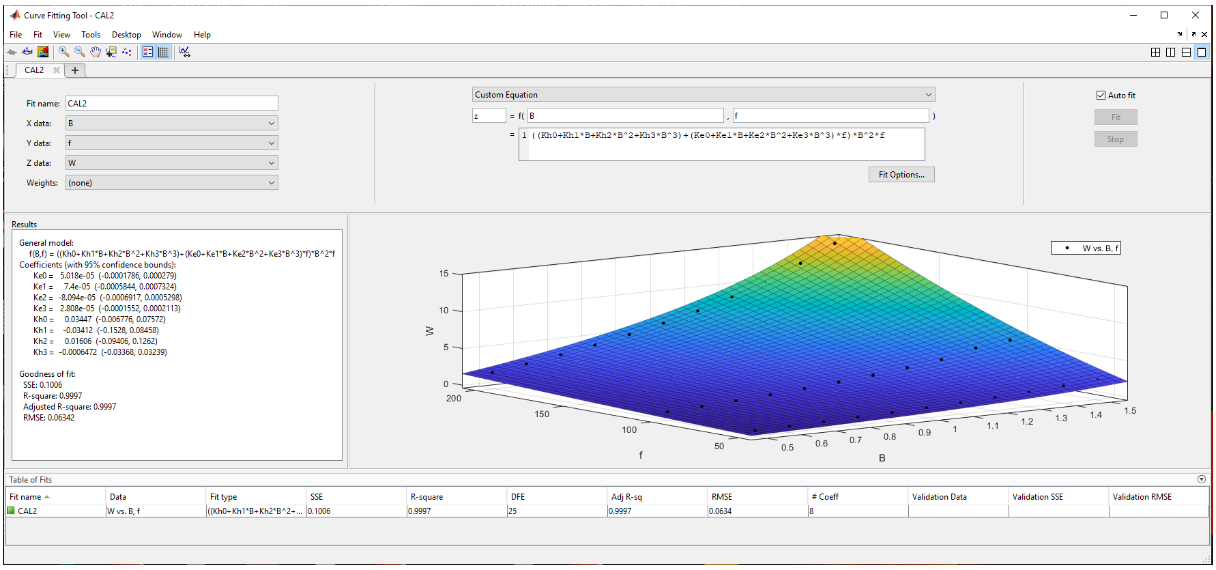

Fit name: CAL2
X data: B
Y data: f
Z data: W
Weights: (none)

Custom Equation
z = f(B , f)
= 1 ((Kh0+Kh1*B+Kh2*B^2+Kh3*B^3)+(Ke0+Ke1*B+Ke2*B^2+Ke3*B^3)*f)*B^2*f

☑ Auto fit

Results

```
General model:
  f(B,f) = ((Kh0+Kh1*B+Kh2*B^2+Kh3*B^3)+(Ke0+Ke1*B+Ke2*B^2+Ke3*B^3)*f)*B^2*f
Coefficients (with 95% confidence bounds):
    Ke0 =   5.018e-05  (-0.0001786, 0.000279)
    Ke1 =     7.4e-05  (-0.0005844, 0.0007324)
    Ke2 =  -8.094e-05  (-0.0006917, 0.0005298)
    Ke3 =   2.808e-05  (-0.0001552, 0.0002113)
    Kh0 =     0.03447  (-0.006776, 0.07572)
    Kh1 =    -0.03412  (-0.1528, 0.08458)
    Kh2 =     0.01606  (-0.09406, 0.1262)
    Kh3 =  -0.0006472  (-0.03368, 0.03239)

Goodness of fit:
  SSE: 0.1006
  R-square: 0.9997
  Adjusted R-square: 0.9997
  RMSE: 0.06342
```

Table of Fits

Fit name	Data	Fit type	SSE	R-square	DFE	Adj R-sq	RMSE	# Coeff	Validation Data	Validation SSE	Validation RMSE
🟩 CAL2	W vs. B, f	((Kh0+Kh1*B+Kh2*B^2+...	0.1006	0.9997	25	0.9997	0.0634	8			

Figure 78: Fitting App - MATLAB

11.2 Design philosophy

The design philosophy of a superconducting machine is not well-defined. Thus, the procedure followed in this thesis is presented in figure 79.

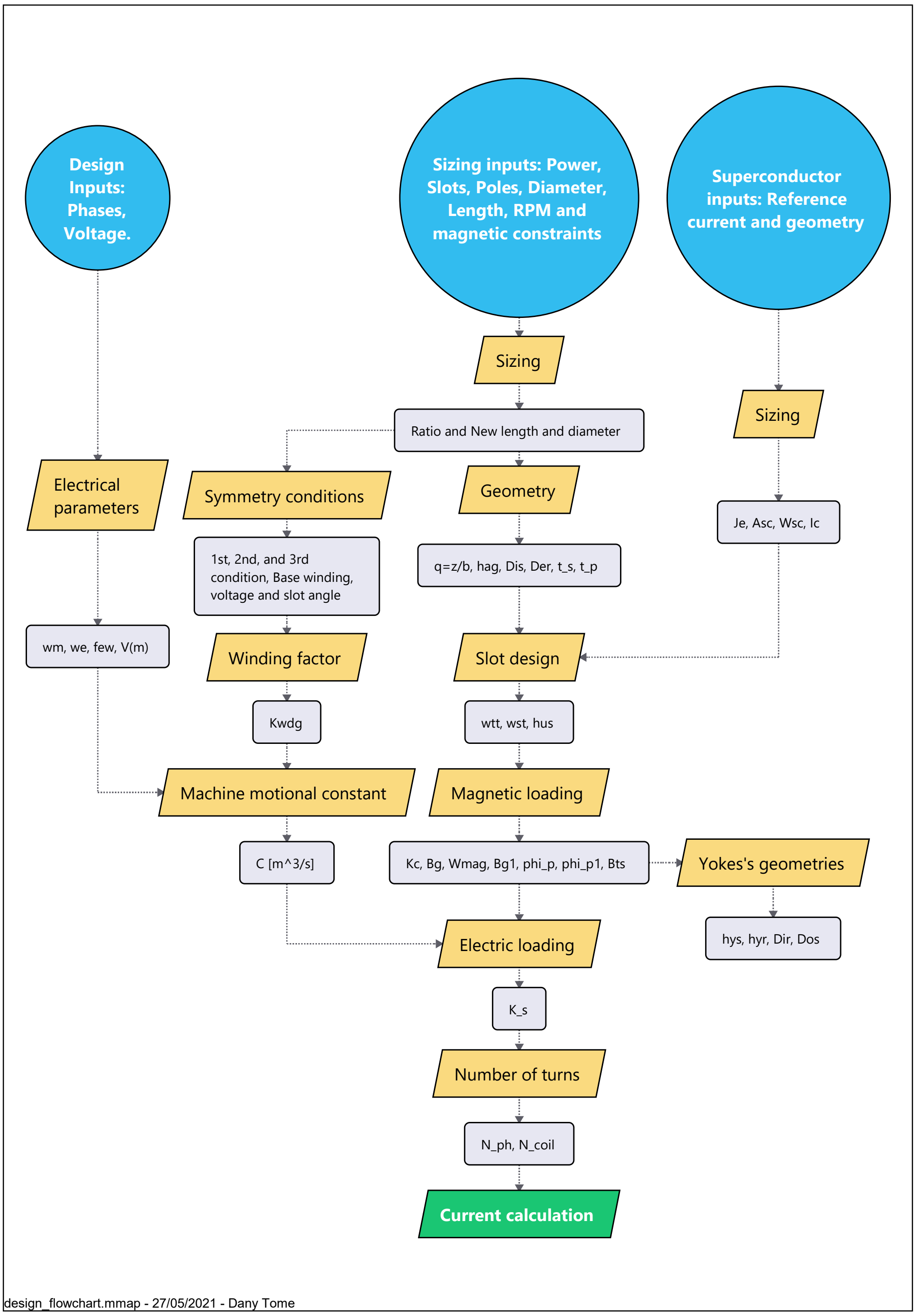

design_flowchart.mmap - 27/05/2021 - Dany Tome

Figure 79: Design flow chart

And the MATLAB Code for design is as follows:

```
%% Designing CODE

% Dany Josue Tome Robles
% Superconducting multiphase generator

clear all
close all
clc

%% Magnetic material parameters

mu_0        = (4*pi*1e-7);      %Magnetic permeability of free space
mu_r        = 1.05;             %Magnets relative permeability

%% Reference Data 10 MW 3ph AC Superconducting generator - Geometricy reference

% pr=22; %for 24-phases winding layout

Qs          = 48;               %Number of slots in the stator
pr          = 20;               %Pole pairs
L           = 1.215;            %Effective length
V           = 3300;             %Rated voltage [V]
Pref        = 10e6;             %Power [W]
Dag         = 5.4;              %Airgap diameter [m]

%% Sizing the new machine to 15 MW

P           = 15e6;             %Reference power of the new machine 15MW
n_10        = 9.6;              %RPM 10MW
n           = 7.56;             %RPM 15MW Mechanical speed REFERENCE
% n           = 6.82;           %RPM 20MW Mechanical speed REFERENCE

ratio       = L/Dag;            %Aspect ratio of the machine
L           = (ratio^2*P/Pref*Dag^2*L*n_10/n)^(1/3); %Effective length of the machine ...
    15MW [m]
Dag         = L/ratio;          %Airgap diameter for 15MW machine [m]

%% Electromechanical parameters

wm          = 2*pi*(n/60);      %Mechanical angular speed [Rad/s]
we          = wm*pr;            %Electrical angular speed [Rad/s]
fe           = we/2/pi;         %Frequency [Hz]

T           = P/wm;             %Torque [N]

%% Phases and Symmetry conditions of the winding layout

t           = gcd(Qs,pr);       %Greatest common divisor
LCM         = lcm(Qs,2*pr);     %Least commom multiple
m           = 3*4;              %Number of phases
q           = Qs/2/pr/m;        %Slots per pole per phase

%Integer windings
First   = Qs/m;                 %Natural number
Second  = Qs/t/m;               %Natural number

%Fractional slot windings
[z,b]       = rat(q);
First   = 2*pr/b;               %Natural number
Second  = b/m;                  %Non-natural number

t       = 2*pr/b;               %t
Qb      = Qs/t;                 %Number of slots in base winding
```

```
pb      = pr/t;                 %Number of pole pairs in base winding
tb      = 1;                    %Number of base windings in a base winding

alpha_z  = 2*pi/Qs*t;           %Voltage phase angle
alpha_u  = b/2*alpha_z;         %slot angle

Numbering_ph = (pb/tb)-1;       %Number of  phasors skipped in the numbering

Z       = Qb/m;                 %Number of phasors in one phase


%% Magnetics constraints and geometrical inputs

Byr          = 1.3;             %Rotor yoke flux density [T]
Bys          = 1.1;             %Stator yoke flux density [T]
% Bts          = 1.5;           %Stator teeth flux density [T]
Br           = 1.47;            %Remanent magnetic flux density [T]
lm           = 80e-3;           %Magnet height [m] reference model Dong Liu et al. 10 ...
    MW SPMG
hag          = Dag/1000;        %Airgap length 1/1000th of airgap diameter
hag          = 7.4e-3;          %Airgap length 1/1000th of exterior stator diameter

%% Designing

Dis          = Dag + hag;       %Stator inner diameter
Der          = Dis-2*hag-2*lm;  %Exterior rotor diameter

t_s          = pi*Dis/Qs;       %Slot pitch
t_p          = pi*Der/2/pr;     %Pole pitch
W            = t_p-t_s;

%% Slot design and airgap flux density
wst          = 0.200;           %Slot width calculation including cryostat
wtt          = t_s-wst;         %Teeth width calculation

b14 =wst;                       %Design with cooling system
gamma1  = 4/pi*(b14/(2*hag)*atan(b14/(2*hag))-0.5*log(1+(b14/(2*hag))^2));  %GIERAS ...
    reference
% gamma1  = 2/pi*(atan(b14/(2*hag))-2*hag/b14*0.5*log(1+(b14/(2*hag))^2));    %Pyrhonen ...
    reference
Kc      = t_s/(t_s-gamma1*hag);  %GIERAS reference
% Kc      = t_s/(t_s-gamma1*b14);  %Pyrhonen reference
heq = Kc*hag;                   %Equivalent airgap

Bg           = Br/(1+Kc*hag*mu_r/lm); %Airgap magnetic flux density - Gieras formula

%% EuBCO Cable - Superconducting cable design

hsc_ref      = 5e-3;            %Superconductor reference height
wsc_ref      = 0.1e-3;          %Superconductor reference width
I_ref        = 1460;            %Superconductor reference current
N_ref        = 9;               %Superconductor wire reference number of turns
Asc_ref      = hsc_ref*wsc_ref; %Superconductor wire reference area
Je           = I_ref/Asc_ref/N_ref; %Engineering current density
Ic_ref       = Je*Asc_ref;      %Critical engineering current
hsc          = 20e-3;           %Superconductor height
wsc          = 0.2e-3;          %Superconductor width
Asc_wire     = hsc*wsc;         %Superconductor wire area
Ic           = Je*Asc_wire;     %Critical current superconductor design

%% Geometry calculations

alp_m        = 0.8;             %Relative magnet width selected
w_m           = (Der+2*lm)*pi/(pr*2)*alp_m; %Magnet width according to model in EMETOR
% alp_m        = wm/t_p;        %Relative magnet width calculated by formula
```

```
Bg1         = 4/pi*Bg*abs(sin(alp_m*pi/2)); %Peak value of the fundamental distribution ...
    of the airgap magnetic flux density

phi_p       = Bg*w_m*L;         %Flux per pole
phi_p1      = 2/pi*Bg1*t_p*L;   %Fundamental space component flux per pole

ki          = 0.96;             %Lamination pack coefficient - Stacking factor (steel ...
    sheets - silicon sheets)

% Byr         = (phi_p/2)/((Der-Dir)/2*L*ki); %Rotor yoke magnetic flux density
hyr         = (phi_p/2)/(Byr*L*ki); %Rotor yoke height
Dir         = Der - 2*hyr;      %Rotor interior diameter

hys         = Bg/(Bys*ki)*alp_m*t_p/2; %Stator yoke height

% wtt         = Bg1/(Bts*ki)*t_s; %Stator teeth width (modified to Fundamental airgap ...
    flux density)
% wtt         = Bg/(Bts*ki)*(alp_m*t_p-(t_s-t_p)/2); %Stator teeth width if the ...
    circumferential magnet coverage
                                                     %is comparable or lower than the ...
                                                         stator slot pitch

% wst         = pi*Dis/Qs-wtt;  %Top slot width

Bts         = Bg/(wtt*ki)*(alp_m*t_p-(t_s-t_p)/2);      %Flux density in the teeth of ...
    the stator
wsb         = wst;              %Bottom slot width
alp_u       = 2*pi*pr/Qs;

kwdg        = sin(pi/(2*m))/(z*sin(pi/(z*2*m)))*cos((pi-alp_u)/2);  %Winding factor

% Dag         = Der+2*lm+hag;   %Airgap diameter

C           = pi^2*kwdg*Dag^2*L*fe/pr; %Machine geometrical-motion constant

if m==3
    ic=(1+sqrt(3)/2);           %Slot current for 3-phase machine
elseif m==12
    ic=(sqrt(3)+1)/sqrt(2);     %Slot current for 12-phase machine
elseif m==24
    ic=1.982889719624021;       %Slot current for 24-phase machine
end

K_s         = 2*P/(C*Bg1);      %Electrical loading
sigma       = K_s*Bg1/2;        %Shear stress calculation

%% Fill factor

kfill       = 0.5;              %Fill factor normally 0.5 due to Cooling requirements

%% Useful slot area
Aus         = (K_s*t_s)/(Je*kfill); %Slot useful area

%% End winding calculations

% Lewg         = pi/2*pi/(2*pr)*(Dis+hus); %End winding length
% Lave        = 2*(L+Lewg);     %Average winding length
% Lew         = 0.48*mu_0*2*pr*(q*Qs)^2*Lewg; %End winding inductance
% calculation

%% Voltage and current calculations

Nph         = 3*V/sqrt(3)/m/(sqrt(2)*pi*fe*kwdg*phi_p1); %Number of turns per phase ...
    calculation
% Ns          = round(Nph/(2*pr*q),0); %Number of turns per coil
```

```
% calculation
Ns =15;                         %Fixed number of turns per coil

%% Voltage, Current and Power calculations

Ir          = 4500;             %Fixed current for all the machine models
Eo          = 2*q*Ns*we*kwdg*Bg1*L*Dag*0.8; %Back EMF calculation
% Ir          = P/(m/2*Eo);     %Current calculation
N_parallel  = ceil(Ir/(Asc_wire*Je)); %Parallel superconducting wires
Ls          = 2*(4*m*mu_0*fe*(Ns*2*pr*q)^2/(pi*pr)*t_p*L/(hag*Kc+lm/mu_r)/(2*pi*fe)); ...
    %Inductance

Vr          = (Eo-(i*2*pi*fe*(Ls))*Ir); %Terminal voltage complex form
Va          = abs(Vr);          %Terminal voltage absolute value

Z_L         = Vr/Ir;            %Impedance
R_L         = real(Z_L);        %Resistance
X_L         = -imag(Z_L);       %Reactance
Xpu         =X_L/R_L;           %Reactance per unit

S_mph       = m/2*Vr*Ir;        %Complex power
S_apa       = abs(S_mph);       %Aparent power
pf          = cos(angle(S_mph)); %Power factor

V_L         = Vr*sqrt((1-cos(2*pi/m))); %Line voltage RMS
I_L         = Ir/sqrt(2);       %Line current RMS

P_calc      = S_apa*pf/1e6;     %Power [MW] %Assuming a sinusoidal behavior of the ...
    voltages and currents RMS: sqrt(2)
Q_calc      = imag(S_mph)/1e6;  %Reactive power [MVAr]

%% Rectangular slots
% hus          = Aus/wst;        %Stator slot height for copper calculations

hus = N_parallel*Ns*wsc+2*40e-3; %Stator slot height including cooling system

Dos         = Dis+2*hus+2*hys;  %Outer stator diameter

%% Electrical loadability

K_s           = Ns*Ir*ic/t_s;
S             = C*K_s*Bg1/2;    %Power
sigma_tan_mg  = K_s*Bg1/2;             %Electromagnetic tangential stress [Pa] assuming ...
    pf=1
Te            = sigma_tan_mg/2*Dag^2*pi*L;   %calculated torque
sigma_tan_mc  = 2*T/(Dag^2*pi*L);        %Mechanical tangential stress [Pa]
sigma_rel     = sigma_tan_mc/148500;     %Mechanical limit in percentage

EL          = K_s*Je;          %Electrical loadability [A2/m3]
Acu         = 0.6*Aus;         %Copper area with 60% filling factor
Jcu_eq      = Acu/(Asc_wire*N_parallel)*Je; %Current density copper equivalent [A/m2] ...
    Assuming Kcu=0.5
Jcu_max     = 10e6;            %Maximum copper current density [A/m2]
Kcu_max     = 200e3;           %Maximum copper linear current [A/m]
EL_max      = Kcu_max*Jcu_max; %Maximum electrical copper loadability [A2/m3]

Iu          = K_s*t_s;         %Slot current [A*turns]
Iu_cu       = Kcu_max*t_s;     %Slot current maximum copper [A*turns]
Iu_rel      = Iu/Iu_cu;        %Relation between slot current SC vs Cu

EL_rel      = EL/EL_max;       %Relation between electrical loadability SC vs Cu
J_rel       = Jcu_eq/Jcu_max;  %Relation between current density SC vs Cu
Ks_rel      = K_s/Kcu_max;     %Relation between linear current SC vs Cu
```

MMF harmonic calculation code

```matlab
%% Winding harmonics fast calculation

% Dany Josue Tome Robles
% Superconducting multiphase generator

clear all
close all
clc

%% Calculations

Harm=1000;
HarmPlot=50;
ph=[3,12,24,13];

%% Slot current computation

for n=1:4
m=ph(n);
if m==3
%     currentTot = [-2 1.5 -1 0 1 -1.5 2 -1.5 1 0 -1 1.5];
    Qs=12;
    currentTot=size(1,Qs);
    for k=1:Qs/2
        currentTot(2*k-1) = (-1)^(k)*2*sin(pi/2-2*pi/m*(k-1));
        if k > Qs/4
            currentTot(2*k) = -(sin(pi/2-2*pi/m*(k-1))-sin(pi/2-2*pi/m*(k)));
        else
            currentTot(2*k) = (sin(pi/2-2*pi/m*(k-1))-sin(pi/2-2*pi/m*(k)));
        end
    end
elseif m==12 %12-phase machine
    Qs=12;
    currentTot=size(1,Qs);
%     currentTot = [-(1+sqrt(3)/2) (1+sqrt(3))/2 -0.5 -0.5 (1+sqrt(3))/2 -(1+sqrt(3)/2) ...
    1+sqrt(3)/2 -(1+sqrt(3))/2 0.5 0.5 -(1+sqrt(3))/2 1+sqrt(3)/2];
    for k=1:Qs
        currentTot(k) = (-1)^k*(sin(pi/2-2*pi/m*(k-1))+sin(pi/2-2*pi/m*(k)));
    end
elseif m==24 %24-phase machine
    Qs = 24;
    currentTot=size(1,Qs);
    for k=1:Qs
        currentTot(k) = (-1)^k*(sin(pi/2-2*pi/m*(k-1))+sin(pi/2-2*pi/m*(k)));
    end
elseif m==13 %13-phase machine
    Qs = 13;
    currentTot=size(1,Qs);
    for k=1:7
        currentTot(2*k-1) = sin(pi/2-2*pi/m*(k-1))-sin(pi/2-2*pi/m*(k+6));
    end
    for k=1:6
        currentTot(2*k) = sin(pi/2-2*pi/m*(k+6))-sin(pi/2-2*pi/m*(k));
    end
end

%% Angle calculation

for k=1:Qs
    angle(k)=(k-1)*2*pi/Qs;
end

```

```
%% MMF computation

for k=1:Harm
    M(k)=0;
    for number=1:Qs
        M(k)=M(k)+2/(k*2*pi)*currentTot(number)*exp(-i*k*angle(number));
    end
end

%% Harmonics computation

r=0;
for k=1:HarmPlot
    r(k)=abs(M(k));
    if r(k) < 0.0001
        r(k)=0;
    end
end

if m==3
    r_3ph=r;
elseif m==12
    r_12ph=r;
elseif m==24
    r_24ph=r;
elseif m==13
    r_13ph=r;
end
end

%% Plots

figure()
bar([(1:HarmPlot)],[r_3ph./max(r_3ph); r_12ph./max(r_3ph); r_24ph./max(r_3ph); ...
    r_13ph./max(r_3ph)],1.2)
title('MMF Spectra')
legend('3-phase winding','12-phase winding','24-phase winding','13-phase winding', ...
    'location','best')
xlabel('Harmonics')
ylabel('Relative amplitude')
ylim([0 1.1])
xticks(0:1:HarmPlot)
yticks(0:0.1:1.1)
grid on
% grid minor
```

11.3 Tesla's egg of Columbus

To explain further the advantages of multiphase machines, the Tesla's egg of Columbus is proposed to have a reasonably simple example. The geometries of all machine models configurations are depicted in figure 80 as a magnetic flux density 2D plot. The dimensions of the machines are the same, whilst the number of turns are reduced accordingly to have the same current density for all models.

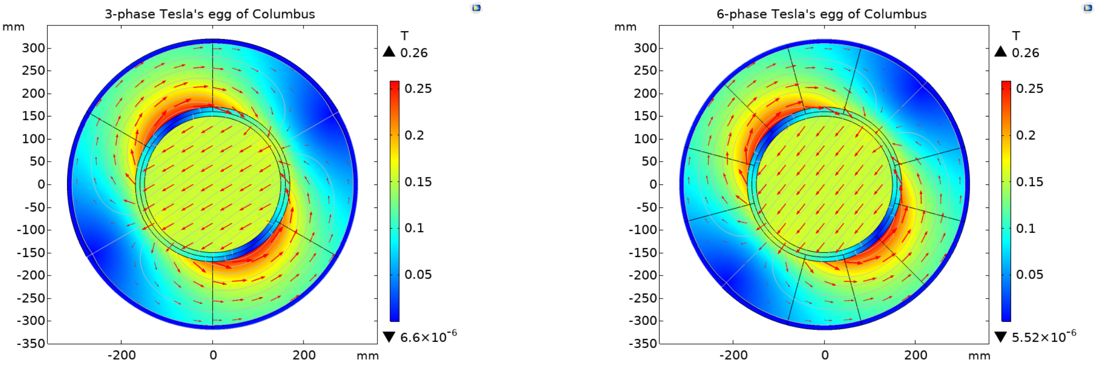

(a) 3-phase (b) 6-phase

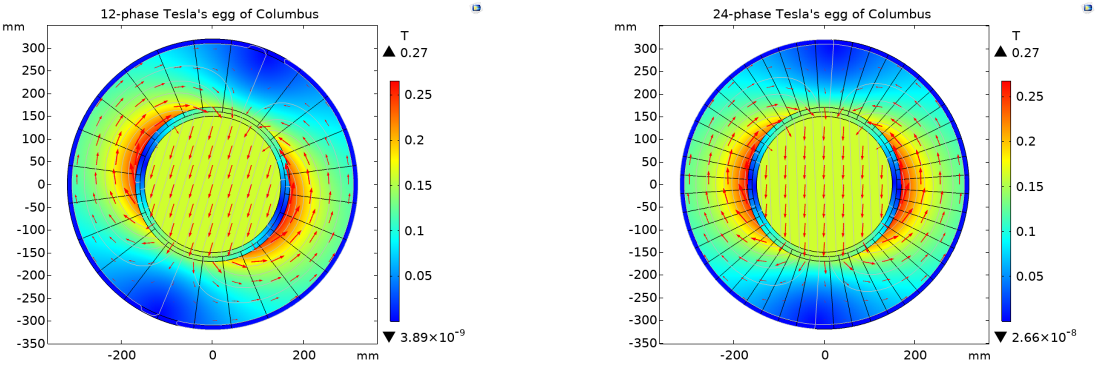

(c) 12-phase (d) 24-phase

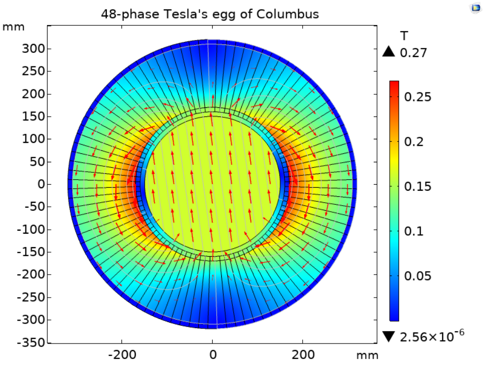

(e) 48-phase

Figure 80: Tesla's machines

Moreover, it is shown in figure 81 the generated phase voltages, in which the value decrease accordingly to the number of turns per phase. However, minor improvements are made by the 12, 24 and 48-phase Tesla's machines because the winding factor is enhanced due to a better winding distribution. For instance, the 12-phase machine should have a voltage amplitude value of 87.5 V. However, it shows a higher value than 90 V, which is similar for the 24 and 48 phases machines.

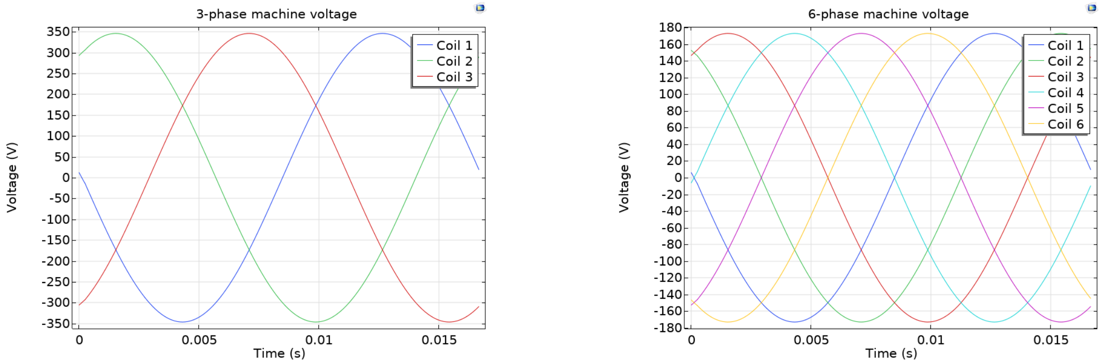

(a) 3-phase (b) 6-phase

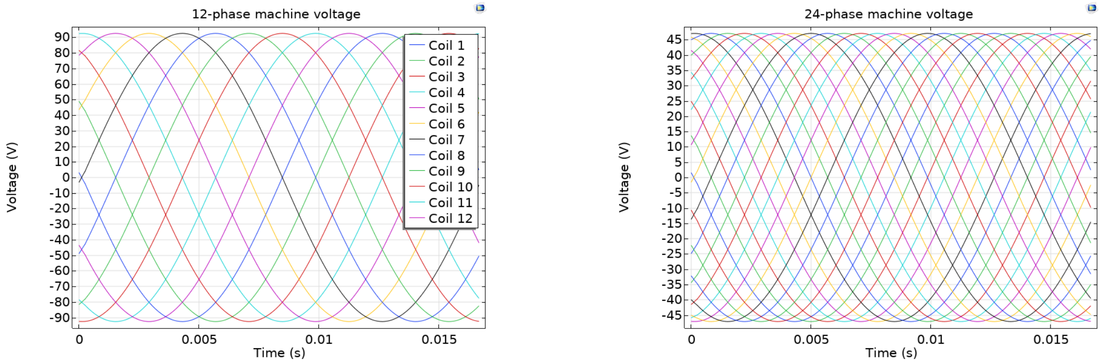

(c) 12-phase (d) 24-phase

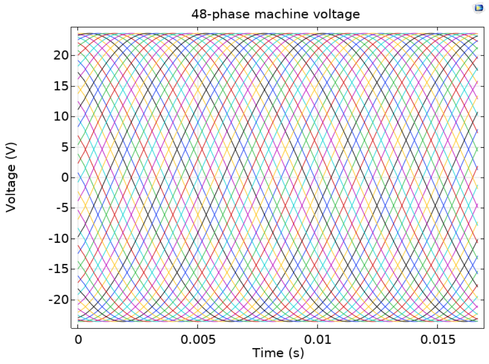

(e) 48-phase

Figure 81: Tesla's machines voltages

The enhancement of the voltages can be seen in the overall machine power output. Where the 12, 24 and 48-phase have a slight increment, as is shown in figure 82. E.g., the power for the 48-phase machine for each phase should be around 112.5 V. Nonetheless, the value obtained with the simulation is around 120 V. Thus, by only designing a different winding configuration with high-phase order, the output power is enhanced.

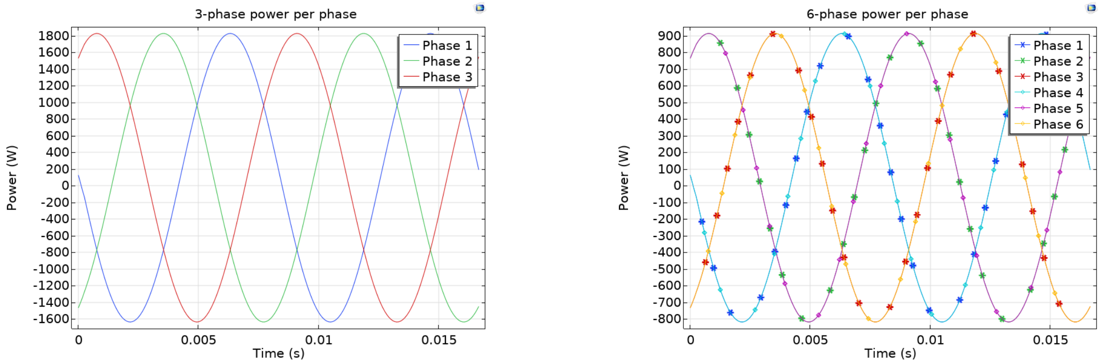

(a) 3-phase (b) 6-phase

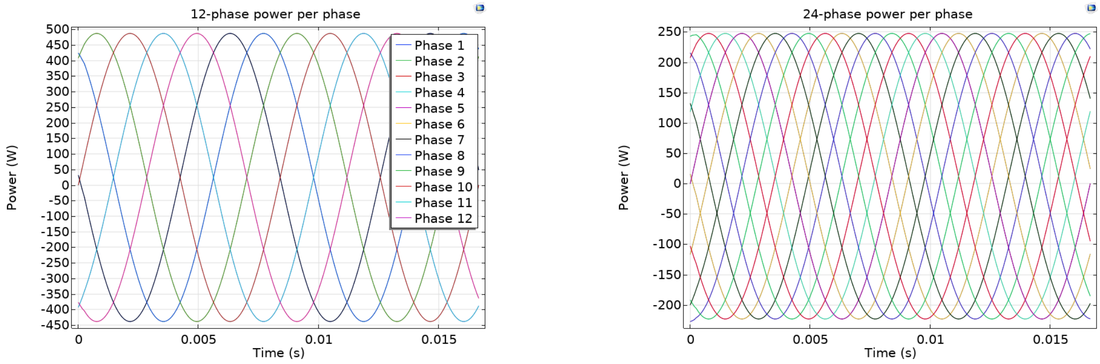

(c) 12-phase (d) 24-phase

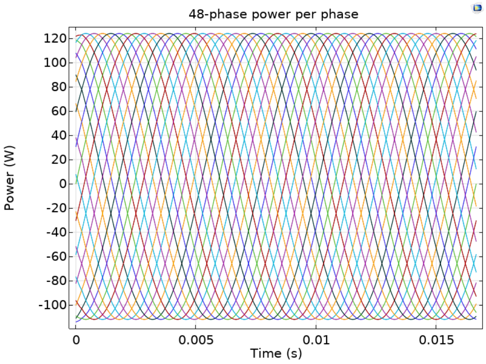

(e) 48-phase

Figure 82: Tesla's machines voltages

For the case of the magnetic flux density behaviour in the iron, it is shown in figure 83 that for a high-phase order, the variation of both average and maximum magnetic flux density norms are more stable. Furthermore, the average magnetic flux density norm is enhanced compared to the 3-phase machine case. Moreover, as discussed before, the iron losses can be further reduced by reducing the variation of the magnetic flux density.

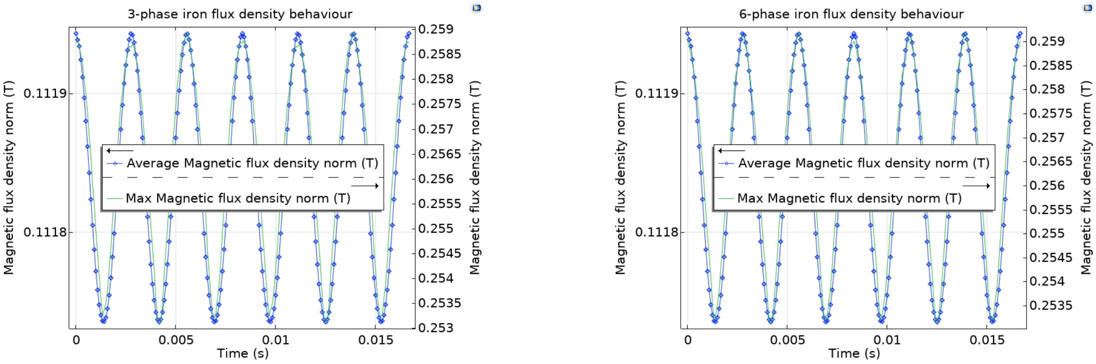

(a) 3-phase (b) 6-phase

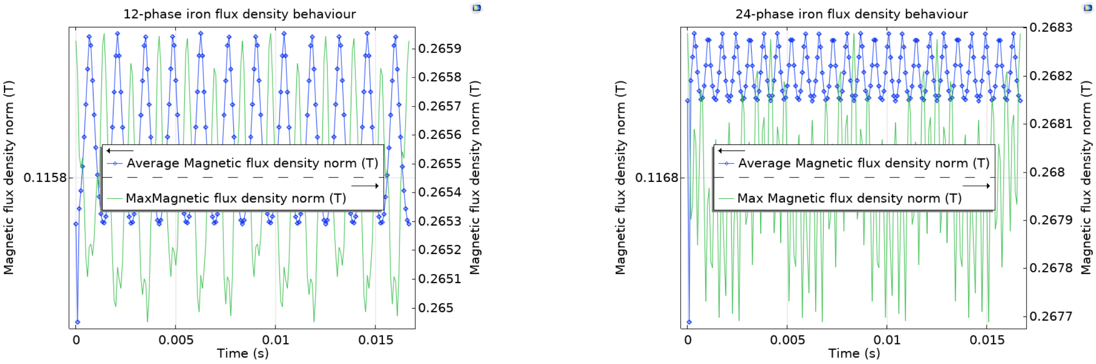

(c) 12-phase (d) 24-phase

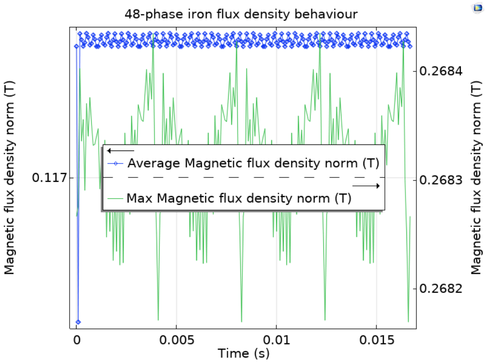

(e) 48-phase

Figure 83: Iron magnetic flux density comparison

11.4 Rotor's new design approach

In this section, additional figures of the new rotor's design approach (bulkier PM rotor) are shown to demonstrate the machine's performance.

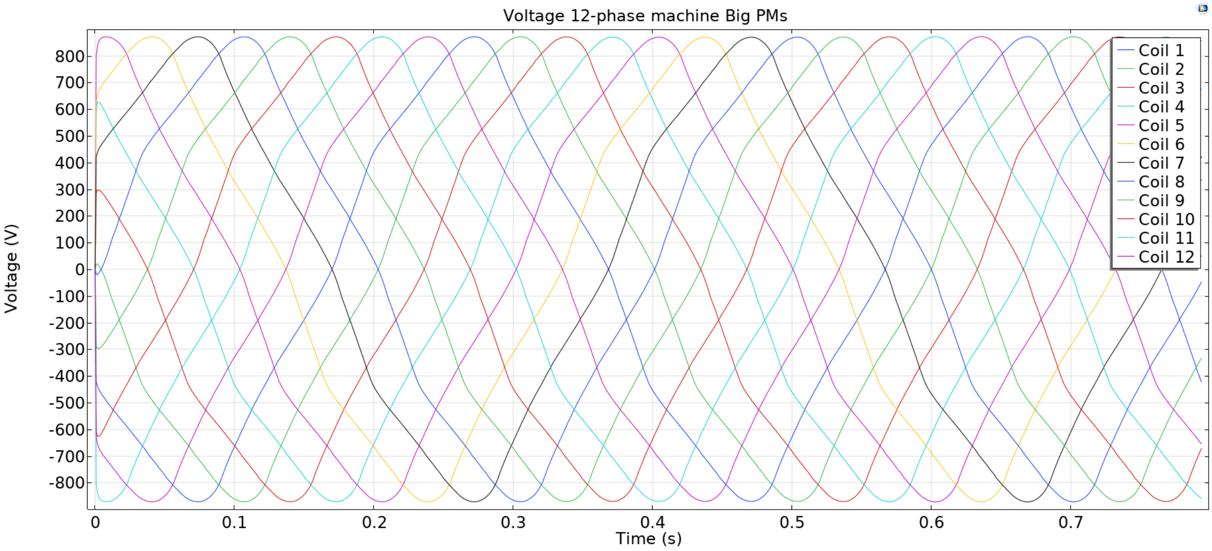

Figure 84: Voltage new rotor's design

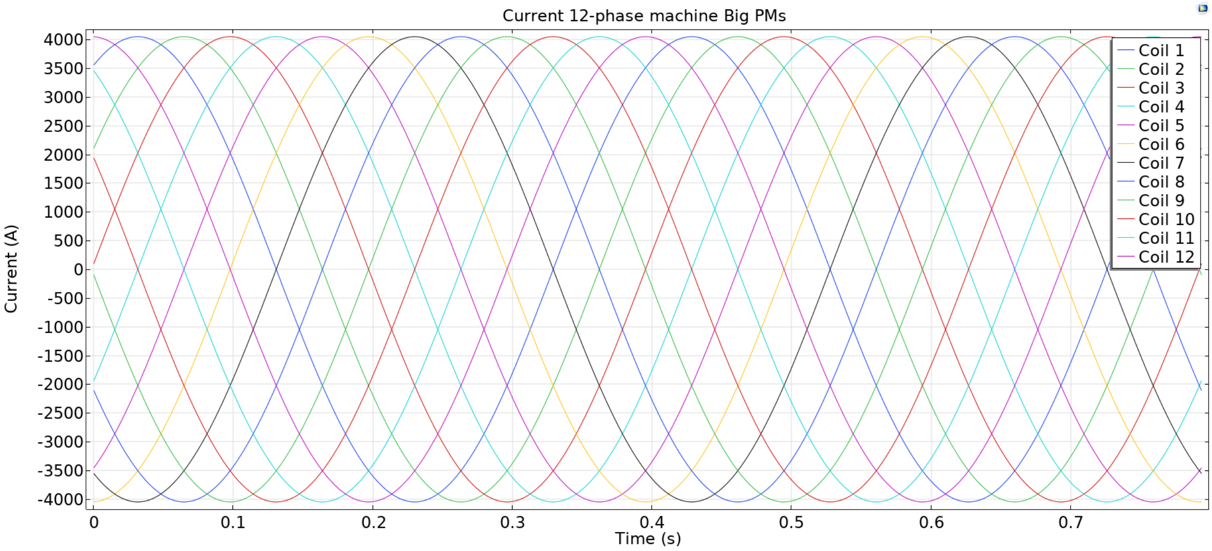

Figure 85: Current new rotor's design

In figures 84 and 85, the voltage and currents are depicted. Where is shown that the 12-phase machine is used, and the current is reduced since the demagnetization is diminished, and the design output power is 15 MW.

The power and shear stress are shown in figures 86 and 87. As is expected, the Meisner effect is present. Thus, the fluctuating behaviour of the power with Arkkio's method calculation is present, so is in the shear stress computation.

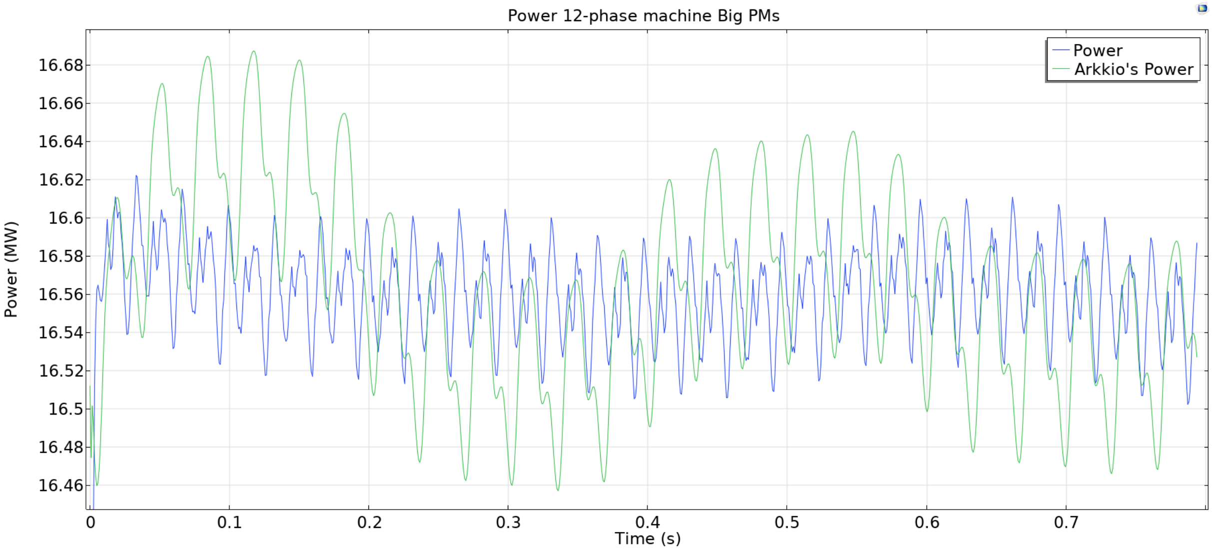

Figure 86: Power new rotor's design

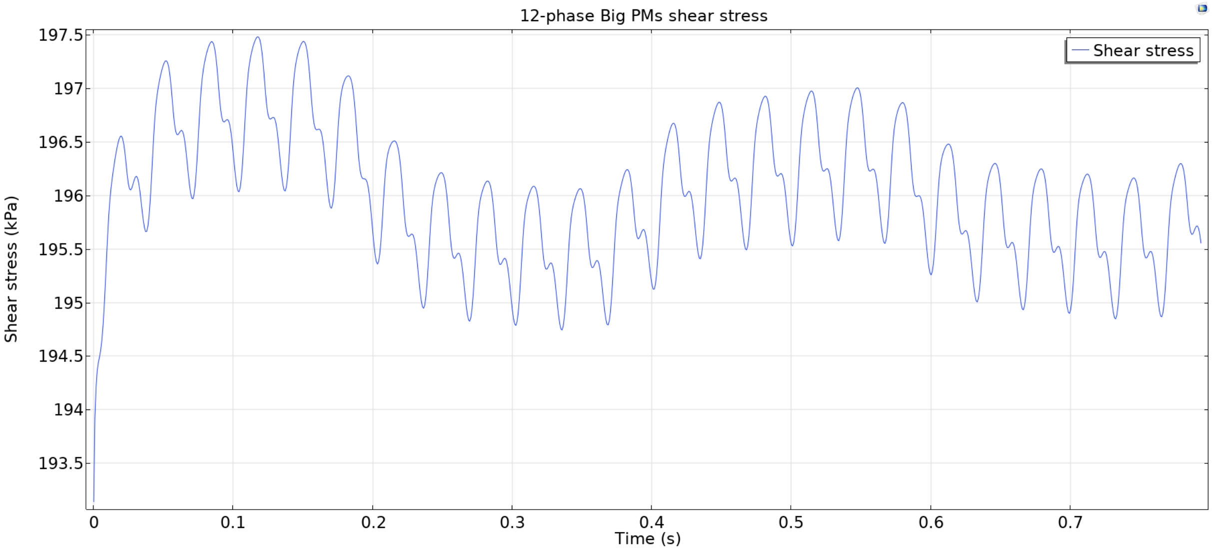

Figure 87: Shear stress new rotor's design

The magnetic flux density in the airgap is depicted in figure 88 over the Arkkio's band and in figure 89 over the airgap line. It is important to notice that the magnetic angle calculated with the Maxwell Stress Tensor analysis is smaller compared to other configurations in which the magnets are not bulky. The reduction in the magnetic angle is mainly because of the compactness of the machine. However, the armature reaction is smaller than the other configuration because the rated current is smaller than the 4500 A. Thus, this contributes too to a smaller magnetic angle.

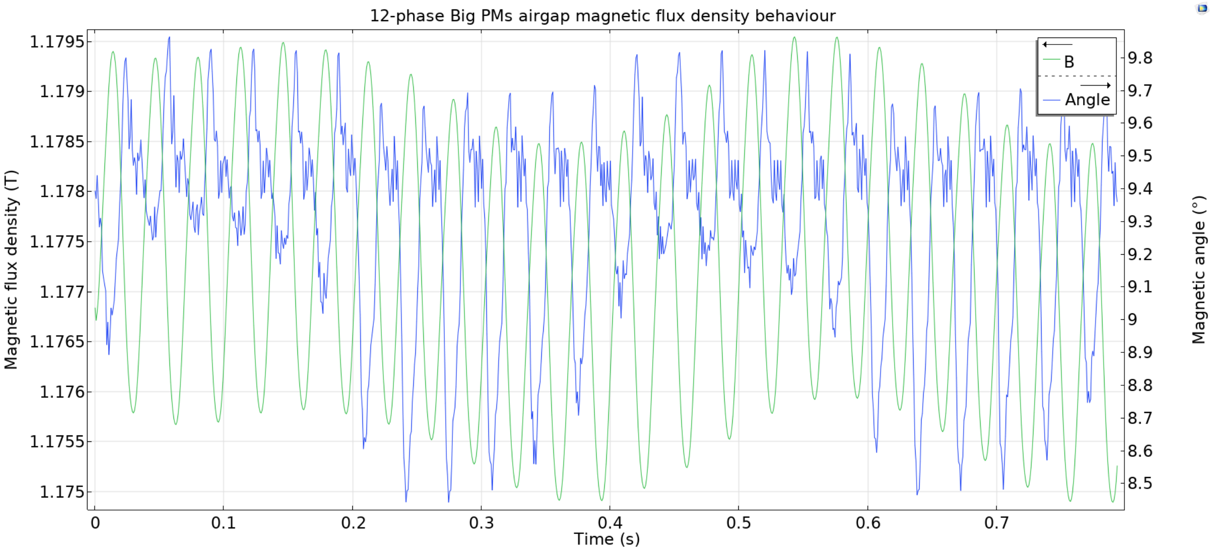

Figure 88: Airgap Magnetic flux density behaviour - new rotor's design

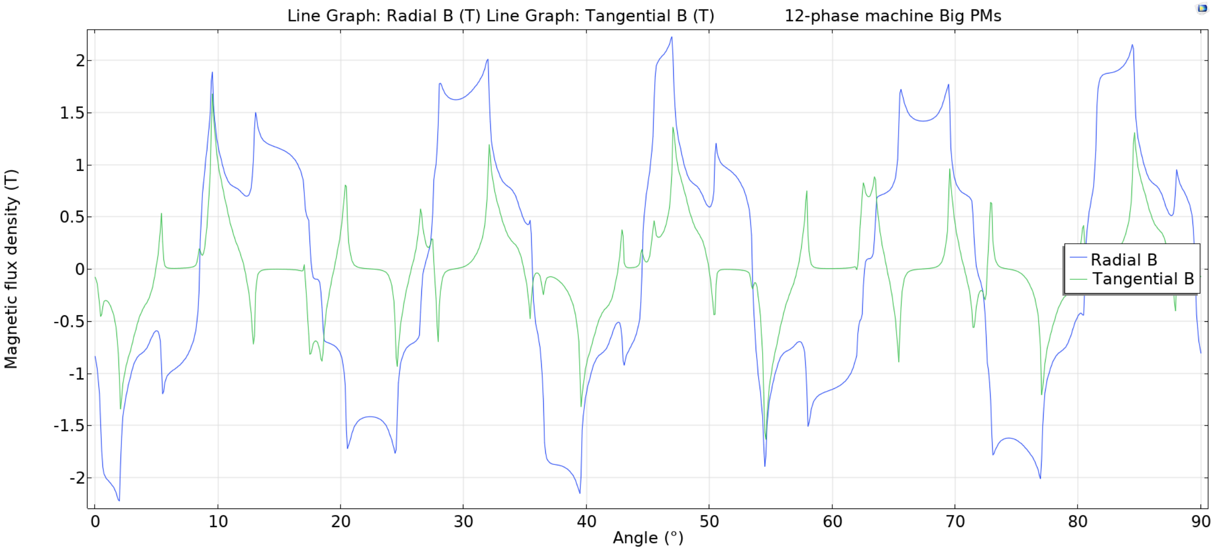

Figure 89: Airgap Magnetic flux density line graph - new rotor's design

The magnetic angle's reduction in the airgap also means a reduction in the radial and tangential forces angle in the airgap of the machine. Figure 90 shows the expected force angle reduction, and therefore, the increase in the radial force.

For the case of the magnetic flux density behaviour inside the permanent magnets, the magnetic angle is reduced an the amplitude increased, as is shown in figure 91.

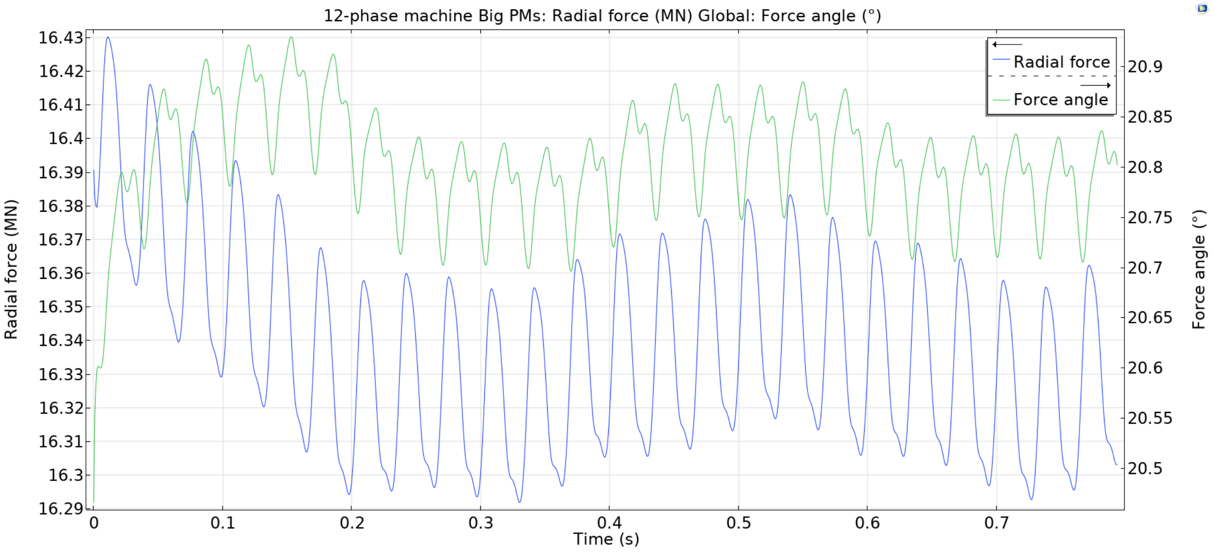

Figure 90: Force new rotor's design

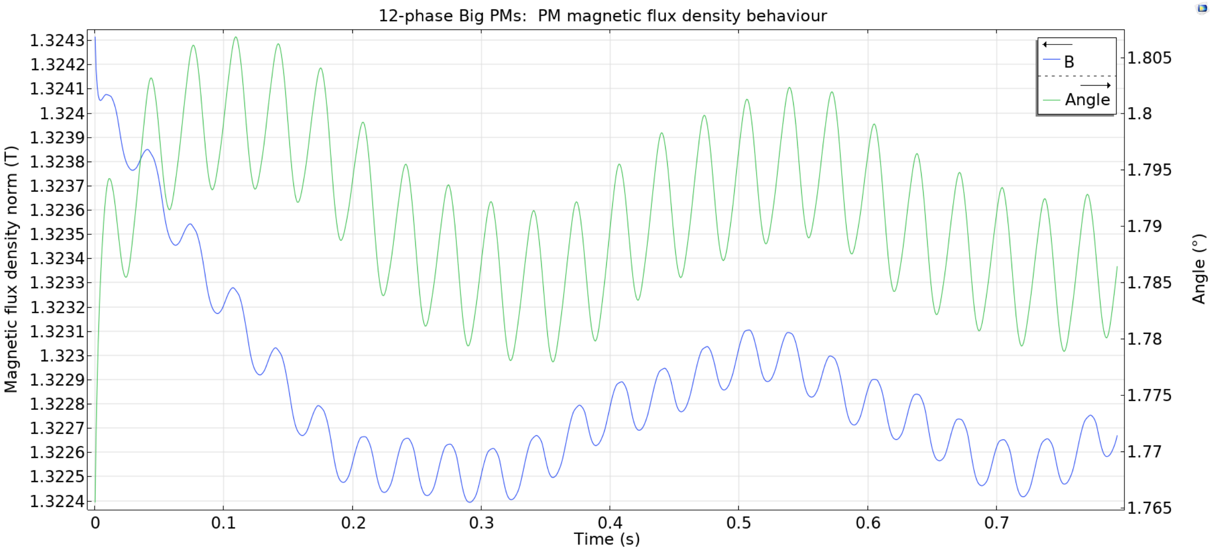

Figure 91: PMs magnetic flux density behaviour - new rotor's design

The power factor and reactance behaviour over time are presented in figures 92 and 93.

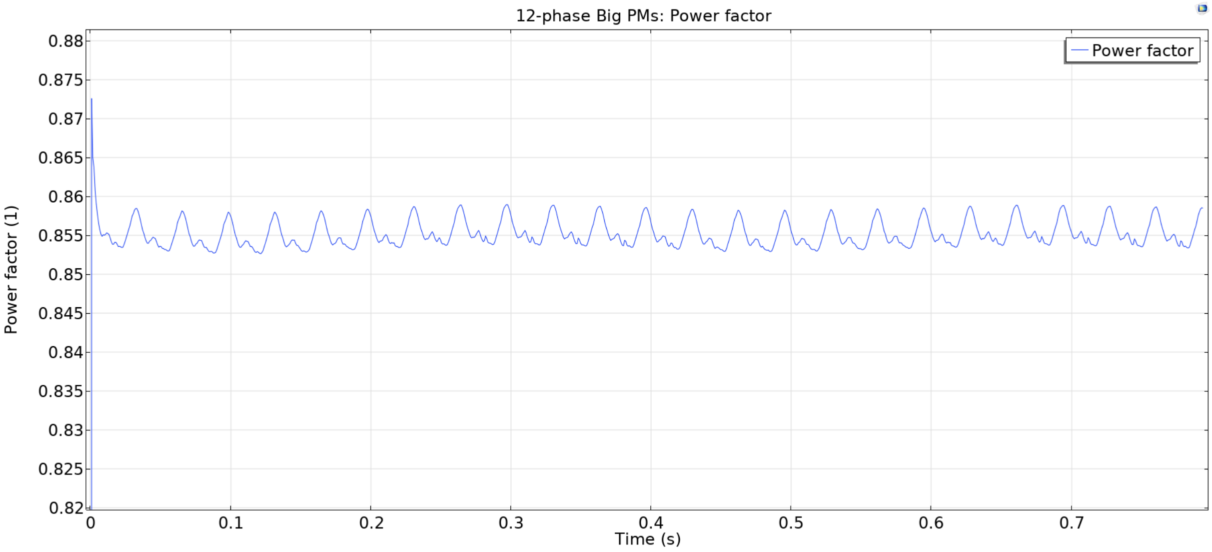

Figure 92: Power factor behaviour - new rotor's design

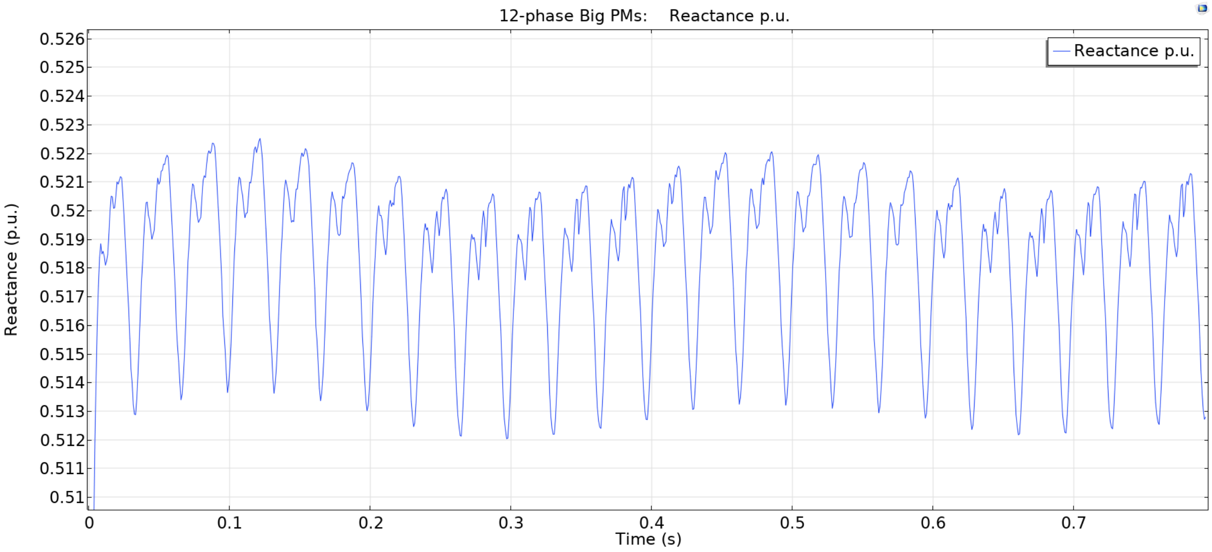

Figure 93: Reactance in per unit behaviour - new rotor's design

Finally, a demagnetization figure is presented in figure 94. Where 100 % means that the magnets are not demagnetized.

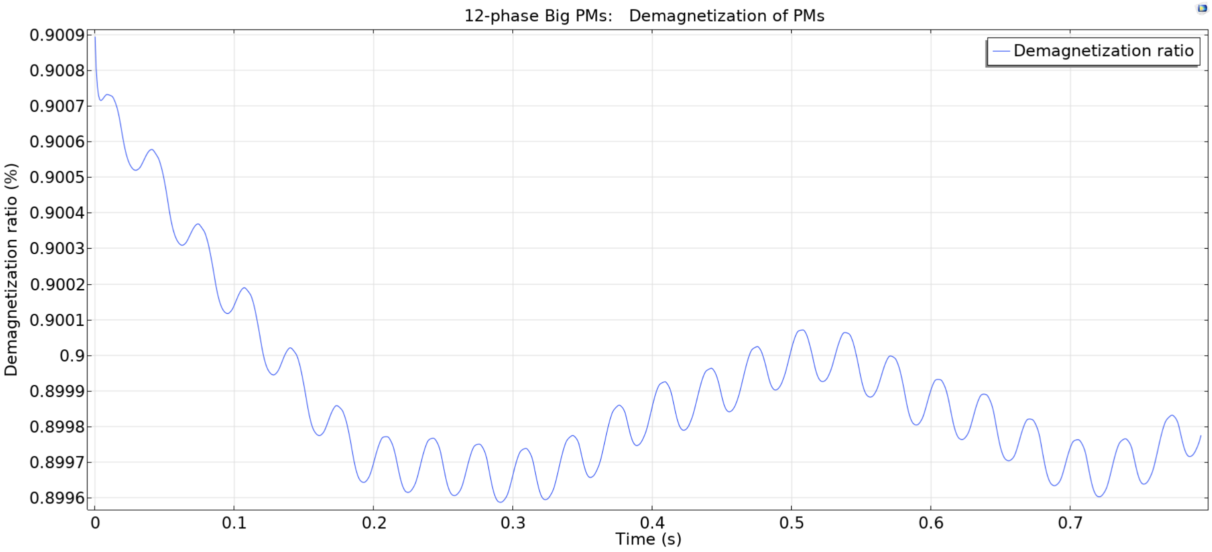

Figure 94: PMs demagnetization - new rotor's design

11.5 13-phase winding layout design

In this section, the additional figures for the new winding layout proposal are shown. The winding layout is presented in figure 95.

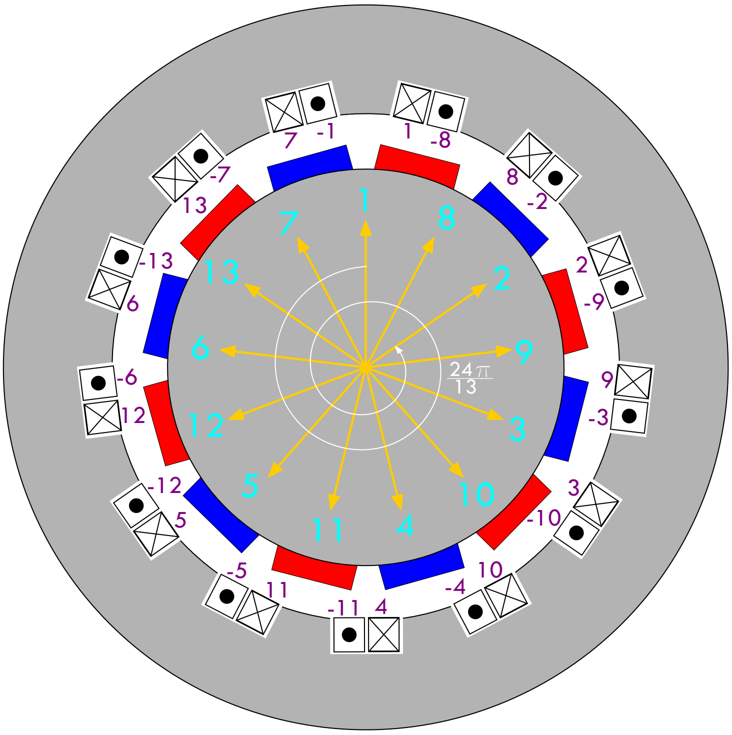

Figure 95: 13-phase winding layout

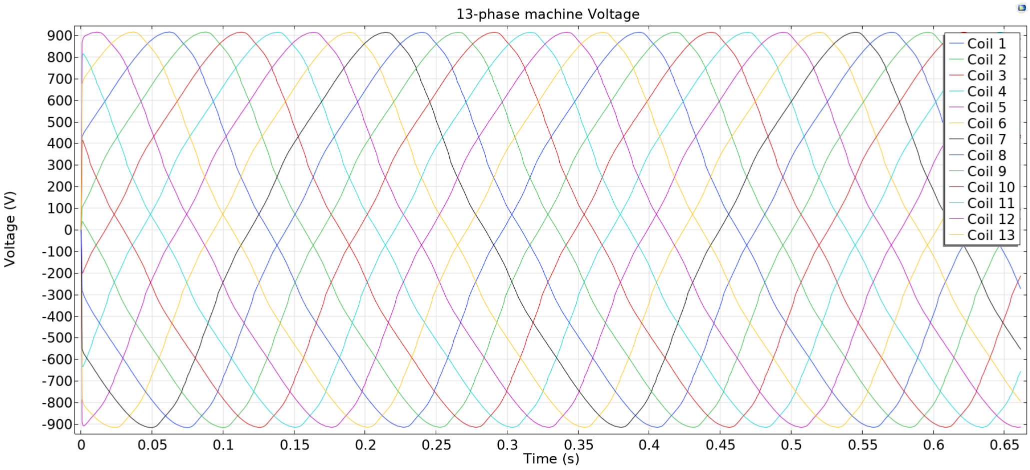

Figure 96: Voltages - 13-phase winding layout design

The voltages for the 13-phase winding layout are presented in figure 96. And the currents are presented in figure 97.

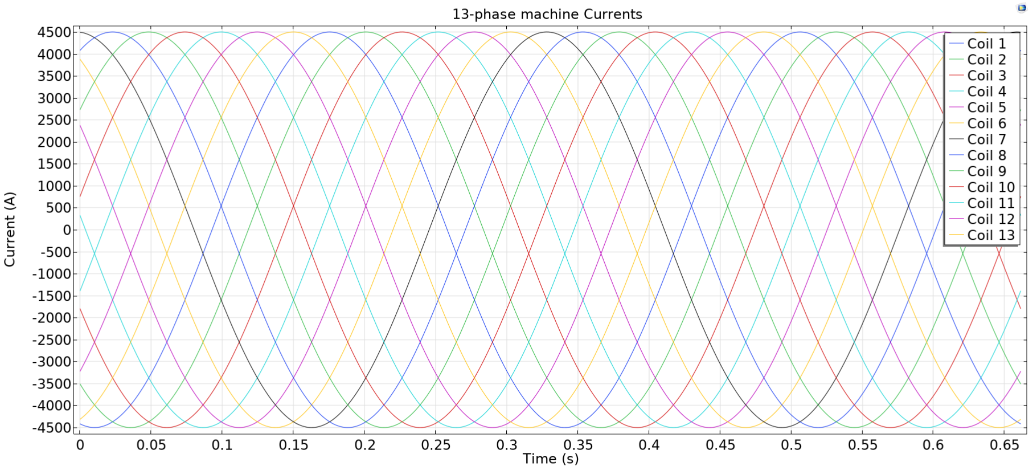

Figure 97: Currents - 13-phase winding layout design

In figure 98, a shear stress comparison is depicted. Where the 13-phase machine outperformed the other configurations. The higher shear stress is because the higher frequency operation regime, and the better winding factor. Which in this present work can be compared directly with the motional constant, as is shown in table 19.

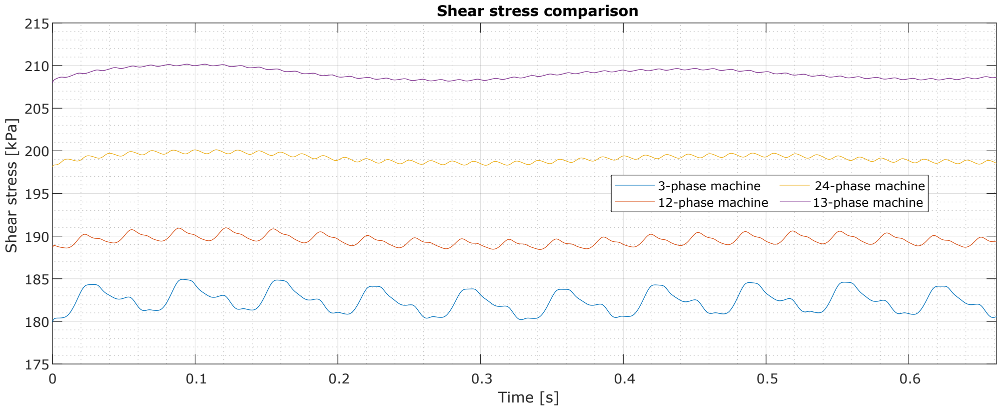

Figure 98: Shear stress 13-phase winding layout design

Topologies	3ph	12ph	24ph	13ph
C_m	$78.3001\,\mathrm{m^3/s}$	$81.0622\,\mathrm{m^3/s}$	$83.2038\,\mathrm{m^3/s}$	$83.3099\,\mathrm{m^3/s}$

Table 19: Motional constants comparison

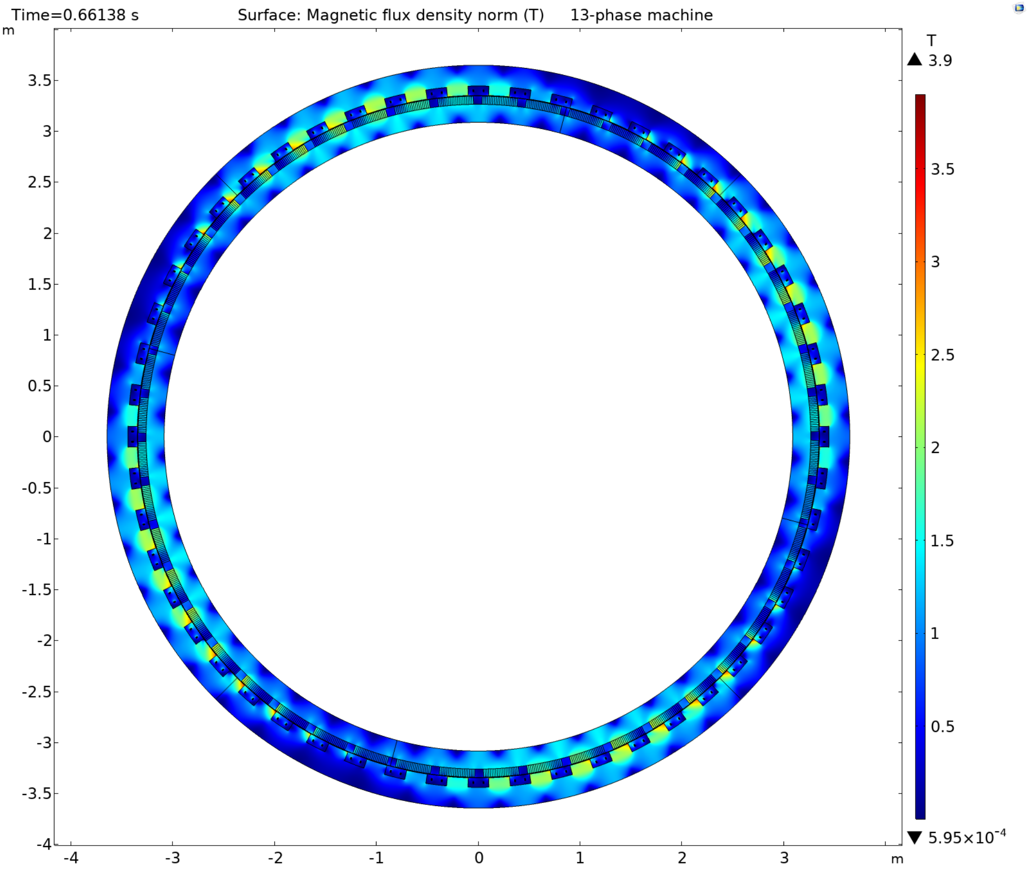

Figure 99: Simulation - 13-phase winding layout design

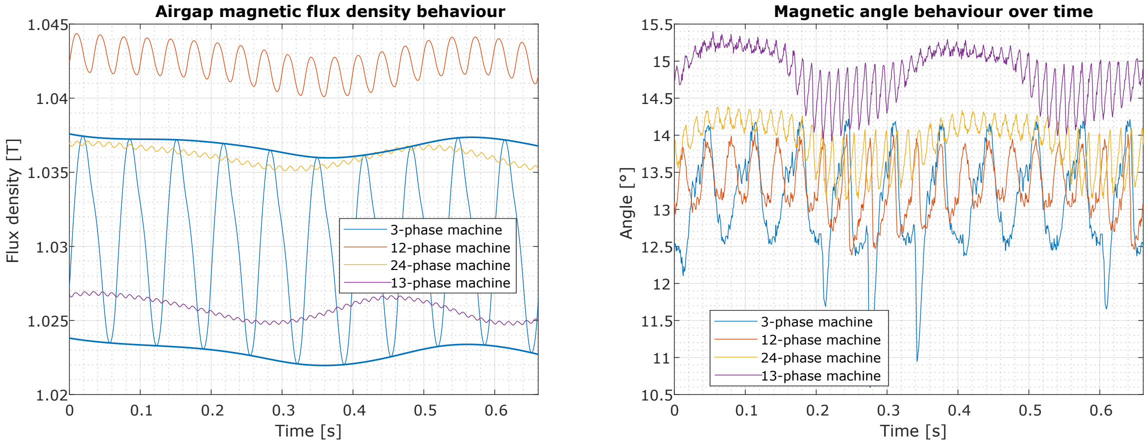

(a) Magnetic flux density (b) Magnetic angle

Figure 100: Airgap magnetic flux density behaviour 13-phase winding layout design

Since the 13-phase machine has the higher shear stress and output power, it is expected to have a higher magnetic angle and a smaller magnetic flux density amplitude because of the demagnetization of the PMs, as is shown in figure 100.

Therefore, the force angle is expected to be higher and the radial force smaller. This is confirmed in figure 101.

The demagnetization can be observed in figure 102, where the amplitude of the magnetic flux density for the 13-phase machine is the smallest, and the magnetic angle inside the magnets is the highest.

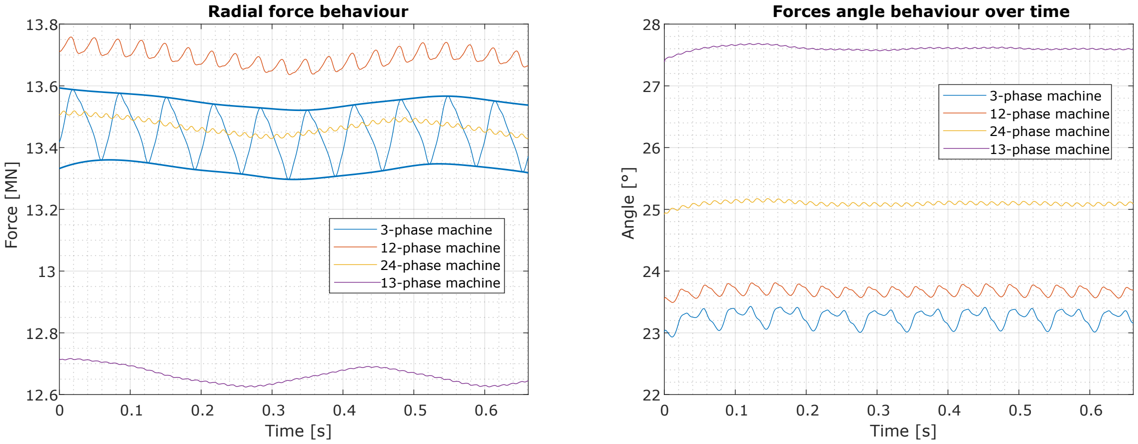

(a) Radial force (b) Force angle

Figure 101: Force behaviour 13-phase winding layout design

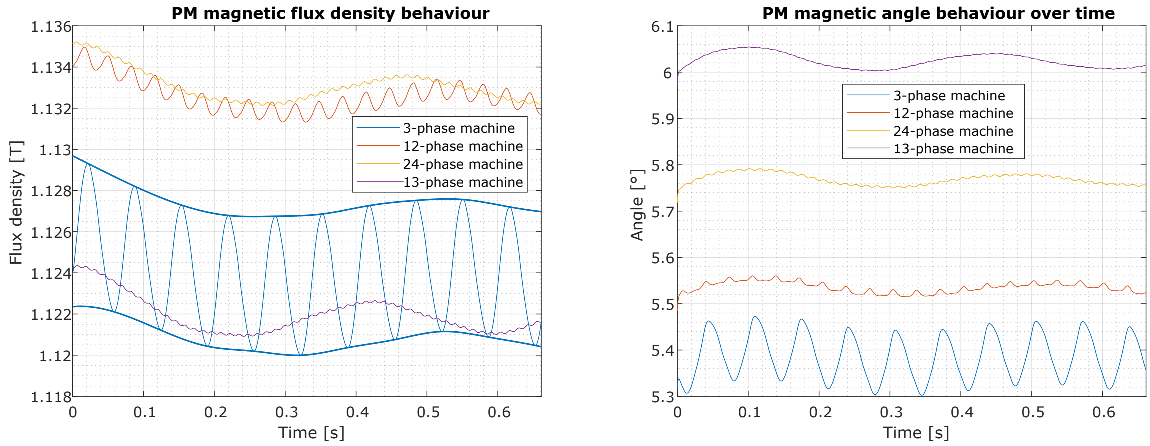

(a) PM magnetic flux density (b) PM magnetic angle

Figure 102: PMs magnetic flux density behaviour 13-phase winding layout design

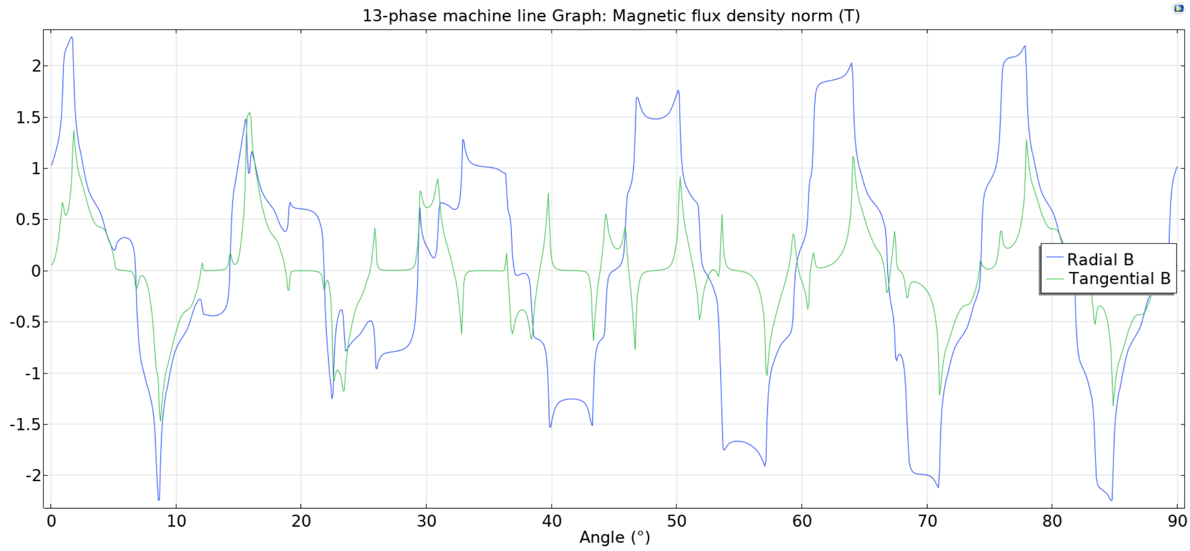

Figure 103: Airgap magnetic flux density line graph - 13-phase winding layout design

The line graph for the airgap magnetic flux density is presented in figure 103. The most relevant output from this graph is that 12 peaks represent each slot in the base winding.

The harmonic analysis is depicted in figure 104. The space working harmonic is confirmed to be the 6th harmonic. Moreover, it presents zero sub-space harmonics as the other high-phase order machine configurations.

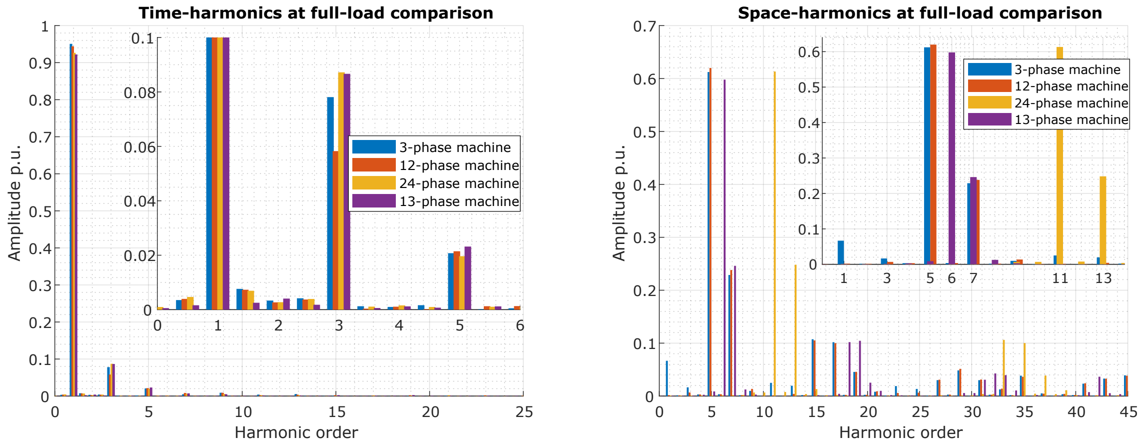

(a) Time harmonics (b) Space harmonics

Figure 104: Harmonic analysis - 13-phase winding layout design

11.6 Final design

In this section, the final design of a 13-phase bulky PM AC superconducting machine is presented.

The output power is depicted in figure 105. And the voltage and currents for 13-phase machine validation are shown in figures 106 and 107.

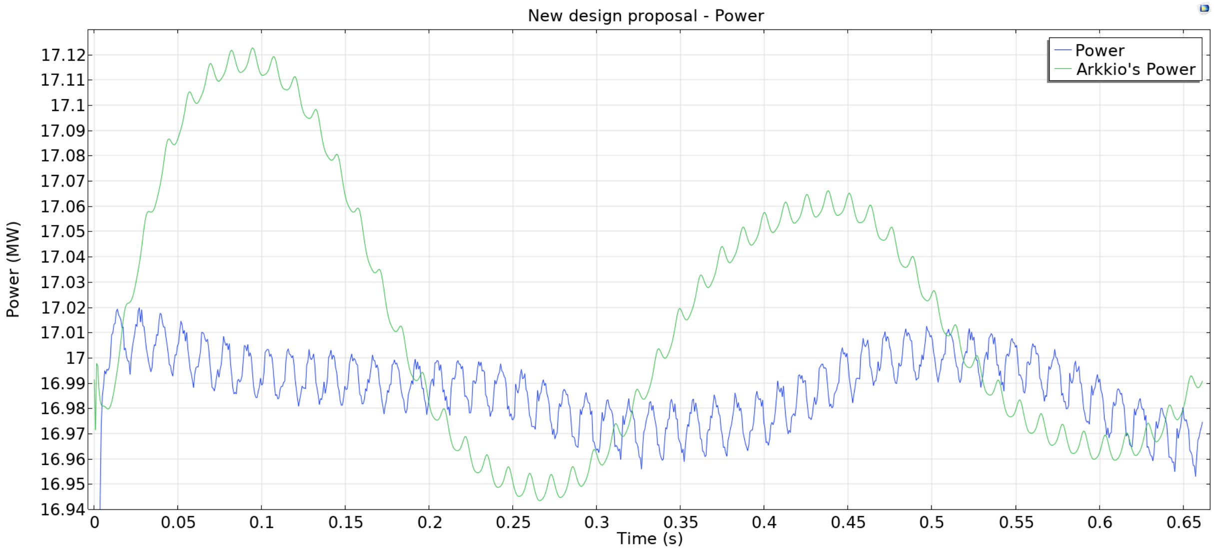

Figure 105: Power - New design proposal

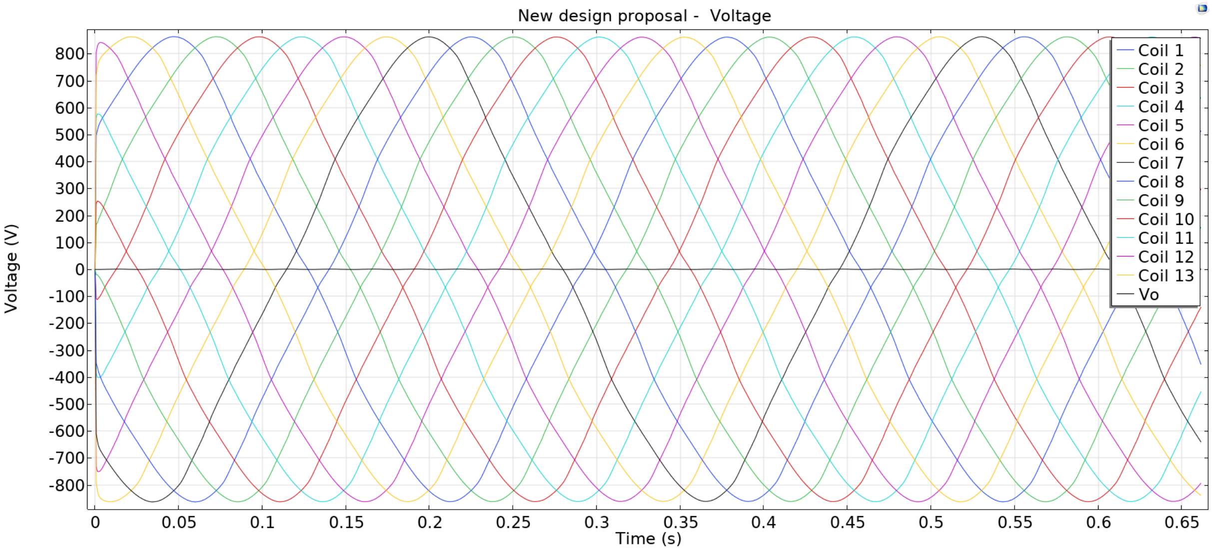

Figure 106: Voltages - New design proposal

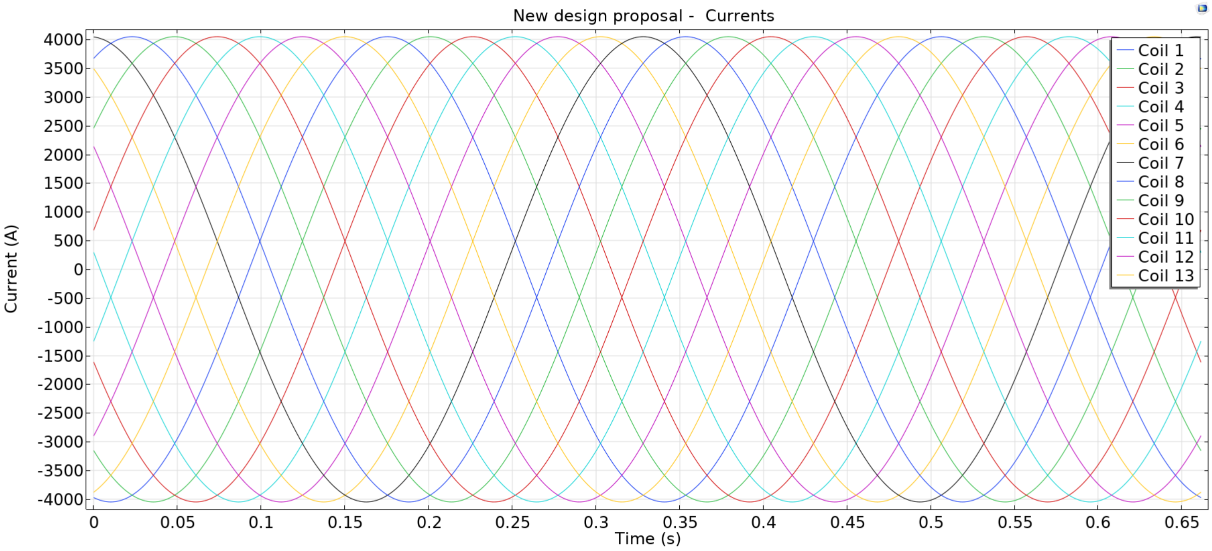

Figure 107: Currents - New design proposal

Figure 108 shows the shear stress for the new design proposal. It can be seen the meisner effect.

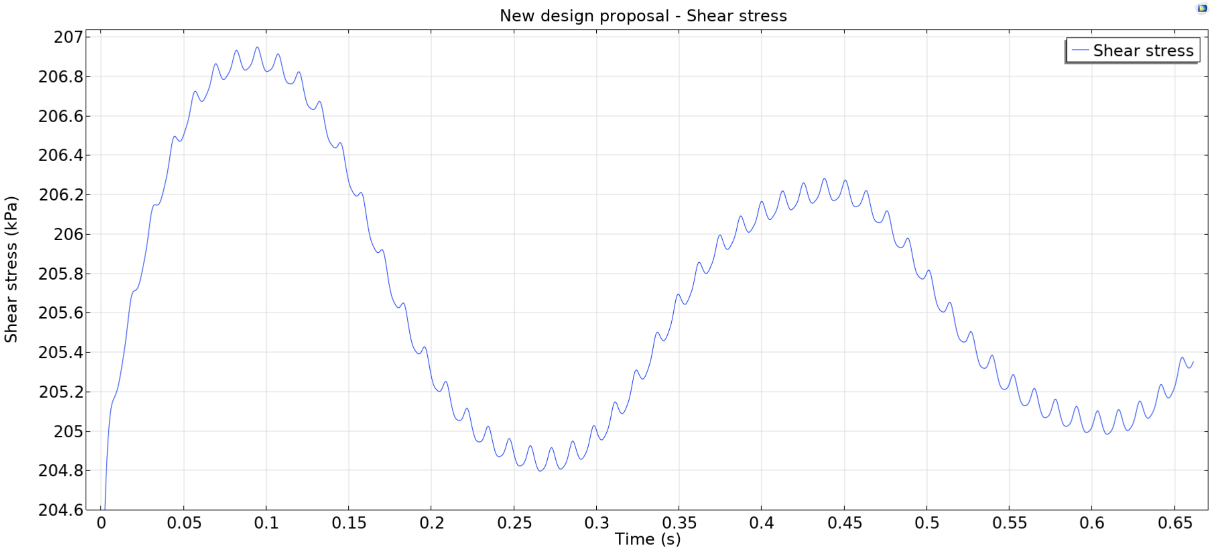

Figure 108: Shear stress - New design proposal

For the case of the magnetic flux density in the airgap depicted in figure 109, the magnetic angle is reduced compared to the other examples. The magnetic angle reduction is because the armature current is less than 4500 A.

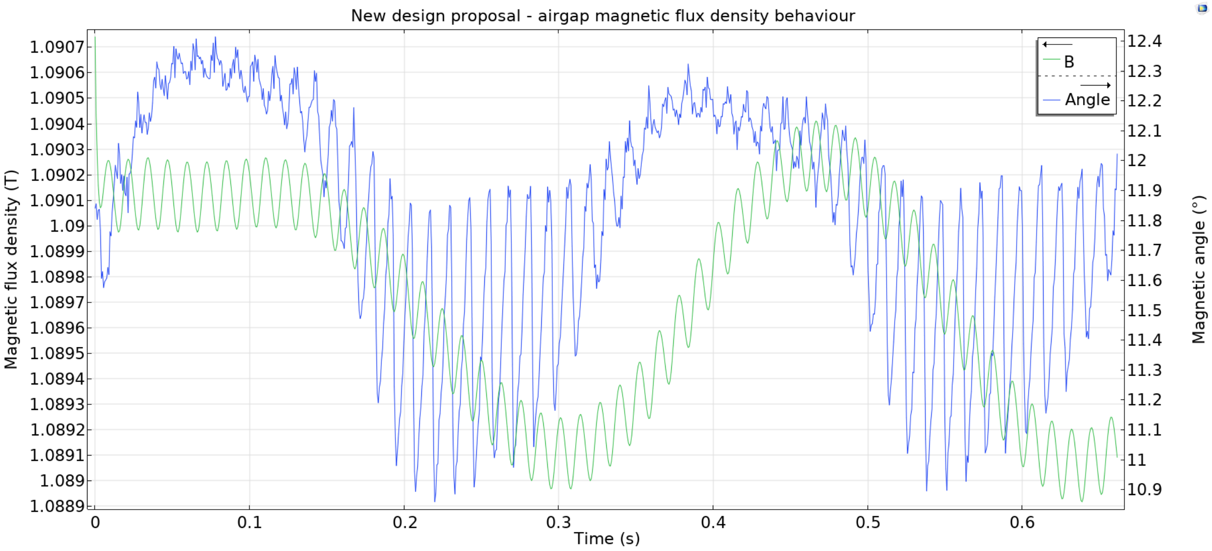

Figure 109: Airgap magnetic flux density behaviour - New design proposal

Moreover, for the case of the line graph for the airgap magnetic flux density in figure 110, the graph shows a better depiction of each slot interaction.

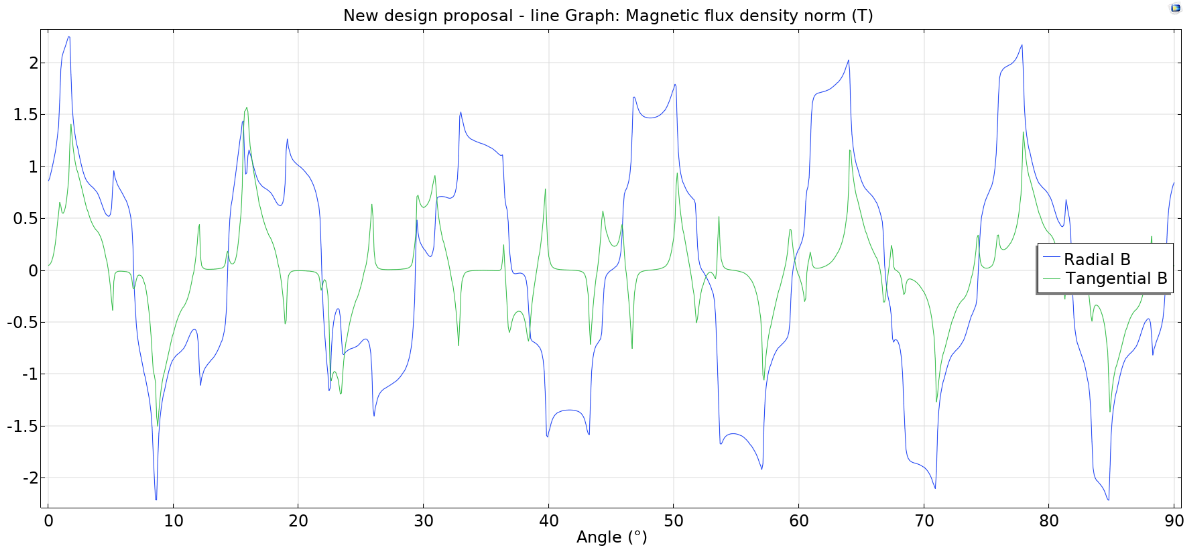

Figure 110: Airgap magnetic flux density line graph - New design proposal

The force behaviour is shown in figure 111, where the force angle and radial force amplitude are similar to the previous examples. Similar values can be explained by maintaining the same machine's dimensions. Thus, it has the same compactness.

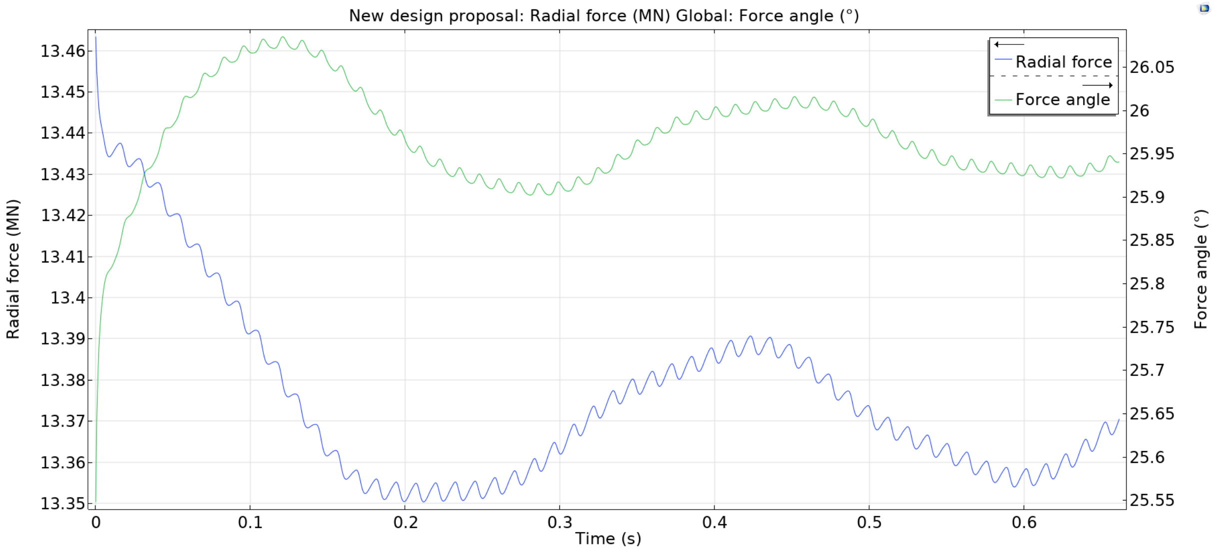

Figure 111: Force behaviour - New design proposal

For the magnets case, it shows similar results as the previous configuration. The PMs magnetic flux density is depicted in figure 112.

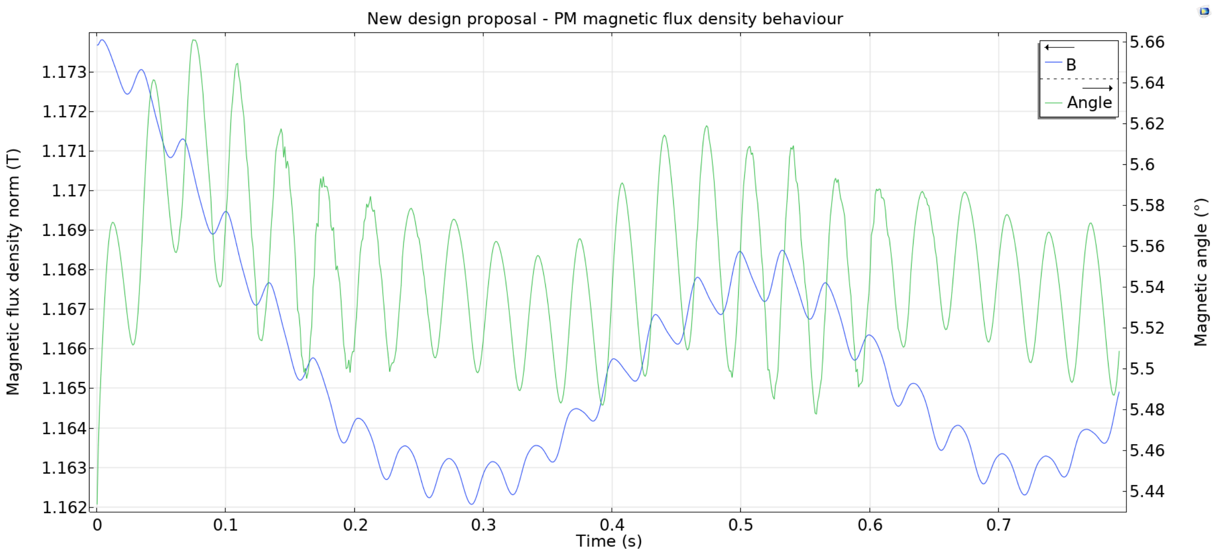

Figure 112: PMs magnetic flux density behaviour - New design proposal

Finally, the power factor and reactance behaviour over time are depicted in figures 113 and 114.

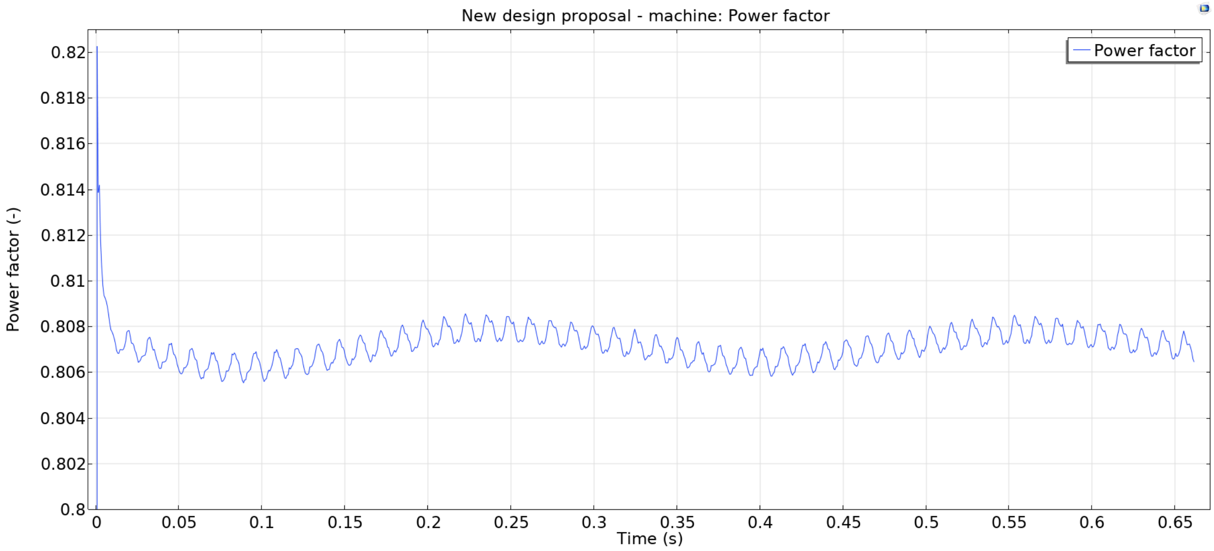

Figure 113: Power factor - New design proposal

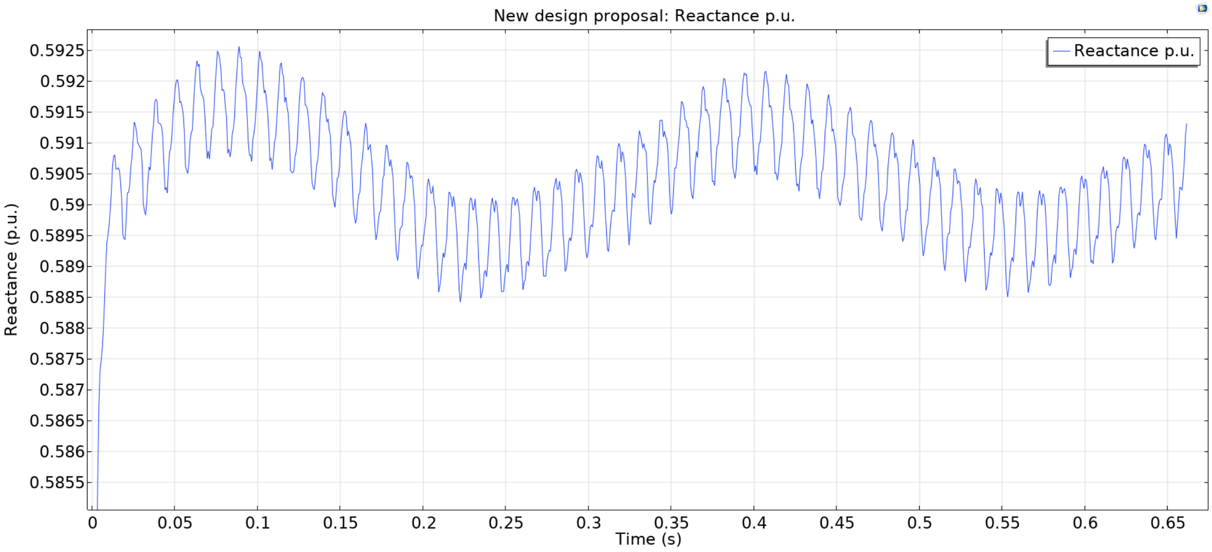

Figure 114: Reactance per unit - New design proposal

11.7 Paper preprint: TechRxiv

Finally, a preprint paper published in TechRxiv is added in the appendix [8]. The title is **Comparison of AC-Superconducting Multi-Phase Symmetric-Winding Topologies for Wind Power Generators with Passive PM Rotors**. The abstract is: In this paper, an AC superconducting multi-phase symmetric-winding machine is designed for a wind power generator to improve its performance and reduce losses, where four handpicked topological designs were explored and compared. In particular, it is found that using high-phase order of unique phasors further improves the performance. The iron losses are reduced, and the rippling behaviour is reduced due to the smoother airgap magnetic flux density. Furthermore, a higher LCM is achieved due to a better slot-pole combination for fractional slot concentrated windings without having space subharmonics. Nonetheless, it is shown that creating a smooth air gap magnetic flux density does not improve the AC hysteretic superconducting losses; thus, further analysis with another approach must be done. Moreover, it is found that the Meisner effect is present in the machine and is inversely proportional to the AC hysteretic superconducting losses. Finally, it shows that a 13-phase AC-superconducting machine can achieve a theoretical limit approaching 101.7017 Nm/kg for the torque-to-weight (TTW) ratio, outperforming classic winding layouts.

The DOI is https://doi.org/10.36227/techrxiv.15123966.v1. The paper is shown on the following pages.

Comparison of AC-Superconducting Multi-Phase Symmetric-Winding Topologies for Wind Power Generators with Passive PM Rotors

Dany Tomé, *Graduate Student Member, IEEE,* Robert Nilssen, and Jonas Kristiansen Nøland, *Member, IEEE*

***Abstract*—In this paper, an AC superconducting multi-phase symmetric-winding machine is designed for a wind power generator to improve its performance and reduce losses, where four handpicked topological designs were explored and compared. In particular, it is found that using high-phase order of unique phasors further improves the performance. The iron losses are reduced, and the rippling behaviour is reduced due to the smoother airgap magnetic flux density. Furthermore, a higher LCM is achieved due to a better slot-pole combination for fractional slot concentrated windings without having space subharmonics. Nonetheless, it is shown that creating a smooth air gap magnetic flux density does not improve the AC hysteretic superconducting losses; thus, further analysis with another approach must be done. Moreover, it is found that the Meisner effect is present in the machine and is inversely proportional to the AC hysteretic superconducting losses. Finally, it shows that a 13-phase AC-superconducting machine can achieve a theoretical limit approaching $101.7017\,\mathrm{Nm/kg}$ for the torque-to-weight (TTW) ratio, outperforming classic winding layouts.**

***Index Terms*—Superconducting coils, AC losses, Multiphase symmetric windings, Iron losses, Fractional Slot Concentrated Windings, Harmonics.**

I. INTRODUCTION

NOwadays, the electric sector is changing rapidly towards a more sustainable energy supply. In particular, the growth of offshore wind power generation has been driven towards bigger wind turbines. Thus, the challenge to create more compact and lightweight structures and machines have become a necessity for the industry.

One of the technologies that have been investigated to create compact generators in recent years is electrical machines (EMs) made with superconductors. Recently three projects have been developed to prove the feasibility of DC-based superconducting machines (SCMs), i.e., a superconducting field winding to enhance the magnetic loading of the machine. Those are INNWIND [1], Suprapower [2], and EcoSwing [3]. The latter has been successfully proved with a technology readiness level (TRL) equal to 7, achieving an airgap shear stress that doubles compared to a permanent magnet generator (PMG) and a weight reduction up to $24\,\%$. In addition, there has been documentation on the reliability and robustness of the generator design [1]–[7].

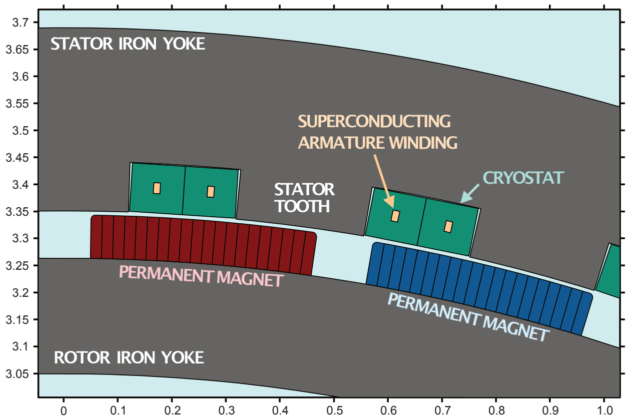

Fig. 1. Illustration of wind generator's machine geometry considered in the paper with slots designed according to cryostat requirements.

Further development of fully superconducting solutions has been achieved for low-speed machines, in which the low electrical frequency cause the AC losses to decrease. Moreover, it is reported that one strategy to minimize total AC loss is by increasing airgap flux density as a result of reducing the armature current needs, which also gives a safety margin to avoid quenching [8]. However, fully superconducting generators require a rotating cryostat which makes them more difficult to manufacture.

PM superconducting wind power generators do not have moving cryostat. However, the main issue is the demagnetization of the PMs, which is strogly related to the interaction with the stator slot design. It is influences by the PM dimensions and the current applied to the superconducting (SC) coils, which is the source of the magnetomotive force (MMF) for demagnetization. In order to avoid the demagnetization of the PMs, the MMF produced by the SC coil is restricted. In particular, the airgap flux density is tried to be ket at least $B_\delta \geq 0.25\,T$ [9]. Also, it has been proved that an iron-cored, both stator and rotor, has better output torque capability and higher efficiency, compared to an iron-cored rotor air-cored stator [9]. Moreover, slotted machines give better support to the coils, higher main flux and save SC material. Fig. 1 depicts an example topology, which will be further explored herein.

Another remarkable technology to improve the performance and compactness is multiphase electrical machines (MEMs), which have been slightly assessed in prior studies. Nonetheless, the major research focus has been on asymmetric wind-

---

D. Tomé is a Master's student of the European Wind Energy Master (EWEM) at TU Delft and NTNU

J. Nøland and R. Nilssen are professors from NTNU

ings, which have multiple sets of m-phase windings, letting aside the symmetric windings of high-phase order. The main difference in having symmetric windings is that they are electromagnetically coupled with all the phases. In contrast, multiple asymmetrical sets of windings are magnetically coupled and electrically isolated in [10]. Furthermore, related to power electronics, symmetric multiphase windings required control of only one electrical system, while asymmetric ones must control multiple electrical systems.

A higher number of phases can produce a more sinusoidal magnetic field than a machine with fewer phases, even if it has a similar number of slots. Also, its harmonics that contribute to useful "saturation harmonics". Extra torque contributions are obtained because the air gap's flux distribution is flattened, avoiding the iron saturation and achieving a wider operational range. In summary, a MEM improves torque density, decreases cogging torque, reduces ripples, reduces rotor losses, and is more fault-tolerant [11]–[14].

This paper performs an investigation into AC-superconducting Multi-Phase Symmetric-Winding Topologies for wind power generators with passive PM rotors to achieve compactness and feasibility. The usage of PM machines contributes to two utmost questions. 1) The performance of multiphase superconducting PM machines; and 2) The effects of smoother magnetic fluxes into the AC armature superconducting coils. The in-depth study is provided in the finite element analysis (FEA) environment.

The present paper is divided into the following five sections. Section II discusses the multiphase winding layouts and the design theory of high-phase order symmetric windings. Moreover, four windings layouts are taken as case designs and compared to assess the multiphase windings. In Section III, the SCMs, their theory, and the formulation behind their superconductivity behaviour are addressed. Finally, Section IV presents the main analysis and results before the paper is concluded in Section V.

II. MULTIPHASE WINDING LAYOUTS

A double-layer fractional-slot concentrated-winding (DL-FSCW) was conveniently selected to compare the various multiphase topologies easily. In comparison, an integer slot winding layout requires different arrangements of poles. The larger the number of phases, the smaller the number of poles, which means lower electrical frequencies and more superconductive material. It is also worth mentioning that a stator with many slots is not possible because of the bending constraints of the superconducting armature coils, which makes a case for the chosen DL-FSCW. For the case of winding layout design of m-phase fractional slot windings, it is useful to comply with specific conditions. First, q has to be reduced so that the numerator and the denominator are the smallest possible integers as follows,

$$q_s = \frac{Q_s}{pm} = \frac{z}{b}, \tag{1}$$

where Q_s is the total number of slots, p is the number of poles, m is the number of phases, and q_s is the number of slots per pole and phase.

A. Conditions of Symmetry

To comply with symmetrical winding for the DL-FSCW, the three following conditions must be fulfilled.

1) First condition of symmetry: For double-layer windings, the first condition of symmetry requires that in the equation

$$\frac{Q_s}{m} = pq_s = p\frac{z}{b}, \quad \frac{p}{b} \in \mathbb{N} \tag{2}$$

2) Second condition of symmetry: This condition is related to the divider t of Q_s and p. Which, in the end, can be written simply in the form: b and m cannot have a common divider.

$$\frac{b}{m} \notin \mathbb{N} \tag{3}$$

3) Third condition of symmetry: For a 24-phase winding, with $Q_s = 48$ and $p = 40$, $q_s = 1/20$ is obtained, complying with the first and second symmetry condition. However, it does not generate 24 symmetric phases. Thus, the third condition for symmetry is proposed as follows:

$$\frac{Q_s'}{m} \in \mathbb{N} \tag{4}$$

Which states that to achieve a multiphase winding, the slots per phase in a base winding shall be an integer number. The number of slots of a base winding is calculated as follows:

$$Q_s' = \frac{Q_s}{t} = \frac{Q_s}{GCD(Q_s, p/2)} \tag{5}$$

For instance, if a 9-phase machine wants to be constructed with a $Q_s = 48$ and $p = 40$, it is impossible because the number of slots per phase is fractional. Thus, a stator in which Q_s is not multiple of m cannot be constructed. Hence, a slot-pole combination of $Q_s = 45$ and $p = 40$ will have 1 slot per phase, which gives a well designed multiphase machine.

B. Multiphase Winding Design

The reference machine is taken from Dong Liu et al [15], [16]. Which is a 48 slots and 40 poles. With this the base winding are calculated, and the winding layouts are designed as follows.

1) 12-phase winding layout: A 12-phase winding layout is selected because it is the highest possible number of phases with the same geometry as a 3-phase winding layout. Both winding layouts are shown in figure 2. Thus, the comparison between them is more straightforward, meaning that the only difference between the two geometries is how the coils are connected. Further, it is essential to notice that the configuration layout has 12 coils as a symmetric winding design. However, there are only six unique phasors, resulting in a dual-six-phase machine.

2) 24-phase winding layout: A 24-phase winding is designed to endorse the finding of the 12-phase machine because it doubles the number of phases. Thus, in principle, the performance enhancement is superior. Moreover, the 24-phase symmetric winding layout has twelve unique phasors, resulting in a dual-twelve-phase machine.

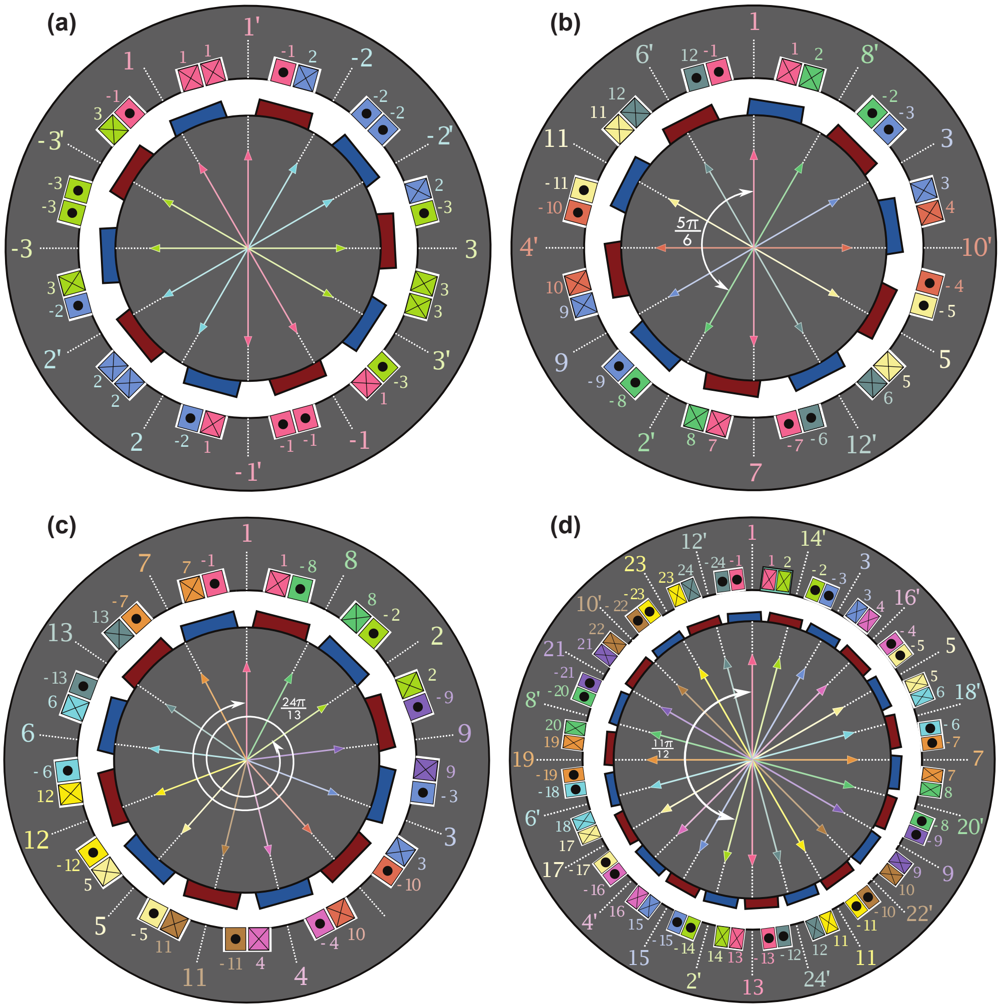

Fig. 2. Base winding topologies of different multiphase configurations. **(a)** 3-phase. **(b)** 12-phase (dual 6-phase). **(c)** 13-phase. **(d)** 24-phase (dual 12-phase).

3) 13-phase winding layout: Furthermore, a 13-phase winding layout shows that having a high order of unique phasors (odd phase number) is the most intelligent way to design a symmetric multiphase winding. Because the 24-phase machine only has 12 unique phasors. Hence, a 13-phase machine with 13 unique phasors enhances further the machine's performance.

III. SUPERCONDUCTING COIL

A superconductor's main characteristic properties are its high conductivity and the expelling of the magnetic field fluxes from the core material. These originate a zero DC resistance under specific conditions of 1) the temperature, 2) the critical current, 3) the magnetic field inside the material, and 4) its pressure. The latter property is particularly essential for room temperature superconductivity [17], while the others are important for low and high-temperature superconductivity $(4 - 77\,K)$.

The first three parameters presented in Table I must be within the critical range to avoid quenching of the superconductivity. This depends on the superconducting material characteristics and the fabrication process. For use in EMs, the superconducting AC losses have to be reduced to obtain a good performance of the generator or motor. In particular, M_gB_2 is a good candidate due to low AC losses, and low price [18]. However, this wire is produced with a cylindrical shape, which means that the magnetic field fluxes are isotropic around the whole material, yet this is true for one wire. For EM applications, the coils are constructed with several wires in which the penetration of magnetic field fluxes depends on the arrangements of the wire in the coil. Thus, the losses will depend on these topological arrangements. For model simplicity and computability purposes, a high-temperature rectangular bulk superconductor wire is considered herein.

A typical superconductor wire is constructed with 4 layers arranged according to the geometry to improve stability, strength, and insulation, as shown in Fig. 3. Having these layers, 4 types of losses taking place in the wire, e.g., 1) eddy current losses due to conducting layers; 2) coupling losses along with the metal layer between superconducting material filaments; 3) ferromagnetic losses that are the hysteresis losses of the metal itself; 4) superconducting hysteresis losses due to varying fields. For the present paper, only the latter is considered.

TABLE I
MODEL PARAMETERS FOR EQS. (6)-(8) REPRESENTING THE SUPERCONDUCTING WIRE

Symbol	Quantity	Value
σ_c	critical conductivity	3.2444×10^{12} S/m
E_c	critical electric field	1×10^{-4} V/m
J_c	critical engineering current density	324.44 A/mm^2
n	exponent factor[1]	25

[1] The exponent factor is handpicked to be in between MgB_2 and REBCO typical values [19], [20].

The E-J power-law is used to formulate the superconductor's conductivity to properly model its interaction with the magnetic vector potential formulation in the COMSOL finite element analysis (FEA) environment (rotating magnetic machinery module). Moreover, in order to account for the non-bounder origin [21], the following consideration is made.

$$J_c = \sigma_c E_c \tag{6}$$

$$|\mathbf{E}| = E_c \left(\frac{|\mathbf{J}|}{J_c} \right)^n \tag{7}$$

$$\sigma(|\mathbf{E}|) = \sigma_c \left| \frac{|\mathbf{E}| - E_c}{E_c} \right|^{1/n-1} \tag{8}$$

The parameters used in eqs. (6)-(8) are given in Table I. For the case of the AC losses (P_{AC}), the superconductor material is assumed to be the entire geometry of the coil. The local current density variable $\mathbf{J}$ is computed as the engineering current density to account for the percentage of superconducting material in the whole wire. Thus, the losses are determined only by hysteresis behaviour by the following expression

$$P_{AC} = \frac{1}{T} \int_{t_0}^{t_0+T} \left[\iint_S \mathbf{J} \cdot \mathbf{E} \, dS \right] dt, \tag{9}$$

where the integration is taken over the conductor's cross-sectional area. In order to account for the transient phenomena due to the bounded origin condition, the t_0 for the integration of eq. (9) is postponed to the steady-state condition is reached. An existing superconductor model from [22]–[24] is used as a reference geometry for this paper. The width and height are increased to be more manageable and achieve a higher critical current as shown in Fig. 3. The coil is modeled as a bulk superconductive surface with an engineering current density ($\mathbf{J}$). The coil's geometry with its 15 turns (n_{coil}) is depicted in Fig. 3, where 4 parallel wires are incorporated in the total area of one turn to handle the rated current. With this new geometry, the following obtained values are given in Table II. All the machine's configurations are designed and simulated with 15 turns per coil and 4500 A as nominal current. The armature's coils are modelled radially aligned for easier construction of the superconductor's racetrack.

IV. TOPOLOGICAL PERFORMANCE ANALYSIS

The topologies are simulated with the specifications shown in Tables III, IV and V, with a machine geometry already depicted in Fig. 1 above. For a surface-mounted PM machine, the torque is as follows.

$$T = \frac{m}{4} \cdot p \cdot \Psi_m \cdot i_q \tag{10}$$

$$P = \frac{2}{p} \cdot \omega \cdot T \tag{11}$$

Here, Ψ_m is the flux linkage of the magnet in the d-axis direction and i_q is the current magnitude aligned in the q-axis. A maximum torque per ampere approach is targeted by aligning the current with the back-EMF voltage (i.e., q-current). This optimal angle is tracked to provide the basis for performing the dq0-transformation in the COMSOL Multiphysics numerical

TABLE II
KEY GEOMETRICAL QUANTITIES AND ELECTRICAL CHARACTERISTICS OF THE SUPERCONDUCTING WIRE

Symbol	Quantity	Value
h_{sc}	height of turn	20.0 mm
w_{sc}	width of turn	0.8 mm
A_{sc}	cross-sectional area of turn	16.0 mm^2
w_{coil}	coil width	12.0 mm
I_s	strand critical current	162.2 A
c_s	no. of parallel strands	8
I_c	wire critical current	1297.7 A
I_w	wire current	1125.0 A
i_w	normalized transport current (I_w/I_c)	0.867
c_w	no. of parallel wires[1]	4

[1] The number of parallel wires required to avoid superconducting quenching.

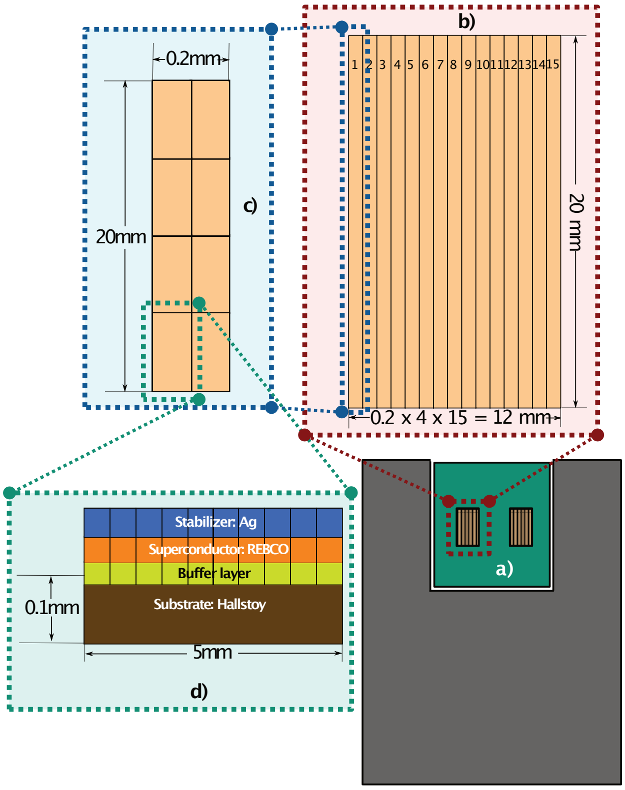

Fig. 3. a) SC coils tangentially arranged inside machine's slots, b) SC coil with its 15 turns, modelled as a bulk superconductive surface ($I_r = 4500\,A$), c) A resized SC wire that represent a quarter of one turn ($I_c = 1297.7\,A$), and d) SC real strand with its 4 layers for stability, strength and insulation ($I_s = 162.2\,A$).

TABLE III
RATED SPECIFICATION OF THE
HANDPICKED WIND POWER GENERATOR

Symbol	Description	Value
P	electrical power[1]	15.00 MW
U	terminal voltage (rms)	$3300/\sqrt{3}\,V$
I	phase current (rms)	$4500/\sqrt{2}\,A$
S	apparent power	18.19 MVA
$\cos(\varphi)$	power factor	0.825
n	mechanical speed[2]	72.2 r/min
T	mechanical torque	18.95 MNm

[1] A 15 MW machine is chosen because it is the biggest wind turbine reference model by the International Energy Agency (IEA) [25].

[2] The mechanical speed is obtain from the reference model.

TABLE IV
DESIGN SPECIFICATIONS OF THE
HANDPICKED WIND POWER GENERATOR

Symbol	Description	Value
D_δ	air gap bore diameter	6693.8 mm
l_a	machine's active length	1.5061 m
B_r	remanent magnet flux density	1.47 T
l_m	magnet's height	80 mm
α_m	magnet's coverage ratio	0.8
N_{coil}	number of turns per coil[1]	15
w_{cryo}	Cryostat's width	100 mm
h_{cryo}	Cryostat's height	92 mm

[1] The number of turns is obtained using the design equations. [26]

TABLE V
INVESTIGATED WINDING DESIGNS
FOR THE WIND POWER GENERATOR

Symbol	Description	#3ph	#12ph	#13ph	#24ph
m	no. of phases	3	12	13	24
p	no. of poles	40	40	48	44
Q_s	no. of slots	48	48	52	48
q_s	slots per pole & phase	$2/5$	$1/10$	$1/12$	$1/22$
N_{ph}	no. of turns per phase	240	60	60	30
k_{wdg}	Winding factor	0.9330	0.9659	0.9927	0.9914
LCM	$LCM(Q_s, p)$[1]	240	240	624	528

[1] The least common multiple between the number of slots and poles gives the cogging torque's empirical "goodness" value. The higher, the better. [27]

environment. Using the dq-transformed voltages, the power factor and the reactance per unit can be calculated as well.

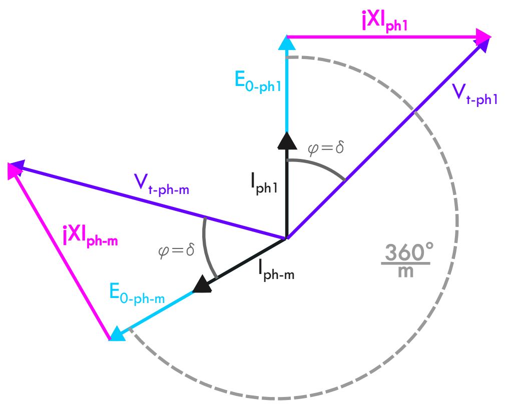

Fig. 4. Phasor diagram for m-phases with the current aligned in the q-axis.

Further, to determine the iron losses, the CAL2 method is employed [28]. For this approach, the α coefficient of the hysteresis loss density is set to 2, where the eddy current coefficient is replaced by a dynamic coefficient and the anomalous losses are not present due to the accuracy of the power coefficient of 1.5, whilst the hysteresis coefficient is kept as the Bertotti's model. The CAL2 method is expressed as follows.

$$p_{CAL2} = K_h(f, B) \cdot \hat{B}^2 f + K_d(f, B) \cdot \hat{B}^2 f^2 \tag{12}$$

According to [29], the third order polynomial to fit K_h and K_d for a low frequency range machine (e.g. $< 400Hz$) can be assumed to vary only in terms of the magnetic flux density $\hat{B}$, thus the third order polynomial curve fit for the propose of this work are described yielding

$$\begin{aligned} K_h(\hat{B}) &= k_{h0} + k_{h1}\hat{B} + k_{h2}\hat{B}^2 + k_{h3}\hat{B}^3, \\ K_d(\hat{B}) &= k_{d0} + k_{d1}\hat{B} + k_{d2}\hat{B}^2 + k_{d3}\hat{B}^3, \end{aligned} \tag{13}$$

where k_{hj} and k_{dj}, for $j = 0, 1, 2, 3$, are constant to be determined by the curve fit. This is done by inserting these expressions into eq. (12) and using the specific loss data for the iron core material in a curve fitting tool. This is provided in Fig. 12 in the appendix. In order to compute the losses of the machine, the calculation has to be done in time domain by time-stepping computations using FEA. In [30], the calculation of the loss density components are formulated as follows.

$$\begin{aligned} p_h &= \frac{1}{\pi T} \int_0^T K_h(f_1, \hat{B}) \cdot B(t) \cdot \left[\frac{dB(t)}{dt}\right] \cdot dt \\ p_d &= \frac{1}{2\pi^2 T} \int_0^T K_d(f_1, \hat{B}) \cdot \left[\frac{dB(t)}{dt}\right]^2 \cdot dt \end{aligned} \tag{14}$$

Furthermore, to compute the total component losses, volumetric integration is conducted, yielding

$$\begin{aligned} P_h &= \rho l_a N_{sector} \iint_S p_h \, dS, \\ P_d &= \rho l_a N_{sector} \iint_S p_d \, dS, \end{aligned} \tag{15}$$

where ρ is the density of the material, l_a is the active length of the machine, N_{sector} is the number of segments or sector in which the entire machine is divided to be simulated in COMSOL, and S is the total integration area of the iron core of the machine.

A. Power, Shear Stress and Power Factor Analysis

The machine's power generation performance comparison is provided in Fig. 6. The rippling behaviour is even further reduced for the 13-phase machine than the 24-phase machine due to the unique phasors. Furthermore, fluctuating behaviour is observed in Arkkio's method used power calculation via the electrical torque. This is due to the Meisner Effect of the armature superconducting coils, which is better highlighted in Fig. 5. Further, it shows that the 13-phase machine has the lowest average of the airgap magnetic flux density generated by the PMs, expecting the lowest power factor among all topologies. On the other hand, the output power for the 13-phase machine is increased because of the higher electrical frequency due to the 48 poles, as shown in Tables VI and VII.

TABLE VI
OBTAINED MEAN ELECTRICAL POWER OVER TIME

Topology	**FEA**	**Analytical**[1]	**Deviation** (%)
3ph machine	15.1871 MW	15.9404 MW	+4.7257 %
12ph machine	15.7861 MW	16.3722 MW	+3.5799 %
24ph machine	16.5837 MW	17.4556 MW	+4.9950 %
13ph machine	17.4137 MW	18.3546 MW	+5.1262 %

[1] Calculated from eq. (11) and the values obtained of the flux linkage from table VII.

TABLE VII
OBTAINED FLUX LINKAGE AND RATED FREQUENCY

Topology	**Flux linkage** (FEA)	**Electrical frequency**
3ph machine	149.1473 Wb	2.5200 Hz
12ph machine	38.2969 Wb	2.5200 Hz
24ph machine	18.5595 Wb	2.7720 Hz
13ph machine	33.0260 Wb	3.0240 Hz

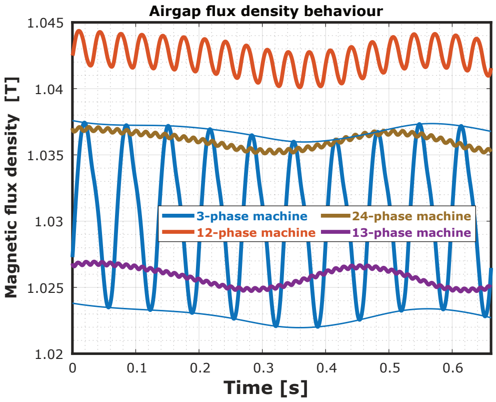

Fig. 5. Airgap magnetic flux density behaviour over time calculated inside the Arkkio's band.

According to Pyrhönen [31], the conventional shear stress for an air-cooled machines is around 59.5 kPa, so at least to double that, the shear stress of a SCM should be around 120 kPa. For the present work, the calculated shear stresses surpass this criterion. In Table VIII, the shear stress values are presented, proven to be at least three times classical machines.

TABLE VIII
OBTAINED SHEAR STRESS FOR THE STUDIED SCM TOPOLOGIES

Topology	**Shear stress**	**Increase**
3ph machine	182.3180 kPa	0.00 %
12ph machine	189.4731 kPa	+3.92 %
24ph machine	199.1164 kPa	+9.21 %
13ph machine	209.0452 kPa	+14.66 %

By increasing the number of phases enhances, the output power and the rippling behavior is further reduced. For the 12-phase winding layout, the output power, compared to the 3-phase, is enhanced even though they share the same geometry and slot-pole combination. For the 24-phase and 13-phase winding layouts, the output power is further increased due to the increase of poles, which means higher electrical frequency.

Moreover, the cogging torque is further reduced with a multiphase fractional winding layout because the LCM is further increased. For the 3-phase and 12-phase winding layouts, the LCM is 240. For the 24-phase and 13-phase windings layouts, the LCMs are 528 and 624, respectively. Hence, the slot-pole combination can be further improved with multiphase FSCW, whilst achieving a good winding layout design.

The power factor and reactance per unit are calculated for each model, as is shown in Table IX. Compared to the reference machine, the power factor is enhanced due to the higher remanent flux density used in the magnets. On the other hand, the power factor depends on the magnetic storage capability of the PM rotor. Two main phenomena are present for a high-phase order machine that reduces the magnetic storage capability of the magnets, resulting in a lower power factor: 1) a high armature reaction that demagnetizes more the PMs; 2) the reduction in the PMs volume by increasing the number of poles for the same machine's diameter.

TABLE IX
OBTAINED POWER FACTOR AND MACHINE REACTANCE

Topology	**Power factor**[1](pf)	**Reactance**[2](x)	**Reactance**[3](x)
3ph machine	0.7267	0.6856 pu	0.6597 pu
12ph machine	0.7309	0.6800 pu	0.6769 pu
24ph machine	0.7184	0.6954 pu	0.7363 pu
13ph machine	0.7076	0.7064 pu	0.7346 pu

[1] Calculated with the dq voltages as follows: $V_q/\sqrt{V_d^2+V_q^2}$

[2] Calculated with the power factor as follows: $\sqrt{1-pf^2}$

[3] Calculated with the terminal voltage, Back-EMF and rated current as follows: $\sqrt{V_t^2-E_0^2}/I_{rated}$

B. Space Harmonics

The space harmonics are calculated from the airgap radial magnetic flux density as is shown in Fig. 7. The multiphase winding layouts eliminate the space sub-harmonics, which explains why the 12-phase machine gives better output than the 3-phase machine, even sharing the same geometry. Furthermore, the working space harmonic for the 13-phase winding layout is lower than the others, as shown in table X. However, the higher electrical frequency in which the machine operates gives a better output power. Nonetheless, a high super-harmonic close to the working harmonic could be further reduced with proper winding designs.

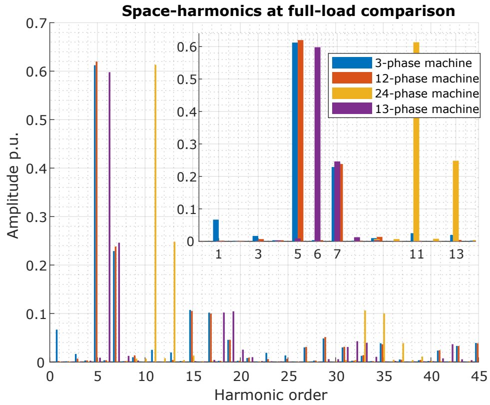

Fig. 7. Space harmonics comparison.

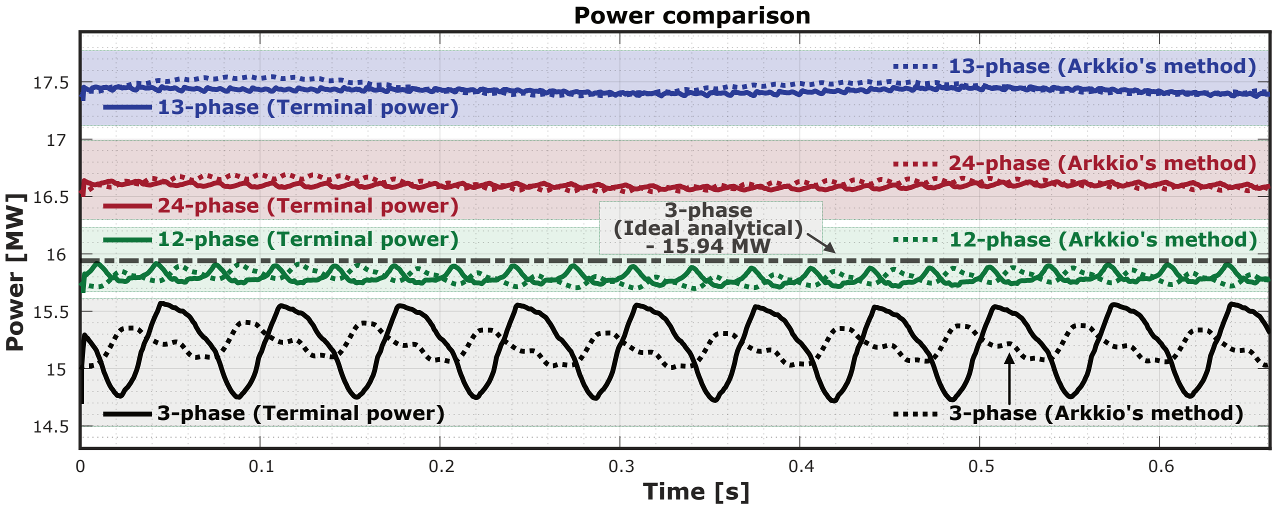

Fig. 6. Machine's power comparison with only q-axis current of 4500 A and mechanical speed of 72.2 r/min. Arkkio's power are obtained from the Maxwell stress tensor, while the reference power calculation is made adding up the instantaneous AC power for all the phases. Straight line, obtained from eq. 11 which gives a deviation of 4.73%.

TABLE X
OBTAINED SPATIAL HARMONICS

Topology	Sub-harmonic value	Working Harmonic	
		Order	Value
3-phase	0.066 69	5	0.6123
12-phase	0	5	0.6199
24-phase	0	11	0.6132
13-phase	0	6	0.5979

TABLE XI
IRON LOSSES COMPARISON.

Model	Hysteresis losses	Dynamic losses	Total iron losses
3ph machine	36.4075 kW	0.7481 kW	37.1556 kW
12ph machine	32.5027 kW	0.5686 kW	33.0712 kW
24ph machine	35.6964 kW	0.7384 kW	36.4348 kW
13ph machine	36.1478 kW	0.8552 kW	37.0030 kW

C. Iron Core Losses

The iron losses (CAL2 method= are presented in Table XI. Furthermore, a relative percentage comparison is made between the models in Figure 8, in which the 3-phase machine is taken as a reference, where the other topologies losses are re-computed relatively to the 3-phase machine to make a proper comparison. First, the iron losses are computed as a percentage of the total machine electrical power. This graph shows that the ripple reduction of high-phase order machines contributes to the reduction of iron losses. The advantages are clear to assess for the 12-phase machine, which has the same geometry as the 3-phase machine, shows a reduction of 14.35 % in the relative iron losses. The 24-phase machine has a reduction of the percentage of iron losses compared to the 3-phase machine. However, due to iron saturation and frequency operation regime, the 24-phase is not improved further than the 12-phase case. The same happens to the 13-phase machine. Nonetheless, it is essential to remark that for the 13-phase machine, the power is increased by 14.66 %, and the relative total iron losses are decreased 13.14 % compared to the 3-phase machine.

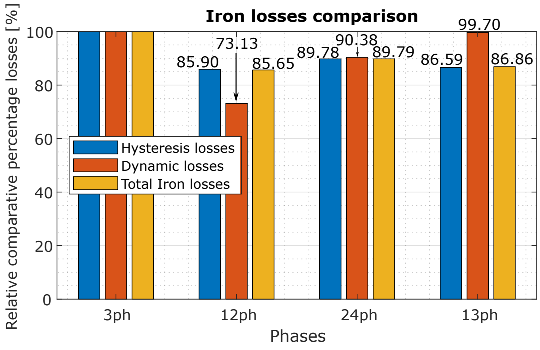

Fig. 8. Iron losses comparison. Relative comparative percentage.

TABLE XII
AC SUPERCONDUCTING LOSSES WITH OR WITHOUT LASER-SCRIBING TECHNIQUE

Model/Fabrication	Non-scribed	Scribed - 10 filaments
3ph machine	83.0558 kW	8.3056 kW
12ph machine	83.6445 kW	8.3645 kW
24ph machine	72.0425 kW	7.2043 kW
13ph machine	59.7262 kW	5.9726 kW

D. AC Superconducting Losses

The AC losses can be reduced per every filament scribed by applying laser-scribing fabrication techniques. The wire is scribed with 10 filaments. Hence, the AC losses are reduced to a tenth of the non-scribed version. In Table XII, the AC losses are presented for all the models with the assumption of the laser scribing technique to reduce further the AC losses.

A good multiphase winding layout design enhances the performance by reducing the iron losses and overall rippling behavior. However, the smoothness of the magnetic flux den-

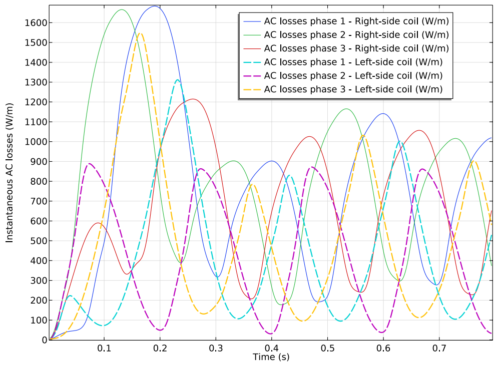

Fig. 9. Instantaneous AC losses for all the phases in a 3-phase machine. One coil side for each phase is shown to identify the different behaviour of the AC losses depending on the amount of magnetic flux density lines crossing the coil.

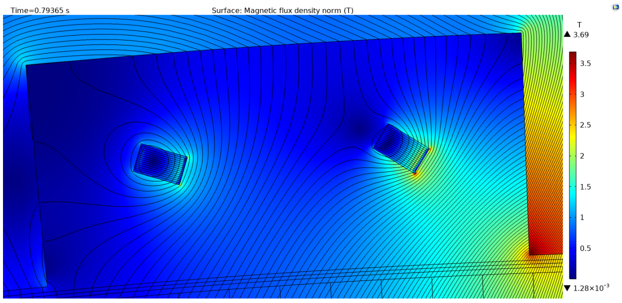

Fig. 10. Coils' angle optimization, where the left coils and right coil are at $-20\,^\circ$ and $-35\,^\circ$ measured from the horizontal axis, respectively.

sities in the air gap provided by high-phase order machines does not reduce the hysteresis AC superconducting losses because it depends mainly on the magnetic flux lines' tilt angle. Moreover, it is known that the stronger the armature reaction, the more tilted is the magnetic flux lines' angle. Thus, the magnetic flux lines are assessed by computing the instantaneous AC losses for the 3-phase machine for one coil side of each phase to depict the AC losses depending on the coil's location inside the slot. For example, Fig. 9 shows that the right-side coils have more AC losses due to there are more magnetic flux lines, hence, higher magnetic flux density in that region of the slot, as is shown in Fig. 10.

Further, a manual parametric sweep of the coil's angular position is performed in steps of $5\,^\circ$ to find a local minimum of AC losses for the 12-phase machine, as is shown in Tables XIII and XIV. With a coil's angular position of $-35°$ for the right-side coil and $-20°$ for the left-side coil, the AC losses are reduced up to $4.5815\,\mathrm{kW}$ for ten filaments scribed. The angle is measured with respect to the horizontal axis, and the center of the coils is the slot's center, as shown in Fig. 10. Furthermore, it is seen that the flux lines enter more perpendicular to the coil's side. In Fig. 11 it can be seen that with a reduction in the AC losses, the fluctuating behavior calculated with Arkkio's method increases, meaning the Meisner effect increases as well. Thus, perpendicular flux lines to the coil's side can decrease further the AC losses. However, this also creates more repulsion of the magnetic flux densities, Meisner effect, creating a stronger magnetic flux density fluctuation in the airgap, harming the machine's mechanical integrity.

TABLE XIII
AC LOSSES - COIL'S ANGLE DEPENDENCY

Coil angle	AC losses	Reduction
$0\,^\circ$	68.2201 kW	0.00 %
$-5\,^\circ$	63.3444 kW	-7.15 %
$-10\,^\circ$	59.3590 kW	-12.99 %
$-15\,^\circ$	55.2684 kW	-18.99 %
$-20\,^\circ$	51.7830 kW	-24.09 %
$-25\,^\circ$	49.6070 kW	-27.28 %
$-30\,^\circ$	47.6165 kW	-30.20 %
$-35\,^\circ$	46.4383 kW	-31.93 %
$-40\,^\circ$	46.8285 kW	-31.36 %
$-45\,^\circ$	47.4000 kW	-30.52 %

TABLE XIV
LEFT COIL ANGLE VARIATION

Left coil angle	Right coil angle	AC losses	Reduction
$-30\,^\circ$	$-35\,^\circ$	46.1453 kW	-32.36 %
$-25\,^\circ$	$-35\,^\circ$	45.9993 kW	-32.57 %
$-20\,^\circ$	$-35\,^\circ$	45.8149 kW	-32.84 %
$-15\,^\circ$	$-35\,^\circ$	45.9966 kW	-32.58 %

Therefore, depending on the machine's loading, the magnetic angle is further tilted, changing the superconducting AC losses of the coils. Thus, a design philosophy for one angular position of the armature superconducting coils at full load and/or no-load is not a good design since the superconducting AC losses are very sensitive to the magnetic flux density angle inside the slot. One solution could be a new design of the slots. However, this complicates the design of the cryocooler. Hence, a 3D design of the superconducting armature coils can solve the angle sensitivity by arranging twisted or non-planar coils inside the racetrack.

E. *Efficiency and Torque Density*

The overall efficiency is calculated as follows.

$$\eta = \frac{P_{out}}{P_{out} + {}^{P_{loss}}/_{COP} + P_{iron}} \times 100\% \tag{16}$$

Here, P_{out}, P_{loss}, COP and P_{iron} are output power, AC losses in armature windings, coefficient of performance of cryocooler, and iron loss respectively. Here, the COP is set to 0.06 at 65 K according to [23].

TABLE XV
CALCULATED EFFICIENCY

Topology	Efficiency (η)
3ph machine	98.8571 %
12ph machine	98.9192 %
24ph machine	99.0651 %
13ph machine	99.2220 %

It is shown in Table XV that the 13-phase machine has higher efficiency than the other topologies. Furthermore, in Table XVI, the highest torque-to-weight (TTW) is for the 13-phase machine. In comparison to the work done by Sung et

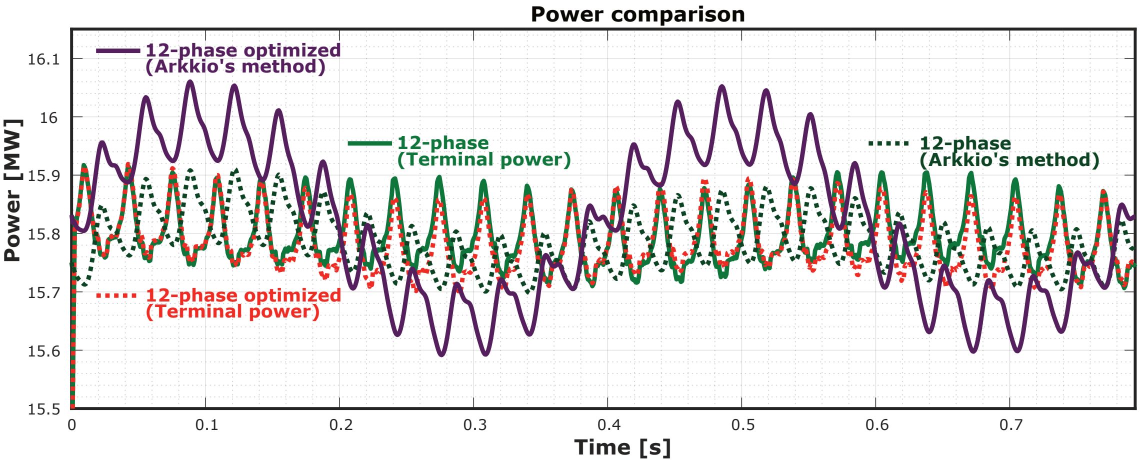

Fig. 11. Power comparison of the 12-phase and optimize version. It is depicted with the Arkkio's method calculation the Meisner effect increases when the AC losses are reduced.

TABLE XVI
TORQUE-TO-WEIGHT (TTW) COMPARISON FOR THE FOUR HANDPICKED MULTIPHASE TOPOLOGIES

Parameter	3ph	12ph	24ph	13ph
W_{iron}	124.1029 ton	124.1029 ton	113.8873 ton	103.8549 ton
W_{SC}[1]	284.1975 kg	284.1975 kg	284.1975 kg	307.8806 kg
W_{mag}[2]	14.7915 ton	14.7915 ton	14.7902 ton	14.7901 ton
W_{total}[3]	139.1790 ton	139.1790 ton	114.1863 ton	118.9529 ton
TTW_{active}[4]	137.8322 Nm/kg	143.2685 Nm/kg	183.4497 Nm/kg	184.9122 Nm/kg
TTW_{Total}[5]	75.8077 Nm/kg	78.7977 Nm/kg	100.8973 Nm/kg	101.7017 Nm/kg

[1] The weight density of the REBCO superconducting tape is $8.19\,\mathrm{g/cm^3}$ according to [22].
[2] The neodymium magnet density is set to $7.4\,\mathrm{g/cm^3}$.
[3] Active weight of the machine.
[4] The Torque-To-Weigth is calculated with FEA values from table VII and equation 11.
[5] TTW calculated by assuming a non-active mass of $55\,\%$ of the total machine's weight.

al. [32] showcases an HTS field winding for a wind power generator that has a TTW of $137.3832\,\mathrm{Nm/kg}$ for the active weight. For the present paper, the TTW for the 3-phase machine is $137.8322\,\mathrm{Nm/kg}$ (i.e., only active mass, which verifies the design's effectiveness. In the end, the 13-phase machine with TTW of $184.9122\,\mathrm{Nm/kg}$ increases by $34\,\%$ the torque density, which means that it has the highest torque density.

V. CONCLUSIONS

In this paper, superconducting machines (SCMs) are analyzed with multiphase topologies. It found that the use of unique phasors or an odd number of phases is an effective winding layout design since only the unique phasors reduce rippling behavior. Moreover, it is proved that the iron losses are further reduced because of the smoother behavior of the magnetic flux densities inside the iron yokes.

The use of symmetric multiphase fractional slot concentrated windings (FSCWs) can further improve the cogging torque without creating space sub-harmonics due to the slot-pole combination gives higher LCMs. Furthermore, a third condition of symmetry is proposed to achieve an optimal design of a multiphase symmetric-winding SCM. Among the topologies compared, the 13-phase machine stands out by improving up to $34\,\%$ in the torque density, in comparison to a conventional 3-phase machine, and with an efficiency limit of $99.2220\,\%$. It is also found that the AC hysteresis superconducting losses in a low-frequency machine are strongly affected by the penetration of the magnetic flux lines into the superconductive material, which depends on the tilting angle of the flux lines. Thence, the AC losses can be further reduced by changing the tilting angle of the flux lines by increasing the armature reaction or changing the coil's angular position. However, decreasing the AC losses means that Meisner's effect is increased because there is less penetration of the magnetic flux lines. Therefore, having a strong Meisner's effect in the SCM weakens the machine's mechanical integrity by increasing the pulsating radial forces in the airgap. Thus, twisted or non-planar superconducting armature coils must be designed in 3D with a better superconducting formulation, e.g., T-A formulation, and an SC model with all the wire layers to optimize the AC losses and reduce the magnetic field's repulsion, the so-called Meisner effect.

From the findings, it is advised to build an alternating current SCM for the purpose of measuring the fluctuating magnetic behavior due to the Meisner effect and validate the results. In addition, a different PM rotor design could be achieved to improve the magnetic storage capability to enhance the power factor. On the one hand, investigate increasing the PM volume, and on the other hand, using PM Halbach array-based rotors. Moreover, the design of a power electronic control unit and an algorithm for high-phase order multiphase symmetric-winding is also part of future work.

APPENDIX A
IRON MATERIAL

The M235-A35 iron material is used in the yoke of the stator and rotor to calculate the iron losses. The B-H curve used in COMSOL is presented in fig. 12. The fitting MATLAB App generates the hysteresis and dynamic losses parameters to calculate the iron losses.

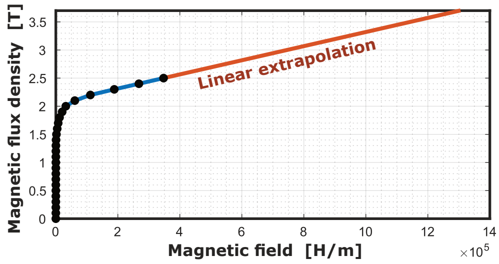

Fig. 12. Curve-fit of the B-H curve of M235-A35 lamination at room temperature.

REFERENCES

[1] D. L. Asger Bech Abrahamsen and H. Polinder, “Final assessment of superconducting (SC) and Pseudo Direct Drive (PDD) generator performance indicators (PI’s). Document information,” INNWIND Project, Tech. Rep. Deliverable D 3.44, 2017. [Online]. Available: https://www.innwind.eu/-/media/Sites/innwind/Publications/Deliverables/DeliverableD344_Final AssessmentSCandPDD_Final_27October2017_Uploaded.ashx?la=da&hash=1E1B17BAFF6FCE3176C6356834F96495F7E1F809

[2] E. Union, “SUPRAPOWER: Superconducting, reliable, lightweight, and more powerful offshore wind turbine,” This project has received funding from the European Union’s Seventh Programme for research, technological development and demonstration under grant agreement number: 308793, Tech. Rep., 2017. [Online]. Available: https://cordis.europa.eu/docs/results/308/308793/final1-suprapower-final-report-tecnalia-20170922-rev-1.pdf

[3] X. Song, C. Buhrer, A. Molgaard, R. S. Andersen, P. Brutsaert, M. Bauer, J. Hansen, A. V. Rebsdorf, J. Kellers, T. Winkler, A. Bergen, M. Dhalle, S. Wessel, M. T. Brake, J. Wiezoreck, H. Kyling, H. Boy, and E. Seitz, *Commissioning of the World’s First Full-Scale MW-Class Superconducting Generator on a Direct Drive Wind Turbine.* IEEE, 2020, vol. 35, no. 3.

[4] I. Marino, A. Pujana, G. Sarmiento, S. Sanz, J. M. Merino, M. Tropeano, J. Sun, and T. Canosa, “Lightweight MgB_2 superconducting 10MW wind generator,” *IOP Science : Superconductor Science and Technology*, vol. 29, no. no. 2, pp. 1–11, 2016.

[5] D. Liu, “Increasing the Feasibility of Superconducting Generators for 10 MW Direct-Drive Wind Turbines,” Ph.D. dissertation, TU Delft, 2017.

[6] A. Bergen, R. Andersen, M. Bauer, H. Boy, M. ter Brake, P. Brutsaert, C. Bührer, M. Dhallé, J. Hansen, H. ten Kate, J. Kellers, J. Krause, E. Krooshoop, C. Kruse, H. Kylling, M. Pilas, H. Pütz, A. Rebsdorf, M. Reckhard, E. Seitz, H. Springer, X. Song, N. Tzabar, S. Wessel, J. Wiezoreck, T. Winkler, and K. Yagotyntsev, “Design and in-field testing of the world’s first ReBCO rotor for a 3.6 MW wind generator,” *Superconductor Science and Technology*, vol. 32, no. 12, p. 125006, dec 2019.

[7] X. Song, A. Bergen, T. Winkler, S. Wessel, M. T. Brake, J. Kellers, H. Putz, M. Bauer, H. Kyling, H. Boy, E. Seitz, C. Buhrer, P. Brutsaert, J. Krause, A. Ammar, J. Wiezoreck, J. Hansen, A. V. Rebsdorf, and M. Dhalle, “Designing and Basic Experimental Validation of the World’s First MW-Class Direct-Drive Superconducting Wind Turbine Generator,” *IEEE Trans. Energy Convers.*, vol. 34, no. 4, pp. 2218–2225, 2019.

[8] T. Balachandran, D. Lee, and K. S. Haran, “Optimal design of a fully superconducting machine for 10- mw offshore wind turbines,” *Proc. IEEE Int. Electr. Mach. Drives Conf. (IEMDC)*, pp. 1903–1909, 2019.

[9] X. Huang, C. Zhou, K. Zhang, L. Wu, J. Zhang, and W. Cao, “Comparison of electromagnetic performance of scpm wind power generators with different topologies,” *IEEE Trans. Appl. Superconduct.*, vol. 29, no. 2, pp. 13–17, 2019.

[10] A. Tessarolo, “Modelling and analysis of multiphase electric machines for high-power applications,” Ph.D. dissertation, University of Trieste, 2011.

[11] C. H. Lee, “Saturation Harmonics of Polyphase Induction Machines,” *Trans. American Inst. Electr. Eng.. Part III: Power App. Syst.*, vol. 80, no. 3, pp. 597–603, 1961.

[12] A. S. Thomas, Z. Q. Zhu, R. L. Owen, G. W. Jewell, and D. Howe, “Multiphase Flux-Switching Permanent-Magnet Brushless Machine for Aerospace Application,” *IEEE Trans. Ind. Appl.*, vol. 45, no. 6, pp. 1971–1981, 2009.

[13] V. Kindl, Z. Ferkova, and R. Cermak, “Spatial harmonics in multi-phase induction machine,” in *2020 ELEKTRO*, May 2020, pp. 1–4.

[14] V. Kindl, R. Cermak, Z. Ferkova, and B. Skala, “Review of time and space harmonics in multi-phase induction machine,” *Energies*, vol. 13, no. 2, 2020.

[15] D. Liu, X. Song, and X. Wang, “Design challenges of direct-drive permanent magnet superconducting wind turbine generators,” in *Proc. Int. Conf. Electr. Mach. (ICEM).* Institute of Electrical and Electronics Engineers Inc., aug 2020, pp. 640–646.

[16] D. Liu, X. Song, X. Wang, M. Elhindi, U. Hasanov, X. Gou, and C. Ye, “Short-circuit characteristics of superconducting permanent magnet generators for 10 MW wind turbines,” *IEEE Trans. Appl. Superconduct.*, vol. 31, no. 5, pp. 4–8, 2021.

[17] E. Snider, N. Dasenbrock-Gammon, R. McBride, M. Debessai, H. Vindana, K. Vencatasamy, K. V. Lawler, A. Salamat, and R. P. Dias, “Room-temperature superconductivity in a carbonaceous sulfur hydride,” *Nature*, vol. 586, no. 7829, pp. 373–377, oct 2020.

[18] M. D. Sumption, F. Wan, M. Rindfleisch, and M. Tomsic, “Ac loss of superconducting materials-refined loss estimates of mgb2 wires for superconducting motors and generators,” *AIAA Propulsion and Energy Forum and Exposition, 2019*, no. August, 2019.

[19] K. Tsuchiya, A. Kikuchi, A. Terashima, K. Norimoto, M. Uchida, M. Tawada, M. Masuzawa, N. Ohuchi, X. Wang, T. Takao, and S. Fujita, “Critical current measurement of commercial REBCO conductors at 4.2 K,” *Cryogenics*, vol. 85, pp. 1–7, jul 2017.

[20] F. Wan, M. D. Sumption, M. A. Rindfleisch, M. J. Tomsic, and E. W. Collings, “Architecture and Transport Properties of Multifilamentary MgB2 Strands for MRI and Low AC Loss Applications,” *IEEE Transactions on Applied Superconductivity*, vol. 27, no. 4, pp. 1–5, 2017.

[21] R. Brambilla, F. Grilli, L. Martini, M. Bocchi, and G. Angeli, “A finite element method framework for modeling rotating machines with superconducting windings,” *arXiv*, vol. 28, no. 5, 2017.

[22] M. Komiya, T. Aikawa, H. Sasa, S. Miura, M. Iwakuma, T. Yoshida, T. Sasayama, A. Tomioka, M. Konno, and T. Izumi, “Design Study of 10 MW REBCO Fully Superconducting Synchronous Generator for Electric Aircraft,” *IEEE Trans. Appl. Superconduct.*, vol. 29, no. 5, pp. 1–6, aug 2019.

[23] S. Miura, M. Iwakuma, and T. Izumi, “Lightweight Design of Tens-MW Fully-Superconducting Wind Turbine Generators with High-Performance REBa2Cu3Oy Wires,” *IEEE Trans. Appl. Superconduct.*, vol. 30, no. 4, pp. 3–8, 2020.

[24] M. Komiya, R. Sugouchi, H. Sasa, S. Miura, M. Iwakuma, T. Yoshida, T. Sasayama, K. Yamamoto, A. Tomioka, M. Konno, and T. Izumi, “Conceptual Design and Numerical Analysis of 10 MW Fully Superconducting Synchronous Generators Installed with a Novel Casing Structure,” *IEEE Trans. Appl. Superconduct.*, vol. 30, no. 4, 2020.

[25] E. Gaertner, J. Rinker, L. Sethuraman, F. Zahle, B. Anderson, G. Barter, N. Abbas, F. Meng, P. Bortolotti, and W. Skrzypinski, “Definition of the IEA 15-Megawatt Offshore Reference Wind Turbine,” National Renewable Energy Laboratory NREL, Tech. Rep., 2020.

[26] S. Vaschetto, A. Tenconi, and G. Bramerdorfer, “Sizing procedure of surface mounted PM machines for fast analytical evaluations,” *2017 IEEE International Electric Machines and Drives Conference, IEMDC 2017*, vol. 63, 2017.

[27] Z. Q. Zhu and D. Howe, “Influence of design parameters on cogging torque in permanent magnet machines,” *IEEE Transactions on Energy Conversion*, vol. 15, no. 4, pp. 407–412, 2000.

[28] D. M. Ionel, M. Popescu, M. I. McGilp, T. J. E. Miller, S. J. Dellinger, and R. J. Heideman, “Computation of core losses in electrical machines

using improved models for laminated steel," *IEEE Trans. Ind. Appl.*, vol. 43, no. 6, pp. 1554–1564, Nov 2007.

[29] T. H. Akinaga, T. Staudt, W. Hoffmann, C. E. Soares, A. A. De Espindola, and J. P. Bastos, "A comparative investigation of iron loss models for electrical machine design using FEA and experimental validation," in *Proc. Int. Conf. Electr. Mach. (ICEM)*. Institute of Electrical and Electronics Engineers Inc., oct 2018, pp. 461–466.

[30] D. M. Ionel, M. Popescu, M. I. McGilp, T. J. E. Miller, S. J. Dellinger, and R. J. Heideman, "Computation of Core Losses in Electrical Machines Using Improved Models for Laminated Steel," *IEEE Trans. Ind. Appl.*, vol. 43, no. 6, pp. 1554–1564, 2007.

[31] J. Pyrhönen, T. Jokinen, and V. Hrabovcov, *Design of Rotating Electrical Machines*. Chichester, UK: John Wiley & Sons, Ltd, dec 2008.

[32] H.-J. Sung, M. Park, B.-S. Go, and I.-K. Yu, "A study on the required performance of a 2G HTS wire for HTS wind power generators," *Superconductor Science and Technology*, vol. 29, no. 5, p. 054001, may 2016. [Online]. Available: https://iopscience.iop.org/article/10.1088/0953-2048/29/5/054001

Dany Josué Tomé Robles was born in Tegucigalpa, Honduras, in 1992. He received two Bachelor's degrees in Physics and Electrical Engineering from the National Autonomous University of Honduras (UNAH). He is currently finishing a joint MSc degree from the European Wind Energy Master (EWEM) program at Delft University of Technology (TU Delft), the Netherlands, and the Norwegian University of Science and Technology (NTNU), Norway. His research interests include AC superconducting coils, Multi-Phase machines, the design of compact machines, electromagnetics, Power System Analysis and Dynamics.

Robert Nilssen received the M.Sc. and Ph.D. degrees from the Norwegian University of Science and Technology (NTNU), Trondheim, Norway, in 1983 and 1989, respectively, specializing in finite-element analysis (FEA) and electrical machines (EMs). He is currently a Full Professor with the Department of Electrical Power Engineering (IEL), NTNU. His research interests include design, optimization, and modeling of industrial EMs for various applications.

Jonas Kristiansen Nøland (S'14-M'17) was born in Drammen, Norway, in 1988. He received the Ph.D. degree in engineering physics from Uppsala University, Uppsala, Sweden, in 2017. Since 2018, he has been an Associate Professor with the Norwegian University of Science and Technology. His main research interests are enabling technologies for electrification in the energy generation and transportation sectors. Dr. Nøland serves as an Editor for the IEEE TRANSACTIONS ON ENERGY CONVERSION and as an Associate Editor for the IEEE TRANSACTIONS ON INDUSTRIAL ELECTRONICS.

[This page intentionally left blank]

NTNU
Norwegian University of
Science and Technology

TUDelft
Delft
University of
Technology